DEVELOPMENT OF MICROSTRUCTURE IN HIGH-STRENGTH WELD DEPOSITS

By
Jer-Ren Yang
Trinity College
Cambridge

A dissertation submitted for the degree of
Doctor of Philosophy
at the University of Cambridge, November 1987.

PREFACE

This dissertation, which is submitted for the degree of Doctor of Philosophy in the University of Cambridge, describes research carried out under the supervision of Dr. H.K.D.H. Bhadeshia in the Department of Materials Science and Metallurgy, Cambridge, between October 1984 and October 1987. Except where acknowlegement and reference to previous work has been made, this work is, to my best knowledge, original and has been done without collaboration. Neither this dissertation, nor any one substantially similar to it has been or is being submitted for a degree, diploma or other qualification at any other University. This dissertation consists of less than sixty thousand words.

Jer-Ren Yang
November 1987

ACKNOWLEDGEMENT

I would like to express my deepest gratitude to Dr. H.K.D.H. Bhadeshia for his continued guidance, encouragement and support throughout the course of this study, and to Professor D. Hull for the provision of laboratory facilities at the University of Cambridge. I am also grateful to my colleagues in the Phase Transformation group, in particular Mr. S.A. Khan and Mr. A. Ashraf. I am indebted to Mrs. S.M. Barkham for her careful typing of this text.

Thanks are also extended to the technical staff of the Department, for maintenance of equipment and for technical advice, particularly Mr. J. Leader (dilatometer) and Mr. D. Nickel (transmission electron microscope).

I greatly acknowledge my wife Hsiang-Yu for her moral support during the period of my research. I also express my gratitude to my parents for their constant encouragement in the time of need.

This work is supported by the Ministry of Education, Republic of China and ESAB Ltd. (U.K.) to whom acknowledgement is also made.

To My Parents

DEVELOPMENT OF MICROSTRUCTURE IN HIGH-STRENGTH WELD DEPOSITS

Jer-Ren Yang

Abstract

The microstructure of high-strength weld deposits has been investigated using thermodynamic analysis and phase transformation theory, backed by experimental confirmation. The microstructures of both the fusion and reheated zones of multirun alloy-steel weld deposits have been studied. The transformation mechanism of acicular ferrite has been established, and a theory for reaustenitisation in steel weld deposits has also been proposed. In addition to the studies on weld metals, some model alloys were fabricated and tested in order to confirm some of the predictions made by the new theory for reaustenitisation.

All the weld metals studied in this investigation possess good hardenability. The primary microstructures of the fusion zone of these weld deposits consist mainly of acicular ferrite with very little allotriomorphic ferrite, Widmanstätten ferrite or microphases. Using transmission electron microscopy, it was confirmed that acicular ferrite had in three dimensions, a thin-plate morphology. In addition to intragranular nucleation on inclusions, acicular ferrite also nucleates sympathetically, giving rise to an interlocking formation of lenticular plates. The microstructure of the reheated zones in these multirun welds has also been examined, and found to be banded due to alloying element segregation during solidification.

It was found that the formation of acicular ferrite at any particular transformation temperature ceased as the carbon concentration of the residual austenite made further diffusionless transformation thermodynamically impossible, and that the transformation exhibits an "incomplete reaction phenomenon". The maximum extent of the acicular ferrite transformation increased with undercooling below the bainite-start temperature. The growth of acicular ferrite is consequently diffusionless, with carbon partitioning into austenite after the transformation event. In this respect, acicular ferrite is found to be identical to bainite. Its morphology differs from that of bainite simply because the former nucleates intragranularly at inclusions within large austenite grains and because of hard impingement between acicular ferrite plates nucleated on adjacent inclusions. It is concluded that acicular ferrite is in fact bainite which nucleates intragranularly within the large austenite grains typical of weld deposits.

Reaustenitisation of high-strength weld deposits, beginning with a microstructure of just acicular ferrite plus austenite, or bainite plus austenite has been studied under

isothermal conditions and in circumstances where the nucleation of austenite is not necessary. It is found that the reverse transformation from acicular ferrite (or bainite) to austenite does not happen immediately the temperature is raised (above that at which the acicular ferrite formed), even though alloy may be within the $\alpha+\gamma$ phase field. Reaustenitisation only occurs when the alloy is heated to a temperature where the carbon concentration of residual austenite exceeds the $\gamma/\alpha+\gamma$ phase boundary. Complete transformation to austenite only occurs at a temperature where the alloy composition equals the austenite equilibrium composition. These results follow directly from the mechanism of the acicular ferrite transformation and can only be explained if acicular ferrite growth is diffusionless.

A theory of kinetic isothermal reaustenitisation for starting microstructures acicular ferrite plus austenite, and bainitic ferrite plus austenite has also been proposed, and found to be in very good agreement with experimental data. It predicts that for a specific amount of reaustenitisation, the transformation time taken is governed not only by the parabolic growth rate constant of austenite but also the surface area of α/γ boundary per unit volume.

Reaustenitisation in a silicon steel has also been investigated. It is found that the last stages of reaustenitisation, which involve long-range diffusion, are tortuously slow. The decomposition of residual austenite during a slow heating has also been studied.

The microstructure of the heat affected zone adjacent to the capping layer of a multirun weld has been studied. It is found that as the austenite grain size decreases, the rate of allotriomorphic ferrite formation increases significantly.

The work provides a basis for the development of computer models for predicting the complete microstructure of steel weld deposits.

CONTENTS

NOMENCLATURE

Braces are used exclusively to denote functional relations; X{T} therefore implies that T is the argument of the function X.

α	allotriomorphic ferrite
α_w	Widmanstätten ferrite
α_a	acicular ferrite
α_b	bainite
γ	austenite
δ	delta-ferrite
α_1	parabolic thickening rate constant
Ae_3	equilibrium $\gamma/(\alpha+\gamma)$ phase boundary
Ae_1	equilibrium $\alpha/(\alpha+\gamma)$ phase boundary
Ae_3'	paraequilibrium $\gamma/(\alpha+\gamma)$ phase boundary
Ae_1'	paraequilibrium $\alpha/(\alpha+\gamma)$ phase boundary
Ar_3	upper temperature limit of the $\alpha+\gamma$ phase field during cooling
Ar_1	lower temperature limit of the $\alpha+\gamma$ phase field during cooling
Ac_3	upper temperature limit of the $\alpha+\gamma$ phase field during heating
Ac_1	lower temperature limit of the $\alpha+\gamma$ phase field during heating
T_o	temperature at which austenite and ferrite of identical composition have the same free energy
T_o'	temperature at which austenite and ferrite (with a certain amount of stored energy associated with transformation strains) of identical composition have the same free energy
W_s	Widmanstätten ferrite start temperature
B_s	bainite start temperature
M_s	martensite start temperature
t	time
T	absolute temperature
$\Delta L/L$	relative length change during isothermal transformation
ΔL_m	maximum relative length change observed during isothermal transformation

$\bar{a}_\alpha$	lattice parameter of ferrite at ambient temperature (25°C) measured by X-ray diffraction
a_α	lattice parameter of ferrite at reaction temperature
$\bar{a}_\gamma$	lattice parameter of austenite at the beginning of an isothermal transformation
a_γ	lattice parameter of austenite at any stage of an isothermal transformation
e_α	linear expansion coefficient of ferrite
e_γ	linear expansion coefficient of austenite
$\overline{X}$	average carbon concentration of alloy
X_i	concentration of alloying element i
S	amount of carbon locked up in ferrite either as carbides or in solution
k_i	partitioning coefficient for alloying element i
T_a	temperature at which acicular ferrite forms
T_γ	temperature of isothermal reaustenitisation
$T_{\gamma 1}$	minimum temperature at which reaustenitisation commences
$T_{\gamma 2}$	minimum temperature at which alloy becomes fully austenitic
V_γ	equilibrium volume fraction of austenite
X_γ	carbon concentration of austenite
X'_γ	carbon concentration of residual austenite when the formation of acicular ferrite ceases
$X_{T'_o}$	carbon concentration given by the T'_o curve
X_{Ae_3}	carbon concentration given by the Ae_3 curve

Chapter One

General Introduction

1.1 Introduction

During the past few years welding has assumed an even greater role in the fabrication of metals, chiefly because of the development of new alloys with enormously increased strength and toughness. However, while considerable progress has been made in the development of steel weld metals largely by an empirical approach, it has become apparent that substantial further improvements were unlikely to be made with this expensive approach without paying careful attention to the development and control of weld microstructure.

The microstructure of steel weld deposits is complex, and its investigation has evolved somewhat separately from that of mainstream of steel research. Indeed, there are considerable problems in identifying microstructural constituents which differ in transformation mechanism rather than just in morphology. The large number of variables associated with the welding process has even made it difficult to quantitatively understand the microstructure. The development of the optimum microstructure also entails considerable empirical and increasingly expensive experimental work. For this reason, a properly developed model is a basic requirement for relating processing conditions to the microstructure and properties of welds. A computer model for the prediction of the microstructure of the fusion zone in low-alloy steel weld deposits has been established [1], but there are many approximations, and it needs to be refined. As to the reheated and heat affected zones, no proper model has yet been proposed, and much further research is necessary.

This work is an attempt to understand the development of microstructure in high-strength steel weld deposits, focussing on the as-deposited and reheated zones of multi-run welds. The microstructure of a steel weld deposit is first surveyed, and the respective phase transformation mechanisms are considered in detail. It will be shown later that the most desirable phase found in welds, acicular ferrite, is in fact intragranularly nucleated bainite, so a review on the bainite transformation is also presented. The reheated zone of a weld deposit undergoes reaustenitisation to varying degrees and a survey of reaustenitisation is also included. Finally, the microstructure of the heat affected zone in the parent metal is also reviewed.

1.2 Solidification Structure of Weld Deposits

Solidification in low-alloy low-carbon steel weld deposits involves the epitaxial growth of delta-ferrite (δ) from base-plate grains at the fusion boundary [2-5]. Due to the constitutional supercooling (Fig. I.1) and the high thermal gradients present in arc welding, solidification proceeds in a cellular manner [6-8]. The resulting δ-ferrite grains have an anisotropic columnar morphology, with their major axes following the direction of maximum heat flow. They grow towards the centre of the weld pool, and solute segregation occurs along their boundaries (Fig. I.2a). On further cooling, austenite (γ) allotriomorphs nucleate (Fig. I.2b) at the delta-ferrite boundaries and further anisotropic austenite growth along delta-ferrite boundaries leads to the formation of columnar austenite grains (Fig. I.2c) which closely resemble the original delta-ferrite morphology. Because of the complex nature of heat flow during arc welding, the isotherms that exist during solidification are in general differently oriented when compared with those present during the $\delta \rightarrow \gamma$ transformation [9]. In these circumstances, the columnar γ grains can curve away from the growth direction of the original δ grains. The daughter austenite grains can sometimes be finer than the delta-ferrite grains if the nucleation rate at δ/δ grain boundaries is high [1,10]. If the cooling rate, carbon level or the substitutional alloy content is sufficiently high, then γ is the first solid to form, and austenite grains grow epitaxially from the fusion boundary into the melt to form the classical columnar morphology [11-13].

Because the γ grain size is quite large (about 100μm wide, 3000 μm long in the form of a hexagonal prism) [14], nucleation both at γ boundaries and within the grains can become important during cooling of the weld deposit. The γ grain size and shape is important in determining the nature of subsequent transformation products such as allotriomorphic ferrite (α), Widmanstätten ferrite (α_w) and acicular ferrite (α_a) (to be discussed later). Bhadeshia et al. [1] have demonstrated quantitative relationships between the γ grain size and the volume fractions of allotriomorphic, Widmanstätten and acicular ferrite obtained in the as-deposited microstructure. Owing to the columnar structure, the epitaxial 'nucleation' events, and the cellular nature of the solidification front [15], Bhadeshia et al. assumed that the morphology of columnar γ grains could approximately be represented by space-filling hexagonal prisms of length 'C' and cross-sectional side length 'L/2' where $C >> L$ (Fig. I.3). This representation is an approximation, since the columnar grains often curve over long distances, due to the nature of heat flow in weld deposits. However, the importance of austenite grain size becomes clear in this representation, since [1]

(i) the volume fraction of allotriomorphic ferrite when processes at the ends of the

hexagonal prism are ignored, is related to L as

$$V_\alpha = \{8qC_1 (L - 2qC)\} /L^2 \quad (I.1)$$

where q is the allotriomorph half-thickness and C_1 is tan30°, and

(ii) the volume fraction of Widmanstätten ferrite is related to L as

$$V_w = \{C_4 G (L - 4qC_1) t_2^2/L^2\} \quad (I.2)$$

where G is the lengthening rate of Widmanstätten ferrite and t_2 and C_4 are complicated functions of nucleation rate etc.

Several authors [16-19] have suggested that an increase in inclusion content should, owing to boundary pinning, lead to a decrease in the γ grain size of a weld deposit. The volume fraction of inclusions in a weld is known to correlate directly with the total oxygen content of the weld [17,20] since most of the oxygen is present in the form of oxides. Harrison et al. [16-19] reported experiments in which welds with different oxygen concentrations were *reheated* into the γ phase field, and held there to allow grain coarsening. The resulting equiaxed γ grains were found to decrease in size with increasing oxygen content. However, this is not relevant to the as-deposited weld microstructure because their experiments deal with reheated weld metal, the γ grain size being controlled by a coarsening reaction driven by the γ/γ surface energy per unit volume, a driving force amounting to only a few $Jmol^{-1}$. The driving force for the formation of γ from δ-ferrite on the other hand is relatively large, and increases indefinitely with undercooling below the equilibrium transformation temperature; pinning by inclusions cannot be effective in such circumstances. It should also be noted that even if the columnar γ grains form directly from the melt by cellular solidification, the cell size at the solid-liquid interface is determined by interface stability [15] in the concentration field ahead of the interface. Oxide and other inclusions which are present in the liquid become passively included in the solid by being trapped at the advancing interface, and do not seem to play any role in influencing the cell size.

In recent research [1,2], there is strong evidence that oxygen content (121 to 418 p.p.m. by weight) does not determine the size of austenite grains in the as-deposited microstructure.

1.3 Transformation from Austenite in Steel Weld Deposit

There is a considerable literature about the study of alloy steel weld deposits. However, some of the terminology on microstructures in weld metal, which has been used in research institutes or industries, is ambiguous. For example, allotriomorphic ferrite (Dubé classification[21]) is sometimes called "grain boundary proeutectoid ferrite" or just "grain boundary ferrite", but these terms fail to distinguish between Widmanstätten ferrite and allotriomorphic ferrite, both of which can form above the eutectoid temperature and at austenite grain boundaries. This literature survey is intended to describe the morphologies of microstructures in weld metals and to summarise their transformation mechanisms where they are known. In a typical steel weld metal, the phases consist of allotriomorphic ferrite, Widmanstätten ferrite, acicular ferrite, idiomorphic ferrite, microphases and inclusions,etc.

1.3.1 Allotriomorphic Ferrite (α)

Allotriomorphic ferrite (α) is the first phase to form during the cooling of low-alloy steel weld deposits to temperatures below the Ae_3 temperature [22-24]. The ferrite usually nucleates heterogeneously at the boundaries of the columnar austenite grains, and these boundaries rapidly become decorated with virtually continuous layers of polycrystalline ferrite. The morphology of this ferrite is like a layer and does not reflect its crystal symmetry [25]. Many of the grains are expected to have a rational orientation relationship with one of adjacent austenite grains.

In plain carbon steels, allotriomorphic ferrite is a dominant phase over wide ranges of composition and temperature. Classically, it used to be the view [26,27] that transformation occurs with α nuclei forming a partially coherent interface with only one adjacent austenite grain, while a random relation exists with the other. The well matched interface, possessing low energy, is then postulated to move by the displacement of ledges; while the other relatively higher energy interface is supposed to be displaced by the continuous motion of the whole interface. It is now known that a ferrite nucleus can have rational orientation relationships with both the adjacent austenite grains in some cases, as pointed out by Hillert [28]. The growth of α has been shown [29,30] in general to be a diffusion-controlled process.

In the case of weld deposits, which generally contain a very low carbon and substitutional alloy content in order to avoid cold cracking, the time for α to saturate the γ boundaries is so small that the formation of much of the α essentially involves the diffusional thickening of layers of grain boundary allotriomorphic ferrite [31]. For this reason, it is reasonable to model this transformation simply in terms of growth (Fig. I.4a)

with the growth occurring by the normal migration of planar austenite-ferrite interfaces, leading to the thickening of the layer of α.

If it is assumed that the growth of the layers of α is diffusion-controlled (diffusion of carbon in austenite), and that for alloy steels the transformation occurs under paraequilibrium conditions [32], then for isothermal transformation the volume fraction of allotriomorphic ferrite (V_α) should mainly depend on the parabolic rate constant α_1, defined [33] by the equation:

$$q = \alpha_1 t^{0.5} \tag{I.3}$$

where q is the allotriomorphic ferrite half-thickness and t is the time, defined to be zero when q = 0. Most steel weld deposits are at least quartenary alloys, and the diffusion control could arise from the diffusion of carbon or of substitutional alloying elements [34]. However, for alloys higher than ternary alloys, the complexity of treating multi-component diffusion is beyond reason [35]. It is noted that the growth of α in dilute steels occurs without the bulk partitioning of substitutional elements [36], especially when the growth rates involved are large [34,37], as is the case for weld deposits. In these circumstances, ferrite growth can occur at a rate controlled by diffusion of carbon in the austenite ahead of the interface. Bhadeshia et al. [31] have assumed that α growth occurs by a carbon diffusion-controlled paraequilibrium mechanism [32] so that substitutional elements do not partition at all between the phases; subject to this constraint, carbon partitions to an extent which allows its chemical potential to be identical in all phases. It is believed [31] that for low-alloy steel weld deposits, most of the variation in volume fraction of allotriomorphic ferrite (V_α) as a function of composition can be rationalised in terms of the parabolic thickening rate constant α_1. Having calculated q, the volume fraction of allotriomorphic ferrite (V_α) is given, from geometrical considerations by equation I.1.

$$V_\alpha = \{8qC_1 (L - 2qC)\}/L^2 \tag{I.1}$$

However, the above theory consistently underestimates the amount of allotriomorphic ferrite. That procedure works well if the calculated volume fraction is multiplied by a factor of about two [1], as presented in equation I.4:

$$V_\alpha = 2.04 [8qC_1(L-2qC)/L^2] + 0.035 \tag{I.4}$$

Evidently, the major assumption, which causes underestimation, is that γ boundaries become decorated uniformly with a thin layer of α, the α then subsequently thickening

normal to the γ grain boundary. In some relatively heavily alloyed welds this is unjustified since discontinuous layers of α are observed [38]. Even when uniform and continuous layers of α are observed, the early stages must involve a faster rate of transformation since growth is initially not confined to one dimension. It is only when site-saturation follows that the model of one dimensional allotriomorph thickening should be a good approximation.

Recently, Bhadeshia et al. [39] have presented a new model (Fig. I.4b) in which the allotriomorphs prior to site-saturation are modelled as discs parallel to the austenite grain boundary planes. Because allotriomorphic ferrite formation is complete within a few seconds, soft impingement between allotriomorphs growing from opposite grain boundaries should not occur and this method takes account of hard impingement. This analysis has been shown to be a better approximation and is also independent of the γ grain shape. The following equation shows the relations for this model [39].

$$- \ln \{1 - \zeta\} = (2 S_v/\phi) (\alpha_1 t^{0.5}) f \{\theta, \eta\alpha_1, I_B, t\} \qquad (I.5)$$

where ζ = the volume of allotriomorphic ferrite (α) divided by its equilibrium volume,
S_v = surface area of α per unit volume,
ϕ = volume fraction of α at equilibrium,
η = ratio of length to thickness of allotriomorph,
α_1 = parabolic rate constant, and
$f \{\phi, \eta\ \alpha_1, I_B, t\}$ is a complicated function of parabolic rate constant and grain boundary nucleation rate per unit area etc.

This new theory has been developed to allow the calculation of the volume fraction of allotriomorphic ferrite in welds, even when site saturation does not occur at an early stage of transformation.

The formation of fairly uniform layers of allotriomorphic ferrite at the columnar austenite grain boundaries is generally accepted to be detrimental to toughness [40-42]. The continuous layers of such ferrite seem to offer little resistance to crack propagation. Increasing the hardenability of weld metal by addition of alloy elements such as Mn, Cr, Ni or Mo to filler metal substantially decreases the amount of allotriomorphic ferrite to the point of extinction. It would be interesting to investigate the optimum alloy addition by alloy design.

1.3.2 Widmanstätten Ferrite (α_W)

It is believed [41,43,44] that during continuous cooling, the transformation temperature of α_W is just below that of allotriomorphic ferrite. In a typical steel weld deposit, there are usually two kinds of Widmanstätten ferrite to be found. Secondary Widmanstätten ferrite nucleates at the allotriomorphic ferrite-austenite boundaries and grows as sets of parallel plates separated by thin regions of austenite, the latter subsequently being retained to ambient temperature or partially transforming to martensite and/or pearlite. These small quantities of retained-austenite, martensite and degenerate pearlite mixtures are called "microphases" [45]. The Welding Institute therefore refers to this Widmanstätten ferrite and its associated microphases as "Ferrite with Aligned Martensite-Austenite-Carbide"[45]. Primary Widmanstätten ferrite can nucleate directly from austenite grain boundaries which are not covered by allotriomorphic ferrite, although its growth mechanism is identical to that of Secondary Widmanstätten ferrite. Widmanstätten ferrite was also thought to form within prior austenite grain [46], and Dubé had classified this morphology as intragranular Widmanstätten ferrite [21]. However, there is still no conclusive evidence for this in terms of serial sectioning experiments, and it is suggested that α_W growth from allotriomorphic ferrite or from austenite grain boundary is favourable.

On an optical scale, α_W possesses a plate shape with a thin wedge section [47]. The formation of α_W is also accompanied by a shape change [47,48], the shape change due to a single wedge of Widmanstätten ferrite consisting of two adjacent and approximately opposite invariant-plane strain deformation. The surface relief of α_W transformation supports the view that in the process of α_W growth, atomic correspondence is maintained at least for substitutional atoms. In steel weld deposits, α_W plate has an apparent aspect ratio (length/thickness) of 20/1 or greater [49,50], but there are no quantitative data about its length and thickness. Bhadeshia [41] has measured the average length and thickness of α_W in Fe - Ni - Si - C steel, and the mean values were found to be about 156 μm and 1.4 μm respectively, after considering sectioning effects. Using the aspect ratio, the shape strain data and elastic constants, the strain energy of α_W has been calculated [47] as about 50 J/mol. At high temperatures, it is impossible for the ferrite plate to grow on its own, since the strain energy due to the shape change would far exceed the available driving force. Hence the reaction involves the simultaneous and adjacent co-operative growth of two plates, which are crystallographic variants whose shape changes cancel each other, drastically reducing the strain energy term. Both the adjacent variants of Widmanstätten plate have been known to possess a rational KS-NW type orientation relation with austenite [25]. Because α_W forms at the low undercoolings, the diffusion of carbon during growth is thermodynamically necessity; however this redistribution of carbon does not

affect the shape change or the displacive* [51] character of the transformation. It is believed [47] that α_w always has an equilibrium carbon content and grows at a constant rate controlled by the diffusion of carbon in the austenite ahead of the plate tip.

In the microstructure of low-carbon low-alloy steel weld metals, the volume fraction (V_w) of Widmanstätten ferrite can be estimated by considering the Widmanstätten ferrite to nucleate at α/γ boundaries and grow into the interior of the columnar austenite grains; the latter are again assumed to be hexagonal prisms and end effects are neglected. Assuming that the α_w nucleation rate per unit area of α/γ interface is constant, the volume fraction of Widmanstätten ferrite is given by [10]

$$V_w = \{C_4\, G\, (L - 4q'C_1)\, t_2^2/L^2\} \qquad (I.6)$$

where C_4 = a constant independent of alloy composition,
G = lengthening rate of α_w,
$L/2$ = cross-sectional side length of hexagonal austenite grain,
q' = a corrected value of α thickness,
t_2 = the time interval in which α_w grows.

As to the mechanical properties, α_w in weld deposits is generally regarded as an undesirable constituent because it is believed to lead to poor fracture toughness [40,52].

1.3.3 Acicular Ferrite (α_a)

Acicular ferrite has been known to be the most desirable microstructural consistent in steel weld metals because its presence directly correlates with improved toughness [53,55]. However, acicular ferrite is not included in the Dubé classification [21], and is not in general found in wrought steels. α_a is characterised by fine elongated platelets of ferrite arranged in an interlocking pattern [40], i.e., non-parallel plates within the columnar austenite grains. It has been suggested that most of acicular ferrite is about 1μm thick [56], and with an apparent aspect ratio (length/thickness) of 3/1 - 10/1, but these measurements do not account for stereological errors. Some authors [56-58] have proposed that the orientation between adjacent acicular ferrite plates results in a "high-angle" interface between the plates. Ito et al. [57] showed the angle was 26° in their research. It is noted that the orientation relation should include both an axis and an angle to form a complete description [59]. Some authors [56,58] have also suggested that individual acicular ferrite plates contain a relatively high dislocation density, however,

* In interstitially alloyed materials, the substitutional lattice can maintain an atomic correspondence while the interstitials diffuse; this is displacive transformation.

there are no quantitative data on this. It would be interesting to examine in detail the orientation relation and boundary structure between adjacent variants, and dislocation density of acicular ferrite as compared with other transformation products. It is believed [60,61] that acicular ferrite nucleates intragranularly at inclusions, and it has also been suggested [62] that the fine interlocking nature of acicular ferrite is due to sympathetic nucleation [63] of ferrite, during which the austenite/ferrite interface could also become an active nucleation site for further ferrite transformation.

The transformation mechanism of acicular ferrite [64,65] has now been studied in detail. Acicular ferrite seems to be bainite which nucleates intragranularly within the large columnar austenite grains. The acicular ferrite plates form by a diffusionless and displacive transformation mechanism, and immediately after plate growth, carbon is partitioned into the residual austenite. Acicular ferrite differs morphologically from classical sheaf-like bainite simply because acicular ferrite nucleates intragranularly at point sites, and is limited also by hard impingement with other plates which form on neighbouring sites. In relatively pure alloy not containing large numbers of inclusions, the bainite nucleates from austenite grain boundaries and classical bainite sheaves form. Acicular ferrite requires the presence of inclusions to enable intragranular nucleation, and will only form when the austenite grain size is relative large, so that events originated from the grain boundaries do not swamp those occurring intragranularly. Intragranular nucleation on inclusions has a higher activation energy compared with grain boundary nucleation [66] so that the number of grain boundary site must be minimised to obtain acicular ferrite. The results on thermodynamics of acicular ferrite transformation in alloy-steel weld deposit are presented in Chapter Three.

1.3.4 Inclusions

Inclusions in weld metals primarily originate from oxides formed during weld deposition, or from the unintentional trapping of slag forming materials (silicates and sulphides) which are used to protect the molten metal during welding. The mean inclusion diameter in low-alloy steel weld deposit can typically be about 0.3μm [60,61], although some inclusions as large as 1μm [67] are sometimes found. The size distribution of inclusions, together with volume fraction measurement, can be realistically determined by using replica techniques and the electron microscope, because 0.3μm inclusion size is at the lowest limit of resolution of optical microscope. The inclusions in welds probably comprise mixed oxides, nitrides, silicates or sulphides which could contain Fe, Mn, Ti, Al, B, Mg, and Ca etc. [61,62,68]. The chemical compositions of inclusions are very complicated, depending on the processes of fusion welding. Generally the volume fraction of inclusions correlates with the total oxygen content of the weld, because most of the

oxygen is present in the form of oxides and most of the inclusions are oxides. Inclusions act as stress concentrators and crack nucleation sites [69] in weld metals, so their content should be kept to a minimum. On the other hand, it is also believed that they may serve as nuclei for the formation of acicular ferrite, a most desirable phase from the point of view of toughness. In order to reach an optimum inclusion content with the right size distribution, it is essential that a method is developed for quantitatively predicting the important characteristics of inclusions in welds.

Recently, it has been found [70] that in steel weld metals relatively large inclusions segregate preferentially, during solidification, to the columnar grain boundaries of the first phase to solidify, whether this is δ-ferrite or austenite. For a steel solidifying as δ-ferrite, the subsequent transformation to austenite would cause the inclusions to finish up in or near the centre of the columnar austenite grains. It should also be noted that the high cooling rates associated with most arc-welding processes causes non-equilibrium solidification so that the final weld is compositionally heterogeneous. The influence of such segregation relative to the position of the inclusions on the final microstructure should be rather important. However, the subject has not yet been studied.

Ito et al. first proposed [71] that the microstructural component present in a given steel weld metal was dependent on the oxygen content. They showed that in Fe-Si-Mn-Ti-B weld metal, at an intermediate oxygen level (270ppm) acicular ferrite structure was formed, while bainitic ferrite structure was apt to appear at low oxygen levels (60ppm), and allotriomorphic ferrite and Widmanstätten ferrite were formed predominantly at higher oxygen contents (440ppm), although there is no evidence at present whether inclusions enhance the grain boundary nucleation rate of allotriomorphic ferrite and Widmanstätten ferrite as well. Some authors [56,60,72] have proposed that the surface energy between the matrix and inclusion (composition, coherency and crystallinity considerations) and the high strains developing around particles during weld metal shrinkage on cooling are likely to enhance ferrite nucleation. It is expected in this respect that more detailed information will become available as analytical techniques progress.

1.3.5 Microphases

The microphases in weld metals correspond to carbon rich regions, which are the last volumes of austenite to transform. Microphases can be found among the non-parallel plates of acicular ferrite, and appear as fine dispersions of islands [73] under the light microscope. On the other hand, thin layer like microphases are located between the parallel plates of Widmanstätten ferrite, and the Welding Institute therefore refers to this Widmanstätten ferrite and its associated microphases as "Ferrite with Aligned Martensite-Austenite-Carbide" [45,74]. It is reasonable to conclude that the microstructures of

microphases depend upon the degree of carbon enrichment. Rejection of carbon by the growing ferrite grains stabilises the surround austenite. Eventually, after mutual impingement of ferrite grains, entrapped austenite transforms to martensite of degenerate pearlite or is retained to ambient temperature. The volume fraction of microphases may be estimated by equating it to the amount of austenite remaining untransformed at the M_s temperature. There is no quantitative information about how the microphases influence the properties [74-76], but it is evident that a large volume fraction of microphases should be detrimental to the toughness of the weld metals.

1.3.6 Idiomorphic Ferrite

Idiomorphic ferrite [21] has a roughly equiaxed morphology, and usually forms intragranularly, presumably at inclusions or other heterogeneous nucleation sites. Idiomorphic ferrite is also sometimes thought to form [46,74] in steel weld metal (often classified as "intragranular polygonal ferrite"). However, there is no systematic work to prove that the observed effects do not arise as a consequence of sectioning effects. In any case the amount of idiomorphic ferrite reported in normal Fe-C-Mn-Si weld metals is very small or completely absent.

1.4 Model of Microstructure in Weld Deposits

A convincing model for the prediction of the microstructure of the fusion zone of steel welds has been proposed by Bhadeshia et al. [1,31,77-79]. This model has been tested successfully for Fe-C-Si-Mn, Fe-C-Si-Mn-Cr, Fe-C-Si-Mn-Mo and Fe-C-Si-Mn-Ni alloy steel welds. A brief description of this model is given below.

In this model the morphology of prior austenite grains it is assumed can be approximated as hexagonal prisms. Fig. I.5 illustrates schematically the development of microstructure in the low-alloy and high-alloy weld deposits. The hexagons represent cross-sections of columnar austenite grains whose boundaries first become decorated with a uniform layer of polycrystalline allotriomorphic ferrite (α) and Widmanstätten ferrite (α_w) growth follows later. Depending on the growth rate of α_w, the α_w then impinges with α on the opposite boundary in the case of low-alloy deposits, or with acicular ferrite (α_a) nucleated on inclusions (black dots) in the case of relatively high-alloy deposits. The microphases originate from the decomposition of residual austenite, which was originally between the interlocking acicular ferrite plates or between the parallel Widmanstätten ferrite plates.

The flow chart (Fig. I.6) demonstrates the steps involved in the calculation of the microstructure for this model. At first, it requires an input of chemical composition, the

austenite grain parameters and the cooling curve of the weld deposit [73], over the temperature range 800→500°C. Having established the input data, the next step involves the calculation of a multicomponent phase diagram, time-temperature-transformation (TTT) and continuous-cooling transformation (CCT) curves, which when combined with the cooling rate equation [77] gives the various reaction-start and finish temperatures. T_h and T_l are the temperatures at which allotriomorphic ferrite formation begins and ends respectively, and M_s, B_s, W_s are the thermodynamically calculated martensite, bainite and Widmanstätten ferrite start temperatures respectively. The volume fraction of allotriomorphic ferrite can be predicted by assuming the paraequilibrium thickening of layers of ferrite [1], and is given by equation I.4. Widmanstätten ferrite is the next phase to grow on further cooling and its volume fraction V_w is given by equation I.6.

$$V_\alpha = 2.04\,[8qC_1(L - 2qC)/L^2] + 0.035 \qquad (I.4)$$

$$V_w = C_4G\,(L - 4qC_1)t_2^2/L^2 \qquad (I.6)$$

where q is the half-thickness of the α layer at the γ grain boundaries, G is the α_w growth rate and t_2 is the time during which α_w grows. In the flow chart, t_1 is the time available for α growth, and t_3 is the time required for an α_w plate to grow across a γ grain, given by:

$$t_3 = (L \sin 60^\circ - 2q)/G \qquad (I.7)$$

To account for physical impingement between α_w and α_a, a further time interval t_c is defined; if $t_3 < t_c$, α_w growth occurs essentially without impingement and $t_2 = t_3$. If on the other hand $t_3 > t_c$, then $t_2 = t_c$, and α_w plates can only grow to a length Gt_c before growth is terminated by physical impingement with α_a plates. The t_c value can be determined by fitting eqs. I.4, 6 and 7 to data from one weld.

The microphases originate from the decomposition of residual austenite to degenerate pearlite and/or martensite, and their volume fraction (V_m) may be estimated by equating it to the amount of austenite remaining untransformed at the M_s temperature. The quantity of γ can be calculated by assuming that α, α_w and α_a form to the maximum extent specified by the lever rule as applied to the Ae_1 and Ae_3' lines at the M_s temperature. Hence, it is assumed that ferrite formation proceeds until the carbon content of the residual austenite reaches Ae_3', so that V_m in general represents the minimum possible estimate of microphase content. This should be a good approximation for the low-alloy steels since the rate of transformation is very high. After estimating V_m, the volume fraction of acicular ferrite (V_a) can be calculated by:

$$V_a = 1 - V_\alpha - V_w - V_m \qquad (I.8)$$

Published experimental data on the variation of microstructure have been analysed using this model for the development of microstructure in low-alloy steel weld deposits [1,31,77-79]. Although this model is in many ways approximate, the results are on the whole in good agreement with theory. However, it will still be necessary to refine the model in the light of further experimental results and theoretical developments.

1.5 Role of Alloying Elements in Transformation Kinetics

The composition of weld metals is decided by many factors, including the composition of the filler wire, factors such as dilution from the base plate, flux chemistry, sheilding gases etc. However, typically the final composition of deposit lies between that of the filler metal and the base metal. In structural steels, the CCT (continuous cooling transformation) curves or TTT (isothermal time-temperature-transformation) curves can effectively be controlled by careful choice of alloying elements. The effects of alloying elements on the hardenability of steel is related directly to their effects on the nucleation and growth kinetics of allotriomorphic ferrite and other austenite decomposition products. Usually the kinetics of the allotriomorphic ferrite transformation is a principal consideration.

The study of the growth kinetics of allotriomorphic ferrite in Fe-X-C ternary system (X is a substitutional alloying element) has been the subject of a great deal of interest in the past two decades [80]. The effect of alloying elements on the transformation of austenite [34,80-83] has been studied considering the behaviour of an alloying element in and close to the moving interface. The rate at which an interface moves depends both on its intrinsic mobility (related to the process of atom transfer across the interface) and on the ease with which any alloying element partitioned during transformation diffuses ahead of the moving interface [25]. Both of these processes dissipate the free energy (ΔG) available for interface motion; when ΔG is mainly used up in driving the diffusion of solute ahead of the interface, growth is said to be diffusion-controlled. On the other hand, interface-controlled growth occurs when most of ΔG is dissipated in the process of atom transfer across the interface.

These concepts can be easily illustrated in terms of the formation of allotriomorphic ferrite from supersaturated γ in a Fe-C alloy isothermally transformed in the $\alpha + \gamma$ phase field at a temperature T. The notation used is defined as follows: the mole fraction of an element i (i = 1,2,3 for C,X,Fe respectively, where X is a substitutional alloying element) in a phase α at the α/γ interface is written χ_i^α, with $\chi_i^{\alpha\gamma}$ representing the mole fraction of

i in α, when α is in equilibrium with γ. In the same manner, χ_i^{γ} and $\chi_i^{\gamma\alpha}$ are defined. $\bar{\chi}_i$ refers to the average mole fraction of i in the alloy concerned. For isothermal growth of ferrite of composition $\chi_1^{\alpha\gamma}$ involving the movement of a flat α/γ interface, the total composition difference between the ferrite and austenite remote from the interface may be written [25]:

$$\Delta\chi = \Delta\chi_{\infty} + \Delta\chi_I + \Delta\chi_D \qquad (I.9)$$

where
$$\Delta\chi_{\infty} = \chi_1^{\gamma\alpha} - \chi_1^{\alpha\gamma}$$
$$\Delta\chi_I = \chi_1^{\gamma} - \chi_1^{\gamma\alpha}$$
$$\Delta\chi_D = \bar{\chi}_1 - \chi_1^{\gamma}$$

$\Delta\chi_{\infty}$ is the difference of mole fraction of carbon between γ and α in the equilibrium state. $\Delta\chi_I$ and $\Delta\chi_D$ are related to the free energies G_I and G_D dissipated in the interface and diffusion processes, respectively, such that $G_D = 0$ when $\Delta\chi_D = 0$ and $G_I = 0$ when $\Delta\chi_I = 0$. Similarly, ΔG is related to $(\Delta\chi_{\infty} - \Delta\chi)$ and is zero when $\chi_1^{\gamma\alpha} = \bar{\chi}_1$.

Actually the rate of interface motion is always under mixed control (since the two processes are in series) but it is said to be diffusion controlled if $|\Delta\chi_D| >> |\Delta\chi_I|$ and because variations in interface parameters have virtually no effect on velocity. In the same way, interface control implies that $|\Delta\chi_D| << |\Delta\chi_I|$ and variations in diffusion parameters then have a negligible effect. True mixed control implies that $\Delta\chi_D$ and $\Delta\chi_I$ are of comparable magnitude.

The diffusional growth of allotriomorphic ferrite (α) during transformation in the $\alpha+\gamma$ phase field involves the partitioning of carbon. If it is considered that the interface moves at a rate which is under mixed diffusion- and interface-control, then a possible carbon concentration profile developed at the α/γ interface can be illustrated in Fig. I.7. However, a reasonable approximation for diffusion-controlled growth is that the compositions of the phase in contact at the interface are in equilibrium. This is because $\Delta\chi_I$ is relatively small for diffusion-controlled growth. Subject to this approximation, local equilibrium is said to exist at the interface. This involves the assumption that the whole of the concentration gradient can be divided up into a large number of thin slices (or sub-systems), each of which has a definite concentration, so that each of the sub-systems can be considered as if it were in local equilibrium. These assumptions are valid if perturbations from equilibrium are not too large [84] and they allow the application of classical equilibrium thermodynamics to steady-state situations like the irreversible process of diffusion which actually arises due to the lack of equilibrium. It is a common assumption that we may apply equilibrium thermodynamics locally [85].

In Fe-X-C ternary systems (X is a substitutional alloying element), the diffusion-controlled growth is complicated by the fact that both interstitial and substitutional atoms diffusion occurs during transformation. The respective diffusion coefficients differ substantially and this combined with the assumption of local equilibrium at the interface leads to a variety of possible growth modes [34,35,80-83]. These models are discussed as follows.

1.5.1 Diffusion-Controlled Growth of Ferrite in Fe-X-C Alloy: Local Equilibrium

During ferrite growth with local equilibrium, the composition of the ferrite (α) and austenite (γ) at the interface can be connected by a tie-line of $\alpha+\gamma$ phase field in the equilibrium Fe-X-C phase diagram. This tie-line which defines the interface composition does not in general pass through the point in the $\alpha+\gamma$ phase which identifies the alloy composition. This is because the diffusivities of interstitial (C) and substitutional alloying elements (X) in the γ are significantly different. The appropriate tie-line must be chosen to satisfy mass conservation conditions at the moving interface and must be consistent with the partitioning behaviour of the alloying elements. Therefore, the tie-line for an alloy transforming at a low supersaturation is such that there is considerable partitioning and long-range diffusion of substitutional alloying element, while the driving force for carbon diffusion is reduced to a level which allows the substitutional element flux to keep pace with the carbon flux at the interface [25]. This situation [34] is referred to as the partitioning under local equilibrium condition (P-LE), as shown in Fig. I.8a.

On the other hand, at higher supersaturations the determining tie-line cause negligible partitioning of substitutional alloying element (X) between the α and γ phases, so that the gradient of the X element in the γ near the interface is very large. This drastically increases the driving force for X diffusion in γ and allows the flux of X to keep up with the long-range diffusion of carbon in γ [25]. In this situation, the diffusion of substitutional alloying element (X) is extremely short-range, being confined to the immediate vicinity of the interface. This condition [34] is designated as the negligible partitioning under local equilibrium (NP-LE), as presented in Fig. I.8b.

The schematic isothermal equilibrium Fe-Mn-C system phase diagram (Fig. I.8c) shows a division of the $\alpha+\gamma$ phase field into domains where either the P-LE or the NP-LE mechanism can operate [25,34]. It should be noted that both of these modes of transformation involve local equilibrium at the interface and are therefore equally favoured on the thermodynamic considerations. Both carbon and substitutional elements diffuse during growth and their fluxes should satisfy the equations for conservation of mass at the interface. Hence the interface velocity calculated from diffusion of C in γ will be identical to that calculated from diffusion of Mn in γ. Both elements control the

growth rate and neither can be said to restrict the interface motion independently.

1.5.2 Diffusion-Controlled Growth of Ferrite in Fe-X-C Alloys: Paraequilibrium

Kinetic factors can prevent the transformation from occurring under equilibrium conditions. Such a case could arise, for example, when a phase change is so rapid that one or more of the components cannot redistribute among the phases in the time scale of experiment. For transformations in steels, the diffusion coefficients of substitutional and interstitial component differ so greatly that it is possible to imagine circumstances where the sluggish substitutional alloying elements may not have sufficient time to redistribute during transformation of γ to α, even though carbon may partition into the austenite.

The term "paraequilibrium" has been introduced [34,37,86] to describe at very high supersaturations a kinetically constrained equilibrium where the two adjoining phases have identical X/Fe atom ratio, but subject to this constraint, carbon is redistributed so that its chemical potential is identical in both phases at the interface. In other words, ferrite formation under the condition of paraequilibrium implies that the substitutional lattice is configurationally frozen and if interface processes are not limiting, the transformation occurs at a rate controlled by the diffusion of carbon in the austenite. Thus, the chemical potentials of the substitutional elements are not equal in the two phases, but carbon which diffuses faster reaches equilibrium subject to this constraint. Typical paraequilibrium and equilibrium Fe-Mn-C diagrams are illustrated in Fig. I.9. It is clear that for any given alloy, a critical undercooling below the equilibrium transformation temperature is necessary before paraequilibrium transformation become feasible. This is because of the fact that a relatively low free energy change accompanies the formation of ferrite which is forced to accept a non-equilibrium substitutional alloy content. It is also noted that the paraequilibrium boundaries project to the binary equilibrium on the Fe-C side and to the T_0 composition (the point where γ and α of the same composition have the equal free energy) on the Fe-X side.

1.6 The Bainite Transformation in Steels

Acicular ferrite in weld metal seems to be intragranularly nucleated bainite. It would be useful to have a review on the bainite transformation, before presenting the study of acicular ferrite formation. Christian and Edmonds [87] have provided an excellent survey of the bainite transformation regarding the microstructure and the transformation mechanism in steels, which will form a framework for the present review.

1.6.1 TTT Diagram and Isothermal Transformation Curve

Bainite forms by the decomposition of austenite at a temperature above the Ms temperature, but below that of fine pearlite. In low alloy steels, the pearlitic and bainitic temperature ranges overlap each other to a considerable extent, and this makes the interpretation of microstructure and kinetics very difficult. However, in medium alloy steels, the isothermal time-temperature-transformation (TTT) diagram possesses two separate C curves; in such a diagram, the upper C curve represents the time taken for the initiation of diffusional transformations such as allotriomorphic ferrite and pearlite, whereas the lower C curve represents the time taken for the initiation of the Widmanstätten ferrite or bainite transformation. The lower C curve usually exhibits a flat top, which corresponds to the Bs (bainitic start) temperature.

An interesting feature of the isothermal bainite transformation is the existence of the "incomplete reaction phenomenon" [88,89]. At any temperature within the bainite transformation range, and in the absence of any interfering secondary reactions, only a limited quantity of bainitic ferrite forms before the reaction terminates. This apparently premature termination occurs before the carbon content of the remaining austenite reaches the equilibrium level indicated by the extrapolated Ae_3 curve. The maximum extent of transformation that can be achieved increases with undercooling below the Bs temperature.

1.6.2 Microstructure

Bainite is essentially a non-lamellar aggregate of plate-shaped ferrite and carbides. The carbide part of the microstructure is not essential to the transformation and in many cases, for example, upper bainite in silicon steel, carbides are totally absent [90]. The ferrite plate size is typically about 10μm long, with a thickness of about 0.2μm [84]. There are two classical morphologies of bainite: upper bainite and lower bainite.

Upper Bainite

Upper bainite consists of platelets of ferrite adjacent to each other, which are in very nearly the same crystallographic orientation in space, so that wherever two adjacent platelets touch, a low angle boundary arises. Elongated cementite particles usually decorate the boundaries of these platelets, the amount of these slabs of cementite depending on the carbon content of the steel. These ferrite platelets, which form a sheaf, have the same habit plane [91-93], and the sheaf itself has a thin wedge plate morphology in three-dimensions on a macroscopic scale [89]. Sheaves of upper bainite inevitably nucleate at prior austenite grain boundaries, and intragranular nucleation is not to be

found. The slabs of cementite (θ) actually form from the austenite between the ferrite platelets, and hence do not have a rational orientation with the ferrite, but have a Pitsch [94] relation with the austenite, i.e.,

$$(001)_\theta \quad // \quad (\bar{2}25)_\gamma$$
$$[100]_\theta \quad // \quad [5\bar{5}4]_\gamma$$

The bainitic ferrite after transformation may retain a small supersaturation of carbon, and has a rational orientation relationship with the austenite.

In silicon-containing steels, Bhadeshia et al. [89] have shown that sub-units within a sheaf of upper bainite can also be distinguished where no carbides form but where the ferrite plateles are separated by films of carbon-enriched retained austenite.

Lower Bainite

Lower bainite is basically very similar to upper bainite, except that the amount of interplate cementite is less, and carbide can additionally be found within the ferrite plate itself. These intra-ferrite carbides can be epsilon carbide in the case of high carbon steels or cementite in case of low carbon steels. It has been estimated [95] that epsilon carbide will not be formed in bainitic ferrite for steels with a carbon content below approximately 0.55 wt%. The carbide particles usually precipitate in a single crystallographic orientation such that their habit plane is inclined at about 60° to the plate axis. In some cases, several variants have been observed [95,96] although the 60° variant still tends to dominate. The inter-plate carbide does not necessarily exist, and results from the diffusional decomposition of carbon-enriched austenite which has not transformed to ferrite. The intra-ferrite cementite precipitated in a single variant has a Bagaryatskii [97] orientation relationship with ferrite, identical to that found when martensite is tempered, i.e.,

$$[100]_\theta \quad // \quad [0\bar{1}1]_\alpha$$
$$[010]_\theta \quad // \quad [1\bar{1}\bar{1}]_\alpha$$
$$[001]_\theta \quad // \quad [211]_\alpha$$

The orientation relation between lower bainitic ferrite and austenite is close to either the Kurdjumov-Sachs [98] or the Nishiyama-Wasserman [99] orientation. The ferrite also forms as sheaves, so that very low angle boundaries arise between platelets within a sheaf.

1.6.3 Carbides Formation during the Bainite Transformation

It is essential that the nature and significance of carbide precipitation accompanying bainite transformation should be examined during studying the mechanism of transformation. For upper bainite, it has been shown [90] that cementite, formed from carbon-enriched residual austenite, is not connected with the actual formation of bainitic ferrite. These carbides form as a result of the diffusional decomposition of austenite which remains untransformed after bainitic ferrite formation. In lower bainite, there are interplate carbides and intra-ferrite carbides. The formation of interplate carbides is the same in upper and low bainite, so that the intra-ferrite carbide precipitation in lower bainitic ferrite may have a critical role to play in the transformation mechanism itself. However, before this issue can be tackled, it is necessary to resolve whether lower bainitic carbides precipitate from a supersaturated ferrite matrix, or whether such precipitation can be described as "interphase precipitation" [100], or just precipitate from austenite during transformation. A rigorous crystallographic analysis [95] has confirmed that the expected three phase α-γ-θ relationship does not exist, and this is interpreted as evidence that an interphase precipitation mechanism does not operate. From electron microscopy observations [95] and the point of view that austenite can comfortably accommodate a large amount of carbon in solid solution compared with supersaturated ferrite, whose equilibrium carbon content is below 0.03 wt%, it seems therefore that not only do carbides nucleate within the ferrite, but the major part of their subsequent growth is accomplished by relieving carbon supersaturated ferrite.

1.6.4 Shape Change

The remaining characteristic feature of bainite formation is that transformation is accompanied by a shape change [89]. This shape change is an invariant plane strain (IPS) in which the broad (habit plane) face of the ferrite plate corresponds to the invariant plane. Thus, the shape change is similar to that found for martensite, and with a large shear component. This shear mechanism of transformation implies that there is an atomic correspondence between parent and product lattices, so it is expected that at least the substitutional element X/Fe atom ratio remains the same everywhere on bainite transformation. It has been estimated [100] that the strain energy of bainite, due to shape strain, is about 400 J/mol.

1.6.5 Atom-Probe Study

An imaging-atom-probe study of the austenite/bainitic-ferrite interface [101] has shown a uniform distribution of substitutional alloying element even at transformation interface. This direct evidence (on an atomic scale) also rules out the local equilibrium model, in

which a required composition spike exists at the interface. There is no solute segregation at the austenite/bainitic-ferrite interface, so solute drag models [102] cannot therefore be claimed to affect the growth of bainite either. It is noted that excess carbon in bainitic ferrite has been found in this direct detection [101].

1.6.6 Photo-Emission Electron Microscopy

The possibility of bainite growing by a paraequilibrium mechanism has been examined with hot-stage experiments in a photo-emission electron microscope [103], so that the individual sheaf of bainite could be directly resolved during transformation. It has been demonstrated that bainite does not grow under conditions of paraequilibrium; the growth rate as measured experimentally is many orders of magnitude higher than that expected from carbon diffusion control.

1.6.7 Thermodynamic Evidence

One of the outstanding problems associated with the study of transformations in steels is the determination of the carbon content of freshly formed bainitic ferrite. The difficulty arises because direct experimental measurements can only focus on the post-transformation composition, which need not correspond to that existing during growth itself. In particular, any carbon supersaturation in the ferrite can be relieved either by the precipitation of carbides within the ferrite or by the partitioning of carbon into the residual austenite by means of diffusion. Both of these processes can be very rapid, because of the high mobility of carbon in iron, especially at the temperatures where bainite forms.

There is, however, a way in which an indirect solution to this problem can be achieved. Consider the case where bainitic ferrite inherits the full carbon content of the parent austenite during transformation. The reaction should, in principle, go to completion since there is no diffusion necessary. In practice, the whole of the austenite grain does not transform instantaneously because of kinetic restrictions (e.g. heterogeneous nucleation); even if the first plate of bainite forms with full supersaturation, it has the opportunity to reject its excess carbon into remaining austenite. Any further increment of transformation is therefore associated with a lower free energy change, due to the higher carbon content of the austenite from which it has to form. Eventually, a stage is reached (the T'_0 curve)

[47,89,101] where transformation become thermodynamically impossible,* since the free energies of austenite and ferrite of the same composition become identical. Hence by monitoring the stage at which the transformation stops, it should be possible to deduce the level of carbon supersaturation in ferrite during growth. The formation of fully supersaturated ferrite requires the carbon content of the austenite to fall below that indicated by the T_0' curve. A less than full supersaturation would lead to transformation conditions closer to equilibrium and a correspondingly increased maximum possible degree of transformation; the terminal carbon content of the austenite would also be higher, and nearer to that given by the extrapolated Ae_3' phase boundary.

A lot of thermodynamic analysis [47,64,65,89,101,105] have been made in an attempt to understand the nature of the "incomplete reaction phenomenon". In this, the bainite reaction stops after a certain amount of transformation at a given temperature and ideally reaches zero transformation at the Bs temperature. Indeed, the incomplete reaction phenomenon can be useful in deducing the level of carbon-saturation that existed in the ferrite during growth. The data [48,65,84,95,99] have shown that the isothermal transformation of bainite stops far short of the Ae_3' curve but is in excellent agreement with the T_0 and T_0' curves. This provides strong evidence that the bainitic ferrite grows with the precise composition of the parent austenite (i.e., its growth is in essence martensitic).

It can therefore be concluded that the formation of bainite involves the propagation of displacive sub-units with a full carbon supersaturation, and partitioning of the carbon into the residual austenite occurs subsequent to transformation, rather than during the growth process.

1.6.8 Nucleation of Bainite

It is essential to obtain an indication of the amount of driving force (ΔF_N) necessary in order to ensure a detectable nucleation rate for bainite transformation. However current nucleation theories are not sufficiently established to enable the calculation of this quantity from first principles. Bhadeshia [100] has solved this problem by resorting to experimental data of Steven and Haynes [106]. The principle of analysis [100] is described as follows.

---

* The locus of such positions, as a function of isothermal transformation temperature defines the T_0' curve, where austenite and ferrite (with a certain amount of stored energy associated with transformation strains) of the same composition have equal free energy. The corresponding curve for stress-free austenite and ferrite of identical composition is conventionally called the T_0 curve [104]. The Ae_3' curve [47] may be similarly defined for growth involving the paraequilibrium partitioning of carbon (but not of substitutional alloying element). For plain carbon steels, it follows that the Ae_3' and Ae_3 curves are identical.

In alloy steels a pronounced bay appears in the time-temperature-transformation TTT curves. The flat top of the lower C curve corresponds to the temperature where a detectable nucleation rate (for ferrite formation with a shape change) first becomes possible, and also represents the transformation start temperature of Widmanstätten ferrite or bainite. The continuity of W_s and B_s with increasing carbon or alloy content has often been found in various treatments [107]. Bhadeshia [100] has used the extensive data of Steven and Haynes [106] which provides a rich source on the variation of the B_s (or W_s) temperature as a function of alloy composition, in order to calculate ΔF_N. In this analysis, the calculation of ΔF_N is under two circumstances - these are when the ferrite nucleates with the parent austenite carbon content, and when ferrite has an equilibrium carbon content; substitutional element partitioning is not allowed in either case. The results have shown (as shown in Fig. I.10) that the formation of a nucleus with the equilibrium carbon content is the true circumstance; the alternative hypothesis would lead to nucleation against a positive driving force for a few of the steels, or in other words there is insufficient driving force to account for nucleation involving the formation of fully supersaturated ferrite. Intuitively, the formation of a nucleus with an equilibrium carbon content seems more reasonable (irrespective of the carbon content of the ferrite at the growth stage) when we consider that the thermally activated development of an embryo to the critical nucleus size occurs through a large number of small scale fluctuations, rather than a sudden large fluctuation. Under such circumstances the rejection of the few carbon atoms that would be expected within the critical nucleus volume should be readily feasible.

Since the flat top of the lower C curve in TTT curves corresponds to the first temperature at which the nucleation of ferrite (which exhibits an invariant plane strain) first becomes possible [90], the above results suggest that the nucleation of both Widmanstätten ferrite and bainite is similar and involves the equilibrium partitioning of carbon [100].

In Fig. I.10b, the variation of ΔF_N with temperature can be understood if it is accepted that the method involved the calculation of the free energy change $\Delta F^{\gamma\rightarrow\gamma_1+\alpha}$ (accompanying the formation of ferrite which at all times contains an equilibrium carbon content) necessary to give a certain constant, detectable nucleation rate (N), irrespective of the steel used [100]. Through nucleation theory,

$$N \propto \nu \exp(-\Delta F^*/RT) \qquad \text{(I.10)}$$

where ν = pre-exponential attempt frequency factor

ΔF^* = activation barrier

R = gas constant

$$\begin{aligned} \text{and} \quad -\Delta F^* &\propto RT \ln\left(\frac{N}{\nu}\right) \\ -\Delta F^* &\propto \beta T \\ \text{where} \quad \beta &= R \ln\left(\frac{N}{\nu}\right) \end{aligned} \tag{I.11}$$

It follows β is a constant since N is a constant irrespective of the steel used. β is expected to be negative, since the nucleation rate must be less than the attempt frequency. It has assumed [100,108] a linear dependence of activation energy on the chemical driving force as equation I.12:

$$\Delta F^* = \lambda_1 \Delta F^{\gamma \rightarrow \gamma_1 + \alpha} + \lambda_1 F_{st} + \lambda_2 \sigma + \lambda_3 \tag{I.12}$$

where λ_1, λ_2 and λ_3 are assumed constant characteristics of the lattice and of the nucleus, F_{st} is the strain enery per unit volume of the nucleus and σ is the interfacial energy per unit area. From equation I.11 and 12, it follows that

$$-\lambda_1 |\Delta F^{\gamma \rightarrow \gamma_1 + \alpha}| \propto |\beta| T - \lambda_1 |F_{st}| - \lambda_2 |\sigma| - \lambda_3 \tag{I.13}$$

so that $-|\Delta F^{\gamma \rightarrow \gamma_1 + \alpha}| \propto T$, as observed in Fig. I.10b. Therefore the curve can be assumed to be a universal curve expressing ΔF_N as a function of temperature, so that a detectable nucleation rate should only be possible in any particular steel if $|\Delta F^{\gamma \rightarrow \gamma_1 + \alpha}|$ for that steel exceeds $|\Delta F_N|$ at the temperature concerned.

1.6.9 Transition from Widmanstätten Ferrite to Bainite, and Bainite to Martensite

One of the outstanding problems in alloy steel design is to understand why the transformation of Widmanstätten ferrite, bainite and martensite do not necessarily occur in all steels. Bhadeshia [100] has used the concepts of the nucleation of ferrite (which exhibit an invariant plane strain) and stored energy due to shape change, and proposed an excellent model. This thermodynamic model is explained as follows.

For Widmanstätten ferrite and bainite transformation, the nucleation stage involves the equilibrium partitioning of carbon, but the subsequent growth depends on the free energy available for the transformation. Thus two different situations are to be considered - growth with equilibrium carbon partitioning (represented by $\Delta F^{\gamma \rightarrow \gamma_1 + \alpha}$) and growth with full carbon supersaturation (represented by $\Delta F^{\gamma \rightarrow \alpha_s}$), corresponding to the Widmanstätten ferrite and bainite respectively.

Letting F_1 = Stored energy per mole of Widmanstätten ferrite
F_2 = Stored energy per mole of bainite ferrite.

Widmanstätten ferrite will then form below the Ae_3 temperature when

$$|\Delta F^{\gamma\rightarrow\gamma_1+\alpha}| > F_1 \quad \text{(I.14a)}$$

$$|\Delta F^{\gamma\rightarrow\gamma_1+\alpha}| > |\Delta F_N| \quad \text{(I.14b)}$$

Because the driving force necessary for a detectable amount of nucleation (i.e., $|\Delta F_N|$) should always be greater than that necessary to sustain growth, $|\Delta F_N|$ will always exceed F_1 and condition (I.14a) becomes redundant, where F_1 = 50 J/mol.

Bainitic ferrite will form below the T_0 temperature when

$$|\Delta F^{\gamma\rightarrow\alpha_s}| > F_2 \quad \text{(I.14c)}$$

$$|\Delta F^{\gamma\rightarrow\gamma_1+\alpha}| > |\Delta F_N| \quad \text{(I.14d)}$$

However, for any steel where the Widmanstätten ferrite transformation precedes bainite formation, condition (I.14d) will probably be redundant. In the case of bainite formation, $|\Delta F_N|$ is always greater than F_2, where F_2 = 400 J/mol.

In Fig. I.11, steels A, B and C correspond to low, medium and high-alloy steels, as manifested in the relative amounts of transformation driving force available at any specified temperature. The driving force necessary for the athermal nucleation of martensite is indicated to be independent of temperature; such behaviour is approximately representative of martensitic transformation in steels [109]. For steel A, all three transformations (i.e., α_w, bainite and martensite) can occur. In steel B when $|\Delta F^{\gamma\rightarrow\gamma_1+\alpha}|$ become greater than $|\Delta F_N|$, $|\Delta F^{\gamma\rightarrow\alpha_s}|$ also exceeds F_2 so that the first shear transformation to occur would lead to bainite formation. Similarly steel C is expected to exhibit only martensite because above M_s temperature $|\Delta F_N|$ is larger than $|\Delta F^{\gamma\rightarrow\alpha_s}|$. The schematic free energy curves can illustrate why all three shear transformations need not occur in all steels.

1.7 Reaustenitisation

In multirun welds, the layers deposited initially are reheated by the deposition of subsequent layers (as shown in Fig. I.12), with a consequent modification of their microstructure. The volume fraction of the reheated zone depends on the number and the size of the beads deposited [110]. Actually some of the reheated zone of weld metal is involved in the process of reaustenitisation. Reaustenitisation is a complicated process, which has not been investigated widely in the past. This reaction is influenced by heating rate, chemical composition and starting microstructure. In this section, the literature on

reaustenitisation beginning with different starting microstructures is surveyed, although work on reaustenitisation from bainite does not seem to have been reported.

1.7.1 Reaustenitisation from Mixture of Ferrite and Pearlite

Investigation of the process of reaustenitisation from a ferrite and pearlite starting microstructure [111-119] have been stimulated by the development of "Dual-Phase Steels" (low carbon manganese steel containing about 1.5 wt% Mn), in which the steel is at least partially reaustenitised and then quenched to produce a mixed microstructure of ferrite and martensite. Most authors have pointed out that the nucleation of austenite seems to occur rather easily at pearlite-ferrite grain boundaries or at pearlite colony intersections, but not within the pearlite colonies. On the other hand, Navara et al. [119] recently studied austenite forming at a relatively low temperature close to the Ae_1 phase boundary, and proposed that the early stages of austenite formation at low temperatures involved the migration of ferrite boundaries with a zone being left behind the migrating boundary, enriched in the manganese concentration. They have suggested that this initial stage of austenite formation is associated with a manganese diffusion induced ferrite boundary migration [120-122]. However, the mechanism of diffusion induced grain boundary migration has not yet been established clearly and there is no work on diffusion induced interphase boundary migration. Although they claim that cementite particles did not play any role in the nucleation of austenite in the steels studied, they did not provide any microstructural evidence to establish the point.

Speich et al. [111] delineated the process of reaustenitisation in the $\alpha + \gamma$ phase field for such steels into three stages: (1) very rapid growth of austenite into pearlite until pearlite dissolution is complete; (2) slower growth of austenite into ferrite; and (3) very slow final equilibration of ferrite and austenite. These three steps are discussed as follows:

(1) Austenite Growth into Pearlite: The first step consists of pearlite dissolution and growth of austenite into the pearlite at a rate controlled primarily by carbon diffusion in the austenite, with the diffusion path lying along the pearlite-austenite interface, with a diffusion distance about equal to the interlamellar spacing of the pearlite. Generally, because of the very short diffusion distance involved, it is expected that the growth rate of austenite during this step will be extremely rapid, assuming that the processes of atom transfer across the interface is not rate limiting.

(2) Austenite Growth into Ferrite: After completion of the first step, or concomitant with it, the austenite will grow into the surrounding ferrite to achieve its equilibrium volume fraction given by the lever rule in the two-phase region. In this stage, the mechanism of austenite growth depends on the driving force for reaustenitisation. At high

austenitising temperatures close to the Ae_3 phase boundary, the driving force for reaustenitisation is high, and the transformation tends toward paraequilibrium or negligible-partitioning-local equilibrium. The concepts of paraequilibrium and negligible-partitioning-local equilibrium have been reviewed in Section 1.5. Paraequilibrium is a state of constrained equilibrium in which the substitutional lattice is configurationally frozen with respect to the transformation interface. Hence, even though the transformation is diffusional in nature, the ratio X/Fe (atom fraction of substitutional element/atom fraction of iron) is the same in ferrite and in austenite. Thus, the chemical potentials of the substitutional elements are not equal in the two phases. Carbon, which diffuses faster, reaches equilibrium subject to this constraint. In negligible-partitioning-local equilibrium (NP-LE), equilibrium is maintained for all species at the transformation interface, but the diffusion of substitutional alloying elements is extremely short-range, being confined to the immediate vicinity of the interface. Other than in the interface region, the concentration of substitutional element is essentially the same in all phases. At lower austenitising temperatures just above the Ae_1 phase boundary, the degree of supersaturation is decreased, and austenite transformation at a low supersaturation is that there is considerable partitioning and long-range diffusion of substitutional alloying element. However, the driving force for carbon diffusion is reduced to a level which allows the substitutional element flux to keep pace with the carbon flux at the interface. This situation is referred as the partitioning under local equilibrium condition (P-LE). The transition from paraequilibrium or NP-LE condition to P-LE condition as the degree of supersaturation is decreased is analogous to the reverse case where ferrite grows from austenite.

(3) Final Equilibration: In the final stage, the manganese concentration gradients within the austenite will be eliminated by diffusion within the austenite. The diffusivity of manganese in austenite is much slower than in ferrite. The time for completion of this process is extremely long.

There is some work [123-126] on reaustenitisation from a eutectoid pearlite structure. It has been found that nucleation of austenite in pearlitic structures occurs preferentially at the edges of the pearlite colonies on the cementite/ferrite boundaries (as shown in Fig. I.13). No evidence has been found for nucleation of austenite at the cementite interlamellar surfaces [125,126] within pearlite colonies. This is true even though the interfacial area per unit volume of lamellar cementite is many times larger than that of the cementite at the pearlite colony intersection. This is probably because the lamellar cementite sometimes has a Bagaryatskii orientation relationship with ferrite, so the interfacial energy may be lower, when compared with that of cementite at the pearlite colony intersections. Numerous observations [124,125] have shown that some lamellar

cementite still remains as the initial stages of austenitisation reach completion. This residual cementite may eventually dissolve or spheroidise depending on the transformation temperature.

1.7.2 Reaustenitisation of a Mixture of Ferrite and Spheroidal Cementite

The ferrite plus spheroidised cementite structure can be obtained by tempering martensite at a temperature just below the Ae_1 phase boundary. In this condition, the cementite particles end up primarily at the ferrite/ferrite grain boundaries, depending on the duration of the heat treatment. On the other hand, if the material is subsequently heavily cold-deformed and recrystallised at a temperature just below Ae_1 again, then a structure in which almost all the spheroidised cementite particles are dispersed in the ferrite matrix away from the ferrite grain boundaries, can be obtained. Such a "strain-anneal" technique has been used [125,127] in order to study whether ferrite grain boundaries have any effect on the nucleation of austenite. It has been confirmed [112,125,127] that the nucleation of austenite in ferrite plus spheroidised cementite structure preferentially occurs at junctions between the cementite particles and ferrite grain boundaries. This is due to the surface energy contribution to the bulk free energy necessary for the formation of stable austenite nuclei. The energy contribution results when the austenite nucleus replaces a small segment of an α/α boundary. Speich et al. [125] also suggested that the density of carbides in the ferrite grain boundaries essentially controlled the number of nucleation events or initial austenite grain size.

In the initial stages of reaustenitisation, the growth of the austenite across the α/α boundaries is inhibited and eventually the austenite film grows around the spheroidised cementite particle to completely envelope the cementite before an appreciable part of the dissolution process has occurred [125,127]. Further growth of the austenite can occur by carbon diffusing from the dissolving cementite to the austenite envelope. During this stage, a more informative approach to the problem of austenitisation would be to determine the mechanism that controls the rate of dissolution of carbide in austenite and how it is modified by alloying elements. Hillert et al. [128] studied the effect of alloying elements on the formation of austenite and the dissolution of cementite, and proposed that during the austenitisation, local equilibrium is established at the cementite/austenite interface, and that the growth rate of austenite (or dissolution rate of cementite) is governed by the diffusion of carbon and other substitutional elements in austenite. After cementite particles located on ferrite grain boundaries are dissolved in the shell of austenite, the austenite grains grow both away from and, more significantly, along the ferrite boundaries. Nemoto [123] conducted in situ experiments using a high voltage electron microscope, and argued that during austenitisation, mobile austenite-ferrite

interfaces are attracted to cementite particles in ferrite matrix. Once the austenite grain has made contact with that cementite particle, the dissolution will accelerate and the austenite grain will grow rapidly around the particle. This seems to provide evidence that the cementite particles which originally resided in the ferrite matrix do not contribute to austenite nucleation [112].

1.7.3 Reaustenitisation of Martensite

Reaustenitisation of martensite has been studied in dual-phase (ferrite/martensite) steels. These are a new class of high-strength low-alloy sheet steels that have superior combinations of strength and uniform ductility. Thomas et al. [131] have used different heat treatment processes to study the microstructures and the mechanical properties of dual-phase steels, and suggested that dual-phase steels with optimum properties can be obtained when the starting structure is martensite. These steels are produced by heating the martensite in the $\alpha+\gamma$ phase region and then quenching to ambient temperature. During isothermal heat treatment in the $\alpha+\gamma$ field, islands of austenite form, and on quenching, this austenite transforms to martensite in a matrix of equiaxed ferrite. It has been found that there are two types of austenite morphology, called globular and acicular austenite* [132-137], forming from the starting martensitic microstructure. Koo et al.[132] have presented a heat treatment process (as shown in Fig. I.14) to produce controlled dual-phase structures (as shown in Fig. I.15). In Fe-0.5Cr-0.1C (wt%) dual-phase steel (Fig. I.15b), globular austenite particles exhibit a continuous network along the prior austenite grain boundaries with the acicular austenite particles within the prior austenite grains. However, there is a significant change in the morphology of austenite as chromium content increases. For example, Fe-4Cr-0.1C (wt%) dual-phase steel (as shown in Fig. I.15a), globular austenite particles not only continuously decorate prior austenite grain boundaries but also display within the austenite grains. Finally they have shown that in a Fe-2Si-0.1C (wt%) dual-phase steel (as shown in Fig. I.15c) the microstructure exhibits a fine, fibrous and discontinuous distribution of acicular particles in the ferrite matrix. It is seen that the influence of the starting martensitic structure is clearly reflected in the last case. The alloying element effects on these austenite morphologies will be discussed later.

The formation of austenite from martensite may occur by classical heterogeneous nucleation [138] at such lattice imperfections as prior austenite boundaries, martensite lath boundaries and matrix/carbide interfaces etc. The dominating influence of boundaries in the austenite nucleation process arises from the reduced activation energy for nucleation at the boundaries, as predicted by classical nucleation theory. However, some attention

---

* "Acicular austenite" grows along the original martensite boundaries, and the plates of austenite appear to have parallel habit planes within a packet of what was originally martensite. Acicular ferrite nucleates from inclusions in weld deposits, and its morphology consists of non-parallel plates of ferrite.

should be given to the role of substructural features in martensite in order to fully establish the mechanism that leads to the preferential nucleation in a martensitic structure. First of all, concerning the presence of retained austenite trapped between martensite laths, these sites may be preferred for nucleation because of the presence of the transformation products formed when retained austenite in the original microstructure decomposes during heating to the reaustenitisation temperature. That is, during heating of the martensitic structure into the two phase region, the retained austenite may decompose into ferrite and carbides. These carbides would be located at the lath boundaries and can provide active sites for austenite nucleation. On the other hand, if retained austenite remains stable on heating into the $\alpha+\gamma$ region, then the reaustenitisation involves only the growth of extant austenite. The relative significance of retained austenite in this process remains unknown. The other feature which may also have to be taken into account is the auto-tempered carbide which is sometimes present within martensite. Speich et al. [125,127] have shown that while austenite nucleation occurs preferentially at the carbides located at grain boundaries, it does not do so at the carbide present in the matrix. Hence auto-tempered carbides probably do not provide sufficient nucleation sites to compete with the other favourable sites for austenite nucleation.

The influence of alloying elements on the growth pattern of austenite from the starting martensitic structure is very important. Koo et al. [132] have suggested that a fine scale, discontinuous, and fibrous distribution of "acicular" austenite particles (becoming martensite after final quenching) is a desirable microstructure with optimum properties. There is some work [133,139] on the influence of alloying elements upon the morphology of austenite formed from martensite, However, the mechanism for the morphological changes is not clear. Plichta et al. [133] classified many ternary Fe-X-C systems (X being substitutional alloying element) into three groups according to the observed morphology of the dual-phase microstructure. In their work, the view is expressed that competitive processes between the nucleation and growth of austenite at lath boundaries and the migration of these boundaries determine the final product shape. More specifically, according to their explanation, rapid migration of the lath boundaries compared to the kinetics of austenite formation results in the globular shape of austenite. On the other hand, they argue that the high rate of austenite nucleation will restrict the lath boundary migration, thereby ensuring the growth of acicular austenite. They further argue that the globular shape of the austenite particles in Fe-Cr-C dual-phase steels can be attributed to a solute drag effect [102] upon growth. However, their explanations are inconclusive. For example, they have not recognised the drastic change in morphology that occurs as a function of alloying element concentration. An "acicular" shape of austenite was observed in a Fe-0.5Cr-0.1C (wt%) dual-phase steel, where, as a globular morphology was obtained in a Fe-4Cr-0.1C(wt%) dual-phase steel.

It is believed that during reaustenitisation, a local equilibrium may be established at the γ/α boundaries. In this condition, substitutional elements may be required to diffuse for a short distance depending on the driving force of reaustenitisation. This idea basically leads to the presence of a narrow concentration "spike" just ahead of and in contact with the advancing boundary. The existence of such a narrow concentration "spike" has been considered in negligible-partitioning local equilibrium (NP-LE), as discussed in Section 1.5.

Assuming the presence of the concentration "spike", it becomes obvious that the kinetics of γ/α boundary migration should be influenced strongly by the type of alloying element present in the dual-phase steels. The microstructures (as shown in Fig. I.15), which Koo et al. [132] have presented for Fe-2Si-0.1C (wt%), Fe-0.5Cr-0.1C (wt%) and Fe-4Cr-0.1C (wt%) dual-phase steels, may qualitatively be explained as follows. In the case of Si steels, the Si concentration "spike" will act as a barrier to carbon diffusion from ferrite to austenite because of the repellent interaction between silicon and carbon atoms [140]. As a result, once austenite nucleation occurs, the lateral thickening of the austenite particles at the lath boundaries will be restricted, and austenite grows in an acicular manner along the lath boundaries, clearly reflecting the starting martensitic structure. In the case of Fe-0.5Cr-0.1C steel, the influence of the boundary diffusion process may overcome the effect of the concentration "spike" with a result that austenite particles grow predominantly along the lath. This situation is entirely changed as the concentration "spike" becomes higher, and hence more influential with increased chromium content. In the case of Fe-4Cr-0.1C steel, the dominating effect of the "spike" on carbon diffusion encourages three-dimensional growth, resulting in the globular shape of austenite particles. This concentration "spike" model seems to be able to explain the observed alloying element effect. It needs further fundamental studies to clarify the role of alloying elements on transformation kinetics.

1.8 The Heat Affected Zone

When base plates are joined by fusion welding, the material of the plates near the fusion boundary is heated to its melting point and then cooled rapidly under conditions of restraint imposed by the geometry of the joint. As a consequence of this severe thermal cycle the original microstructure of the base metal in a region close to the weld is changed; this microstructure is usually referred to as the heat affected zone (HAZ). Experience has show that failures occur frequently in the HAZ. Much work has been devoted to correlating the presence of unfavourable microstructures and the various failure modes that are obtained. Although some work has been done [141-146] on the study of microstructures in the HAZ, a model for predicting the microstructure has not been developed as yet.

The microstructure of the HAZ is influenced by both the peak temperature which determines the austenite grain size and the cooling time over the temperature range 800 → 500°C. Ashby and Easterling [141] have presented a schematic diagram (as shown in Fig. I.16) to divide the HAZ of a single run weld (alternatively the capping layer of a multirun weld) into a number of sub-zones for plain carbon steel. Each zone is characterised by a specific peak temperature (T_p) interval:

(i) solid-liquid transition zone: Tp close to the melting point;
(ii) coarse austenite grain zone: 1100°C < T_p < 1450°C;
(iii) austenite grain refined zone: Ar_3 < T_p < 1100°C;
(iv) partially transformed zone: Ar_1 < T_p < Ar_3; and
(v) tempered zone: Tp below Ar_1.

Each sub-zone refers to a different type of microstructure and, perhaps more importantly, each type of structure possesses different mechanical properties. For instance, the larger austenite grain size can shift the CCT curve to longer reaction times producing more Widmanstätten ferrite, or increasing the possibility of martensitic or bainitic transformation products on cooling. This, together with the larger grain size, may lower the toughness and increase the risk of hydrogen cracking* [147]. The structure type and its sub-zone width are determined by the thermal cycle, i.e., the complete cycle of heating and cooling due to the movement of the arc and the thermal properties of the base metal. However, the prior thermal and mechanical history of the material are very important factors as well. For example, the recrystallisation behaviour during the heating cycle is affected by whether the original material was in cold rolled or annealed condition prior to welding. In microalloyed steel base plate, the onset and extent of the grain growth are influenced by the presence of precipitates and their solubility at high temperature. Thus in order to obtain a reasonable understanding of the HAZ, it is necessary to consider the whole range of phase transformations in the complete thermal cycle.

1.8.1 The Temperature Profiles

With the aim of predicting thermal cycles, most studies of heat flow in HAZ has been undertaken in two discrete areas: computation and direct measurement. Some research [141,143,145] has led to the calculation of the temperature/time profiles in the heat affected zone using the theory of Rosenthal [148], which is found to give a good

* The main source of hydrogen in welding arises from the dissociation of water vapour in the welding arc. The solubility of hydrogen in austenite is much higher than in ferrite. Therefore, as the transformation $\gamma \rightarrow \alpha$ proceeds the austenite becomes progressively more enriched in hydrogen. This may be the reason why cold cracking is so sensitive to the presence of martensite, since the martensite transformation occurs at the lowest temperature and originates from the most hydrogen enriched austenite.

description of the actual thermal cycle. The equations give the temperature T {r,t} at a point lying a distance r from the weld centre-line, as a function of time t, caused by a point heat source moving with velocity υ across the surface. The temperature rises to a peak T_p, and then falls, the time to drop from 800 to 500°C being designated Δt. Two limiting solutions are used. For thick plates, and assuming an instantaneous application of heat, we have [143]

$$T = T_o + \frac{q/\upsilon}{2\pi\lambda t} \text{Exp}(-\frac{r^2}{4at}) \quad \text{(I.15a)}$$

$$Tp = T_c + \frac{2}{\pi e}\frac{q/\upsilon}{\rho c r^2} \quad \text{(I.15b)}$$

$$\Delta t = \frac{q/\upsilon}{2\pi\lambda}\{\frac{1}{773 - T_c} - \frac{1}{1073 - T_c}\} \quad \text{(I.15c)}$$

while for a thin plate, for an instantaneous application of the heat

$$T = T_c + \frac{q/\upsilon}{d(4\pi\lambda\rho ct)^{1/2}} \text{Exp}(-\frac{r^2}{4at}) \quad \text{(I.16a)}$$

$$Tp = T_c + (\frac{2}{\pi e})^{1/2}\frac{q/\upsilon}{2d\rho cr} \quad \text{(I.16b)}$$

$$\Delta t = \frac{(q/\upsilon d)^2}{4\pi\lambda\rho c}\{\frac{1}{(773 - T_c)^2} - \frac{1}{(1073 - T_c)^2}\} \quad \text{(I.16c)}$$

Here q is the arc power, υ the arc speed, e base of natural logarithms = 2.718, λ the thermal conductivity, ρ the density, c the specific heat, a the thermal diffusivity, T_c the preheat temperature and d the plate thickness.

It has found [143] that in the case of thick plates, if the point source of heat is replaced by a circular disc source, the Rosenthal equations can provide a better approximation to arc welding processes. In the case of the HAZ of multirun welds, the effect of superimposition of successive weld thermal cycles on the temperature profile is much more complicated, and much further research is necessary.

1.8.2 Phase Transformations in the HAZ

During the heating cycle, there are several processes occurring in the HAZ, such as α → γ transformation, pearlite/cementite → γ transformation, carbon redistribution in austenite, precipitate (carbonitride) coarsening, precipitate dissolution, austenite grain growth etc. It should be noted that the heating rate is extremely high near the fusion boundary; for example, in normal arc welding it can be of the order of about 200 ~

300°C per second [149], and the continuous heating transformation behaviour will be strongly influenced. This implies that the phase transformations are likely to be affected by the considerable superheating. However, there is little work [150,151] in this area, and further studies are called for. As to the grain growth of austenite, Ion et al. [143] have assumed that grain growth is driven by surface energy. The rate of austenite growth at a fixed temperature T is then given by

$$\frac{dg}{dt} = \frac{k_1}{2g} \exp\left(-\frac{Q}{RT}\right) \tag{I.17a}$$

and the grain size g, after time t is

$$g^2 - g_o^2 = k_1 t \exp\left(-\frac{Q}{RT}\right) \tag{I.17b}$$

where g_o is the initial size, k_1 is a kinetic constant and Q an activation energy. In a weld thermal cycle, the temperature varies with time. Then the grain size g after the cycle is related to the initial grain size g_o by

$$g^2 - g_o^2 = k_1 \int_o^{\infty} \exp\left(\frac{-Q}{RT\{t\}}\right) dt \tag{I.17c}$$

and the relation between final austenite grain size and peak temperature can be calculated. In the case of microalloyed steels, the austenite grain growth is partially controlled by a dispersion of fine precipitates (carbonitrides) which effectively pin the grain boundaries. During the heating cycle the particles coarsen or dissolve depending on the peak temperature, the input energy of the process and the composition of the particles. These problems are very complicated, and need more research [152].

Actually, the grain growth equation should be written as:

$$g^{1/n} - g_o^{1/n} = k_1 \int_o^{\infty} \exp\left(\frac{-Q}{RT\{t\}}\right) dt \tag{I.18}$$

and the prediction of the HAZ austenite grain size on the basis of equation I.18 presupposes that average values of both the time exponent n and the corresponding activation energy Q are available. For most metals and alloys, n varies typically in the range from 0.1 to 0.4 (depending on temperature and composition) even in the absence of effective grain boundary pinning precipitates [153,154]. Only in the case of ultrapure metals annealed at very high temperatures the time exponent n may approach a constant value of 0.5 [154]. In principle, an estimate of n and Q could be obtained from isothermal grain growth experiments [155], but such data are not necessarily representative of the conditions prevailing in a weld HAZ and are likely to be specific to certain alloys. An

additional requirement is that these parameters are essentially constant over a relatively wide temperature range, which clearly is not always met. Although the former problems to some extent can be overcome by the choice of an appropriate calibration technique [143] (i.e., selecting n = 0.5 and fitting the integrals at fixed points to specific data through adjustment of Q), an experimental verification of the various approximations involved is still lacking. More work will be needed in order to predict the grain size of austenite.

During the cooling cycle, the austenite transformation kinetics depend on austenite grain size and chemical composition. The allotriomorphic ferrite usually forms first along the austenite grain boundaries on cooling, and pearlite, Widmanstätten ferrite, bainite and martensite form later. More work is needed to rationalise quantitatively the grain size effect on this part of transformation cycle.

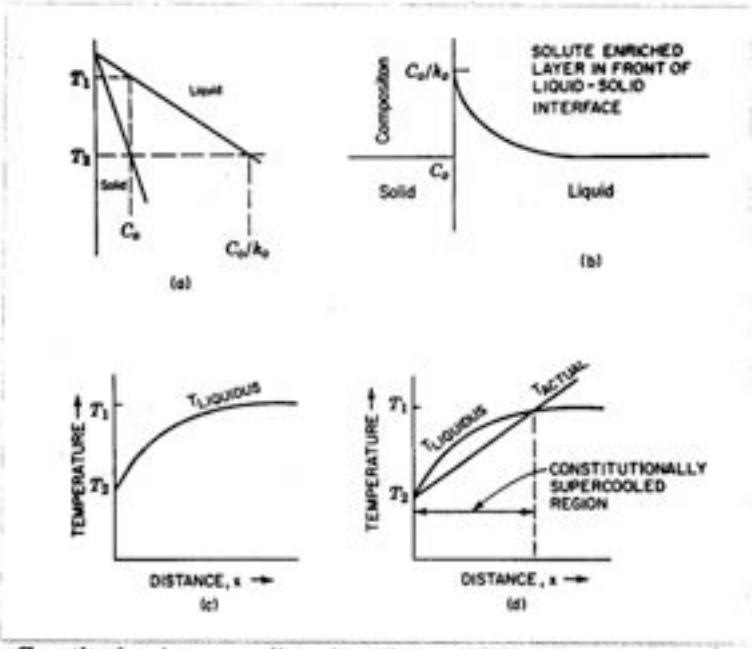

Figure I.1 - Constitutional supercooling in alloy solidification. (a) Phase diagram; (b) solute-enriched layer in front of solid-liquid interface; (c) liquidus versus distance from solid-liquid interface; (d) constitutional supercooling layer.

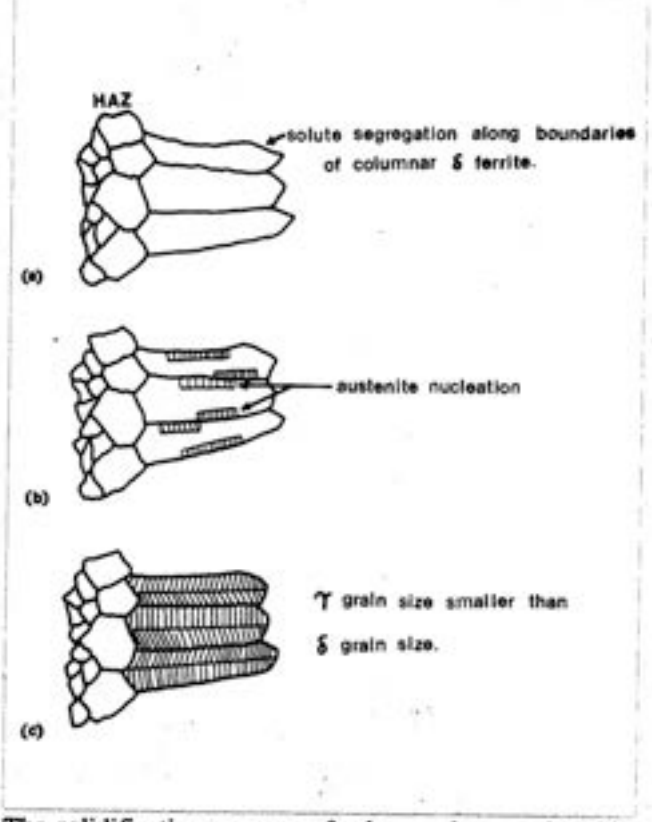

Figure I.2 - The solidification sequence for low carbon steel weld metal deposit.

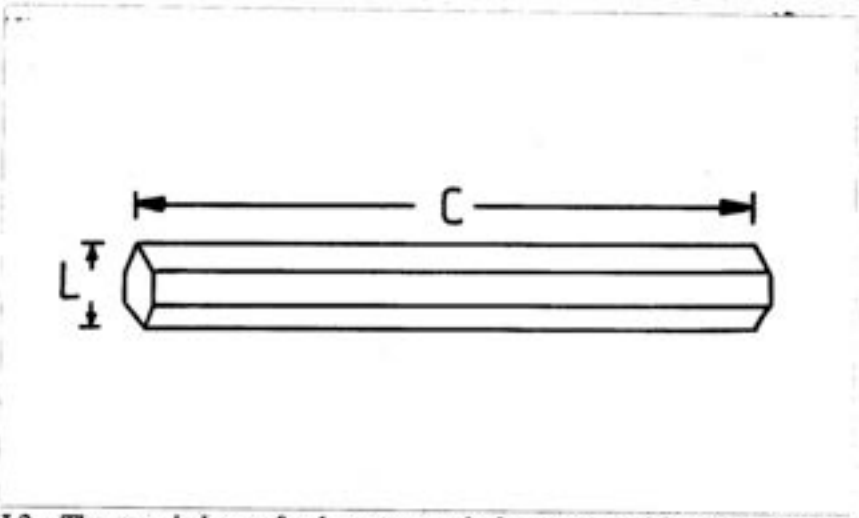

Figure I.3 - The morphology of columnar γ grain is represented by a hexagonal prism.

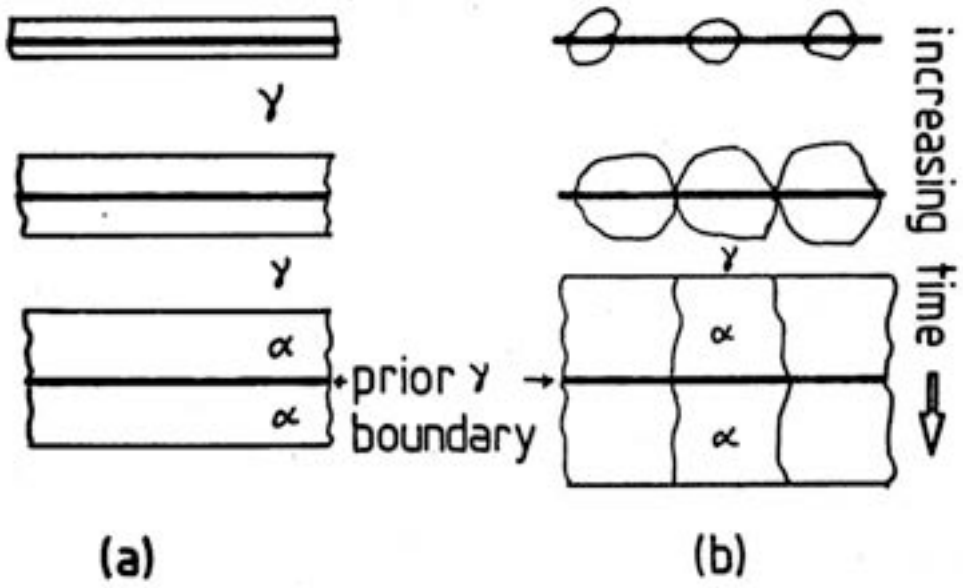

Figure I. 4 - Diagram illustrating the growth of allotriomorphic ferrite as (a) the normal migration of planar γ/α interface, and as (b) is the case of reality. (After Bhadeshia[39]).

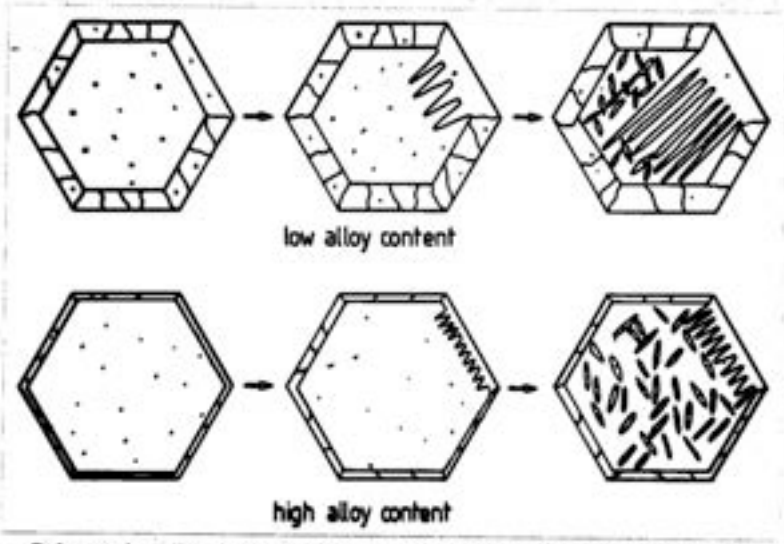

Figure I.5 - Schematic diagrams shows the development of microstructure in weld deposits. (after Bhadeshia et al.[1]).

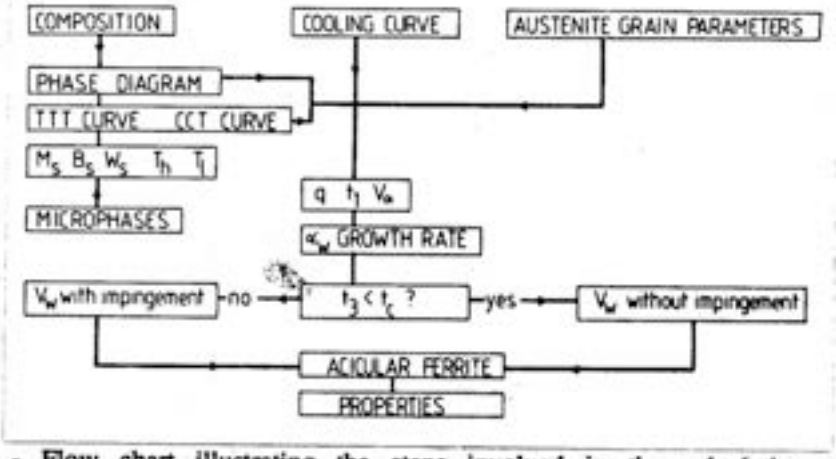

Figure I.6. - Flow chart illustrating the steps involved in the calculation of the microstructure. (after Bhadeshia et al.[1]).

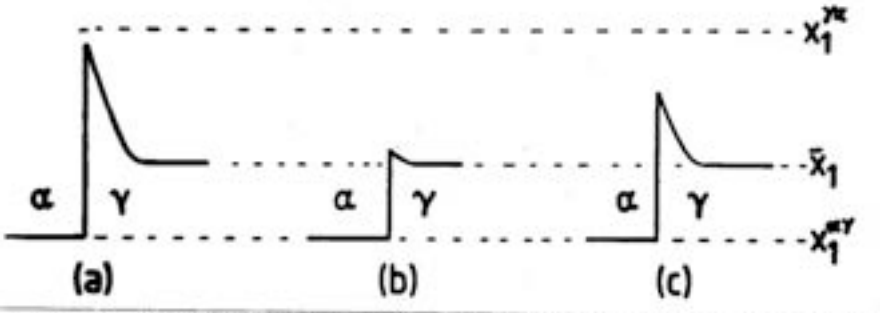

Figure I.7 - Carbon concentration profile at γ/α interface moving under: (a) diffusion-control; (b) interface-control; and (c) mixed interface and diffusion-control.

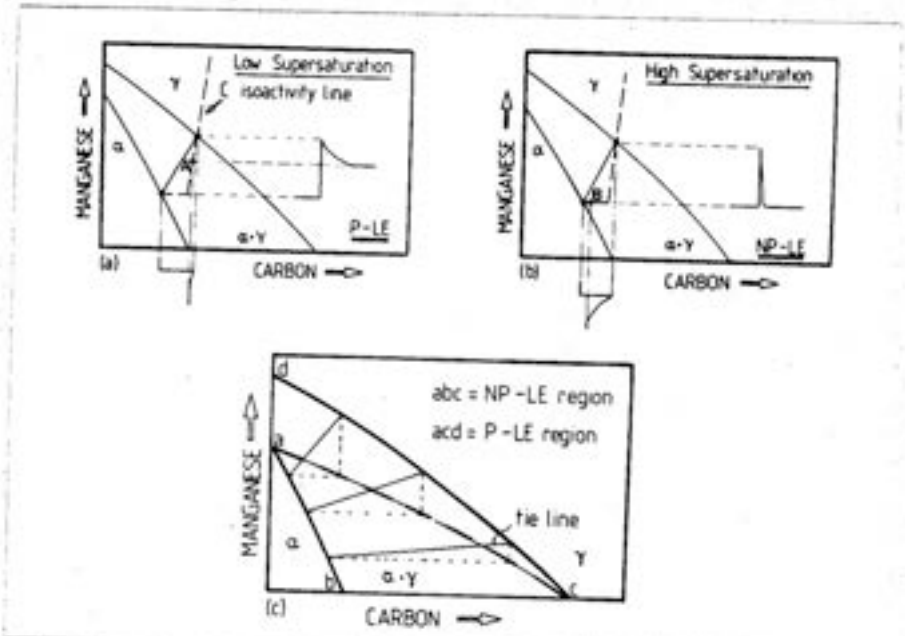

Figure I.8 - Schematic isothermal sections of the Fe-Mn-C system, illustrating ferrite growth occurring with local equilibrium at the α/γ interface. (a) Growth at low supersaturations (PLE) with bulk redistribution of Mn, and (b) growth at high supersaturations (NPLE) with negligible partitioning of Mn during transformation. The bulk alloy compositions are designated "A" and "B" in Fig. I.8(a) and (b) respectively, and (c) division of the α + γ phase field into domains where either the PLE or the NPLE mechanisms can operate.

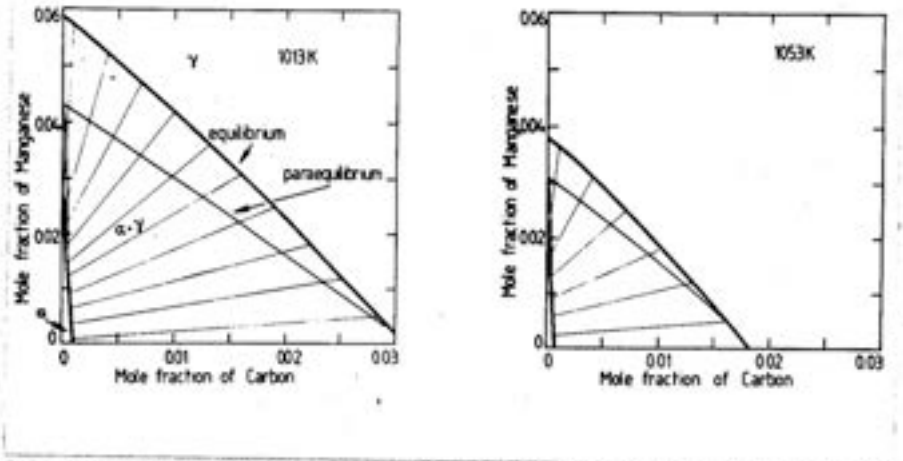

Figure I.9 - Typical calculated isothermal sections of the equilibrium and paraequilibrium phase diagrams of the Fe-Mn-C system (after Bhadeshia[25]). The tie-lines for the paraequilibrium diagram are virtually horizontal since the Fe/Mn ratio is constant everywhere during paraequilibrium transformation.

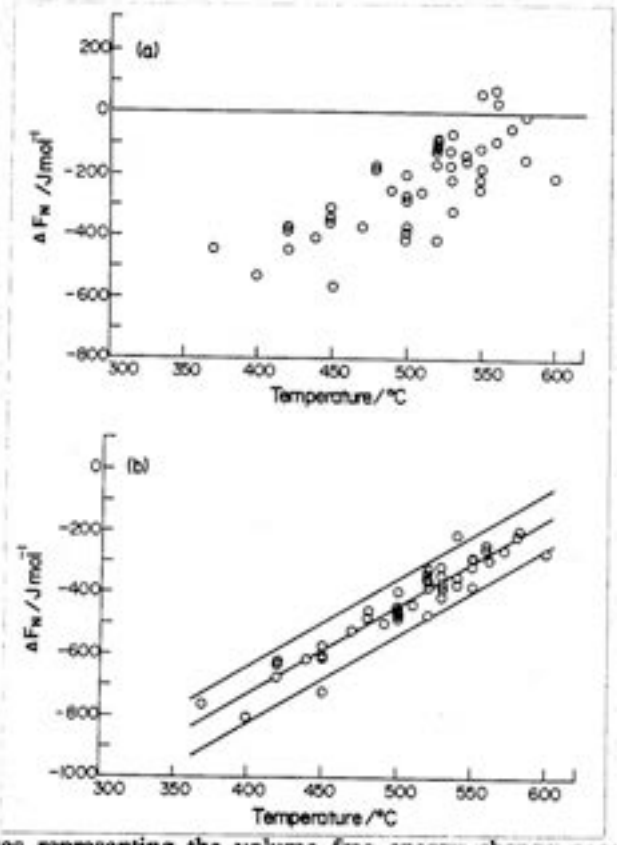

Figure I.10 - Curves representing the volume free energy change necessary in order to obtain a detectable nucleation rate for ferrite forming by shear. (a) The case when the volume free energy change is calculated on the basis that the ferrite nucleus inherits the parent austenite carbon content. (b) The case when the volume free energy change is calculated on the basis that the ferrite nucleus at all times contains only an equilibrium carbon content. The lines bounding the regression line are vertically spaced at distances equivalent to two standard errors of the estimate from the regression line (after Bhadeshia[100]).

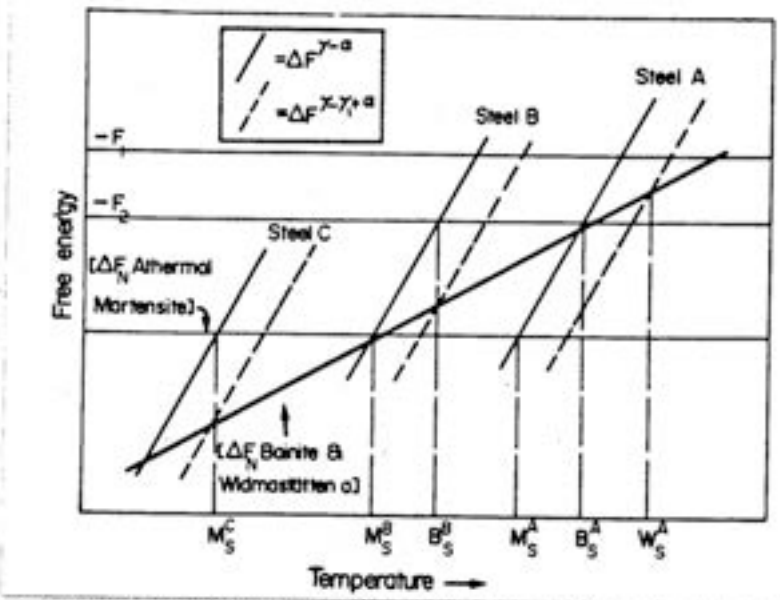

Figure I.11 - Schematic free energy curves illustrating why all three shear transformations need not occur in all steels (after Bhadeshia[100]). It is noted that F_1 = 50 J/mol, for stored energy of α_w, F_2 = 400 J/mol, for stored energy of α_b, and ΔF_N, $\Delta F^{\gamma\to\alpha_s}$ and $\Delta F^{\gamma\to\gamma_1+\alpha}$ all are negative.

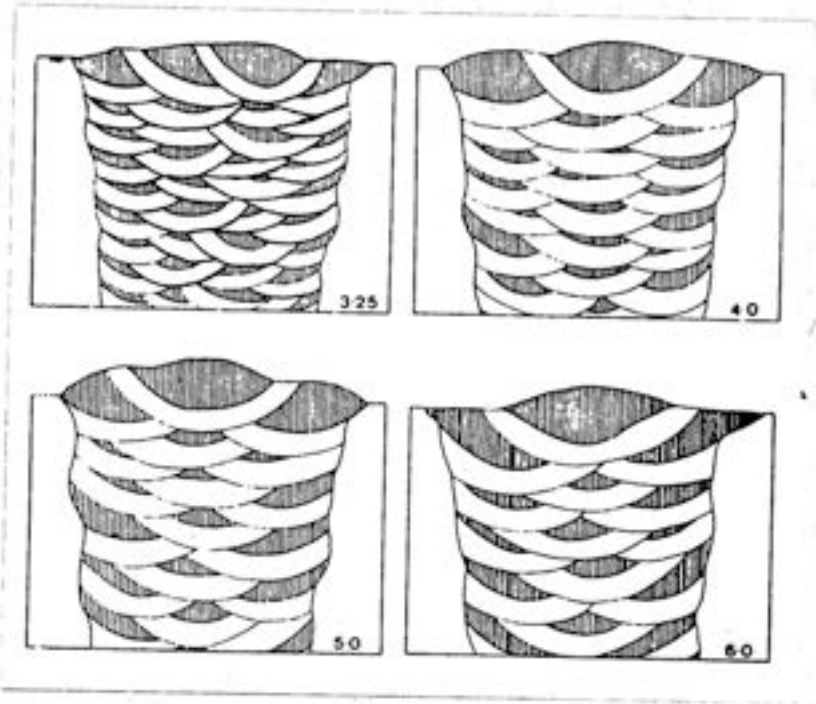

Figure I.12 - Schematic diagram shows the deposition layers and the reheated zones (the white areas) in multirun welds of different electrode sizes (after Evans[110]). The electrode diameters (in mm) are given in the bottom right hand corners of each figure.

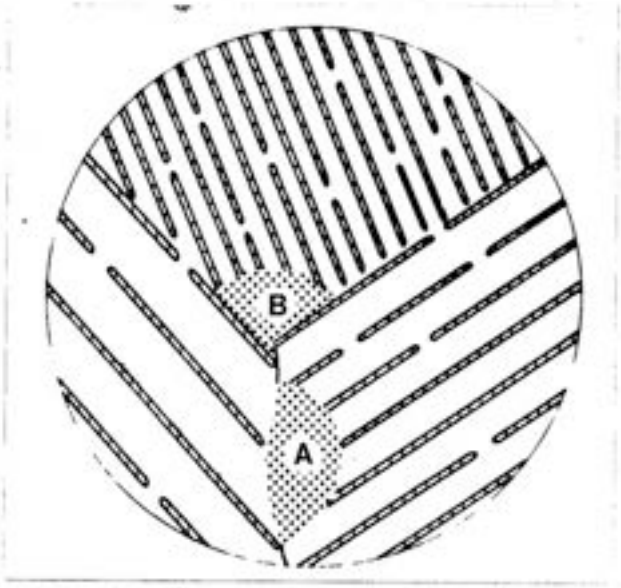

Figure I.13 - Schematic figure shows that preferential nucleation sites of austenite (A) and (B) are located at the edges of pearlite colonies on the cementite/ferrite boundaries (after Roosz[126]).

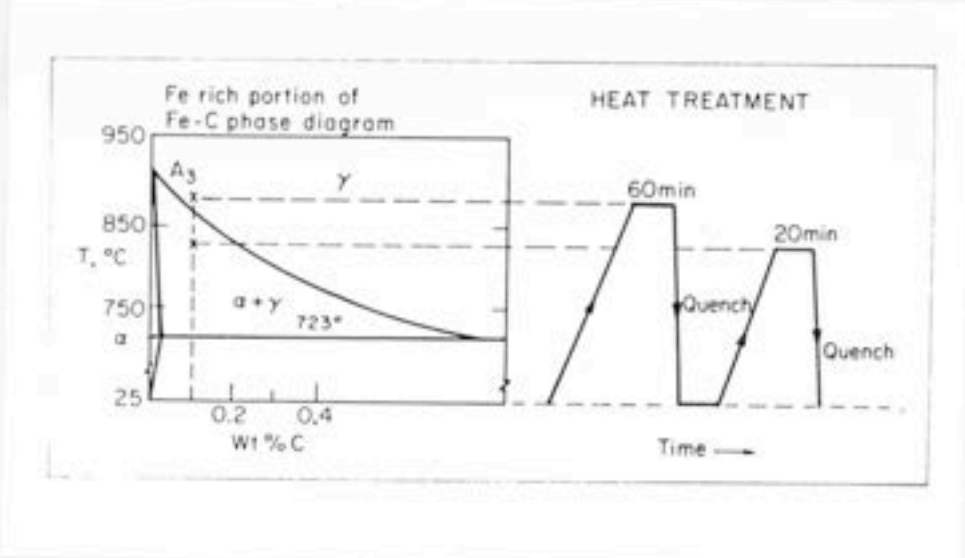

Figure I.14 - Schematic representation of heat treatment to produce controlled dual-phase (ferrite/martensite) structures. (after Koo[132]).

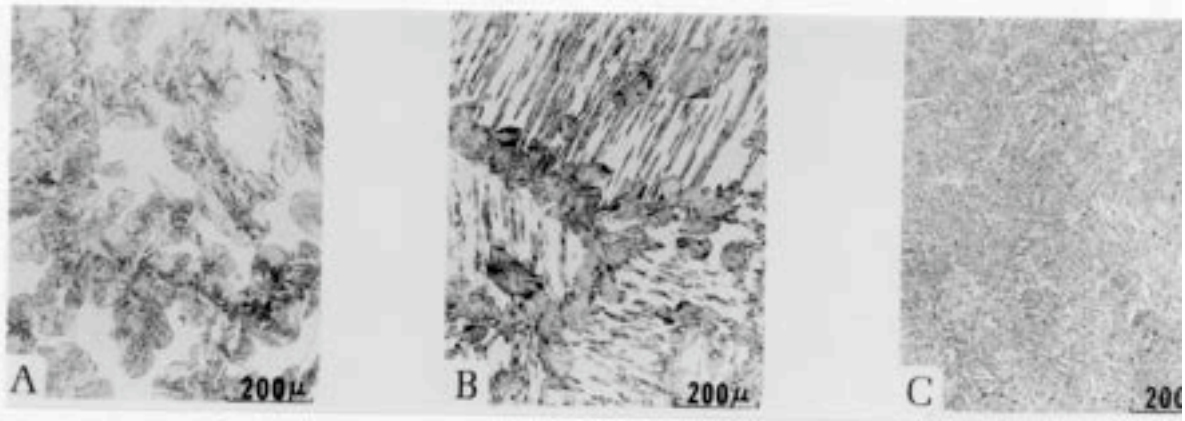

Figure I.15 - Optical Micrographs. (a) Dual-phase microstructure developed in Fe/4Cr/0.1C (wt%) steel shows the globular shape of martensite in the ferrite matrix. (b) Dual-phase microstructure developed in Fe/0.5Cr/0.1C (wt%) steel shows that acicular shape of martensite within prior austenite grain and the prior austenite grain boundaries are decorated with continuous globular shape of martensite particles. (c) Dual-phase microstructure developed in Fe/2Si/0.1C (wt%) steel shows fine, acicular shape of martensite particles in ferrite matrix. Note that martensite was austenite before final quenching. (after Koo[132]).

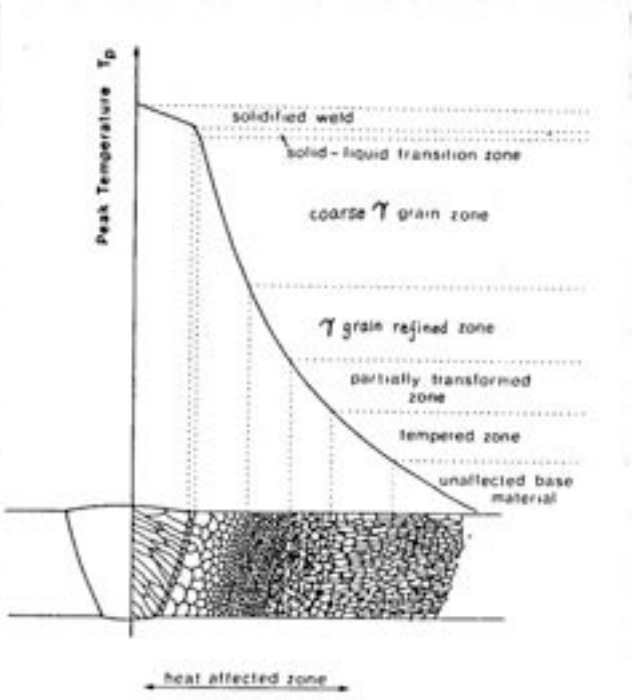

Figure I.16 - A schematic diagram shows various sub-zones of the heat affected zone in a plain carbon steel.

Chapter Two

The Microstructure of High-Strength Weld Deposits

2.1 Introduction

The microstructure of high-strength weld deposits, Fe-C-Si-Ni-Mn-Mo alloys, which have unusually high levels of substitutional alloying additions have been studied. These alloys are being developed to ensure sound, high-strength welds for the Trident Submarine programme. In this work, the welds (provided by ESAB Ltd. UK) were deposited using the manual metal welding technique. The electrodes used were of a nominal E10016-G type as defined by the American Welding Society, the joint geometry being compatible with BS 639. The welding was carried out in the flat position using the stringer bead technique, the parent plate thickness being 20mm. The welding current and voltage used were 180A and 23V (DC+) respectively (arc energy ≈ 2 KJ/mm), the weld consisting of some 21 runs with 3 runs per layer deposited at a speed of about 0.002 m/s; the interpass temperature was typically 250°C. The electrode diameter was 4mm.

By varying the composition of the 4mm diameter electrode used (but keeping the welding conditions constant throughout), weld deposits with different carbon or molybdenum concentrations were obtained; the chemical analyses are presented in Table II.1. The chemical determinations were carried out using a direct reading spectrograph. The level of oxygen and nitrogen were determined using Leco furnaces, and it was found that content of oxygen and nitrogen were about 320 and 100 ppm respectively in all the weld deposits. The mechanical properties of these weld metals except WB are listed in Table II.2.

Before investigating the microstructure of the weld metals, the calculated isothermal transformation curves and phase diagrams of the alloys are presented. In multirun welds, the volume fraction of reheated weld metal is large. Hence, besides the microstructure of fusion zone, that of the reheat zone has also been studied. Inclusions in weld metal have been regarded as an important factor in the development of microstructure; therefore, inclusions are also studied.

2.2 Calculated Isothermal Transformation Curves and Phase Diagrams

It is easier to study phase transformations and to study theoretical alloy steel design if isothermal transformation curves and phase diagrams of the specific alloy steels are available. Bhaseshia [156] has presented thermodynamic models, allowing the calculation of reaction start time for Time-Temperature-Transformation curves, and Bhadeshia and Edmonds [89,100] have also developed the theory for the calculation of phase diagrams

for multicomponent steel. Hence, it is possible to compute the T_0, T_0' and Ae_3' curves which are important in understanding transformation in welds. The T_0 curve [157] is defined such that stress free austenite and ferrite of the same composition (with respect to both the interstitial and substitutional alloying elements) have equal free energy. The corresponding curve for austenite and ferrite (with a certain amount of stored energy associated with transformation strains) of identical composition and free energy is called the T_0' curve [89,100]. On the other hand, with paraequilibrium [32] , the no substitutional element partitioning Ae_3' curve [89,100] describes the equilibrium between α and γ when carbon partitioning is allowed to occur subject to the constraint that the substitutional elements do not redistribute during transformation. An application of such methods towards the prediction of the microstructure (allotriomorphic ferrite, Widmanstätten ferrite, acicular ferrite and microphases) of the fusion zone of low-alloy steel weld deposits has also been considered by Bhadeshia et al. [1]. The thermodynamic calculation presented in subsequent sections were carried out using computer programs developed by Bhadeshia and co-workers.

2.2.1 Theory for the Calculation of Isothermal Transformation Diagrams

Bhadeshia [156] has presented a method to calculate the reaction start times for the Time-Temperature-Transformation (TTT) curves for alloy steels containing C, Mn, Si, Ni, Cr, Mo, and V in any combination, as long as the total substitutional alloying addition is limited to less than about 7 wt%. Such diagrams can be treated as being composed of two C curves. The upper C curve represents the time taken for the initiation of diffusional transformation such as allotriomorphic ferrite and pearlite, whereas the lower C curve represents the time taken for the initiation of displacive transformation such as bainite and Widmanstätten ferrite.

The essence of this method is to fix experimental values to Russell's general equation [158] of incubation time. The incubation time can be expressed as:

$$\tau_s = \left\{ \frac{T}{(\Delta F_m)^p D} \right\} \qquad (1)$$

where the braces imply a functional relation,

τ_s = incubation time taken to establish a steady state nucleation rate,

T = absolute temperature,

D = appropriate diffusion coefficient,

ΔF_m = free energy for nucleation, a function of alloy concentrations and temperature,

and p = a factor depending on the nature of the nucleus.

This method therefore precludes any preconceived ideas regarding the shape, the coherency or the size of the initial nucleus. These calculations generate two 'C' curves as a function of time and temperature. In the case of the lower 'C' curve the diagram is truncated at the bainite start temperature Bs (or Widmanstätten ferrite start temperature Ws) since this represents an upper thermodynamic limit beyond which neither Widmanstätten ferrite nor bainite can nucleate. The flat top of the lower C curve actually corresponds to the temperature at which the nucleation of displacive transformation first becomes possible. It should be noted that although the analysis does not allow for grain size variations, it has been pointed out [159] that such variations are relatively small as far as the initiation of transformation is concerned; in any case, unless site saturation occurs, the reaction-start times should not alter significantly with the usual range of austenite grain sizes obtained following commercial heat treatments.

2.2.2 Calculated Isothermal Transformation Curves

The resultant Time-Temperature-Transformation (TTT) curves for the weld metals studied in this investigation are shown in Figure II.1 and 2, and allow us to study theoretically the effect of alloying elements on the transformation.

Figure II.1 shows the TTT curves of the nine different weld metals studied in this work. It is found that all these weld metals possess good hardenability. Under the usual weld deposition conditions, a typical weld cooling rate [1,16] over the temperature range 800-500°C is less than $20°Cs^{-1}$. Hence, the cooling curve cannot intersect the diffusional C curve. These weld deposits should consist of bainitic ferrite and residual austenite, the latter subsequently being retained to ambient temperature or transforming to microphases. It is interesting to investigate the microstructure of these high strength weld metals in detail to confirm this point.

It has been supposed [53,160] that molybdenum has a positive effect on the weld metal microstructure in the as-welded condition, by increasing the amount of acicular ferrite. The weld metals studied in this investigation were specially designed in order to elucidate any molybdenum effect. The content of molybdenum in these weld metals was varied from 0.01 to 0.57 wt%. Figure II.2 shows the effect of increasing molybdenum on the calculated TTT curves. It is found that the effect is not significant even for the 0.57 wt% of molybdenum containing alloy (as shown in Figure II.2d). This is because of the generally high alloy content of the welds, where manganese and nickel also exert a powerful influence.

2.2.3 Phase Diagrams for Transformation in Steels

It is known that the growth of both Widmanstätten ferrite and bainite is in evidence displacive [100]. Thermodynamically, Widmanstätten ferrite can only form with an equilibrium or paraequilibrium carbon content, so that growth is controlled at a rate depending on the diffusion of carbon in austenite; however, an atomic correspondence is maintained for substitutional atoms, in agreement with the observed shape change effects. On the other hand, the formation of bainite involves the propagation of displacive sub-units with a full carbon supersaturation, and partitioning of the carbon into the residual austenite occurs subsequent to transformation, rather than during the growth process.

To characterise microstructural development under isothermal transformation, the T'_0, T_0, and Ae'_3 curves are very important in understanding transformation mechanism. The calculations of T'_0 T_0, and Ae'_3 curves for weld metals studied in this investigation were carried out using the analysis of Bhadeshia and Edmonds [89], and are demonstrated in the next section. This analysis allows the extent of the isothermal reaction at any temperature to be established assuming either a bainite or Widmanstätten ferrite reaction, since the transformation should stop when the carbon content of the residual austenite reaches either the T'_0 or Ae'_3 phase boundary respectively [89,101].

2.2.4 Calculated T'_0, T_0, and Ae'_3 Curves

The T'_0, T_0, and Ae'_3 curves for weld metals have been calculated and are shown in Figure II.3; the corresponding TTT curves have been presented in Figure II.1. In essence, it should be noted that T'_0 and Ae'_3 curve can be used to define thermodynamically the limits of transformations, but TTT curves determine the kinetics of transformation and both have to be used in the theoretical design of alloys. For example, for low-alloy steels, all reactions are relatively rapid, and it should be difficult to quench γ at a rate fast enough to achieve significant transformation to bainite without avoiding the occurence of allotriomorphic ferrite and pearlite reactions.

The T'_0, T_0, and Ae'_3 curves vary only as a function of the substitutional alloying element content and are unaffected by the average carbon content of the alloy $\overline{X}$. For a given value of $\overline{X}$, when the T'_0 curve shifts to the right, the austenite can tolerate more carbon before bainite transformation becomes thermodynamically impossible, thus increasing the maximum permitted volume fraction of bainite (V_b) at any isothermal transformation temperature. Certainly, an increase in V_b can also be achieved by reducing $\overline{X}$, but the hardenability should be considered first as mentioned above. For the weld metals used in the present work, the T'_0 curves are not very different (Figure II.3), and all the values $\overline{X}$ are very small. It is expected to obtain high volume fraction of bainite in

these weld metals.

2.3 Microstructure of High-Strength Weld Deposits

In Section 2.2, it has been known that all the weld metals studied in this investigation possess good hardenability, and in fact these weld metals are designed to obtain high-strength and high-toughness properties. The aim of this work is to identify the microstructural constituents of these weld metals. A macrograph of the typical manual metal arc weld deposit studied is presented in Figure II.4. It shows that the weld deposit WA1 contains 21 runs in total with 3 beads per layer. The volume fraction of reheated weld metal is large (about 0.3). Hence, besides the microstructure of the fusion zone, that of the reheated zone should be investigated.

Microstructure of the Fusion Zone

The columnar austenite grains of the fusion zone in the weld deposit WA1 are shown in Figure II.5. The austenite grain is very large, and can be treated as the form of a hexagonal prism. The width of austenite grain was measured by 1000 lines normal to grain boundaries on Quantimet 720 image analysing computer, and the value was 55μm. In the case of measurement by randon sections, it was 75μm. In a typical fusion zone microstructure, fairly continuous layer of allotriomorphic ferrite (α) usually outline the columnar grain boundaries of austenite. However, in this higher alloy weld metal WA1, the layers of allotriomorphic ferrite become thinner or even discontinuous. It is believed that solute segregation occurs during weld-pool solidification [8,40,70,78]. The distribution of solute element within austenite grain will in turn affect the final microstructure [78]. The γ/γ boundary is certainly a preferred site for the nucleation of allotriomorphic ferrite. Therefore, it is not just segregation that is important, but position of γ/γ boundary relative to segregation [70,78].

The primary microstructures of fusion zone in the weld deposits WA1, WA2, WB, WC1, WC2, WD1, WD2, WD3 and WD4 are presented in Figure II.6. It is noted that WC2 (Figure II.6e) and WD1 (Figure II.6f) contain 0.01 wt% of molybdenum respectively; WA1 (Figure II.6a), WA2 (Figure II.6b), WB (Figure II.6c), and WC1 (Figure II.6d) and WD2 (Figure II.6g) contain about 0.20 wt% of molybdenum respectively; WD3 (Figure II.6h) contains 0.40 wt% of molybdenum; and WD4 (Figure II.6i) contains 0.57 wt% of molybdenum. All the welds have a similar primary microstructure consisting mainly of acicular ferrite (volume fraction about 0.9), with very little allotriomorphic ferrite, Widmanstätten ferrite and microphases. The calculated TTT diagram indicates that allotriomorphic ferrite and Widmanstätten ferrite should not be

present, probably forming due to the presence of chemical segregation in weld, which cools under non-equilibrium conditions. The γ/γ boundaries are expected to be in solute-depleted regions when the first phase to solidify is δ, since δ/δ boundaries (where the last solute-rich liquid solidifies) are in regions which are solute rich [78]. In the present study, solidification should begin with δ as the first phase to solidify, due to very low carbon content. According to the TTT diagrams, these weld metals should contain a high volume fraction of bainite. However, no classical bainite structure could be found in these primary structures. In order to predict the microstructure of the fusion zone in weld, the mechanism of the acicular ferrite transformation should be understood. A study of the thermodynamics of the acicular ferrite transformation will be presented in Chapter Three.

Thin foil specimens were prepared for transmission electron microscopy from a 0.25mm thick discs slit from the top layer (fusion zone) in weld deposits. The discs were thinned to 0.05mm by abrasion on silicon carbide paper and then electropolished in a twin jet electropolisher using a 5% perchloric acid, 25% glycerol and 70% ethanol mixture at ambient temperature, 45V. The microscopy was conducted on a Philips EM400T transmission electron microscope operated at 120kV.

The detailed morphology of acicular ferrite of these weld metals has been studied by transmission electron microscopy as presented in Figure II.7. Figure II.7a (taken from weld metal WA1) shows inclusions in the acicular ferrite plates, the inclusion diameters being about 0.3-0.6μm. In the upper region of this micrograph the microphases appear like lath martensite. In Figure II.7b (taken from weld metal WA2) the electron micrograph shows elongated microphase decorating the boundaries of ferrite plates. It is noted that a one-to-one correspondence between the number of active-inclusions and the number of acicular ferrite plates is not expected, because subsequent plates may nucleate sympathetically on any inclusion-nucleated plate [62]. Figure II.7c (taken from weld metal WD1) shows platelets of acicular ferrite which have apparently nucleated sympathetically on the austenite/ferrite interface. In some cases, several acicular ferrite plates can grow from one inclusion to give a star shaped cluster as shown in Figure II.7d (taken from weld metal WD2). Figure II.7e (taken from weld metal WD3) shows the acicular ferrite plates, inclusions, elongated microphases and blocky shaped microphases. The blocky microphases are martensite in which the auto-tempering has occurred and cementite has precipitated. In Figure II.7f (taken from weld metal WD4), the electron microscopy shows that due to hard impingement the non-parallel plates of acicular ferrite are arranged in an interlocking pattern, and small amounts of microphases are located among the acicular ferrite plates.

The lenticular shape of acicular ferrite is illustrated in Figure II.7 and since this morphology was always observed, it is concluded that acicular ferrite has in three dimensions a thin-plate morphology. The tips of the acicular ferrite plates are also found to be smoothly curved. These morphological observations are consistent with a displacive transformation mechanism in which the lenticular plate shape of acicular ferrite arises through the need to minimise the strain energy associated with the accompanying shape deformation. The dislocation density of acicular ferrite and the orientation between adjacent acicular ferrite will be dealt with in Chapter Six.

Microstructure of Reheated Zone

It has been supposed [161] that the microstructural development in the reheated zone of weld metal is generally similar to that in as-deposited weld metal, except that there is a progressive decrease in prior austenite grain size with decreasing peak temperature. Consequently, there is a progressive increase also in the ratio of allotriomorphic ferrite to acicular ferrite. The microstructure in the coarse-grained reheated region is expected to resemble that in as-deposited weld metal, except that, in the former, the present austenite grains are equiaxed.

Figure II.8a shows the reheated zone between the top layer and second layer of fusion zones in weld metal WD4. It contains elongated regions, rather like the original columnar γ grains, which are associated with microphases (maybe martensite, retained austenite, or degenerate pearlite). The microphases appear as tiny black islands in higher magnification optical micrographs as shown in Figures II.8b and c. The microphases are aligned as a banded pattern. The width between the bands is less than 20μm. However, the width of original columnar austenite grains in the fusion zone is about 60μm. It is clear that segregation within the original columnar grains causes this effect. Certainly, the banding regions are solute-rich, and are the last transformed structure in the reheated zone. In Figures II.8b and c, the micrographs show the microstructure of the reheated zone consists acicular ferrite, allotriomorphic ferrite and microphases. The volume fraction of acicular ferrite is much less than that in the fusion zone, but the amount of allotriomorphic ferrite and microphases are increased. Probably because the present austenite grains become smaller and the γ/γ boundary is located solute-depleted region, the effects enhance the nucleation and growth of allotriomorphic ferrite; therefore the volume fraction of acicular ferrite decreases in the reheated zone of weld metal studied. In order to elucidate this problem the detailed austenite grain structure and segregation pattern in reheated zone are needed.

Preliminary Study of Inclusion Chemistry

Inclusions in weld deposits have been regarded as an important factor in the development of microstructure. It is interesting to examine whether the inclusion size distribution and inclusion type determine the final microstructure of weld metal. At this stage, the inclusion chemistry of weld metal WB has been studied. The microanalysis was conducted in a Philips EM400T transmission electron microscope operated at 120 kV. An energy dispersive X-ray analysis facility was used for the microanalytical measurements, with the specimens held in a berylium holder tilted from the normal by 35°, which is the take-off angle. The X-ray count rate was optimised to about 1000 counts/s over a livetime of about 100s. The data were analysed using the LINK RTS 2 FLS program for thin foil microanalysis; this corrects that data for atomic number and absorption and accounts for overlapping peaks by fitting standard profiles. Even though the probe diameter used was about 3nm, beam spreading due to scattering of electrons within the thin foil gave an estimated broadened beam diameter of about 20nm.

Eleven different inclusions from the same specimen were tested. Because the inclusion size was large, the probe beam spreading did not cause any difficulties during analysis. The microanalytical data are shown in Figure II.9, from which it can be seen that as Fe content increases, the alloying content of Mn, Ti and Al decrease, and vice versa. It therefore seems likely that the inclusions in this weld metal are composed of two types of oxide - (Fe) oxides and (Mn, Ti, Al) oxides. (Fe) oxides may be FeO or Fe_2O_3, and (Mn, Ti, Al) oxides may be MnO, MnO_2, TiO, Ti_2O_3, TiO_2, or Al_2O_3. Note however, that all inclusions contain significant quantities of each element examined. As inclusions in the weld deposit WB studied are of very complicated composition, it is supposed that the inclusions are complex multiphases, and the potency of inclusions for ferrite nucleation cannot be estimated easily.

2.4 Summary

The calculated TTT curves and phase diagrams (To', To and Ae_3') for the high-strength weld metals have been presented. It has been shown that all the weld metals studied in this investigation possess good hardenability. The primary microstructures of the fusion zone of all weld deposits examined are similar, and consist mainly of acicular ferrite (volume fraction about 0.9), with very little allotriomorphic ferrite, Widmanstätten ferrite and microphases. The morphology of acicular ferrite has been examined by transmission electron microscopy. In addition to intragranular nucleation on inclusions, acicular ferrite also seems to nucleate sympathetically, giving rise to an interlocking formation of

lenticular plates. The microstructure of the reheated zone is complicated, and a banded structure has been found in this zone. The banding region consists mainly of microphases, and reflects the segregation in original columnar austenite grain. It has also been shown that the ratio of allotriomorphic ferrite to acicular ferrite decreases in the reheated zone, probably due to austenite grain refinement and segregation effect. Inclusion chemistry has also been examined but it is difficult to draw any conclusions about nucleation potency because all the inclusions investigated seem to be complex multiphases.

Table II.1 Chemical composition of weld deposits. All concentrations are in weight percent except oxygen and nitrogen in ppm.

Weld	C	Si	Mn	Ni	Mo	Cr	V	S	P	Al	Ti	Nb	O(ppm)	N(ppm)
WA1	0.052	0.36	1.98	2.64	0.24	0.05	0.01	0.008	0.012	0.02	0.03	0.02	ND	ND
WA2	0.054	0.33	1.94	2.44	0.20	0.05	0.01	0.008	0.014	0.02	0.02	0.01	ND	ND
WB	0.060	0.27	1.84	2.48	0.20	0.05	0.01	0.005	0.012	0.01	0.02	0.01	399	111
WC1	0.040	0.37	1.70	2.36	0.20	0.04	0.02	0.008	0.015	0.02	0.03	0.01	317	98
WC2	0.040	0.33	1.62	2.44	0.01	0.04	0.01	0.008	0.014	0.02	0.02	0.01	320	107
WD1	0.030	0.38	1.73	2.39	0.01	0.05	0.01	0.005	0.008	0.02	0.02	0.01	347	58
WD2	0.031	0.40	1.68	2.46	0.17	0.04	0.01	0.005	0.008	0.02	0.03	0.01	333	80
WD3	0.035	0.41	1.89	2.64	0.40	0.05	0.01	0.005	0.010	0.01	0.02	0.01	347	59
WD4	0.034	0.43	1.80	2.48	0.57	0.05	0.01	0.005	0.009	0.01	0.02	0.01	396	61

ND = not detected by spectrographic examination

Table II.2 Mechanical Properties

	WA1	WA2	WC1	WC2	WD1	WD2	WD3	WD4
Yield Pt N/mm^2	849	740	705	667	668	719	ND	ND
UTS N/mm^2	859	781	766	721	709	757	763	759
Elongation %	18	18	24	22	22	22	10	6
Reduction of area %	68	68	ND	ND	ND	ND	ND	ND
Charpy impact energy J								
-20°C	111 99 105	133 129 129	ND	ND	141 168 164	139 148 134	121 149 134	103 106 106
-50°C	75 73 89	75 84 100	101 98 95	86 92 108	89 81 123	82 74 91	100 71 82	72 84 71
-60°C	ND	ND	69 62 94	67 47 61	ND	ND	ND	ND
-70°C	49 57 58	62 64 91	ND	ND	ND	ND	ND	ND
-80°C	ND	ND	ND	ND	33 44 47	33 46 38	43 48 46	51 52 46

ND = not determined.

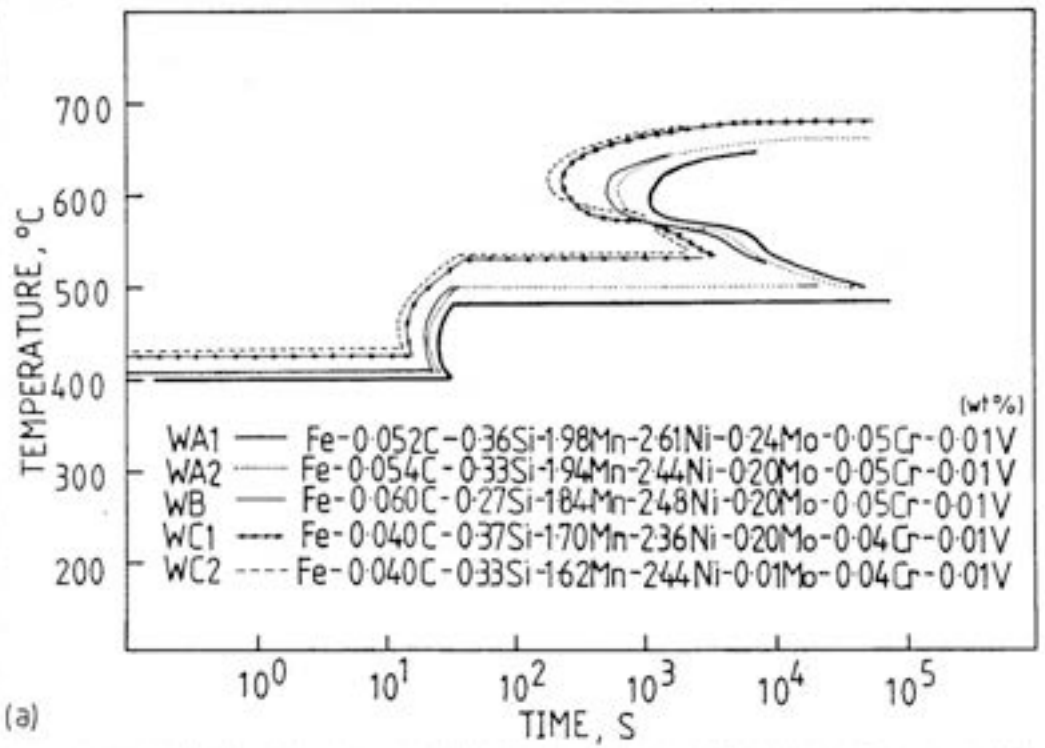

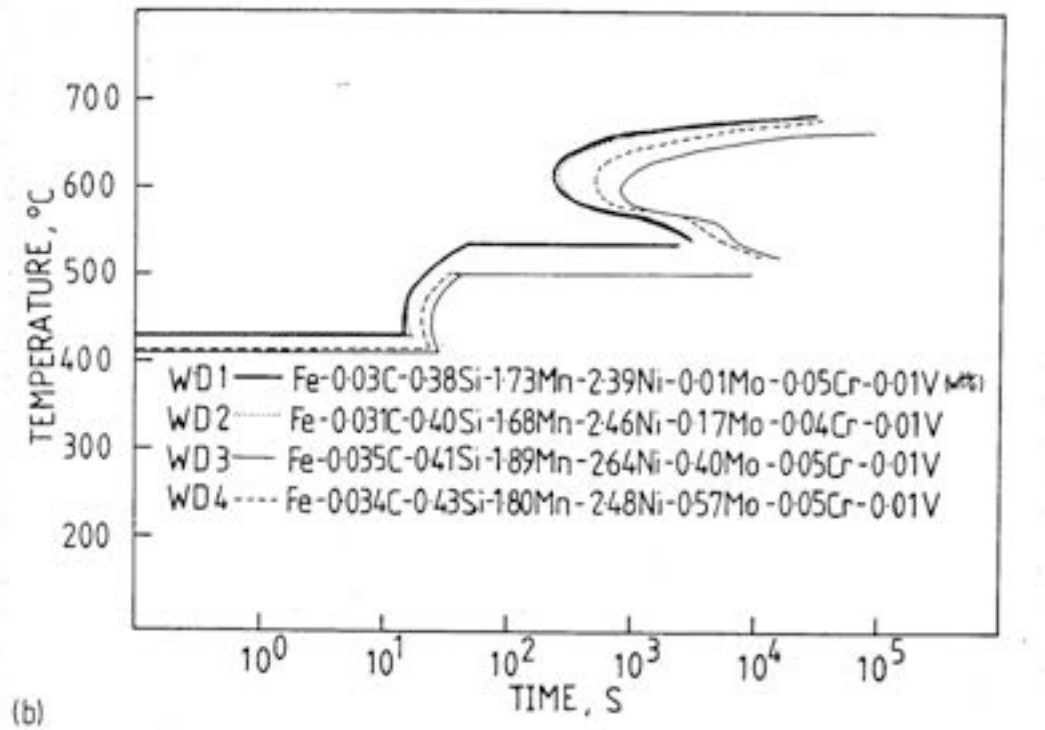

Figure II.1 - Showing the calculated TTT curves for weld metals.

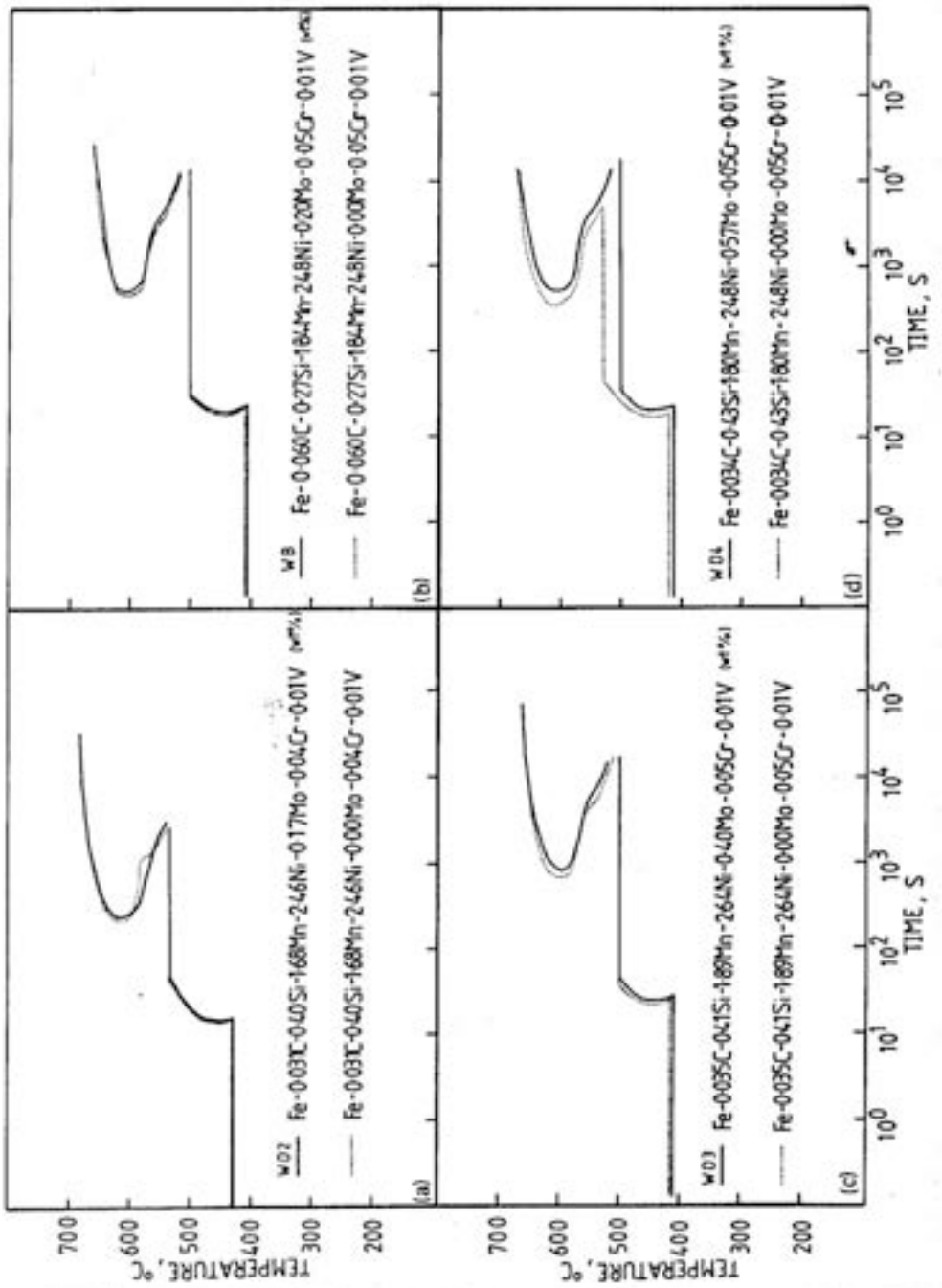

Figure II.2 - Showing the amount of molybdenum effect on the calculated TTT curves for weld metals.

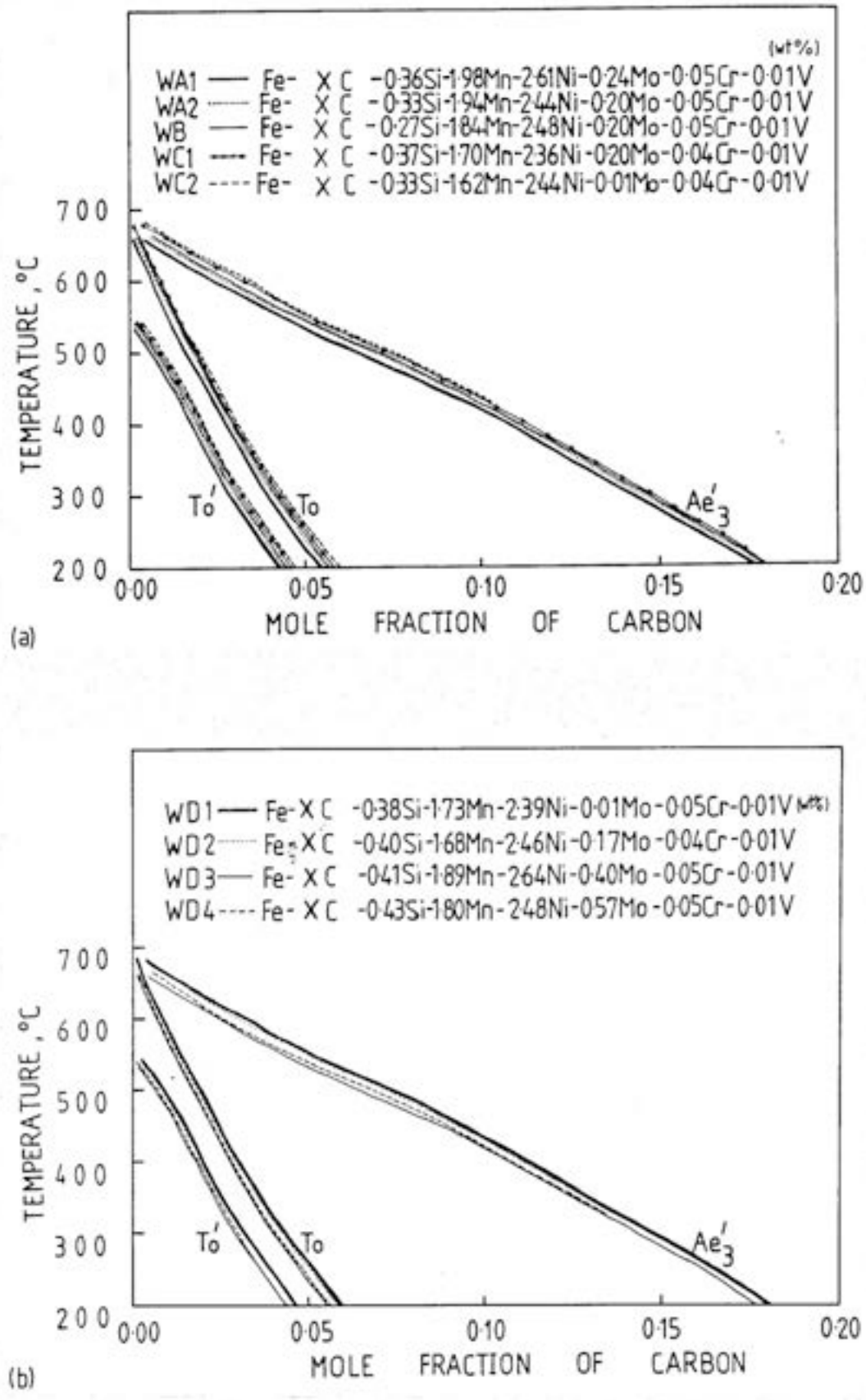

Figure II.3 - Showing the calculated T_o^*, T_o and Ae_3^* curves for weld metals.

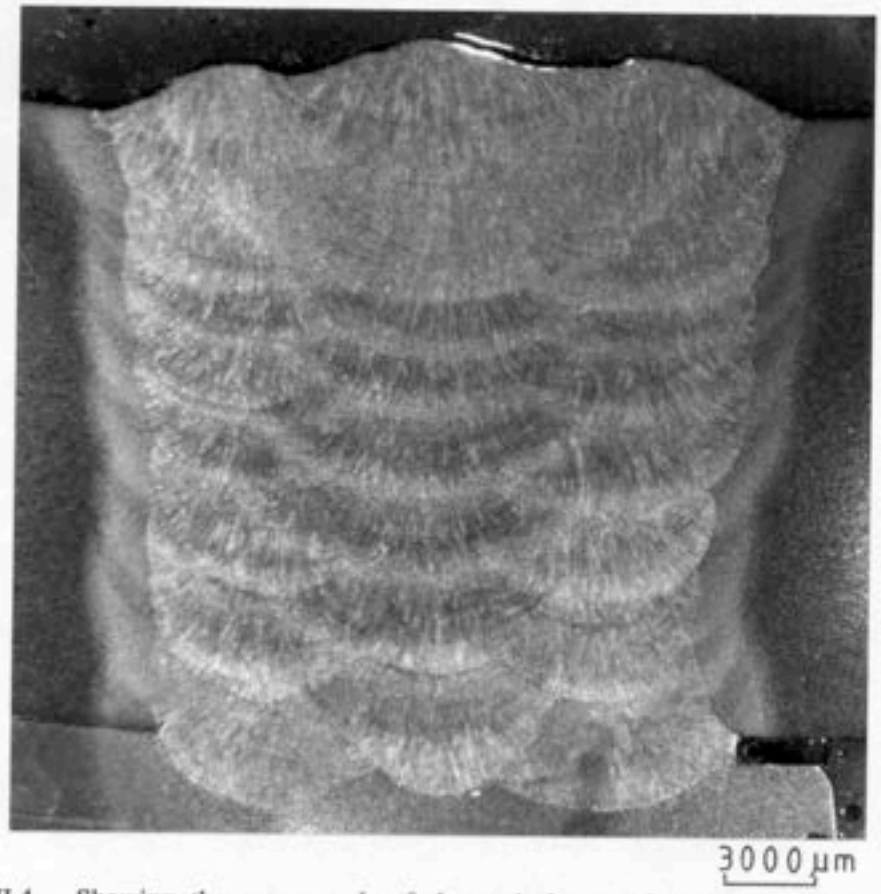

Figure II.4 - Showing the macrograph of the typical manual metal arc weld deposit studied. It contains 21 runs, and 3 beads per layer. The reheated zones can be identified.

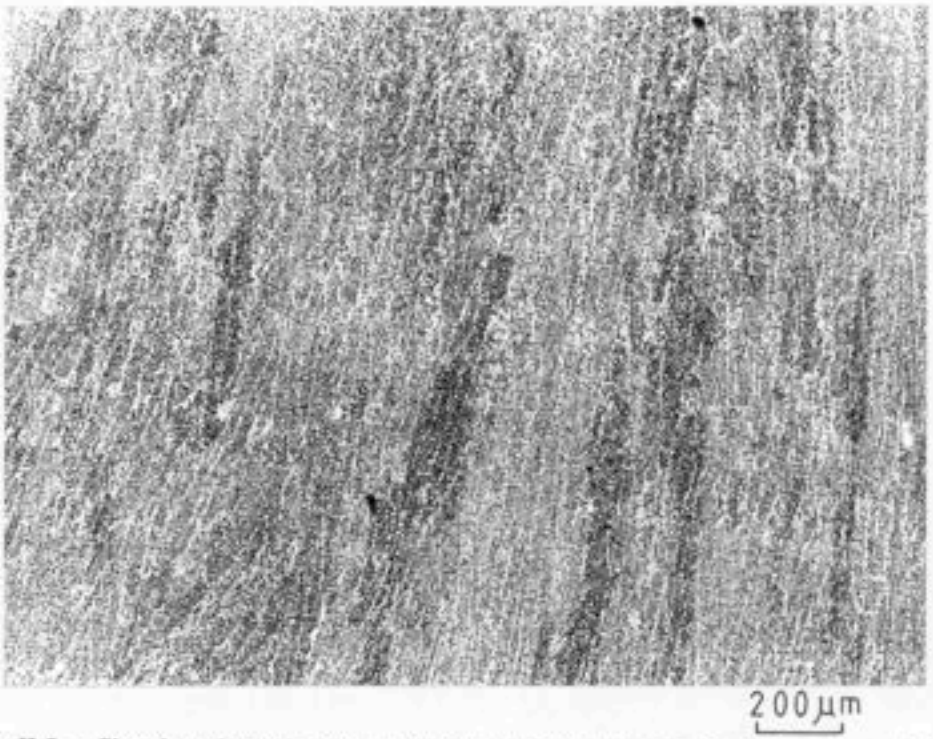

Figure.II.5 - Showing the columnar austenite grain boundaries in fusion zone of weld metal WA1.

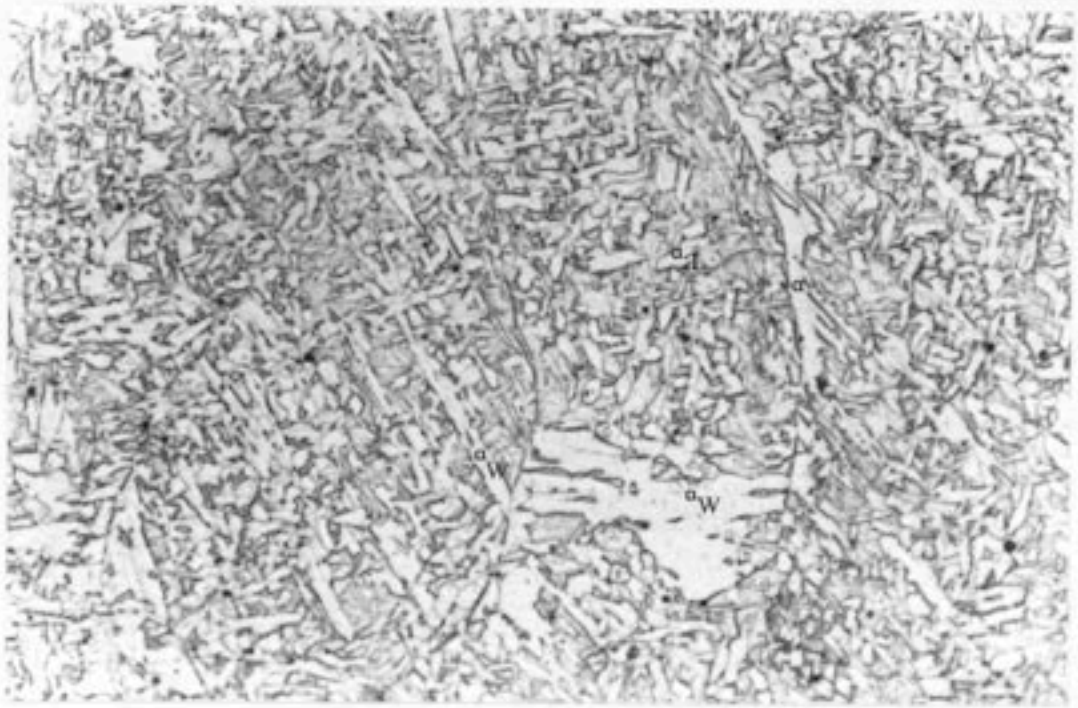

Figure II.6(a) - Primary microstructure of WA1. 10 µm

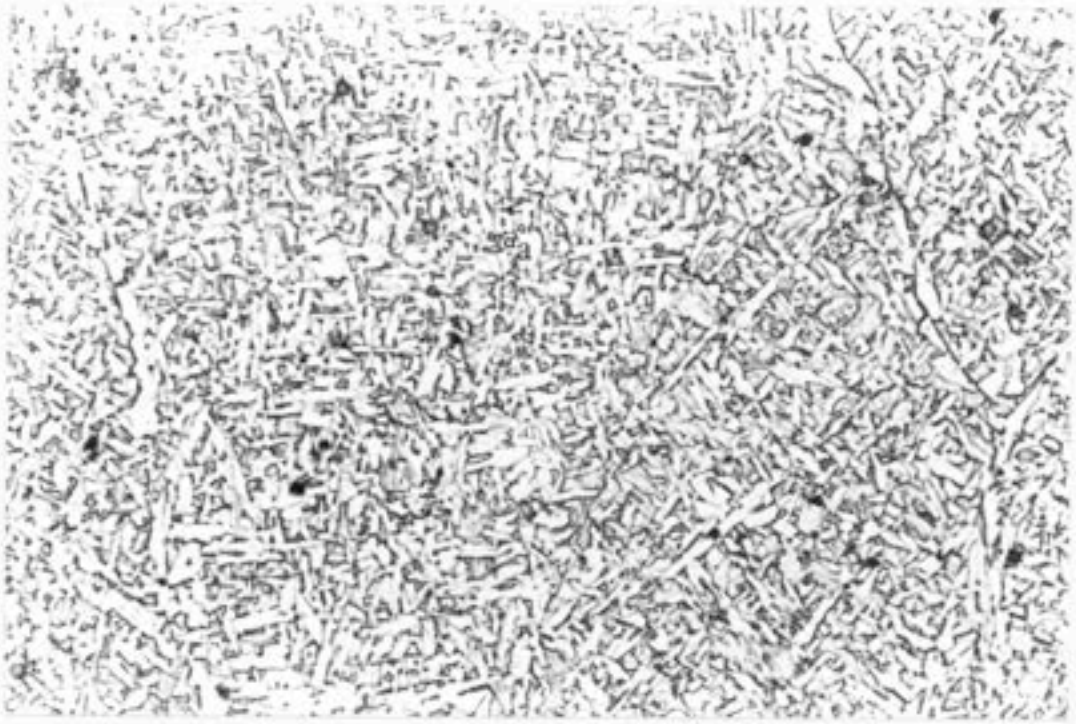

Figure II.6(b) - Primary microstructure of WA2. 10 µm

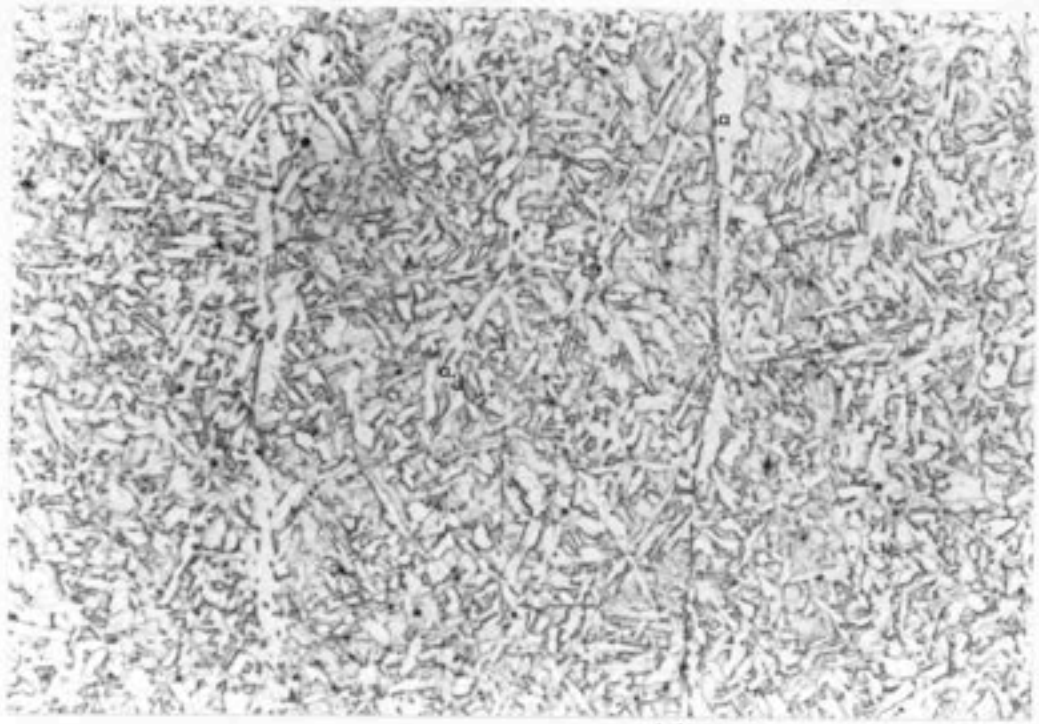

Figure II.6(c) - Primary microstructure of WB.

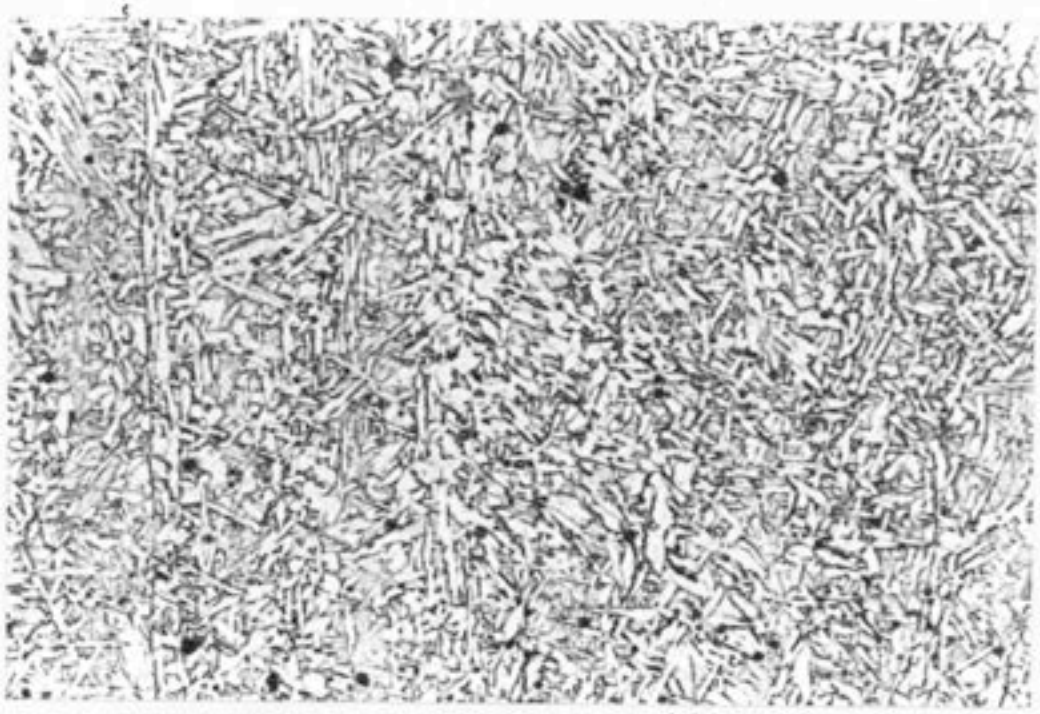

Figure II.6(d) - Primary microstructure of WC1.

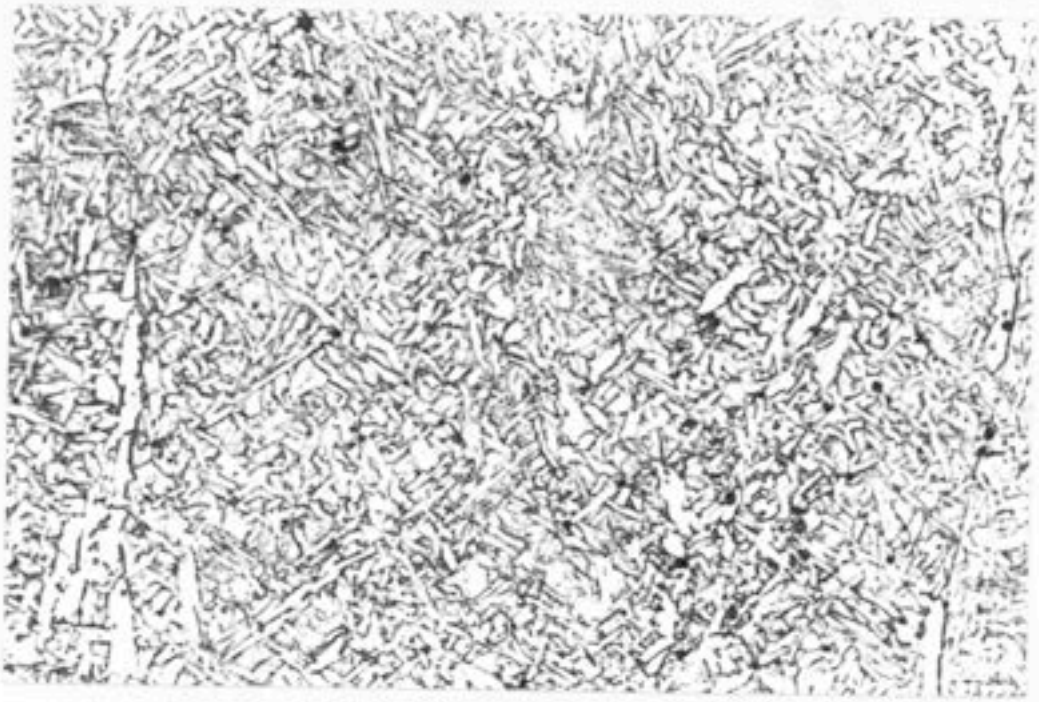

Figure II.6(e) - Primary microstructure of WC2. 10 µm

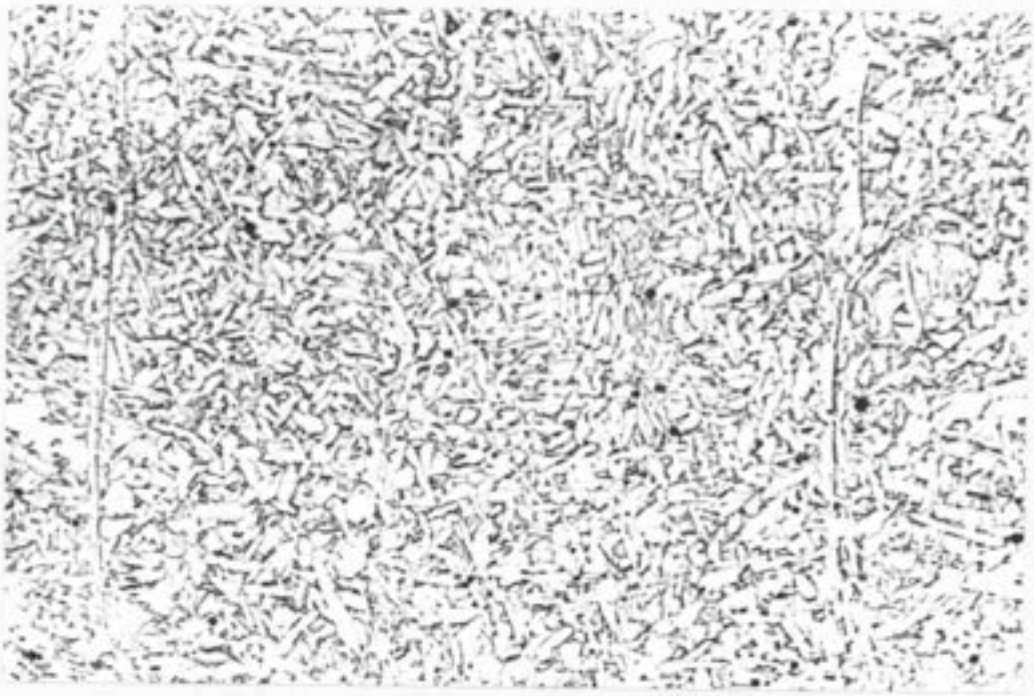

Figure II.6(f) - Primary microstructure of WD1. 10 µm

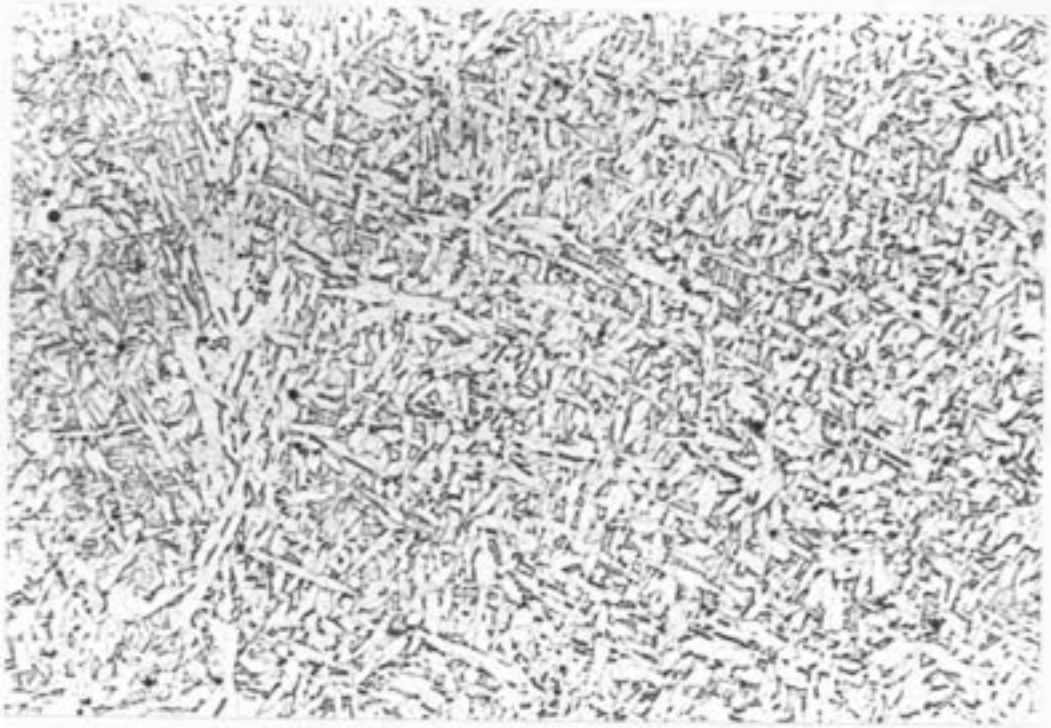

Figure II.6(g) - Primary microstructure of WD2.

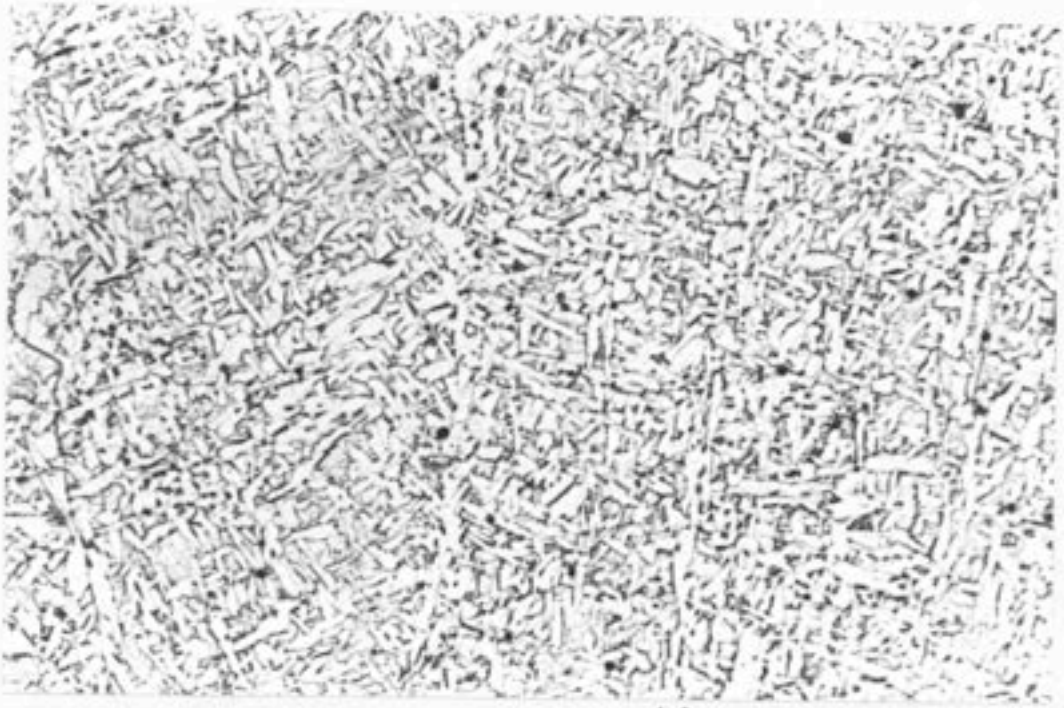

Figure II.6(h) - Primary microstructure of WD3.

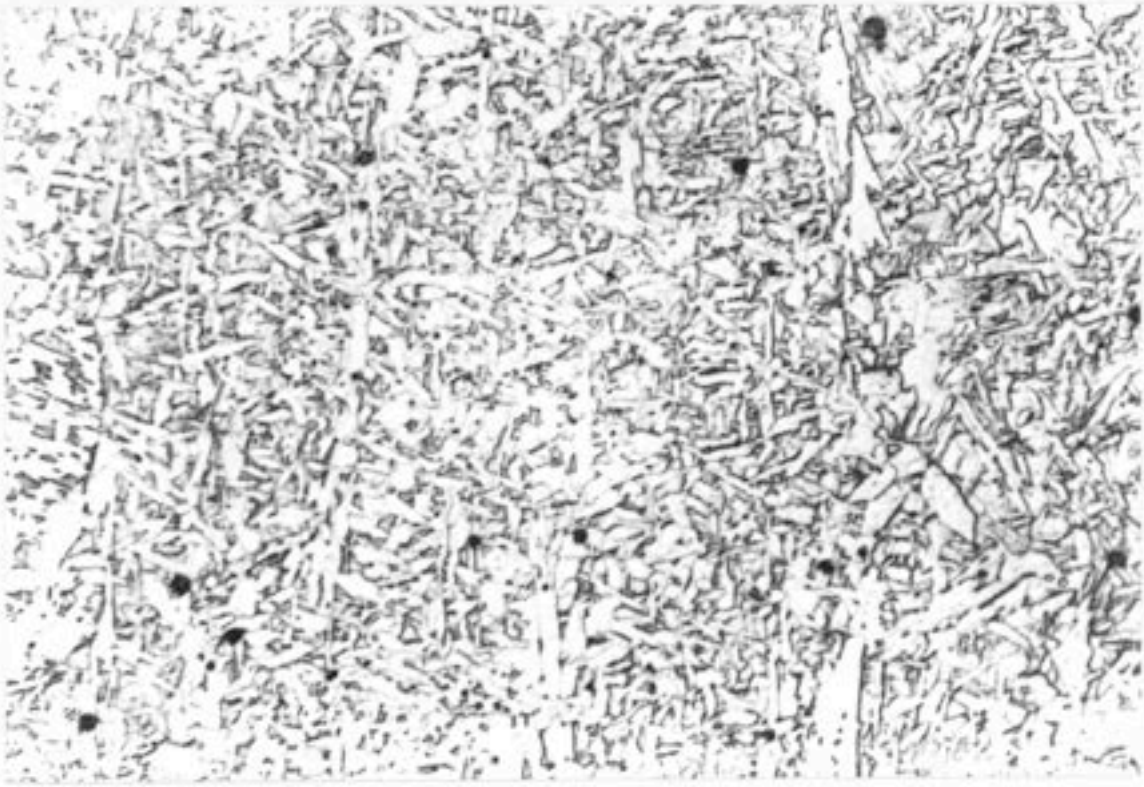

Figure II.6(i) - Primary microstructure of WD4.

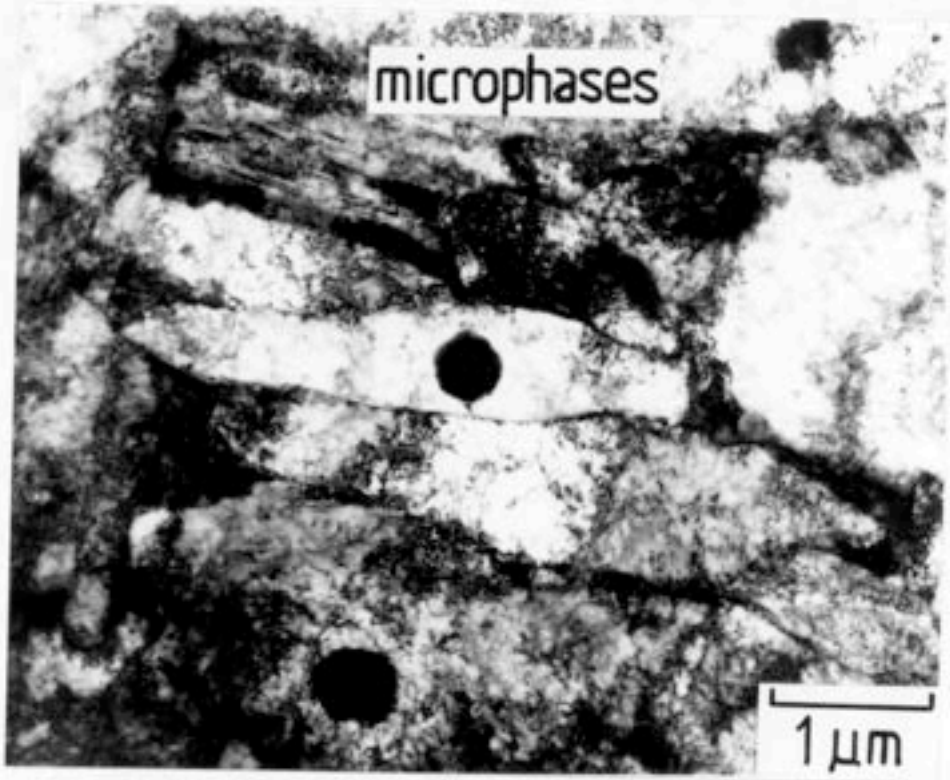

Figure II.7(a) - Electron micrograph shows the acicular ferrite, inclusions and microphases in fusion zone of weld metal WA1.

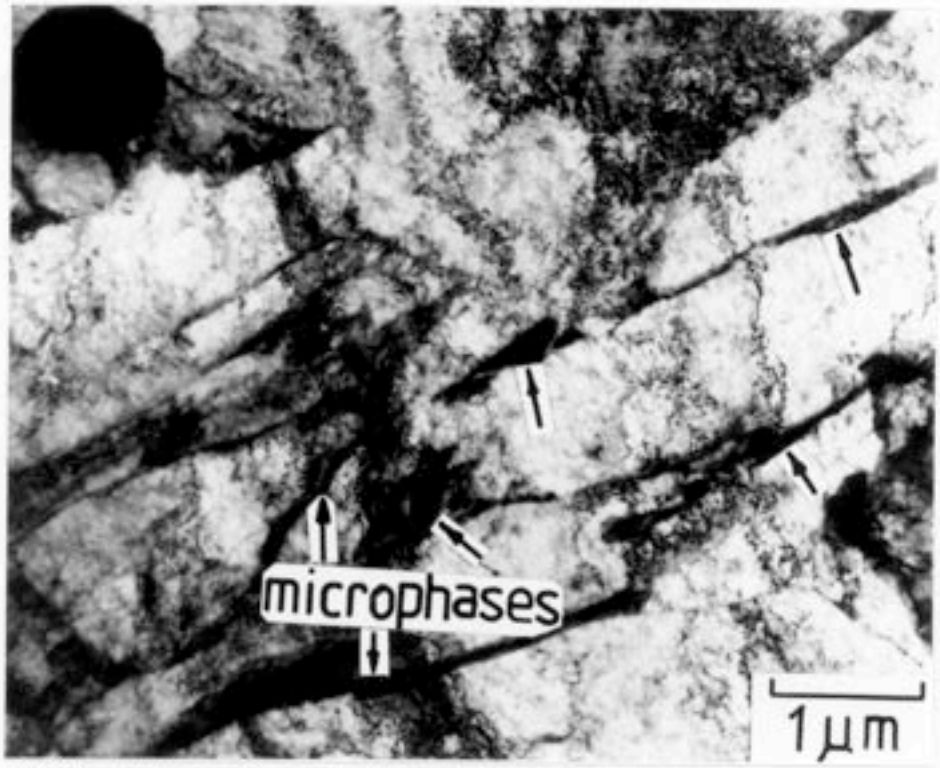

Figure II.7(b) - Electron micrograph shows the microphases between the ferrite plates in fusion zone of weld metal WA2.

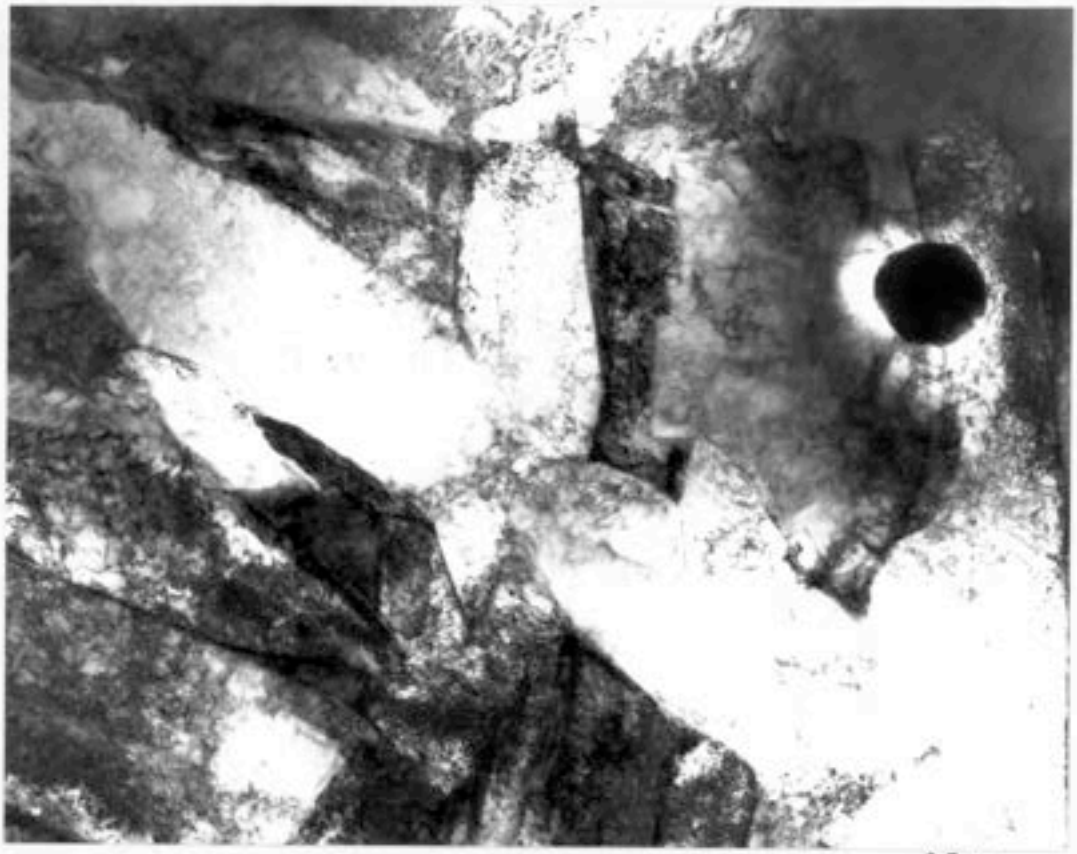

Figure II.7(c) - Electron micrograph shows the acicular ferrite sympathetic nucleation in fusion zone of weld metal WD1.

Figure II.7(d) - Electron micrograph shows that several acicular ferrite plates grow from one inclusion in fusion zone of weld metal WD2.

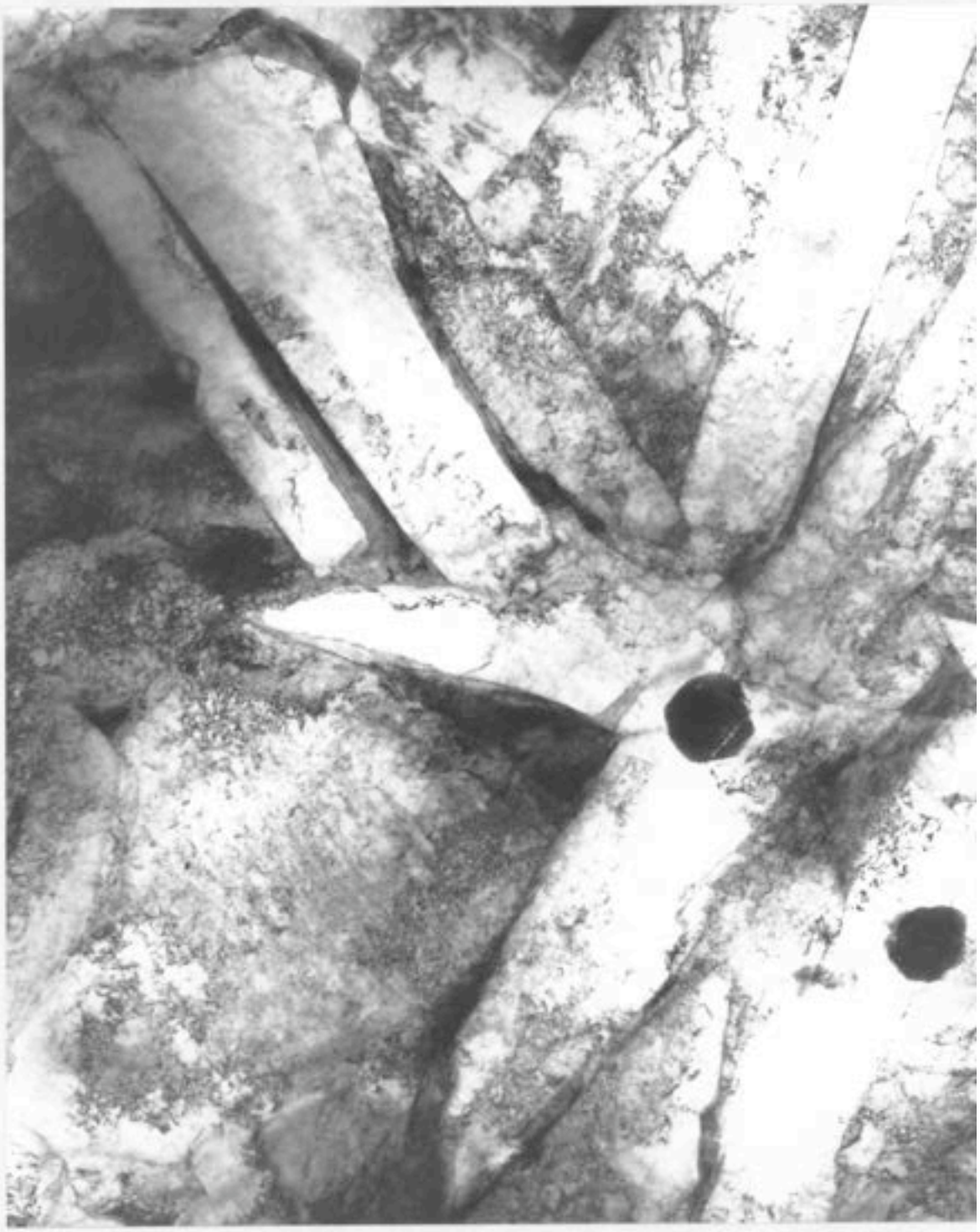

Figure II.7(e) - Electron micrograph shows the acicular ferrite plates, inclusions, elongated microphases and blocky shaped microphases in fusion zone of weld metal WD3.

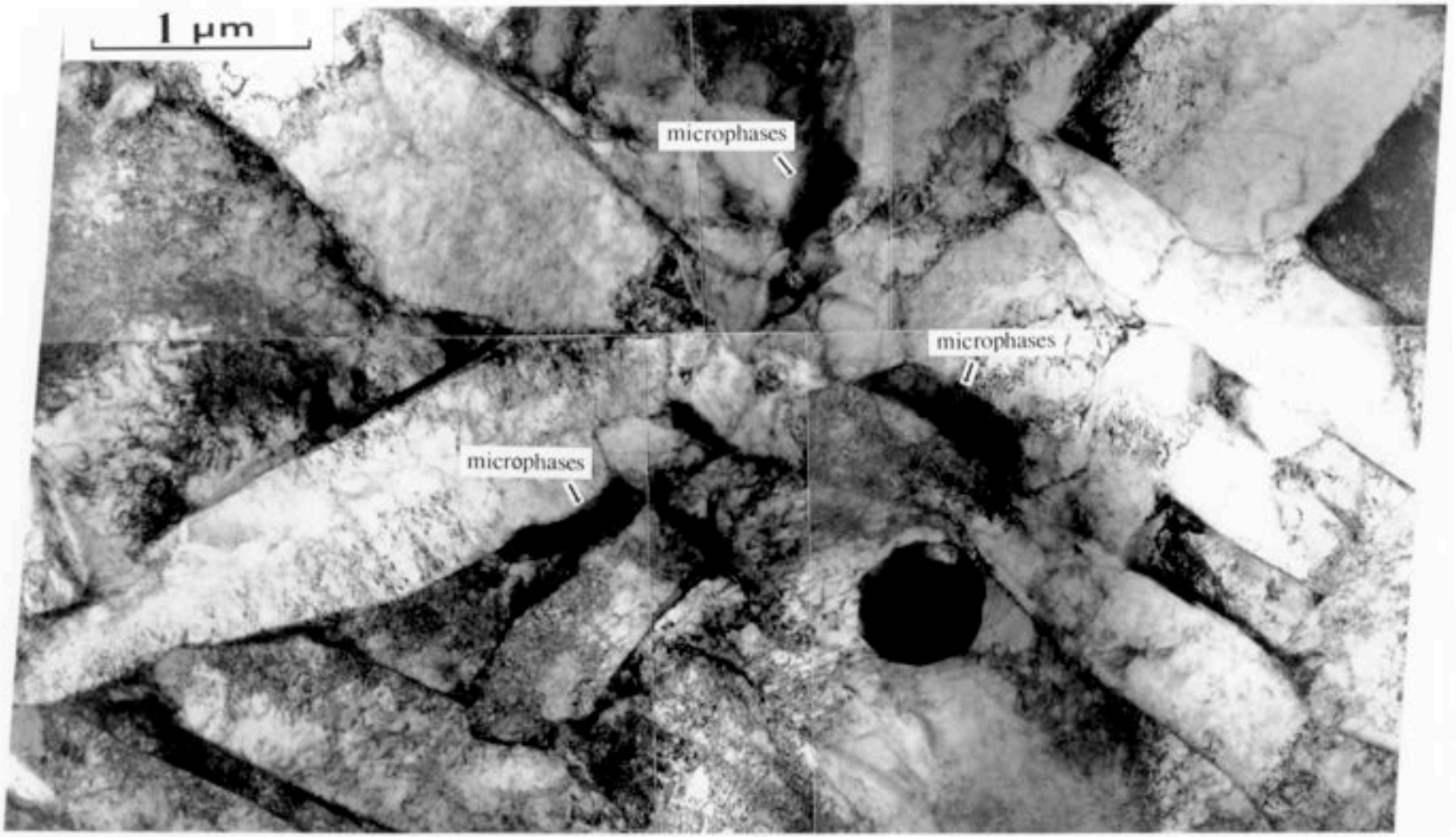

Figure II.7(f) - Electron microscopy shows that due to hard impingement the plates of acicular ferrite are arranged in an interlocking pattern in fusion zone of weld metal WD4.

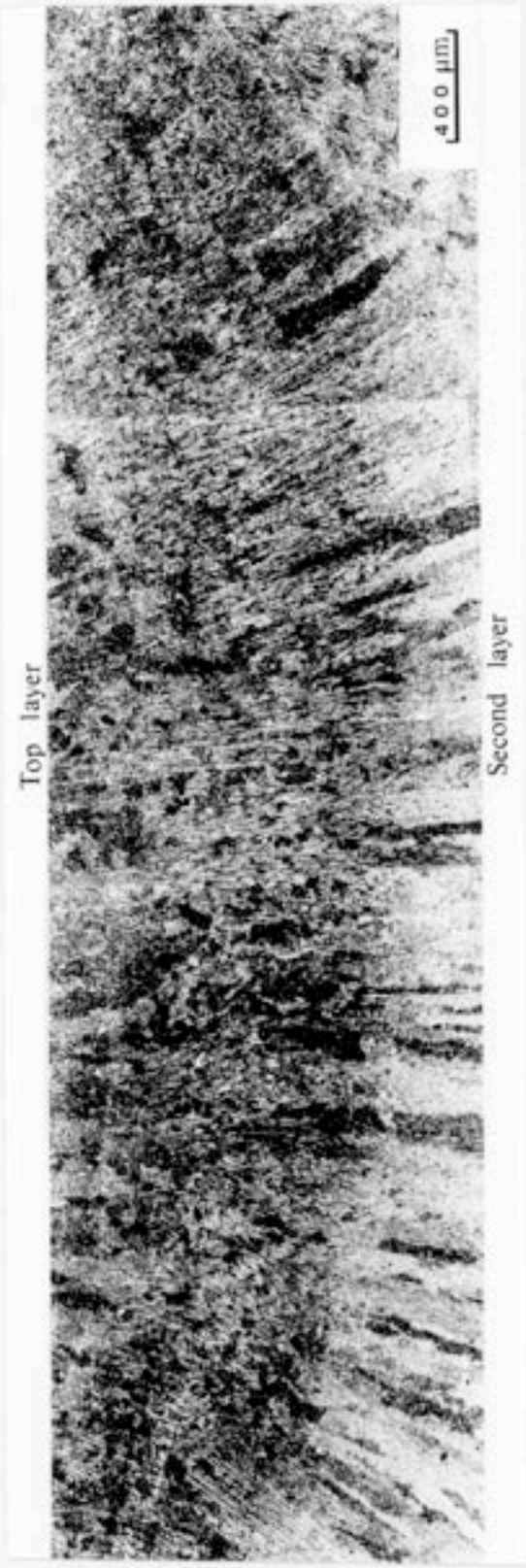

Figure II.8(a) - Showing reheated zone between the top layer and second layer of fusion zones in weld metal WD4.

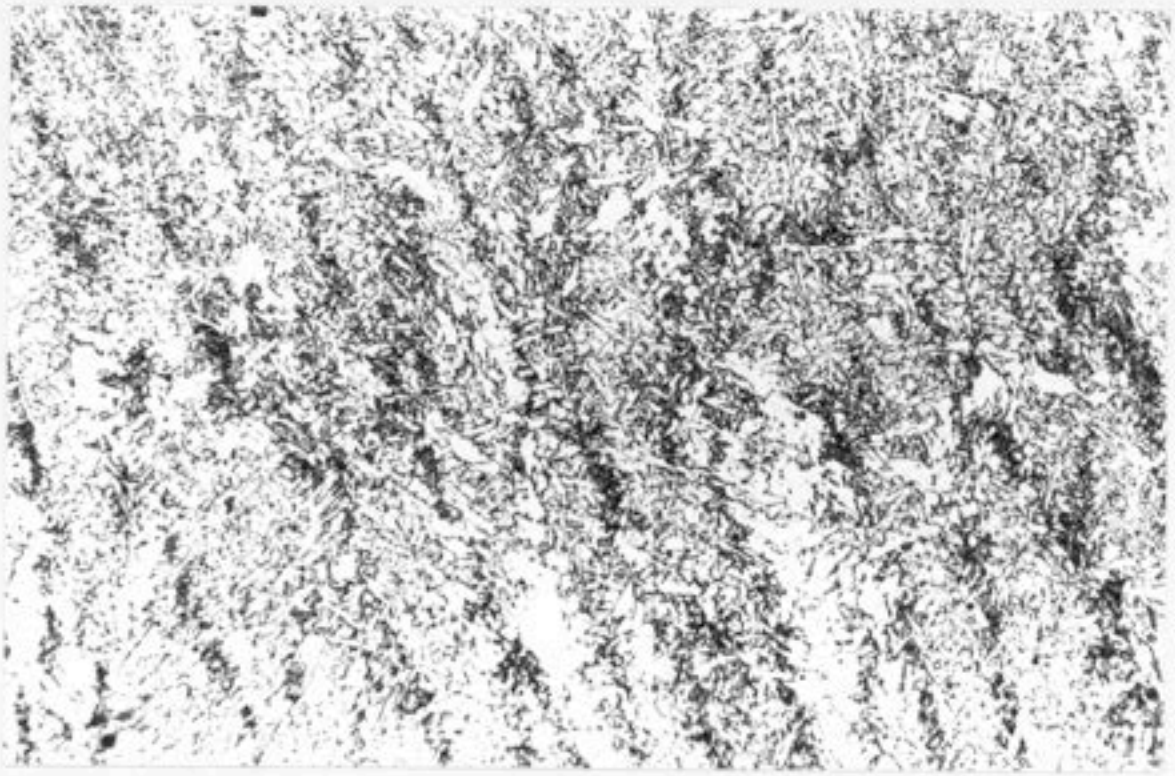

Figure II.8(b) - Showing the microstructure of reheated zone in weld metal WD4. 20 μm

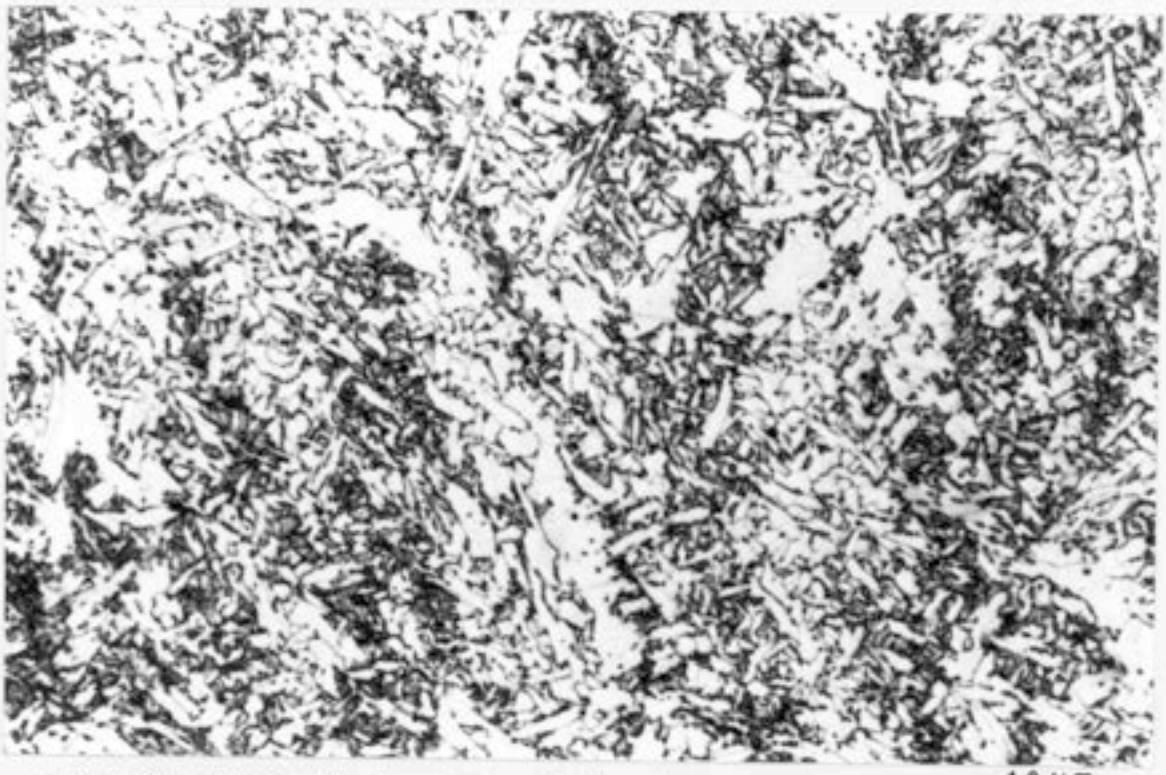

Figure II.8(c) - Showing the microstructure of reheated zone in weld metal WD4. 10 μm

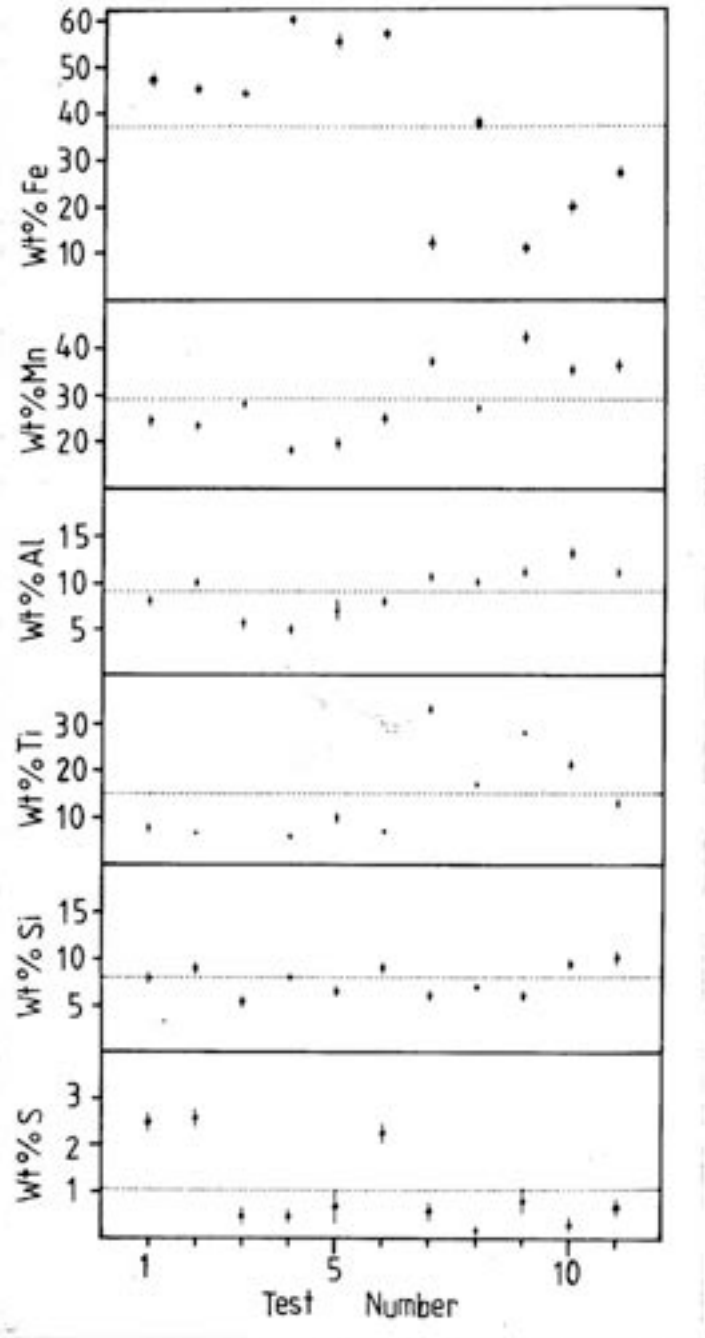

Figure II.9 - Microanalytic data on inclusions of weld metal WB

Chapter Three

Thermodynamics of the Acicular Ferrite Transformation

3.1 Introduction

Acicular ferrite (α_a) is a phase formed by the transformation of austenite (γ) during cooling of low-alloy steel weld deposits [1,162]. It forms in a temperature range where diffusional transformations become relatively sluggish [1] and give way to displacive products such as Widmanstätten ferrite, bainite and martensite. Its morphology consists of non-parallel plates of ferrite, which during the early stages of transformation nucleate on inclusions [60,61] present in the columnar austenite grains typical of weld deposits. Subsequent plates may nucleate sympathetically on these inclusion-nucleated plates [62], so that a one-to-one correspondence between the number of active-inclusions and the number of α_a plates is not expected. However, the mechanism by which acicular ferrite grows is not understood and this hinders the development of phase transformation models for predicting the microstructure of welds. The work below deals with experiments on the thermodynamics of the formation of acicular ferrite from austenite.

The term "acicular" means "shaped and pointed like a needle" but it is generally recognised that α_a has in three-dimensions the morphology of thin-plates. In wrought steels, the formation of plate-shaped ferrite (whether it be bainite or Widmanstätten ferrite) is always accompanied by a change in the shape of the transformed region [48,89,100]. This shape change can be described as an invariant-plane strain with a significant shear component [89,100] and is generally taken to imply a displacive transformation mechanism [51] and the existence of an atomic correspondence between the parent and product phases, at least as far as atoms in the substitutional sites are concerned. Interstitial atoms, such as carbon may diffuse during transformation (especially when the ferrite forms at low-under-coolings where the partitioning of carbon is a thermodynamic necessity), without affecting the shape change or the displacive character of the transformation [25,163]. The shape change accompanying the transformation of acicular ferrite (α_a) has been determined experimentally [65]. Acicular ferrite may in fact be bainite or intragranularly nucleated Widmanstätten ferrite, but its transformation mechanism is not at all established.

The classification of microstructures on the basis of morphology is of considerable use in the study of structure-property relationships, but the prediction of microstructure requires a deeper understanding of the transformation mechanism. It is now well established [53-55] that the presence of acicular ferrite in the primary microstructure of

low-alloy steel weld deposits leads to improved toughness, but the mechanism of its formation is not understood. Attempts at modelling the primary microstructure thus rely on deducing the acicular ferrite content by difference rather than by direct prediction [1]. In this work, the aim was to deduce fundamental information about the growth of acicular ferrite, focussing on whether the growth is diffusionless.

3.2 Experimental Method

To enable the study of acicular ferrite without substantial interference from other reactions, a high-hardenability manual metal arc weld was deposited at a speed of 2 mm/s, using a welding current and voltage of 180A and 23V (DC+) respectively. The joint geometry was compatible with ISO 2560, the weld consisting of 21 runs with 3 runs per layer, the interpass temperature being 250°C. The composition of the weld WB was found to be Fe-0.06C-0.27Si-1.84Mn-2.48Ni-0.2Mo (wt.%) and the deposit contained an oxygen level of 399ppm and a nitrogen level of 111ppm by wt. together with 0.01 Al, 0.02Ti and 0.01Nb wt%.

Specimens for dilatometric experiments were machined from the weld deposits, so that the cylinder axes were parallel to the welding direction. The specimens were machined from regions far from the parent plate and are not affected by dilution from the parent material. All experiments were conducted on specimens which had been homogenised at 1250°C for 3 days, while sealed in quartz tubes containing a partial pressure of pure argon. Finally, the specimens for dilatometry were in the form of 3mm diameter cylindrical rods with a 1.0mm diameter bore and a 20mm length, electroplated with about 0.08mm layer of nickel, to provide constraint and avoid surface nucleation or surface degradation effects. Nickel plating was carried out in two stages - striking and plating. Striking was carried out in a solution made up of 250g $NiSO_4$, 27ml conc. sulphuric acid, and water, amounting to 1 litre in all. The solution was used at 50°C, with a current density of 775mA/cm^2, for 3 minutes. The plating solution consisted of 140g$NiSO_4$, 140g Anhydrous Sodium Sulphate, 15g Ammonium Chloride and 20g Boric Acid, made up to 1 litre with distilled water. The plating was carried out at 50°C, with a current density of 40mA/cm^2, for 15 minutes.

All dilatometry was performed on a Theta Industries high-speed dilatometer, which has a water cooled radio-frequency furnace of essentially zero thermal mass, since it is only the specimen which undergoes the programmed thermal cycle. The length transducer on the dilatometer was calibrated using pure platinum and pure nickel specimens of known thermal expansion characteristics. This enables rapid heating or cooling experiments to be carried out. The dilatometer has been specially interfaced with a BBC/Acron

microcomputer so that length, time and temperature information can be recorded at microsecond intervals, and the data stored on a floppy disc. The information is then transferred to a mainframe IBM3081 computer for further analysis.

The specimens were austenitised at 950°C for 10 minutes (or 1200°C for 30 minutes) before helium gas quenching to the different isothermal transformation temperature (480, 460 and 440°C). The relative length change ($\Delta L/L$) during the isothermal transformation was measured and the corresponding relative length change versus time has been plotted. The carbon content of residual austenite when isothermal transformation ceases is very useful in understanding the transformation mechanism. The maximum relative length change (ΔL_m) can be converted into the volume fraction of ferrite transformed, from which the carbon content of the residual austenite can be calculated. The carbon content of the residual austenite as a function of the relative length change in isothermal transformation can be estimated from equation III.1 and III.2. The relative length change ($\Delta L/L$) corresponding to a volume fraction (V) of ferrite transformed is given [164] by:

$$\Delta L/L = [2V(a_\alpha^3) + (1-V)(a_\gamma^3) - \bar{a}_\gamma^3]/[3\bar{a}_\gamma^3] \qquad \text{(III.1)}$$

where a_α = lattice parameter of ferrite at the reaction temperature,

$\bar{a}_\gamma$ = lattice parameter of austenite at the beginning of the isothermal transformation

a_γ = lattice parameter of austenite at any stage of the isothermal transformation.

$$a_\alpha = \bar{a}_\alpha[1 + e_\alpha(T-293)]$$

where $\bar{a}_\alpha$ = lattice parameter of ferrite, at ambient temperature (293K) measured by X-ray diffraction,

e_α = linear expansion coefficient of ferrite.

$$\bar{a}_\gamma = (a_0 + \Sigma CiXi)\,[1 + e_\gamma(T-293)]$$

where a_0 = lattice parameter of unalloyed austenite,

Xi = concentration of alloying element i,

Ci = coefficients (obtained from Reference 165) relating Xi to the change in a_0. Suppose C_1 for carbon, C_2,C_3 C_4, ... for other substitutional alloy elements.

e_γ = linear expansion coefficient of austenite.

Hence $\bar{a}_\gamma = (a_0 + C_1\bar{X} + C_2X_2\ C_3X_3 + C_4X_4 + \ldots)[1 + e_\gamma(T-293)]$,

and $a_\gamma = (a_0 + C_1X_\gamma + C_2X_2 + C_3X_3 + C_4C_4 + \ldots)[1 + e_\gamma(T-293)]$

where $\bar{X}$ = average carbon concentration of alloy,

X_γ = carbon concentration of residual austenite.

After ferrite formation, the carbon is rejected from ferrite to residual austenite; therefore

$$X_\gamma = \bar{X} + [V(\bar{X} - S)/(1-V)] \qquad \text{(III.2)}$$

where S = amount of carbon locked up in ferrite either as carbides or in solution.

All the concentrations used in the calculation of equation III.1 and III.2 are in wt%. The calculations also require the linear expansion coefficients of austenite and ferrite. The ferrite linear expansion coefficient e_α was determined by first tempering a specimen at 600°C for 10 minutes to decompose any retained austenite and then recording the length change during cooling at a rate of 0.063°C/s. The measurements do not therefore account for the presence of a very small amount of carbide. The graph of relative length versus temperature is plotted in Figure III.1, from which the linear expansion coefficient of ferrite was obtained ($e_\alpha = 1.15 \times 10^{-5} k^{-1}$). The γ expansion coefficient was measured while specimen was in the γ single-phase field, as shown in Figure III.2 ($e_\gamma = 1.769 \times 10^{-5} k^{-1}$). The ferrite lattice parameter ($\bar{a}_\alpha$) at ambient temperature was measured using a Debye-Scherrer technique. The testing specimen had been annealed at 600°C for 1 hour, while sealed in quartz tubes containing a partial pressure of pure argon, and then machined to the form of 0.5mm x 0.5mm x 15mm wire. Finally the specimen was chemically polished in a solution made up of 5% HF, 50% H_2O_2 and 45% H_2O for one minute to remove the deformation layer before testing. In the X-ray lattice parameter measurement, the CuK_α radiation and a standard Debye camera were used. The wave length of CuK_α radiation is 1.5417Å, and the Diameter of the standard Debye camera is 114.60mm. Newton-Ralphson extrapolation [166], using 011, 002, 112, 022, 013 lines, was used to obtain the ambient temperature ferrite lattice parameter $\bar{a}_\alpha = 2.8723$Å as shown in Figure III.3. This parameter differs by only 0.1% from that calculated using data from Reference 167. Using these values and making the appropriate substitution in equation III.1 and III.2, the carbon content of residual austenite X_γ values (Table III.1) are obtained using a computer programme. Since carbide precipitation does not occur rapidly over the time scale of the experiments, S in equation III.2 is taken to be 0.02 wt%, which is approximately the maximum solubility of carbon in ferrite.

3.3 Results and Discussion

The primary as-deposited microstructure of weld metal WB studied in this investigation has been shown in Figure II.6c. It consists chiefly of acicular ferrite, with a small amount of allotriomorphic ferrite, Widmanstätten ferrite and microphases. The calculated TTT curve for the weld metal has also been shown in Figure II.1a. In this alloy, the Widmanstätten ferrite start temperature (W_s) and bainite start temperature (B_s) have been calculated, and it has been found that $W_s = B_s = 500$°C. This means [100] that

Widmanstätten ferrite should not be observed at all and immediately implies that the acicular ferrite observed in the weld deposit is likely to be bainite if it is not a completely new transformation. Figure II.1a also shows that for any reasonable weld cooling rate, the cooling curve cannot intersect the upper C curve (diffusional C curve), so that the alloy can only transform by a displacive mechanism. The alloy is therefore ideally suited to avoid interference from other transformation products during the study of acicular ferrite. In addition, transformation during the quench to the isothermal transformation temperature can easily be avoided. Certainly, a weld deposit is necessarily chemically inhomogeneous, and some formation of allotriomorphic ferrite and Widmanstätten ferrite cannot thus be avoided in the solute depleted regions, as seen in Figure II.6c.

3.3.1 Grain Size Effect

The problem of resolving the nature of acicular ferrite is made worse by the fact that it does not readily occur in wrought steels, due to the absence intragranular heterogeneous nucleation sites and because the austenite grain size of such steels is deliberately kept small; transformations initiated at austenite grain boundaries thus swamp the interior regions as well. However, if after deposition, a weld is reheated into the austenite phase field to generate large austenite grains then these new grains still contain the inclusions which were present in the original deposit. Isothermal transformation of this structure in a temperature range where acicular ferrite usually forms in welds should then lead to the intragranular nucleation and growth of plates whose morphology should be identical to that of the acicular ferrite observed in weld deposits.

The austenite grain sizes for the homogenised specimen austenitised at 950°C for 10 minutes, and at 1200°C for 30 minutes have been investigated. The heat treatment processes were carried out in dilatometer as well. After austenitisation, the specimens were quenched by helium jets and then tempered at 600°C for 1 hour in order to reveal the austenite grain boundaries as shown in Figure III.4. Figure III.4a displays the smaller austenite grain for the specimen austenitised at 950°C for 10 minutes. Figure III.4b presents larger austenite grain for the specimen austenite at 1200°C for 30 minutes. Using linear intercept method, the austenite grains were measured on Quantimet 720 image analysing computer. The average grain size for the former is about 15μm, and for the latter about 45μm. The higher austenitisation temperature has clearly led to a larger austenite grain size. The results of isothermal transformation experiments on reheated weld metal are illustrated in Figure III.5, 6, 7 and 8. The optical micrograph (Figure III.5a) shows some ferrite plates forming after austenitisation of weld metal at 950°C for 10 minutes followed by isothermal transformation at 490°C for 30 minutes prior to quenching to ambient temperature. It is noted that the ferrite plates grow from austenite

grain boundaries and adjacent ferrite plates are parallel to each other. This is the feature of bainitic ferrite. It is also found that the transformation temperature 490°C is very close to the B_S temperature (the calculated B_S temperature is 500°C). Figure III.5b also displays some ferrite plates obtained after austenitisation of weld metal at 1200°C for 30 minutes followed by isothermal transformation at 490°C for 30 minutes. The ferrite plates seem to be scattered in the austenitic matrix (now martensite after quenching to room temperature). It is also noted that the major ferrite plates are not parallel with their adjacent plates. The morphology is like that of acicular ferrite. Figure III.6 demonstrates the results of isothermal transformation at 460°C for 30 minutes; in one case the weld was reaustenitised at 950°C for 10 minutes (Figure III.6a) and another sample was austenitised at 1200°C for 30 minutes (Figure III.6b) before isothermal transformation. It is clear (Figure III.6b) that isothermal transformation with the larger austenite grain condition has led to the intragranular nucleation of plates of ferrite which can be identified morphologically with acicular ferrite found in welds. On the other hand, in the specimen reaustenitised at 950°C, the small austenite grain size has prevented intragranular nucleation, the ferrite plate nucleation at the austenite grain boundaries and growing by a sub-unit mechanism to give the morphology of sheaves of upper bainite (Figure III.6a). The striking transmission electron micrographs in Figure III.7a and b distinctly confirm the morphologies of upper bainite and acicular ferrite in weld metal for the corresponding optical micrographs shown in Figure III.6a and b. In order to investigate the morphologies for higher volume fraction of bainite and acicular ferrite in weld metal, the isothermal transformation was carried out at 440°C for 30 minutes. The results are shown in Figure III.8. Figure III.8a displays large amount of bainite obtained after austenitisation of weld metal at 950°C for 10 minutes followed by isothermal transformation at 440°C for 30 minutes. The micrograph clearly demonstrates that the sheaves of bainite ferrite grow from grain boundaries, swamp the interior region of austenite grains, and them impinge with the opposite austenite grain boundaries. Figure III.8b shows a high volume fraction of acicular ferrite obtained after austenitisation at 1200°C for 30 minutes followed by isothermal transformation at 440°C for 30 minutes. The optical micrograph shows the interlocking nature of acicular ferrite because acicular ferrite nucleates intragranularly at inclusions within large austenite grains, and because of hard impingement between plates nucleated on adjacent inclusions. It is clear that acicular ferrite requires the presence of inclusions to initiate intragranular nucleation, and will only form when the austenite grain size is relatively large, so that events originated from the grain boundaries do not swamp those occurring intragranularly.

3.3.2 The Carbon Content of Residual Austenite

A further experiment is needed to clearly establish that acicular ferrite is similar to bainite and not to intragranularly nucleated Widmanstätten ferrite. Both bainite (α_b) and Widmanstätten ferrite (α_w) grow by a displacive transformation mechanism [25,89,100]. However, the formation of Widmanstätten ferrite involves the redistribution of carbon between the parent and product phases, but bainite initially forms by a diffusionless mechanism and the carbon later partitions into the remaining austenite [25,89,100]. This difference can be exploited to deduce whether acicular ferrite grows like conventional bainite or like Widmanstätten ferrite.

Considering first the diffusionless formation of bainite, the reaction should go to completion since there is no diffusion necessary. In practice, the whole of the austenite grain does not transform instantaneously because of kinetic restrictions (e.g. heterogeneous nucleation); even if the first plate forms without diffusion, it has a opportunity to reject its excess carbon into the residual austenite. Any further increment of transformation is therefore associated with a lower free energy change, due to the higher carbon content of the austenite from which it has to form. Eventually, a stage is reached where the transformation becomes thermodynamically impossible since the free energies of residual austenite and bainitic ferrite of the same composition become identical [25,89,100], as shown in Figure III.9. The locus of such positions, as a function of isothermal transformation temperature defines the T_0' curve [89,100], where austenite and bainite (with a certain amount of stored energy associated with transformation strains) of the same composition have equal free energies. The corresponding curve for stress-free austenite and ferrite of identical composition is conventionally called T_0 [104]. The bainite reaction should therefore stop when the carbon concentration of austenite (X_γ) reaches the level given by the T_0' for the isothermal transformation temperature concerned [100].

The Ae_3' curve (as shown in Figure III.9) may similarly be defined for the growth of Widmanstätten ferrite [100] which involves the paraequilibrium transformation with the partitioning of carbon. If the small amount of strain energy associated with the back-to-back formation of mutually accommodating plates of Widmanstätten ferrite is ignored, the Widmanstätten reaction should stop when X_γ reaches the level given by the Ae_3' curve for the isothermal transformation temperature concerned [100]. For any given Temperature, the carbon concentration given by Ae_3' curve is much larger than that given by the T_0' curve, so that a measurement of X_γ at reaction termination can clearly distinguish between Widmanstätten ferrite and bainite. Hence, the aim was to transform a weld metal isothermally in a temperature range where it is known to transform to just acicular ferrite,

and by studying the maximum extent of transformation in terms of the above criteria, to decide whether acicular ferrite resembles Widmanstätten ferrite or bainite with respect to its growth mechanism.

3.3.3 Dilatometry and Thermodynamic Analysis

The dilatometric specimens were austenitised at 950°C for 10 minutes or at 1200°C for 30 minutes before quenching to the isothermal transformation temperatures 440, 460 and 490°C. The isothermal transformation curves are presented in Figure III.10 and are seen to have a classical sigmoidal shape, with a rapid initial reaction. It is immediately apparent that the maximum degree of transformation at any temperature increases as temperature below the bainite start temperature (B_s = 500°C), showing that the weld metal exhibits the classical "incomplete reaction phenomenon" which is an identifying feature of bainitic transformation [25,89,100]. The carbon content of residual austenite X_γ corresponding to the maximum degree of transformation has been calculated, using equations III.1 and 2 and the following measurements: $e_\alpha = 1.150 \times 10^{-5}k^{-1}$, $e_\gamma = 1.769 \times 10^{-5}k^{-1}$, and the lattice parameter of ferrite in the weld, at ambient temperature. The carbon content of residual austenite (X_γ), the volume fraction of bainite (V_{α_b}) and the volume fraction of acicular ferrite (V_{α_a}) after complete isothermal transformation are shown in Table III.1. X_γ corresponding to the maximum degree of transformation is presented in Figure III.11, along with the relevant phase boundaries T'_σ T_o and Ae'_3 (as calculated in Chapter Two). It is clear that acicular ferrite formation ceases at the T'_o boundary, providing strong evidence that the formation of acicular ferrite is diffusionless, the redistribution of carbon into the residual austenite occurring at a stage after growth. The transformation mechanism of acicular ferrite is clearly established and is the same as that of bainite. The results also imply that the strain energy accompanying acicular ferrite growth is of the order of 400J/mol [100].

3.4 Conclusions

It is found that the formation of acicular ferrite at any particular transformation temperature ceases as the carbon concentration of the residual austenite reaches the T'_o boundary, and that the transformation exhibits an "incomplete reaction phenomenon". The maximum extent of transformation increases with undercooling below the B_s temperature. These results provide strong evidence suggesting that the growth of acicular ferrite is diffusionless, with carbon partitioning into austenite after the transformation event. In this respect, acicular ferrite is identical to bainite. Evidence has also been provided to show that the morphology of acicular ferrite differs from that of bainite simply because the former nucleates intragranularly at inclusions within large austenite

grains and because of hard impingement between plates nucleated on adjacent inclusions. It is concluded that acicular ferrite is in fact bainite which nucleates intragranularly in the large austenite grains typical of weld deposits.

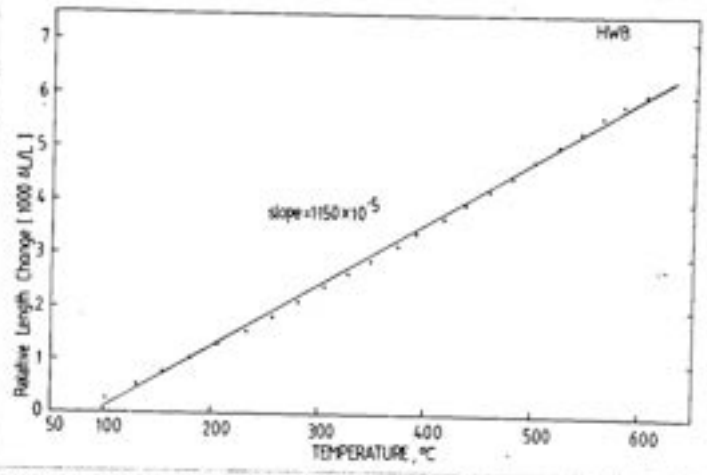

Fig. III.1 - Showing the graphs of relative length change versus temperature, from which the linear expansion coefficient of ferrite is obtained.

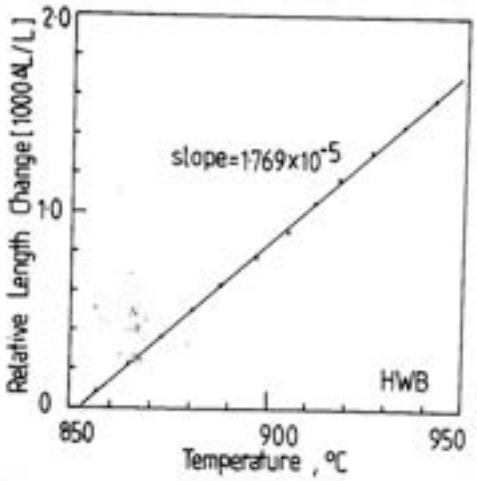

Fig. III.2 - Showing the graphs of relative length change versus temperature, from which the linear expansion coefficient of austenite is obtained.

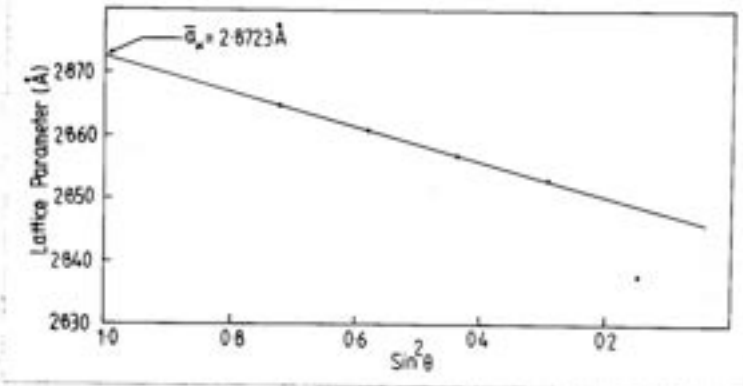

Fig. III.3 - Extrapolation of measured lattice parameter against $\sin^2\theta$. θ is the diffraction angle.

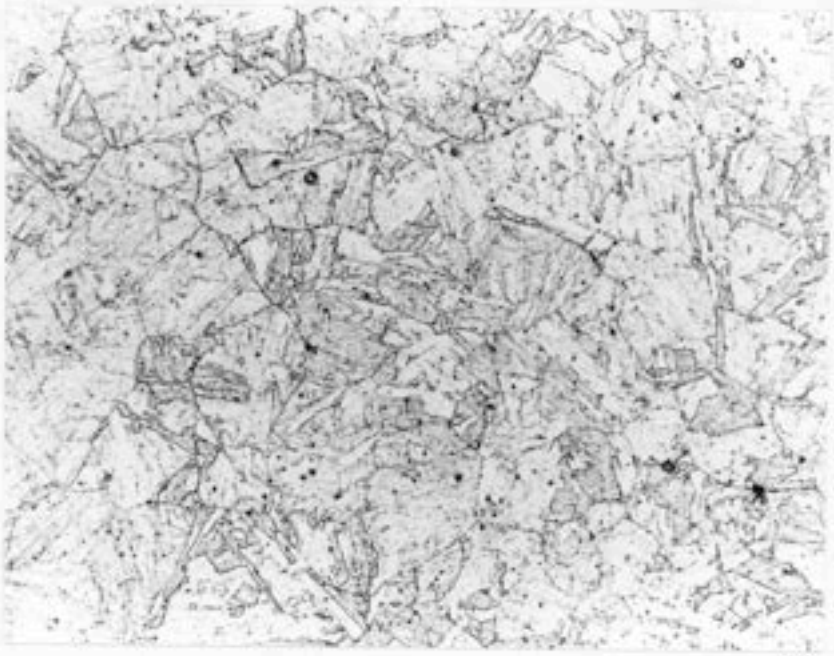

Fig. III.4a - Optical micrograph shows small austenite grains. Weld metal was reaustenitised at 950°C for 10 minutes and quenched by helium jets, and then tempered at 600°C for one hour.

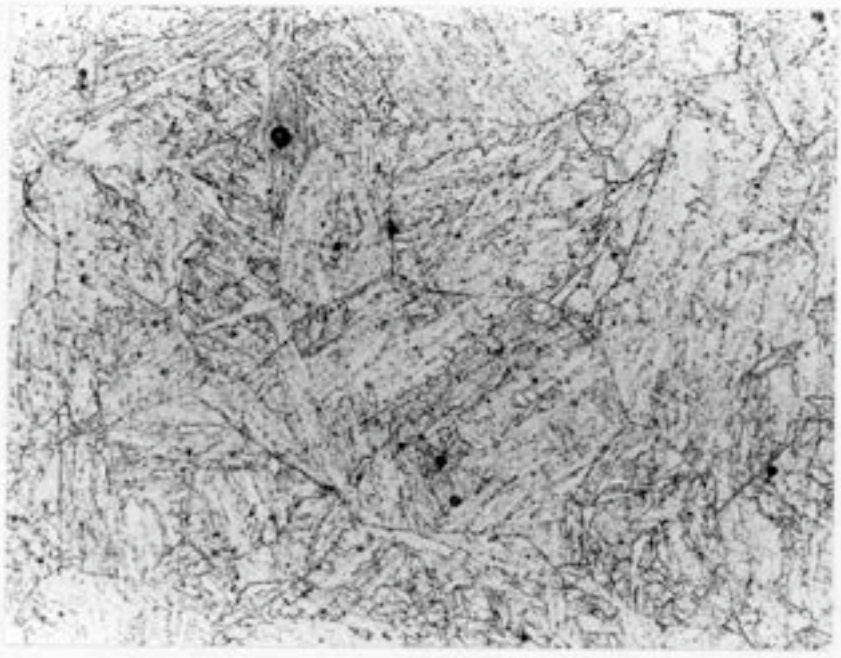

Fig. III.4b - Optical micrograph displays larger austenite grains. Weld metal was reaustenitised at 1200°C for 30 minutes and quenched by helium jets, and then tempered at 600°C for one hour.

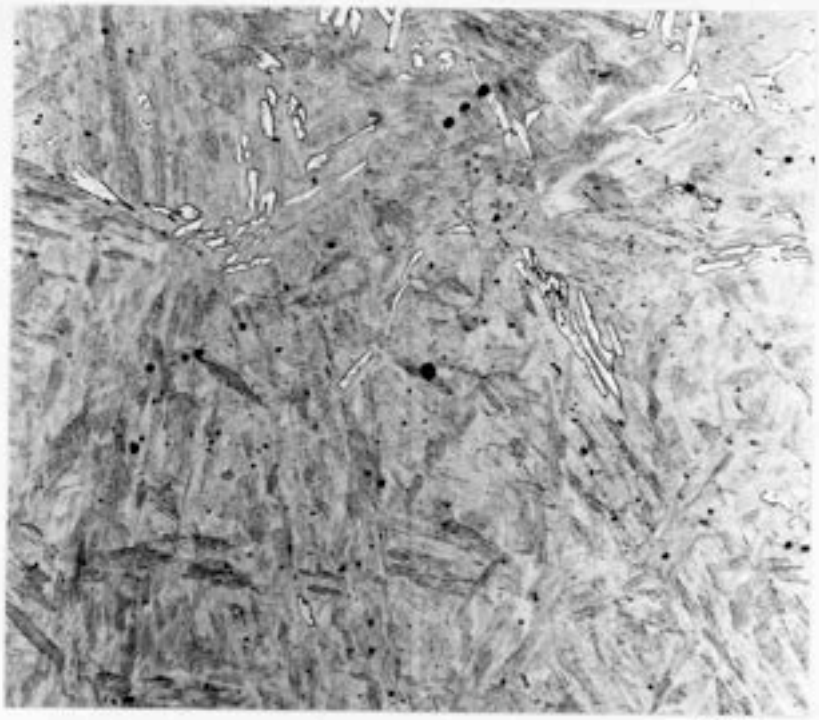

Fig. III.5a - Ferrite plates forming after austenitisation of weld metal at 950°C for 10 minutes followed by isothermal transformation at 490°C for 30 minutes.

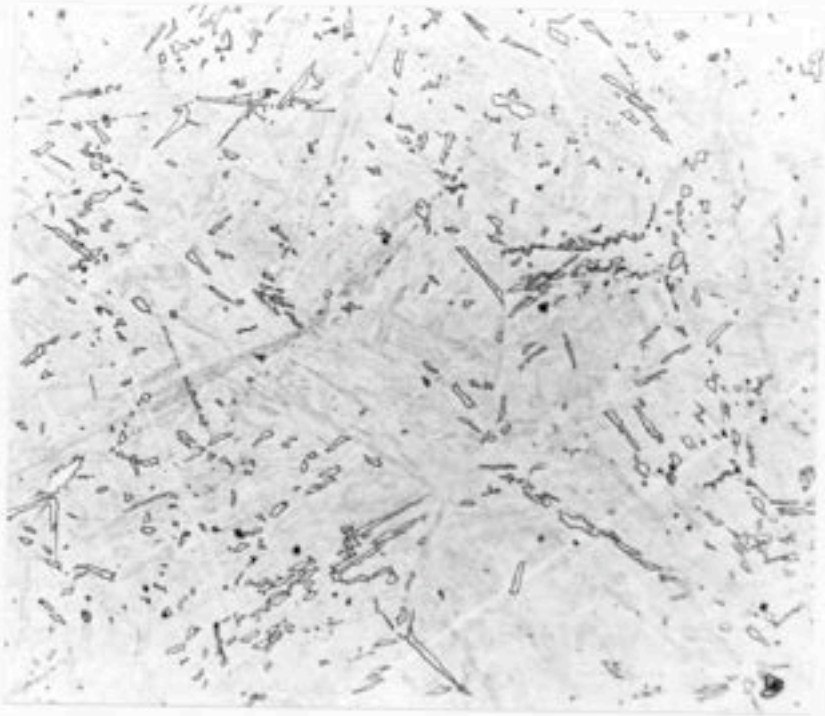

Fig. III.5b - Ferrite plates forming after austenitisation of weld metal at 1200°C for 30 minutes followed by isothermal transformation at 490°C for 30 minutes.

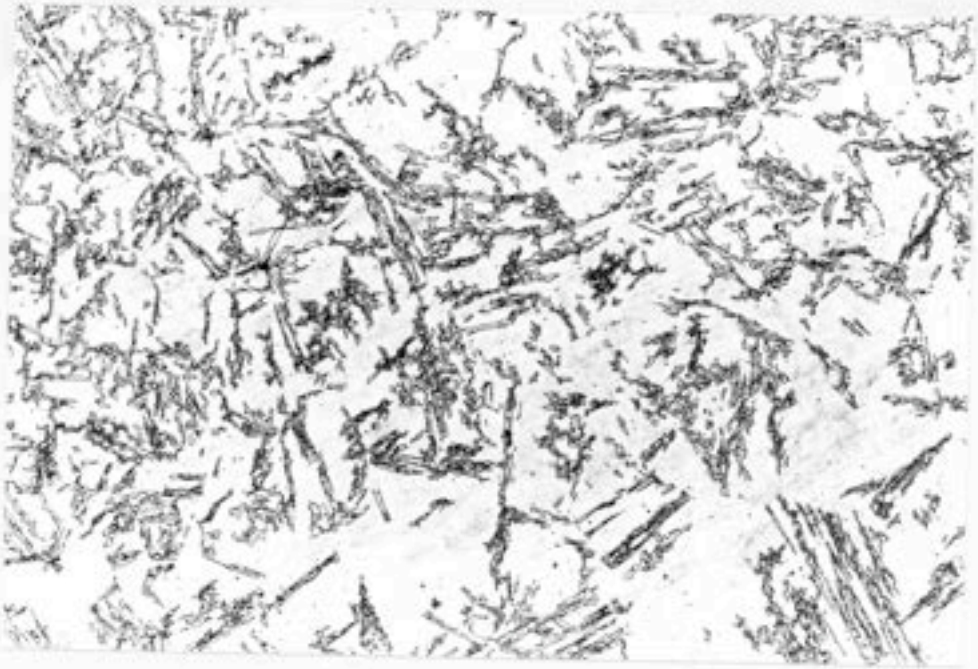

Fig. III.6a - Bainite obtained after austenitisation of weld metal at 950°C for 10 minutes followed by isothermal transformation at 460°C for 30 minutes.

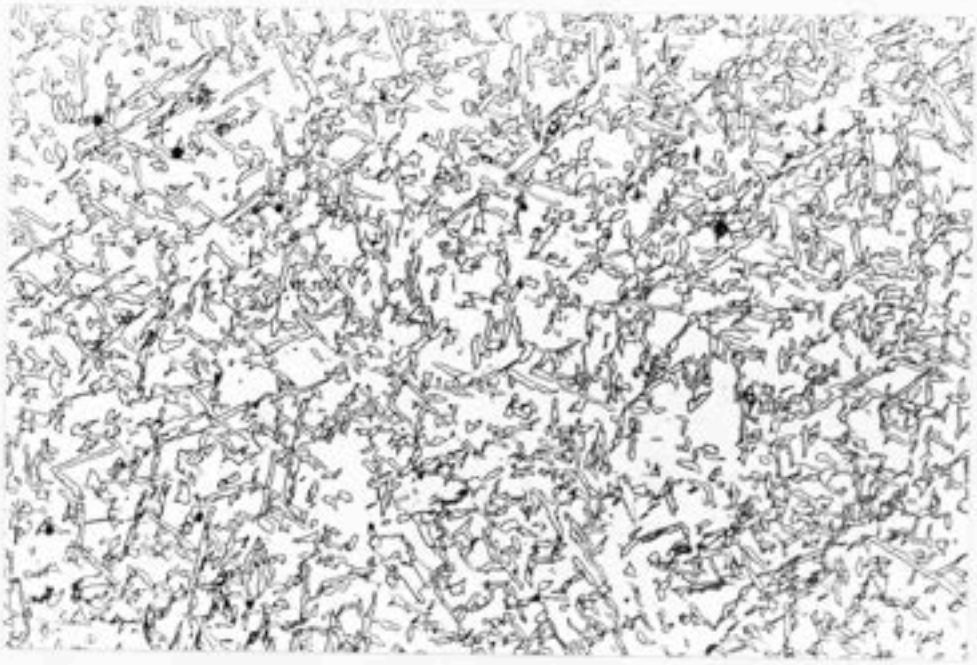

Fig. III.6b - Acicular ferrite obtained after austenitisation of weld metal at 1200°C for 30 minutes followed by isothermal transformation at 460°C for 30 minutes.

Fig. III.7a - Transmission electron micrograph shows classical sheaf of upper bainite. Weld metal was reaustenitised at 950°C for 10 minutes, isothermally transformed at 460°C for 30 minutes and then quenched by helium jets.

Fig. III.7b - Transmission electron micrograph shows acicular ferrite. Weld metal was reaustenitised at 1200°C for 30 minutes, followed by isothermal transformation at 460°C for 30 minutes and then quenched by helium jets.

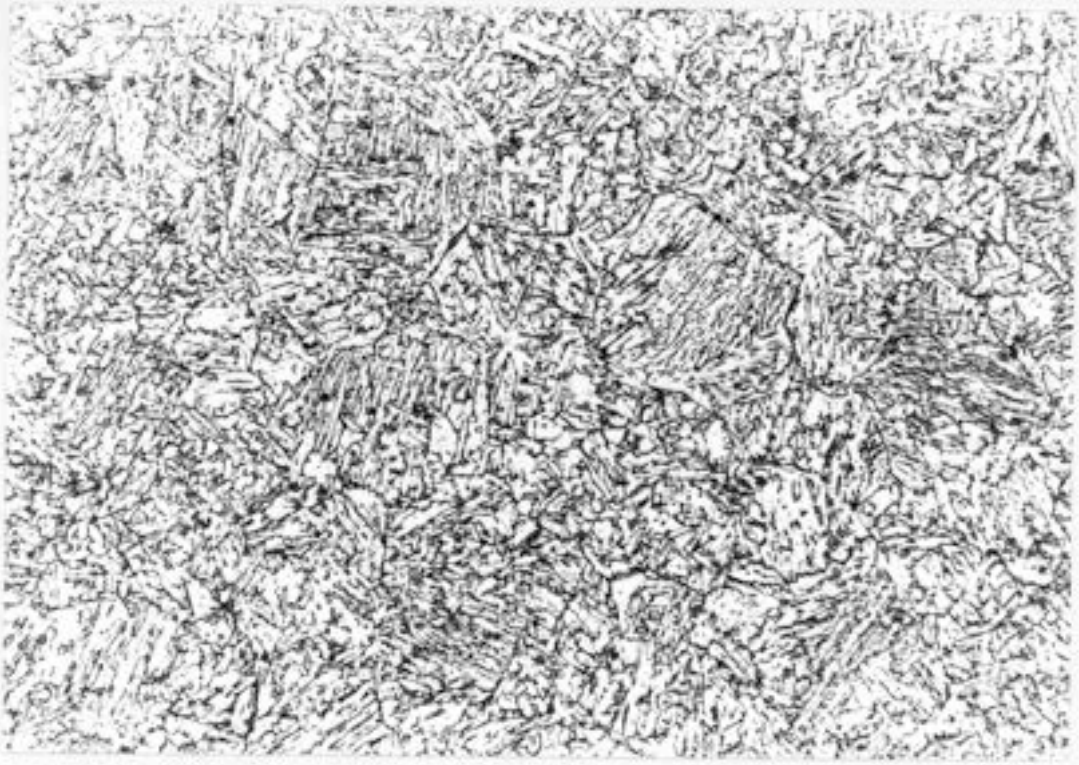

Fig. III.8a - High volume fraction of bainite obtained after austenitisation of weld metal at 950°C for 10 minutes followed by isothermal transformation at 440°C for 30 minutes.

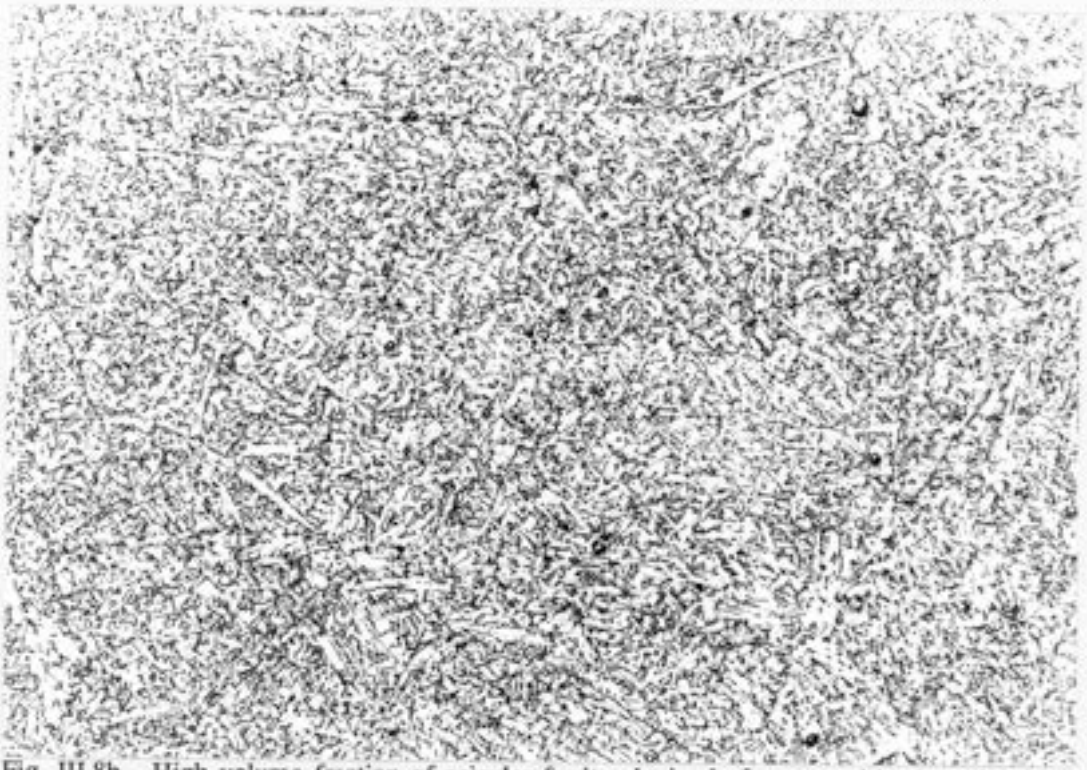

Fig. III.8b - High volume fraction of acicular ferrite obtained after austenitisation of weld metal at 1200°C for 30 minutes followed by isothermal transformation at 440°C for 30 minutes.

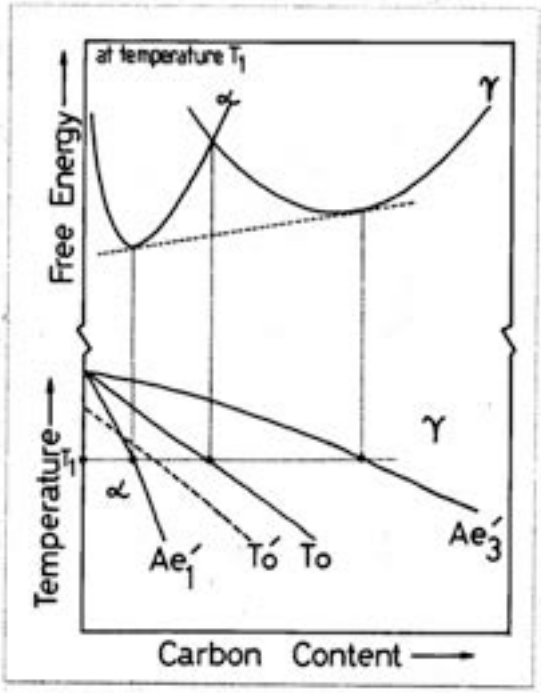

Fig. III.9 - Schematic diagram showing the construction of phase boundaries from free energy data. The T_o' line includes the effect of 400J/mol of strain energy due to transformation.

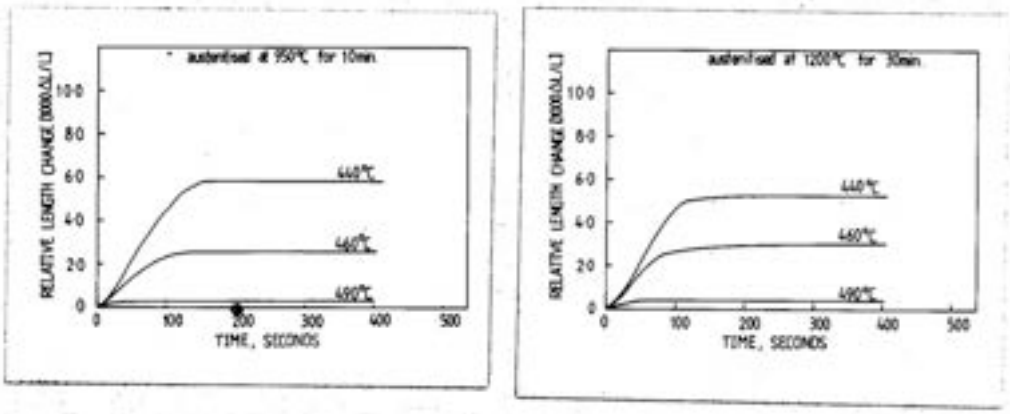

Fig. III.10 - (a) Isothermal transformation curves for weld reaustenitised at 950°C. (b) Isothermal transformation curves for weld reaustenitised at 1200°C.

Table III.1 - The carbon content of residual austenite (X_γ), the volume fraction of bainite (V_{α_b}) and the volume fraction of acicular ferrite (V_{α_a}) after isothermal transformation ceases.

isothermal transformation temperature (°C)	reaustenitisation at 950°C for 10 min. before isothermal transformation		reaustenitisation at 1200°C for 30 min. before isothermal transformation	
T_I	V_{α_b}	X_γ	V_{α_a}	X_γ
490	0.05	0.27×10^{-2}	0.08	0.28×10^{-2}
460	0.37	0.34×10^{-2}	0.40	0.35×10^{-2}
440	0.88	0.53×10^{-2}	0.86	0.50×10^{-2}

Note: X_γ in mol fraction.

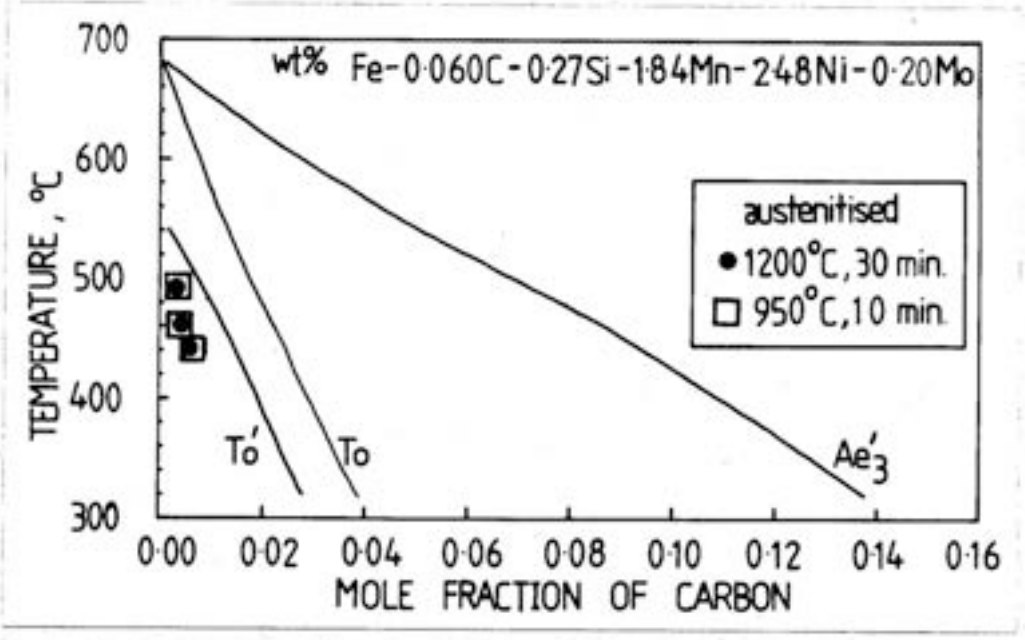

Fig. III.11 - Phase diagram, with experimental data on the carbon concentration of austenite at the termination of isothermal transformation. The reactions stop well before the Ae3' curves are reached.

Chapter Four

REAUSTENITISATION IN STEEL WELD DEPOSITS - PART 1

4.1 Introduction

Much work has recently been done on the prediction of the primary microstructure of fusion zone in weld deposits using detailed phase transformation theory, and this has met with reasonable success [1,31,77-79]. However, there is no corresponding theory available for the reheated microstructure, which can form a substantial proportion of a multipass weld deposit. The thermal cycle experienced in the reheated zone may just anneal the microstructure and cause recrystallisation and grain growth, or if the Ac_1 temperature is exceeded, it may reaustenitise to a degree depending on the thermodynamics and the kinetics of reaustenitisation. In order to establish a quantitative model for reaustenitisation in weld deposits, the work is initially limited to isothermal reaustenitisation experiments, and the starting microstructure is acicular ferrite (α_a) in a matrix of austenite, or bainite (α_b) in a matrix of austenite. The study of the overall transformation kinetics will be presented in Chapter Five.

The alloy HWB used in the investigation is a homogenised weld deposit of composition Fe-0.06C-0.27Si-1.84Mn-2.48Ni-0.20Mo-0.0040O-0.01Al-0.02Ti , wt%. The oxygen is tied up in the form of oxide inclusions. Alloy preparation and the experimental technique of dilatometry have been presented in Chapter Three. The same techniques of transmission microscopy and microanalysis have also been used as demonstrated in Chapter Two.

4.2 Isothermal Reaustenitisation

The aim was to study isothermal reaustenitisation, beginning with a microstructure consisting of bainite and austenite (or acicular ferrite and austenite). For this reason, the experiments were carried out on weld specimens homogenised, austenitised at 950°C for 10 minutes (or at 1200°C for 30 minutes), isothermally transformed to bainite (or acicular ferrite) at a temperature T_a = 460°C for 30 minutes (Figure III.6 and 7) and then rapidly up-quenched to a temperature T_γ for isothermal reaustenitisation. The specimens were not cooled below 460°C, in order to avoid the martensitic decomposition of some or all of the residual austenite at that temperature. It should be noted that 30 minutes at 460°C is more than adequate to allow the bainite (or acicular ferrite) transformation to terminate as shown in Figure III.10. It has also been demonstrated that for the alloy used, the bainite (or acicular ferrite) transformation ceases when the carbon content of residual austenite X_γ reaches the T'_0 curve in Figure III.11. The precipitation of cementite (θ) from austenite is

very slow for this alloy, when compared with the time required for the α_b (or α_a) transformation to cease. For example, no cementite is found long after the completion of the bainite (or acicular ferrite) transformation at 460°C. Even when this mixture of bainitic ferrite and carbon-enriched residual austenite is annealed by raising the temperature to 600°C (directly from 460°C), cementite only precipitates from austenite after about 2 hours (as shown in Figure IV.1 including EDX data). Hence, cementite precipitation does not complicate the interpretation of the results, reaustenitisation being from a mixture of just bainitic ferrite (or acicular ferrite) and carbon-enriched austenite. The dilatometric output also showed (Figure IV.4a) that there was no decomposition of austenite during heating. In these circumstances, reaustenitisation involves just the growth of austenite and nucleation can be ignored.

4.2.1 Dilatometry

The results obtained from dilatometric experiments are presented in Figure IV.2 and 3. The first detectable growth of austenite was found to occur at T_γ = 680°C for both starting microstructures bainite plus austenite (Figure IV.2) and acicular ferrite plus austenite (Figure IV.3). In all cases the transformation rate was initially rapid, but decreased with time so that the specimen length eventually stopped changing, as transformation ceased. It should be noted that a small amount of transformation occurred during the up-quench, when attempts were made to isothermally reaustenitise specimens at temperatures above 725°C for both different starting microstructures. The transformation during the up-quench has been recorded by the computer; it contributes to specimen length change, and a correction for this has been made as shown in Figure IV.4. During continuous heating the specimens length varies linearly with temperature. Figure IV.4a shows the relative length change versus temperature curve for isothermal reaustenitisation at 715°C for 2 hours (from starting microstructure $\alpha_a+\gamma$), from which the maximum relative length change ΔL_m can be directly measured. In the case of higher temperature isothermal reaustenitisation, if the low-temperature part of the curve (in a relative length change versus temperature plot as shown in Figure IV.4b) is extrapolated to T_γ, the vertical difference between the extrapolated curve and the actual curve gives the relative length change ΔL_u due to transformation during the up-quench, which should be added to any relative length change ΔL_I due to isothermal transformation at T_γ. Therefore the maximum relative length change, $\Delta L_m = \Delta L_u + \Delta L_I$ as presented in Figure IV.4b.

The maximum relative length change (ΔL_m) versus the corresponding temperature of isothermal reaustenitisation (T_γ) is plotted in Figure IV.5. In the figure, the curves A and B show the experimental data for starting microstructures bainite plus austenite ($\alpha_b+\gamma$) and acicular ferrite plus austenite ($\alpha_a+\gamma$), respectively. The results are nearly the same,

and show that ΔL_m increases as T_γ increases from 680°C to 760°C and then stays essentially constant with further increase in T_γ. Since the temperature range covered is not very large, the results indicate that below 760°C, reaustenitisation is incomplete, the alloy becoming fully austenitic only above this temperature. Furthermore, the maximum degree of transformation to austenite increases from nearly zero at 680°C to complete reverse transformation at 760°C and above. It is also seen from Figures IV.2 and 3 that the rate of the reverse $\alpha \rightarrow \gamma$ transformation increases with T_γ for the starting microstructures $\alpha_b+\gamma$ and $\alpha_a+\gamma$.

4.2.2 Transmission Electron Microscopy

The transmission electron microscopy for isothermal reaustenitisation from starting microstructures bainite plus austenite, and acicular ferrite plus austenite has been studied as presented in Figure IV.6 and 7, respectively. Figure IV.6a shows micrograph for reaustenitisation at 680°C for 2 hours from starting microstructure $\alpha_b+\gamma$, in which the ferrite plates (original bainitic ferrite sub-units) are parallel to each other and are separated by the austenite layers (now become martensite after cooling to ambient temperature). The thickness of austenite layers does not seem to increase significantly because 680°C is the isothermal reaustenitisation starting temperature as expected from dilatometry. As the isothermal reaustenitisation temperature increases, the austenite layer becomes thicker. However the austenite layers still remain parallel with each other as shown in Figures IV.6b, c and d for reaustenitisation at 700°C, 720°C and 740°C for 2 hours. This provides strong evidence that austenite grows by the movement of the approximately planar γ/α interface. Figure IV.6e shows that there is some ferrite retained after reaustenitisation at 750°C for 2 hours. The electron micrograph in Figure IV.6f present complete martensite structure, which originally was full austenite at 760°C before quenching to room temperature (the helium gas quenching rate in dilatometer ≈ 60 °C/s). The electron microscopy for reaustenitisation from $\alpha_b+\gamma$ is consistent with the dilatometric data.

The electron micrographs in Figure IV.7 demonstrate reaustenitisation from $\alpha_a+\gamma$ at different isothermal transformation temperatures. Figure IV.7a shows the microscopy for reaustenitisation at 680°C for 10 minutes, in which the morphology of acicular ferrite is still clear but some austenite layers (now martensite) acquire protuberances. This indicates that the amount of austenite growth is very small. The micrograph of Figure IV.7b also presents austenite layer swelling towards ferrite in some area when specimen is reaustenitised at 700°C for 10 minutes. Figure IV.7c and d show the microstructures for reaustenitisation at 720°C, and 740°C for 2 hours. The volume fraction of austenite increases as the isothermal reaustenitisation temperature increases. Due to the smoothly

curved lenticular morphology of acicular ferrite, the austenite growth seems to involve the movement of a curved γ/α interface. It is also shown that the reaustenitisation completes at 760°C and above in Figure IV.7e and f.

4.2.3 Microanalysis

The microanalytical data (Table IV.1 and 2, Figure IV.8, 9 and 10) cover a range of times (t) and each T_γ and a range of isothermal reaustenitisation temperatures. The results for the two different starting microstructures $\alpha_b+\gamma$ and $\alpha_a+\gamma$ are generally not very different. They show that for low T_γ substitutional alloying additions redistribute during the $\alpha \rightarrow \gamma$ transformation, even at low t. For low transformation times, the degree of partitioning of alloying elements (as indicated by the deviation of the partition coefficient k_i from unity, where $k_i = X_i^\gamma / X_i^\alpha$) increases with decreasing T_γ. This is consistent with the fact that at low T_γ the redistribution of substitutional alloying elements is a thermodynamic necessity [37,111]. As the driving force for reaustenitisation increases, the transformation tends toward paraequilibrium or negligible-partitioning-local equilibrium; this is illustrated clearly by the data for 760°C, even for times as short as 40 seconds and 2 minutes. In Figure IV.10a, the energy dispersive X-ray spectra show that for the specimen reaustenitised at 760°C for 40 seconds the ratio (atom fraction of Mn/atom fraction of Ni) is the same in the α and γ phases. However in Figure IV.10b, the energy dispersive X-ray spectra show that for the specimen reaustenitised at 680°C for 10 minutes the ratio is much higher than in γ than in α, even though the amount of reaustenitisation is quite small.

The concepts of paraequilibrium and local equilibrium have been reviewed in Section 1.5. Paraequilibrium is a state of constrained equilibrium in which the substitutional lattice is configurationally frozen with respect to the transformation interface. Hence, even though the transformation is diffusional in nature, the ratio (atom fraction of substitutional element i/atom fraction of iron) is the same in α and γ. Thus, the chemical potentials of the substitutional elements are not equal in the two phases. Carbon which diffuses faster reaches equilibrium subject to this constraint. In negligible-partitioning-local equilibrium (NPLE), equilibrium is maintained for all species at the transformation interface, but the concentration of substitutional element is essentially the same in all phases.

The results also show that as t increases for a given T_γ the partition coefficient k_i changes even though the volume fraction of austenite undergoes negligible change. This is strong evidence that the concentrations of alloying elements at the interface during the growth of austenite are not equilibrium concentrations.

These results are qualitatively consistent with the dilatometric data for both starting microstructures $\alpha_b+\gamma$ and $\alpha_a+\gamma$. One of the factors responsible for the increased rate of transformation at high T_γ is the fact that the degree of redistribution of alloying elements during transformation decreases with increasing T_γ. The results again emphasize that although the states of local equilibrium or paraequilibrium are for convenience often assumed to define the compositions at the interface during diffusion-controlled growth, an infinite number of other possibilities exist for multicomponent alloys [25]. All compositions of austenite which allow a reduction in free energy during growth can in principal form from ferrite, giving rise to situations in which one or more of the element is trapped by the moving interface; trapping implies an increase in the chemical potential of that element during transfer across the interface. The prediction of compositions at the interface is then a formidable theoretical problem which cannot be addressed until detailed information on interface mobility becomes available. On the other hand, any system must eventually tend towards equilibrium, so that the limiting composition of austenite can easily be calculated; this is the approach adopted in the present work.

4.3 Theoretical Analysis

In this section a thermodynamic model is presented for the interpretation of the observations on reaustenitisation from starting microstructure acicular plus austenite (or bainite plus austenite). Since after the diffusionless growth of acicular ferrite (bainite), carbon is rapidly and spontaneously redistributed into the residual austenite with an accompanying reduction in free energy, the $\alpha_a \rightarrow \gamma$ ($\alpha_b \rightarrow \gamma$) transformation in its original form is irreversible. The problem of reaustenitisation is therefore considerably different from the case of reverse transformation from martensite to austenite in for example, shape memory alloys.

It is noted that the formation of acicular ferrite (or bainite) ceases prematurely during isothermal transformation when the carbon content of the residual austenite reaches the T_o' curve (the phase diagram for the alloy is presented in Figure IV.11). It follows that the carbon concentration X_γ' of the austenite when the formation of acicular ferrite (or bainite) ceases at T_a, is given by (point marked a in Figure IV.11):

$$X_\gamma' = X_{T_o'}(T_a) \qquad \text{(IV/1)}$$

Furthermore, it is noted that:

$$X_\gamma' << X_{Ae_3}(T_a) \qquad \text{(IV.2)}$$

where $X_{Ae_3}\{T_a\}$ is marked b in Figure IV.11.

Thus, although the formation of acicular ferrite (or bainite) ceases at T_a, because $X'_\gamma << X_{Ae_3}\{T_a\}$, the driving force for austenite to transform diffusionally to ferrite is still negative. Another way of expressing this is to say that the volume fraction of acicular ferrite (or bainite) present when its formation ceases at T_a is much less than is required by the lever rule. In fact, this remains the case until the temperature T is high enough (i.e., $T = T_{\gamma 1}$) to satisfy the equation:

$$X'_\gamma = X_{Ae_3}\{T_a\} \qquad \text{(IV.3)}$$

Hence, reaustenitisation will first occur at a temperature $T_{\gamma 1}$, as indicated in Figure IV11 (marked C), and as observed experimentally. Note that this is a direct consequence of the mechanism of the acicular ferrite (bainite) transformation, which does not allow the transformation to reach completion. If this were not the case, then the lever rule demands that the temperature need only be raised infinitesimally above T_a in order for the reverse $\alpha \rightarrow \gamma$ transformation to be thermodynamically possible!

The theory goes further than explaining just the temperature at which the reverse transformation should begin. It also predicts that any temperature T_γ greater than $T_{\gamma 1}$, the reverse $\alpha \rightarrow \gamma$ transformation should cease as soon as the residual austenite carbon concentration X_γ (initially X'_γ) reaches the Ae_3 curve, i.e., when:

$$X_\gamma = X_{Ae_3}\{T_\gamma\} \qquad \text{(IV.4)}$$

with the equilibrium volume fraction of austenite (at the temperature T_γ), $V_\gamma\{T_\gamma\}$, being given by:

$$V_\gamma\{T_\gamma\} = \bar{X}/X_{Ae_3}\{T_\gamma\} \qquad \text{(IV.5)}$$

assuming that the carbon concentration of ferrite is negligible and $X_{Ae_3}\{T_\gamma\} > \bar{X}$ When $X_{Ae_3}\{T_\gamma\} = \bar{X}$, the alloy eventually becomes fully austenitic (point d, Figure IV.11) and if this condition is satisfied at $T_\gamma = T_{\gamma 2}$, then all $T_\gamma > T_{\gamma 2}$, the alloy transforms completely to austenite.

These concepts immediately explain the dilatometric data in which the degree of $\alpha \rightarrow \gamma$ transformation increase (from ≈ zero at 680°C) with the temperature of isothermal reaustenitisation, until the temperature 760°C = $T_{\gamma 2}$ where the alloy transforms completely to austenite. This theory has been applied using a computer program (in Appendix 1) to

convert the volume fraction of austenite to relative length change for isothermal reaustenitisation as shown in Figure IV.5, in which the calculated curves C and D assume that the α_a (or α_b) reaction stop at T_0 or T_0' curve of the phase diagram, respectively. The calculated results are very consistent with the experimental data.

4.4 Conclusions

Reaustenitisation of a weld deposit, beginning with a microstructure of just acicular ferrite plus austenite, or bainite plus austenite has been studied under isothermal conditions and in circumstances where the nucleation of austenite is not necessary. The same results of dilatometry and microanalysis for isothermal reaustenitisation from starting microstructures $\alpha_a+\gamma$ and $\alpha_b+\gamma$ have been obtained. Because acicular ferrite is in fact intragranular bainite, its mechanism of reaustenitisation is the same as that of bainite. It is found that the reverse transformation from acicular ferrite (or bainite) to austenite does not happen immediately when the temperature is raised (above that at which the acicular ferrite formed), even though the alloy is within the $\alpha+\gamma$ phase field. This is because acicular ferrite plates grow by a diffusionless displacive transformation mechanism (similar to that of bainite) which ensures that the transformation ceases prematurely, before the residual austenite achieves its equilibrium composition. Hence, reaustenitisation only occurs when the alloy is heated to a temperature (well above the Ae_1 temperature of the alloy) where the carbon concentration of the residual austenite exceeds its equilibrium concentration. Complete transformation to austenite only occurs at a temperature where the alloy composition equals the austenite equilibrium composition. However, at all intermediate temperatureures, the reverse $\alpha\rightarrow\gamma$ transformation terminates before the alloy becomes fully austenitic, with the volume fraction of austenite increasing isothermal reaustenitisation temperature.

In the case of a starting microstructure bainite plus austenite, the transmission electron micrographs show that the austenite layers become thicker and still remain parallel with each other as the reaustenitisation temperature increases. This provides strong evidence that austenite essentially grows by the movement of the planar γ/α interface. On the other hand, in the case of starting microstructure acicular ferrite plus austenite, owing to the non-parallel plate and smoothly curved morphology of acicular ferrite, the austenite growth seems to move a curved γ/α interface. The microanalytical date (for both $\alpha_a+\gamma$ and $\alpha_b+\gamma$) show that for low reaustenitisation temperatures, substitutional alloying elements redistribute during the $\alpha\rightarrow\gamma$ transformation, even in a very short period of time. The degree of redistribution of alloying elements during transformation decreases with increasing reaustenitisation temperature. Eventually the partition coefficients k_i for substitutional alloying elements equal unity, as the reaustenitisation temperature raises to

close the fully austenitic temperature. This implies that, as the driving force for reaustenitisation increases, the transformation tends toward paraequilibrium or negligible-partitioning-local equilibrium.

The work has led to a theory for reaustenitisation which explains most of the experimental results. The model predicts accurately the temperature at which reaustenitisation should begin and the degree of transformation to austenite as a function of the isothermal reaustenitisation temperature. All this is in turn a function of the temperature at which the original acicular ferrite (or bainite) itself formed.

(a)

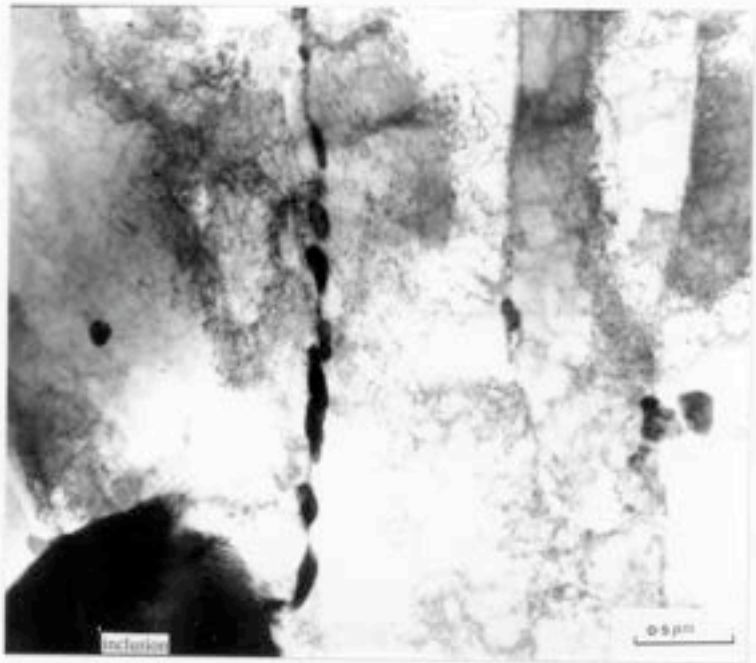

(b)

Figure IV.1 - Effect of tempering on the precipitation of cementite.
(a) 10 mins @ 950°C → 30 mins @ 460°C → 30 mins @ 600°C
(b) 10 mins @ 950°C → 30 mins @ 460°C → 140 mins @ 600°C

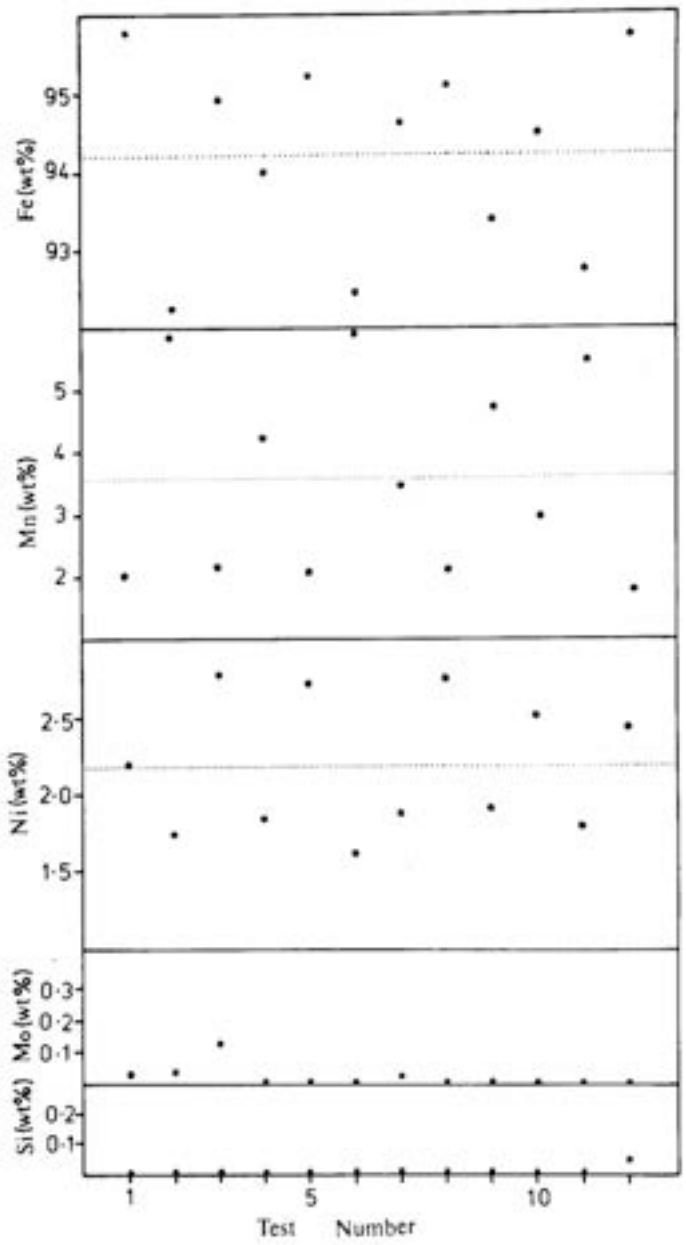

Figure IV.1(c) - Microanalytical data obtained using energy dispersive X-ray analysis on a Philips EM400T for cementite particles as shown in Figure IV.1(b).

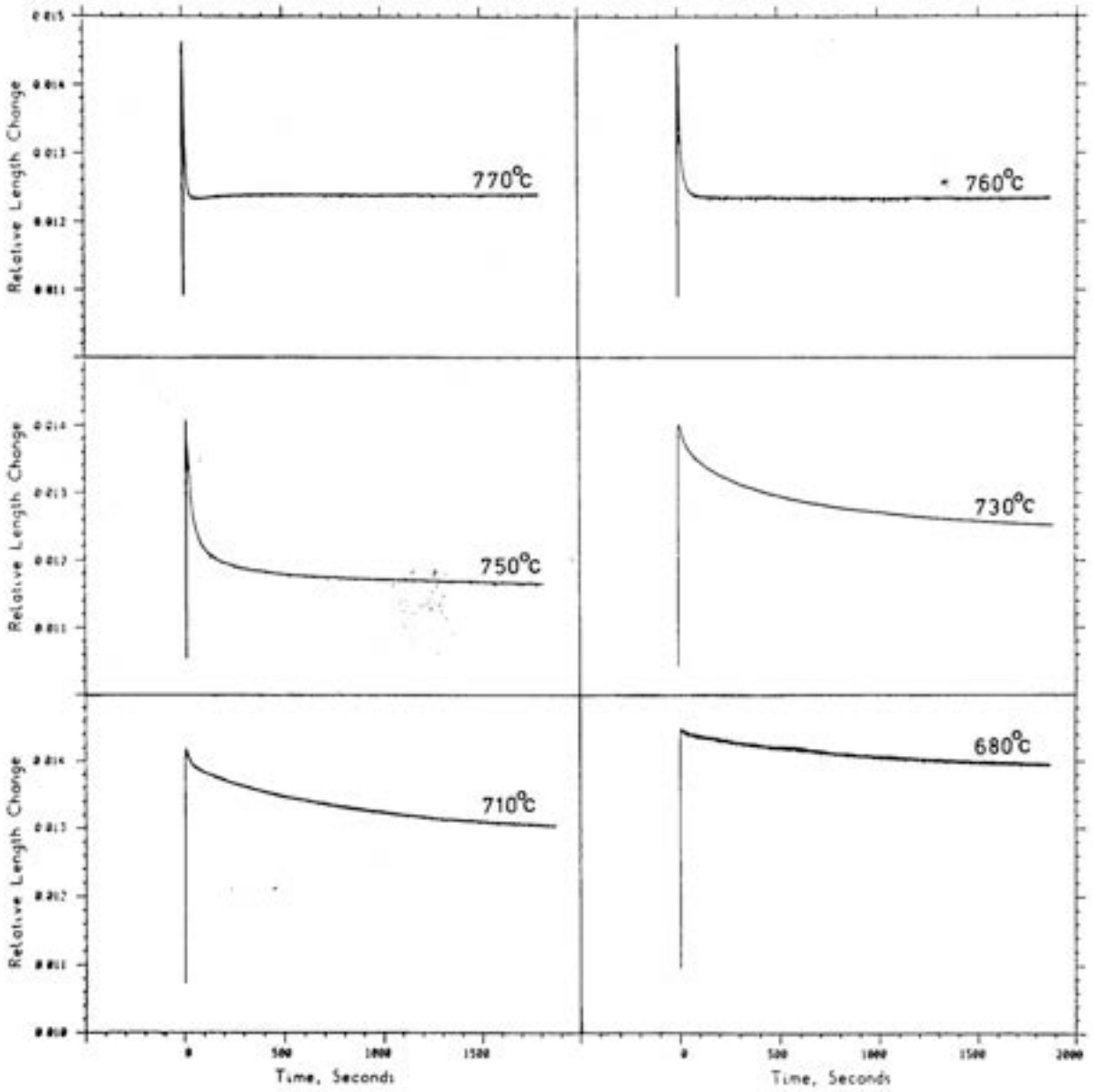

Figure IV.2 - Isothermal reaustenitisation using dilatometry. The specimens were initially austenitised at 950°C for 10 minutes, isothermally partially transformed to bainite at 460°C for 30 minutes and then rapidly up-quenched to an isothermal reaustenitisation temperature.

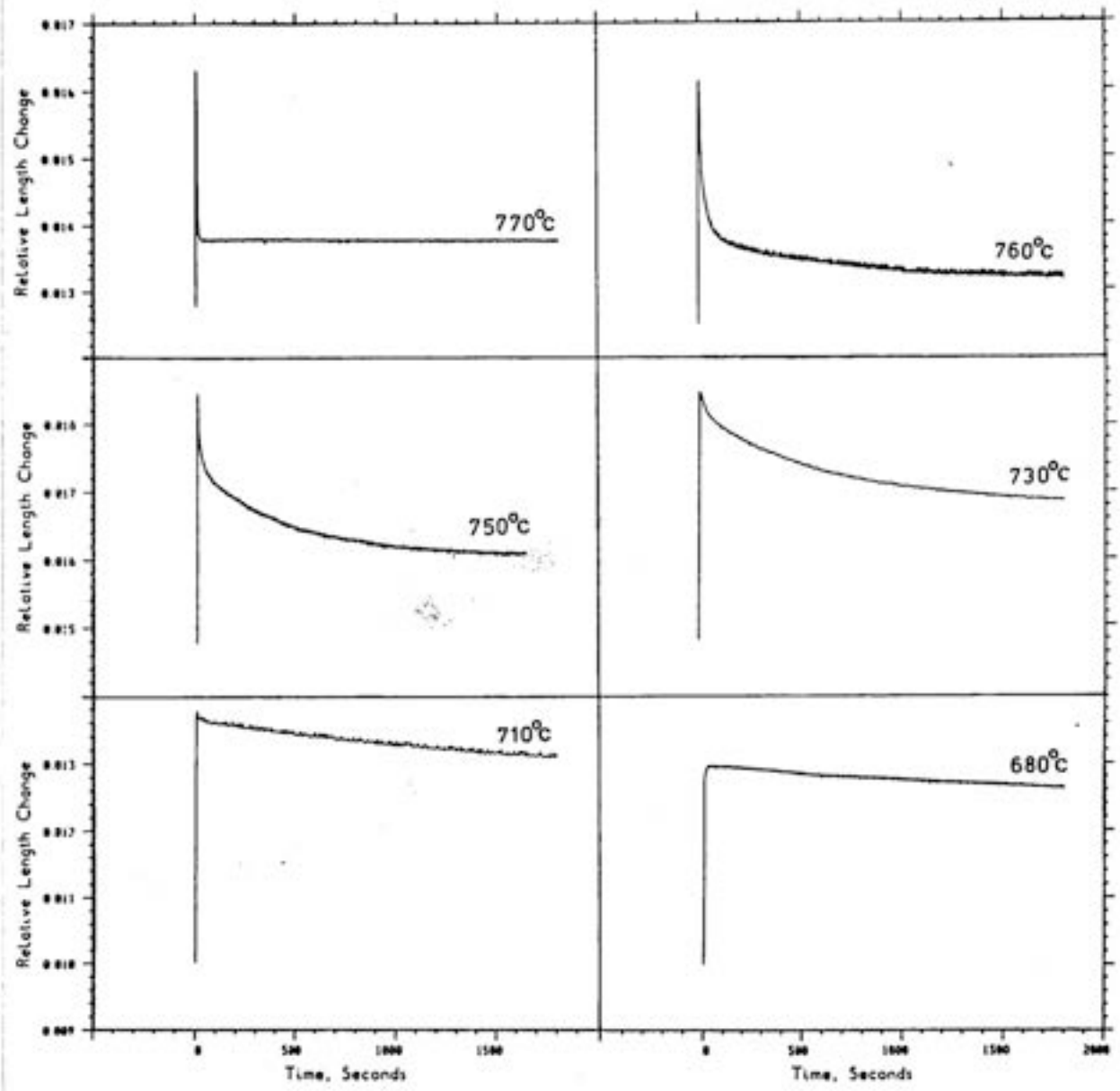

Figure IV.3 - Isothermal reaustenitisation using dilatometry. The specimens were initially at 1200°C for 30 minutes, isothermally partially transformed to acicular ferrite at 460°C for 30 minutes and then rapidly up-quenched to an isothermal reaustenite temperature.

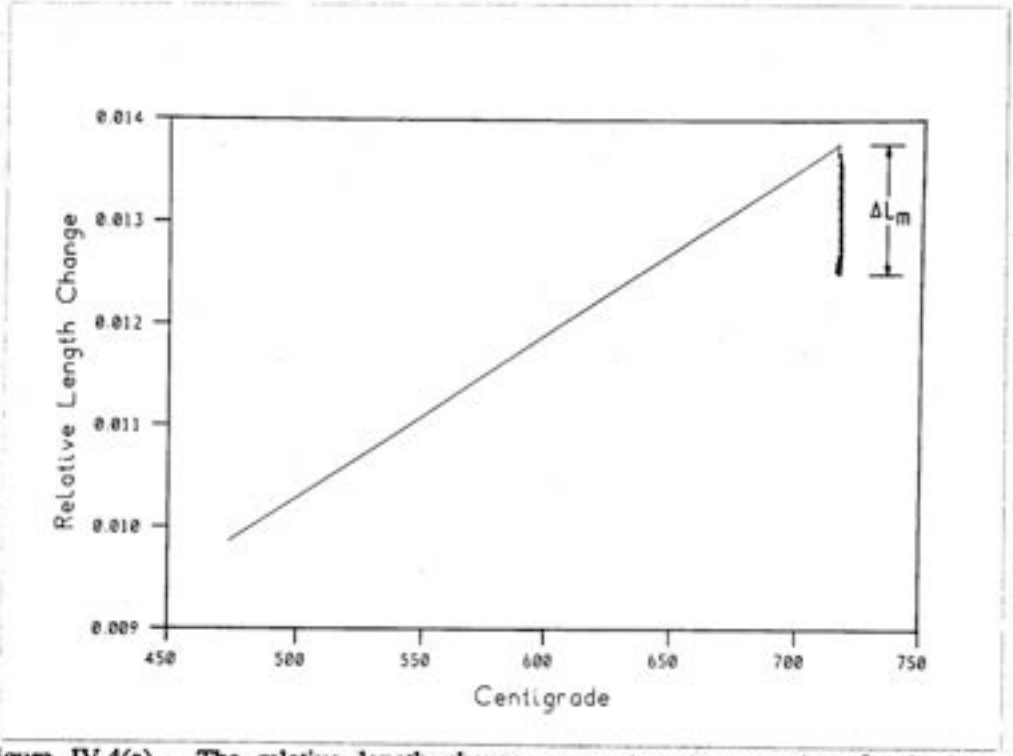

Figure IV.4(a) - The relative length change versus temperature curve for isothermal reaustenitisation at 715°C (from starting microstructure $\alpha_a+\gamma$). The maximum relative length change (ΔL_m) can be directly measured.

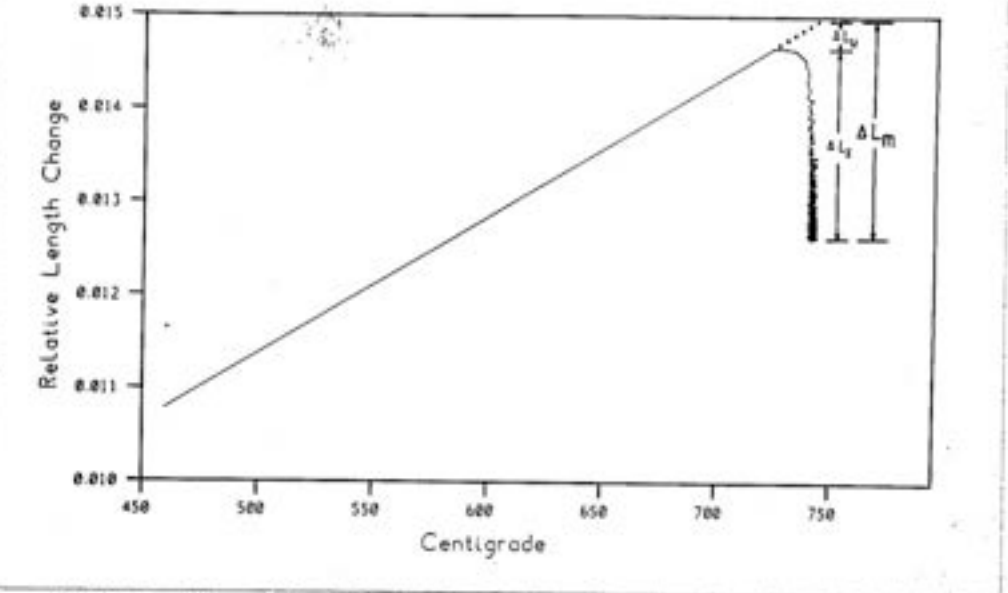

Figure IV.4(b) - The relative length change versus temperature curve for isothermal reaustenitisation at 735°C (from starting microstructure $\alpha_a+\gamma$). ΔL_u is the relative length change due to transformation during the up-quench. ΔL_I is the relative length change during isothermal transformation. Therefore the maximum relative length change $\Delta L_m = \Delta L_u + \Delta L_I$.

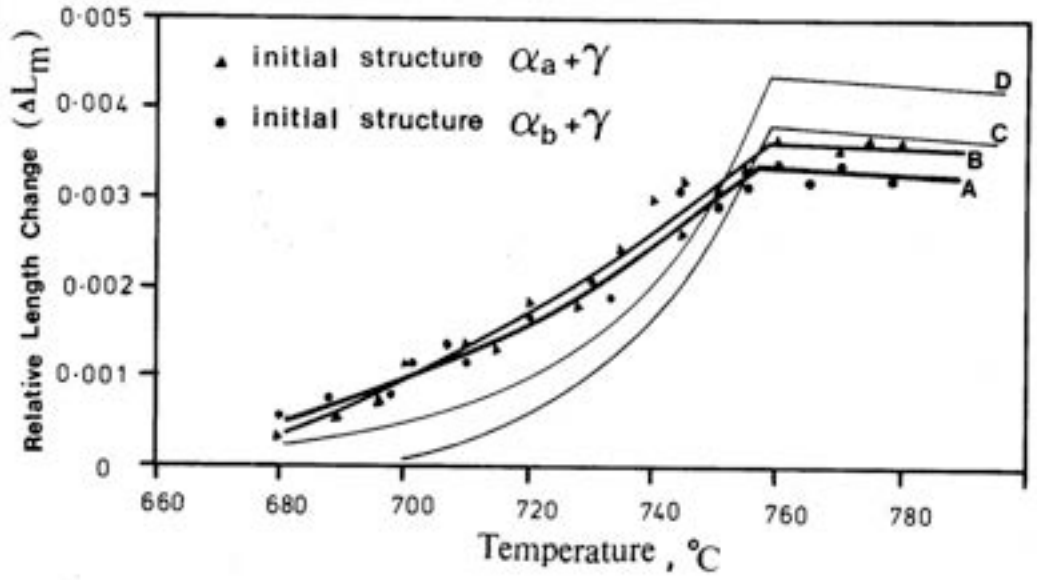

Figure IV.5 - Plot of ΔL_m versus isothermal reaustenitisation temperature. The curve A and B show the experimental data for starting microstructures $\alpha_b+\gamma$ and $\alpha_a+\gamma$, respectively. The calculated curves C and D assume that the α_b (or α_a) reaction stops at the T_o curve or T_o' curve of the phase diagram, respectively.

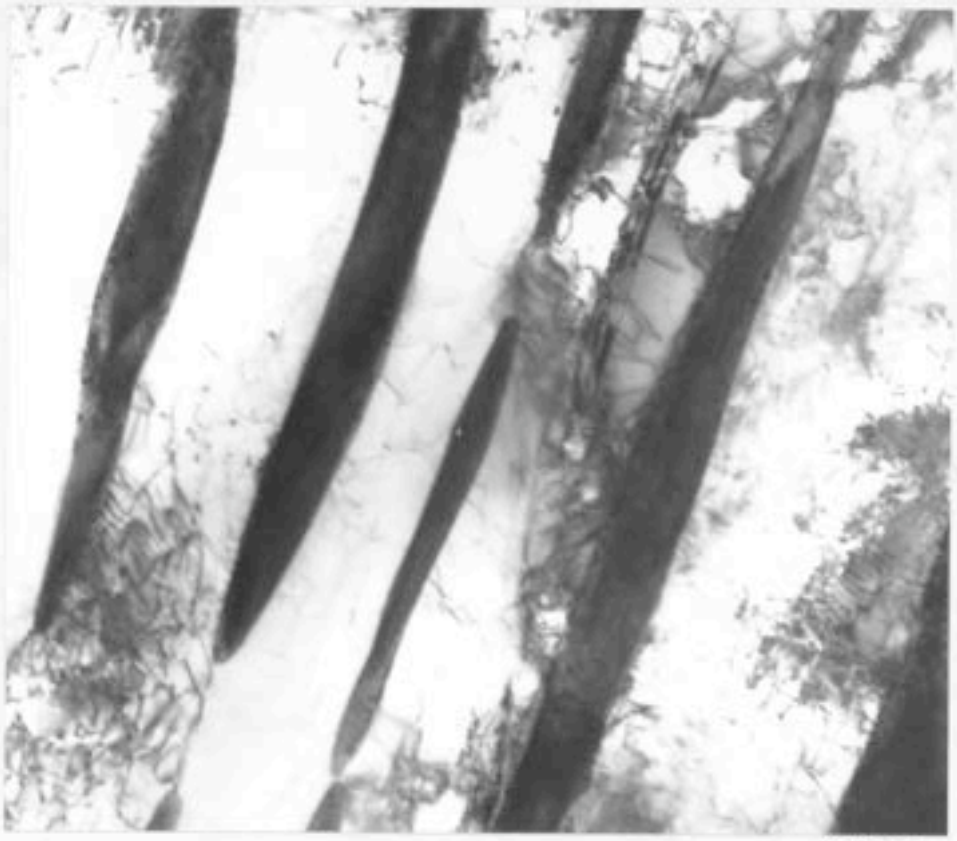

Figure IV.6(a) - Reaustenitisation at 680°C for 2 hours from starting microstructure $\alpha_b+\gamma$.

Figure IV.6(b) - Reaustenitisation at 700°C for 2 hours from starting microstructure $\alpha_b+\gamma$.

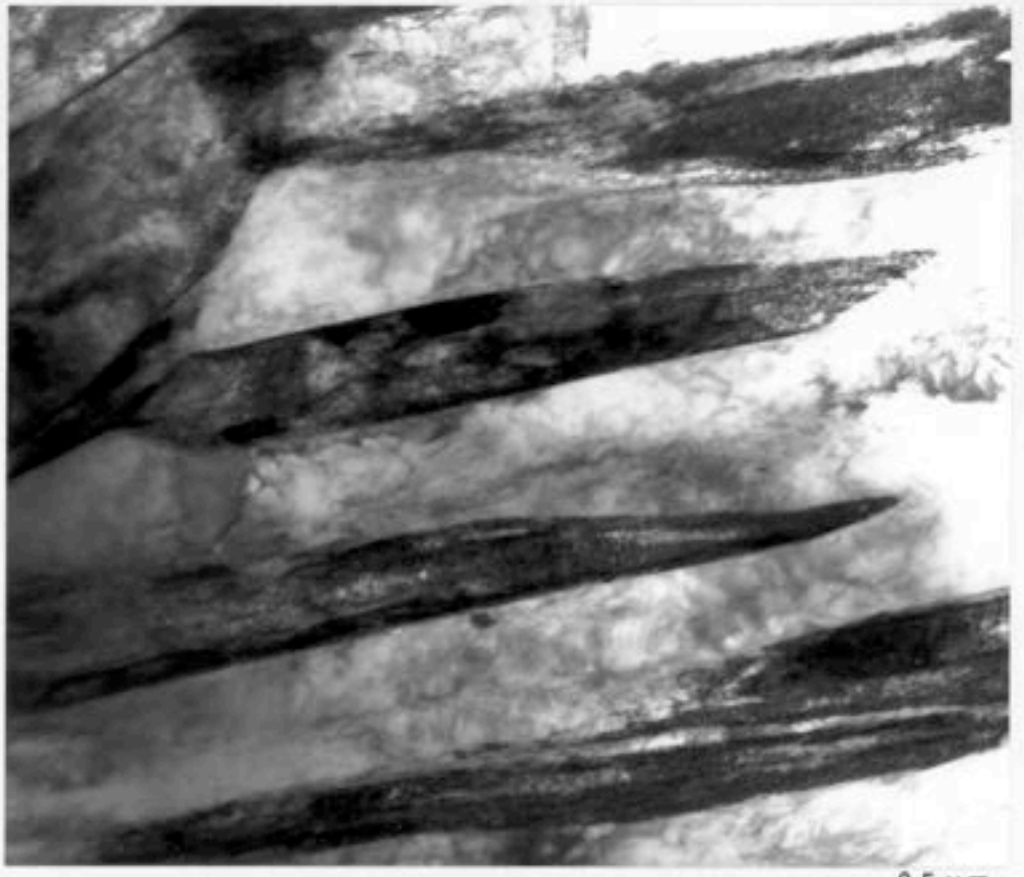

Figure IV.6(c) - Reaustenitisation at 720°C for 2 hours from starting microstructure $\alpha_b+\gamma$.

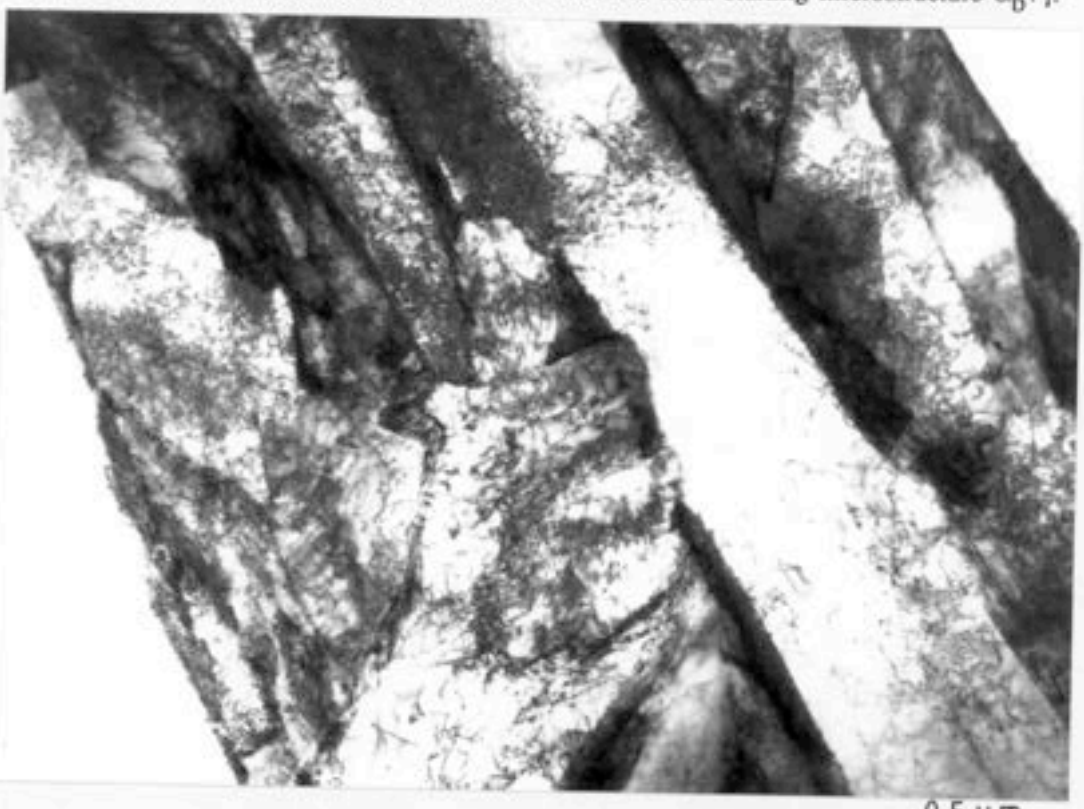

Figure IV.6(d) - Reaustenitisation at 740°C for 2 hours from starting microstructure $\alpha_b+\gamma$.

Figure IV.6(e) - Reaustenitisation at 750°C for 2 hours from starting microstructure $\alpha_b+\gamma$.

Figure IV.6(f) - Reaustenitisation at 760°C for 2 hours from starting microstructure $\alpha_b+\gamma$.

Figure IV.7(a) - Reaustenitisation at 680°C for 10 minutes from starting microstructure $\alpha_a+\gamma$.

Figure IV.7(b) - Reaustenitisation at 700°C for 10 minutes from starting microstructure $\alpha_a+\gamma$.

Figure IV.7(c) - Reaustenitisation at 720°C for 2 hours from starting microstructure $\alpha_a+\gamma$.

Figure IV.7(d) - Reaustenitisation at 740°C for 2 hours from starting microstructure $\alpha_a+\gamma$.

Figure IV.7(e) - Reaustenitisation at 760°C for 2 hours from starting microstructure $\alpha_a+\gamma$.

Figure IV.7(f) - Reaustenitisation at 770°C for 2 hours from starting microstructure $\alpha_a+\gamma$.

Table IV.1 - Microanalytical Data (wt%, error ≈ ± 0.20) for the γ and α during reaustenitisation from starting microstructure $\alpha_b+\gamma$.

Reaustenitisation Temperature(°C)	Time(min)	Mn γ	Mn α	Ni γ	Ni α
680	10	2.50	1.73	2.98	2.45
730	10	2.29	1.36	2.80	2.24
760	0.67	1.75	1.72	2.66	2.62
710	120	2.39	1.09	3.26	1.96
735	120	2.17	1.23	3.00	1.94
760	120	1.83	1.76	2.57	2.65

Table IV.2 - Microanalytical Data (wt%, err ≈ ± 0.15) for the γ and α during reaustenitisation from starting microstructure $\alpha_a+\gamma$.

Reaustenitisation Temperature(°C)	Time(min)	Mn γ	Mn α	Ni γ	Ni α
680	10	2.83	1.79	2.86	2.31
735	10	2.46	1.64	2.69	2.12
760	2	1.93	1.97	2.58	2.50
715	120	2.73	1.39	2.87	1.89
735	120	2.82	1.42	3.05	1.85
760	120	1.97	1.96	2.44	2.44

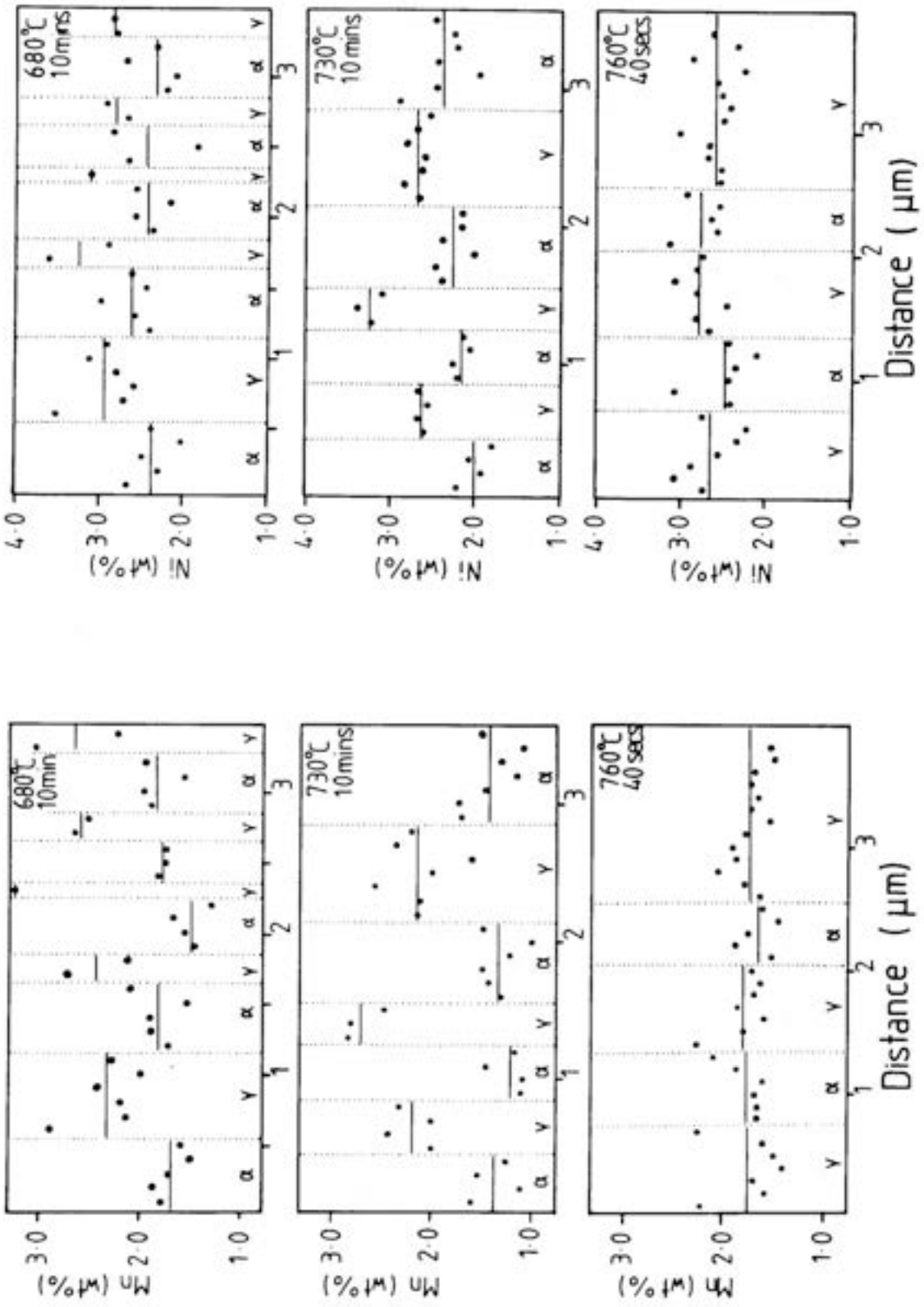

Figure IV.8(a) - Microanalytical data obtained using energy dispersive X-ray analysis on Philips EM400T for specimens reaustenitised from starting microstructure $\alpha_b+\gamma$.

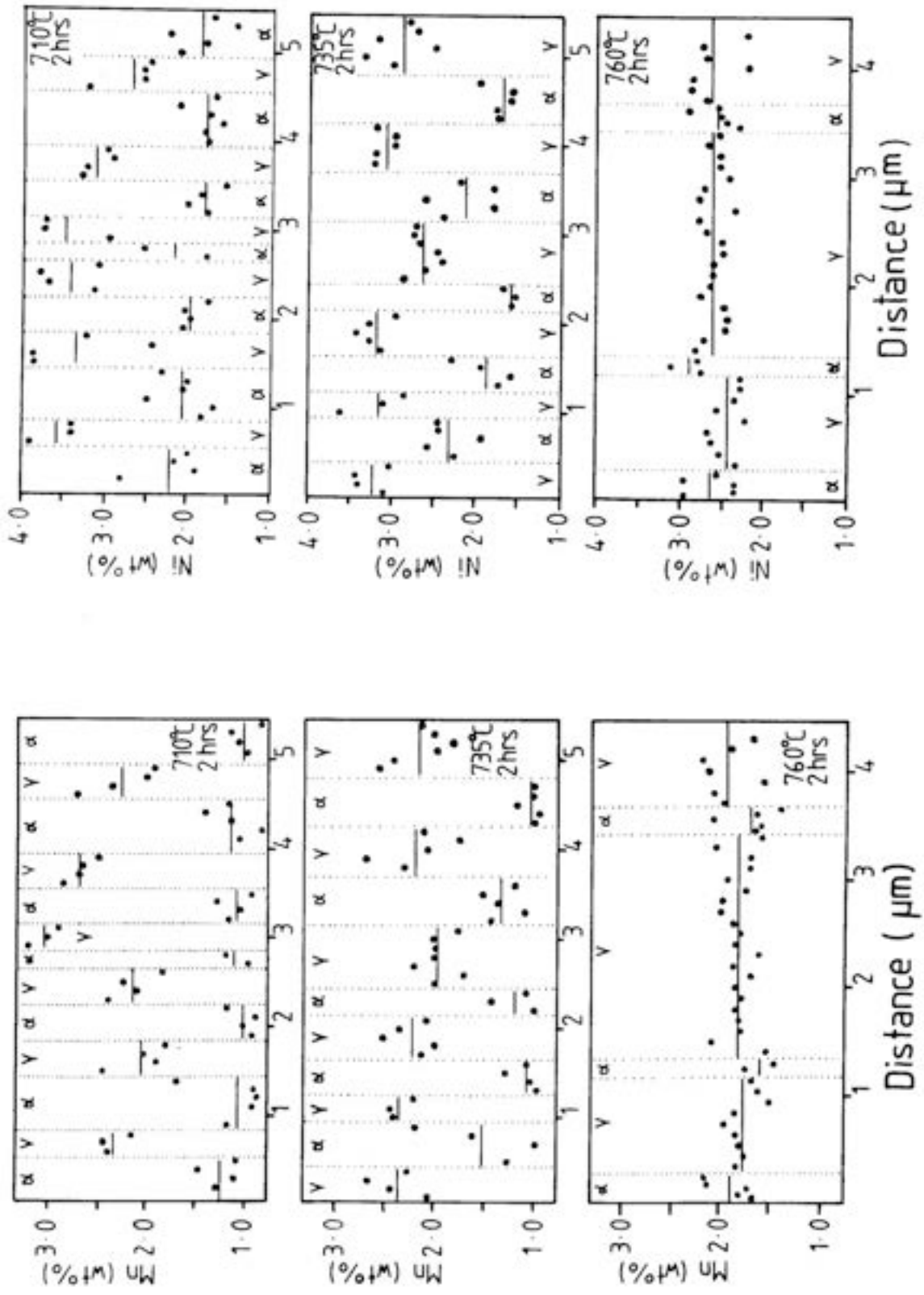

Figure IV.8(b) - Microanalytical data obtained using energy dispersive X-ray analysis on Philips EM400T for specimens reaustenitised from starting microstructure $\alpha_b+\gamma$.

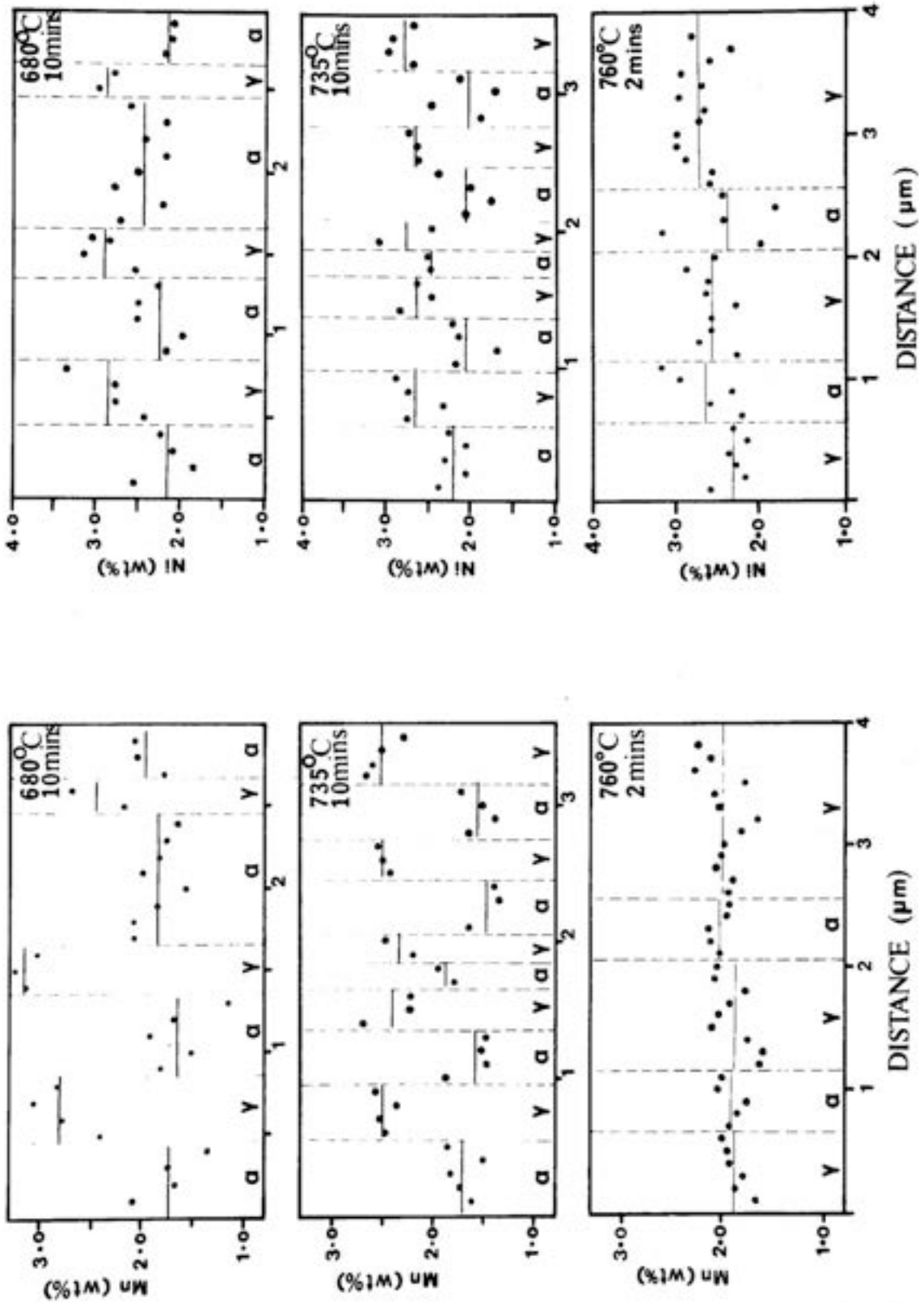

Figure IV.9(a) - Microanalytical data obtained using dispersive X-ray on Philips EM400T for specimens reaustenitised from starting microstructure $\alpha_a+\gamma$.

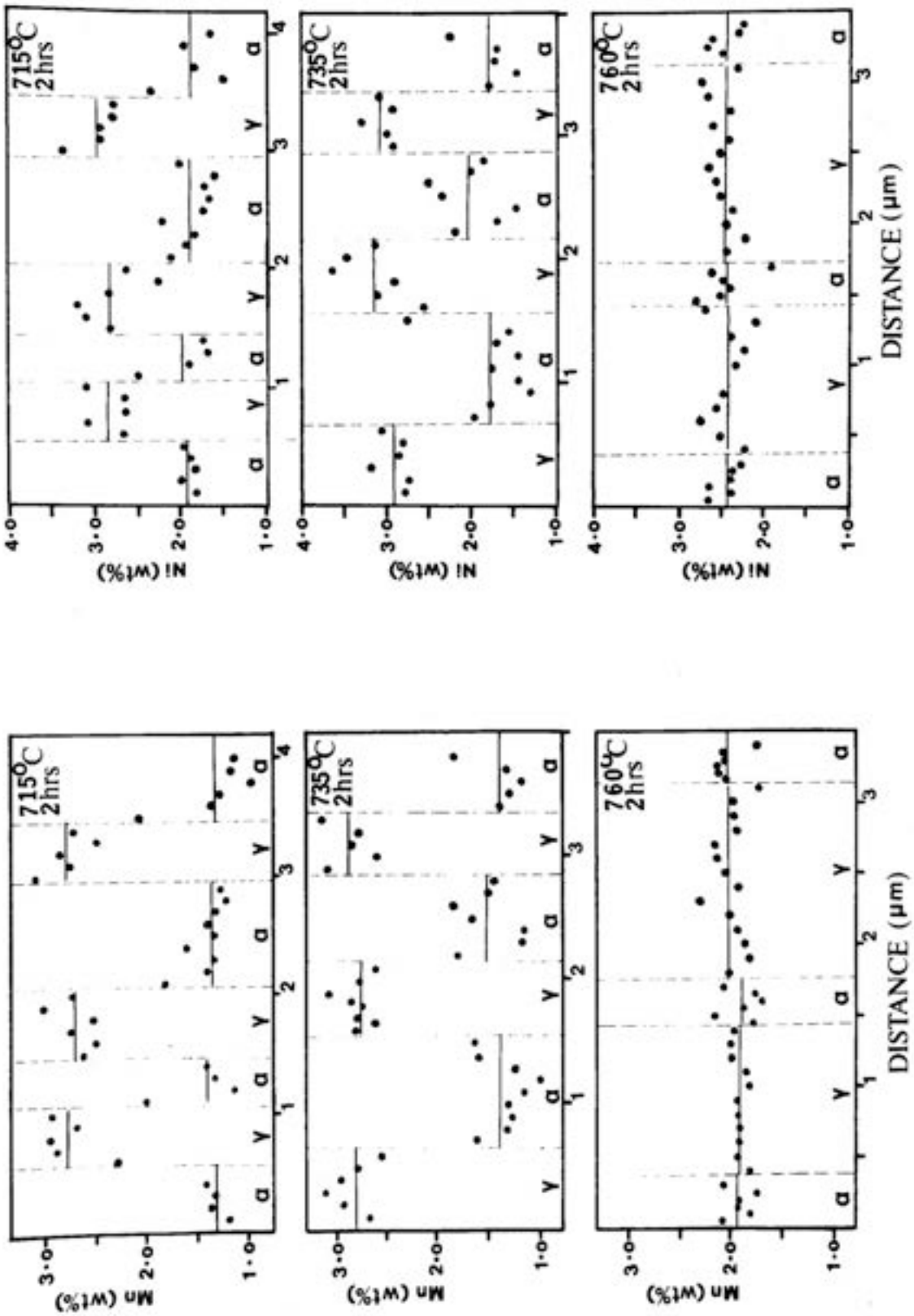

Figure IV.9(b) - Microanalytical data obtained using energy dispersive X-ray anaylsis on Philips EM400T for specimens reaustenitised from starting microstructure $\alpha_a+\gamma$.

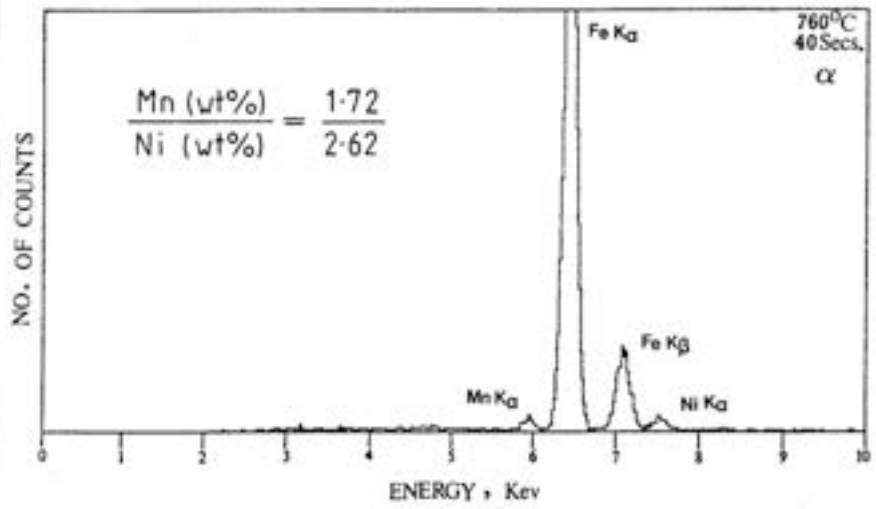

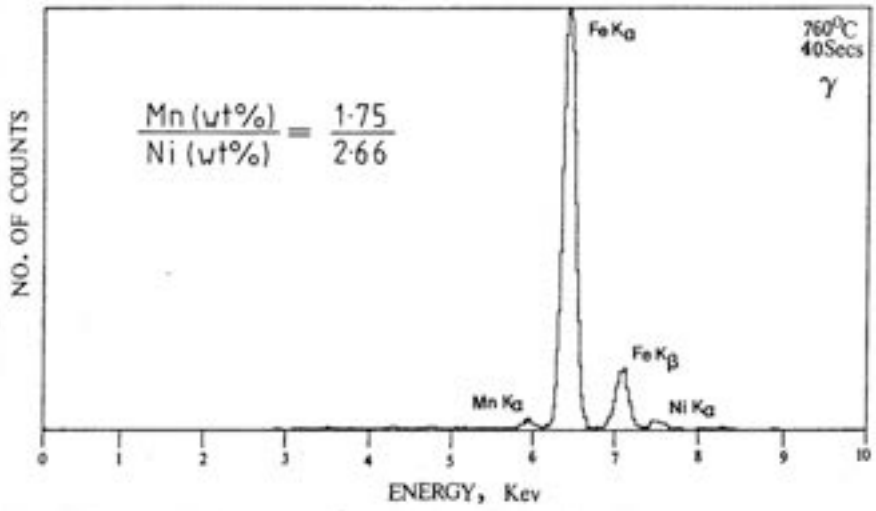

Figure IV.10(a) - Showing the energy dispersive X-ray spectra for the specimen (starting microstructure $\alpha_b+\gamma$) reaustenitised at 760°C for 40 secs. in the α and γ phase respectively.

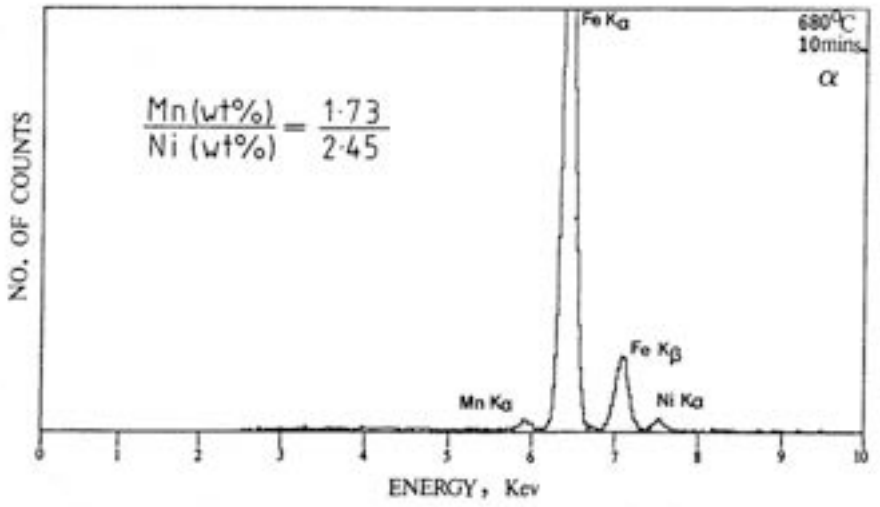

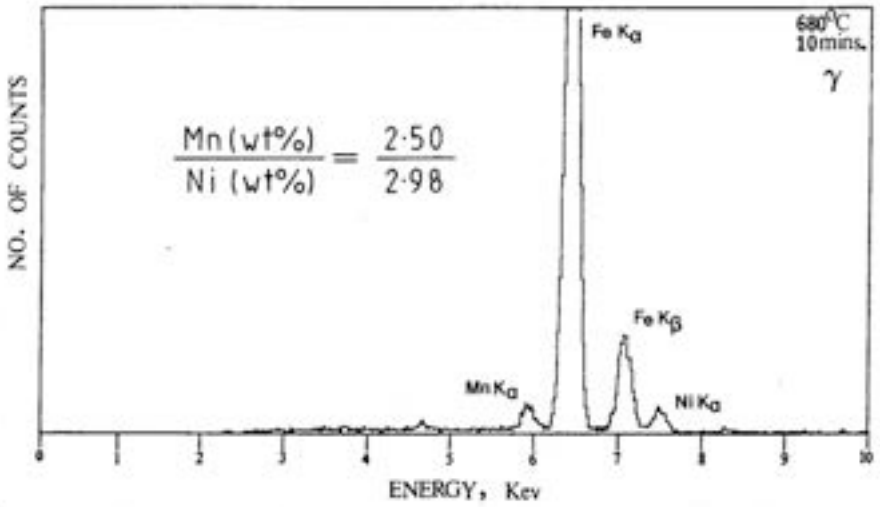

Figure IV.10(b) - Showing the energy dispersive X-ray spectra for the specimen (starting microstructure $\alpha_b+\gamma$) reaustenitised at 680°C for 10 mins. in the α and γ phase respectively.

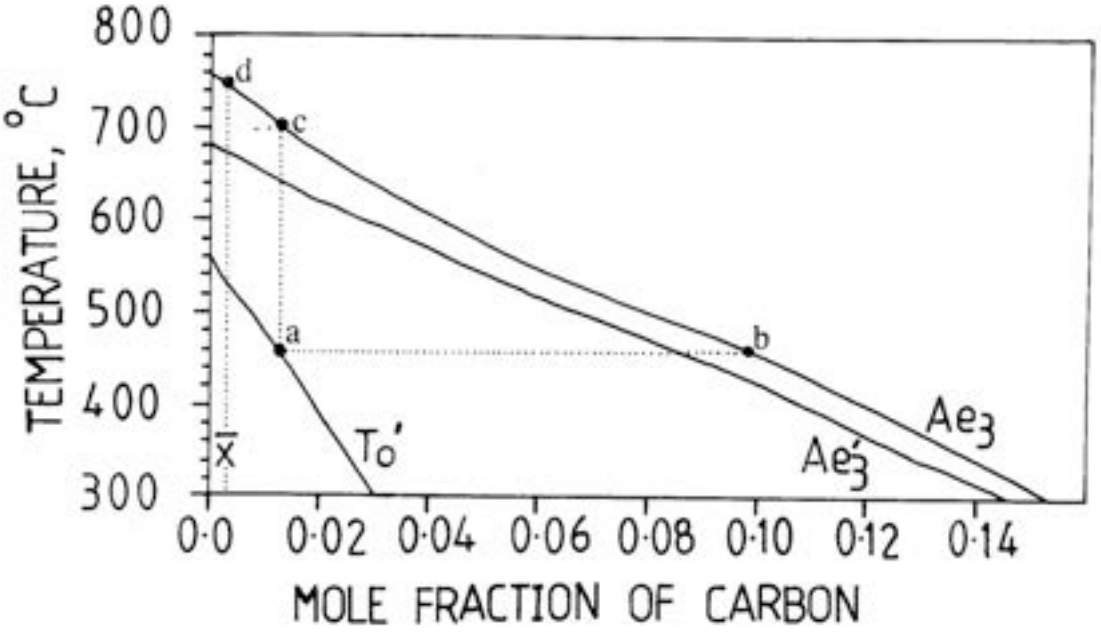

Figure IV.11 - Phase diagram showing the Ae3, Ae3', T_0 and T_0' curves for a Fe-0.27Si-1.84Mn-2.48Ni-0.20Mo wt% alloy. The Ae3', T_0 and T_0' curves are calculated as in Ref. 89,100 and the Ae3 is calculated as in Ref. 179

Intercept of T_0 = B_{T_0}

$\therefore$ $x_{T_0} = B_{T_0} - 8542\,(T)$

Slope of Ae3 line = −3625 °C/mole fraction for T range 758-

Intercept of Ae3 = B_A

$x_{Ae3} = B_A - 3625\,(T)$

$\therefore$ Ferrite initiation begins at a temp T_γ, for an alloy isothermally transformed at T_a when

$$x_{Ae3} = B_{T_0} - 8542(T_a) = B_A - 3625(T_\gamma)$$

$$\therefore \quad T_\gamma = \frac{(B_{T_0} - B_A) - 8542\,T_a}{-3625}$$

$$\therefore \quad \frac{\partial T_\gamma}{\partial T_a} = \frac{8542}{3625}$$

Chapter Five

REAUSTENITISATION IN STEEL WELD DEPOSITS - PART 2

5.1 Introduction

As discussed in Chapter Four, a knowledge of the kinetics of reaustenitisation is vital in understanding and predicting the microstructure of heat affected zones in laser, electron beam and arc welds, and in many other applications where the steel undergoes a transient temperature rise into the $\alpha+\gamma$ phase field. In Chapter Four, isothermal reaustenitisation from the starting microstructures acicular ferrite plus austenite ($\alpha_a+\gamma$) and bainite plus austenite ($\alpha_b+\gamma$) was discussed. In this Chapter, the overall transformation kinetics of reaustenitisation beginning with bainite and with acicular ferrite will be examined and an attempt will be made to interpret the results theoretically. The continuous heating transformation behaviours of homogenised and heterogeneous weld metals are also investigated in order to understand the effect of segregation on the transformation and rationalise a quantitative model, which allows the kinetics of reaustenitisation to be predicted as a function of heating rate, alloy composition and other variables.

This work is connected with some projects on welding, and the alloy used are weld deposits WB, WC1 and WC2. The chemical compositions of the weld deposits are listed in Table II.1. Alloys preparation and other experimental details are the same as presented in Chapter Four.

5.2 Kinetics of Reaustenitisation and Time-Temperature-Transformation Curve

A thermodynamic model for reaustenitisation has been presented in Chapter Four, and most of the experimental results have been explained, but the detailed kinetics of reaustenitisation have not been addressed as yet. In this section, kinetics of reaustenitisation and TTT (Time-Temperature-Transformation) curves are studied in order to approach the prediction of the overall transformation of reaustenitisation.

The process of reaustenitisation using homogenised weld metal HWB, beginning with the microstructure of acicular ferrite and austenite ($\alpha_a+\gamma$), or the microstructure of bainite and austenite ($\alpha_b+\gamma$) has been studied. It has been found that at the final stage of isothermal reaustenitisation at a specific temperature the amount of the transformation is the same for a starting microstructure of acicular ferrite and bainite. However, the kinetics of the transformation are found to be significantly different. Fig. V.1 shows the dilatometry of isothermal reaustenitisation at the initial stage of 300 seconds. For a starting microstructure of acicular ferrite and austenite, specimens austenitised at 1200°C

for 30 minutes were isothermally transformed at 460°C for 30 minutes and then, without cooling below 460°C, rapidly up-quenched to a temperature for isothermal transformation (as shown in Fig. V.1A, B and C). For a starting microstructure of bainite and austenite, specimens austenitised at 950°C for 10 minutes were isothermally transformed at the same 460°C for 30 minutes and then rapidly up-quenched to a temperature for isothermal transformation (as shown in Fig. V.1 D, E and F). It is clear that for the starting microstructure of acicular ferrite and austenite the transformation rate is very slow at 680°C as compared with that of bainite and austenite. However, as the isothermal reaustenitisation temperature increases, the transformation rate increases, and the difference of transformation rate between the two cases becomes small. The time taken for the detectable reaustenitisation has been measured (Table V.1), and the TTT curves are shown in Figure V.2. Due to the driving force of transformation, as the reaustenitisation temperature increases, the time taken for the minimum detectable austenite growth decreases rapidly. The 5% transformation TTT curves have also been calculated by converting the volume fraction change to the relative length change of dilatometry. The calculations are expressed as the following equation.

When the volume fraction of austenite increases by 0.05 during isothermal transformation, the relative length change ($\Delta L/L$) of dilatometry can be written as:

$$\frac{\Delta L}{L} = \frac{1}{3}\left[\frac{(a_\gamma^F)^3 V_\gamma^F + 2(a_\alpha^F)^3 (1-V_\gamma^F) - (a_\gamma^I)^3 V_\gamma^I - 2(a_\alpha^I)^3 (1-V_\gamma^I)}{(a_\gamma^I)^3 V_\gamma^I + 2(a_\alpha^I)^3 (1-V_\gamma^I)}\right] \qquad (V.1)$$

where
- a_γ^F = lattice parameter of austenite at final stage of reaustenitisation.
- a_γ^I = lattice parameter of austenite at initial stage of reaustenitisation.
- V_γ^F = volume fraction of austenite at final stage of reaustenitisation.
- V_γ^I = volume fraction of austenite at initial stage of reaustenitisation.
- a_α^F = lattice parameter of ferrite at final stage of reaustenitisation.
- a_α^I = lattice parameter of ferrite at initial stage of reaustenitisation.

therefore $V_\gamma^F = 0.05 + V_\gamma^I$ (V.2)

If small change in the carbon concentration of the austenite is ignored, then:

$$a_\gamma^F = a_\gamma^I \tag{V.3}$$

$$\text{also} \quad a_\alpha^F = a_\alpha^I \tag{V.4}$$

Combining equation V.1,2,3 and 4, the relative length change ($\Delta L/L$) can be simply described as:

$$\frac{\Delta L}{L} = \frac{1}{3}\left[\frac{0.05\,(a_\gamma^I)^3 - 0.1\,(a_\alpha^I)^3}{(a_\gamma^I)^3 V_\gamma^I + 2(a_\alpha^I)^3(1-V_\gamma^I)}\right] \tag{V.5}$$

From the relative length change corresponding to an increase of 0.05 in volume fraction of austenite at specific isothermal reaustenitisation temperature, and dilatometric data, the transformation time has been obtained (Table V.2). The corresponding transformation TTT curves were plotted in Figure V.3. The results also show that as the reaustenitisation temperature increases, the time taken for increasing the volume fraction of austenite by 0.05 decreases rapidly in the case of $\alpha_a+\gamma$ or $\alpha_b+\gamma$.

5.2.1 Theory of the Kinetics of Reaustenitisation

A theory has been developed in order to predict the time taken for a detectable amount (or some specific amount) of reaustenitisation from bainite plus austenite (or acicular ferrite plus austenite). Because the nucleation of austenite is unnecessary when using high heating rates, reaustenitisation occurs only by the diffusional growth of austenite. Due to austenite layer thickening, the simplest treatment for growth of austenite from a mixture of bainitic ferrite and austenite is a one-dimensional growth model, involving the movement of a planar α/γ interface. This theory also assumes only carbon diffusion controlled growth* of austenite into ferrite, and a lack of soft impingement. It is presumed that for the early stages of transformation the austenite and ferrite are both semi-infinite in extent. The increase in half thickness of austenite can be described as [33].

$$q = \alpha_1 t^{1/2} \tag{V.6}$$

$$dq = 0.5\alpha_1 t^{-1/2} dt \tag{V.7}$$

---

* In fact, the microanalysis results (in Chapter Four) indicate diffusion also of substitutional elements. However, if local equilibrium is even approximately achieved at the transformation interface, then the carbon diffusion controlled growth rate calculated using the equilibrium carbon concentration would not differ from that for the diffusion of substitutional elements. Of course, the choice of the tie line governing the interface composition is then in principle complicated by the need to ensure main balance for all the elements at the interface. In general such a tie line will not pass through the average composition of the alloy, but here the assumption is made such that it does pass through the average carbon concentration. This may be a good approximation since the alloy is in this sense dilute.

where q is the increase in half thickness of austenite layer, starting thickness a_o, and α_1 is one dimensional parabolic thickening rate constant.

The schematic diagrams in Figure V.4 show the original austenite layer and the thickening austenite layer. c is the biggest side in three dimensions of bainitic ferrite plate, (it is usually supposed [25] that a ferrite plate is idealized as a rectangular parallelopiped with sides of length a, b and c, and c = b >> a), therefore c^2 is the boundary area of γ/α interface. The minimum detectable volume fraction change can be written as:

$$\Delta V_v = 2\, N_v c^2 \int_o^{\Delta a_m/2} dq \qquad (V.8)$$

where N_v is the initial number of particles of austenite per unit volume,
and Δa_m is the minimum detectable thickness increase (as shown in Figure V.4b).

Combining equations V.7 and 8, the minimum detectable volume fraction change can be expressed as:

$$\Delta V_V = 2\, N_v c^2 \int_o^{\tau} 0.5\alpha_1 t^{-1/2}\, dt \qquad (V.9)$$

where τ is the time taken for the minimum detectable transformation.

After integration,

$$\Delta V_v = 2\, \alpha_1 N_v c^2 \tau^{1/2} \qquad (V.10)$$

$$\text{hence} \quad \tau = \left(\frac{\Delta V_v}{2\alpha_1 N_v c^2}\right)^2 \qquad (V.11)$$

$$\text{however } 2N_v c^2 = S_v = \frac{2}{\bar{L}}$$

$$\text{therefore} \quad \tau = \left(\frac{\Delta V_v}{\alpha_1 S_v}\right)^2 \qquad (V.12)$$

where S_v is surface area of γ/α boundary per unit volume, and $(1/\bar{L})$ is the number of

intercepts of γ/α boundary per unit length of test line. From equation V.12 it is clear that the value of τ is dependent on not only parabolic rate constant (α_1) but also the surface area of γ/α interface per unit volume (S_v) for a specific amount of reaustenitisation. For the same starting microstructure and a specific amount of transformation τ decreases rapidly as the isothermal reaustenitisation temperature increases due to the α_1 increasing. This equation also indicates that the morphology of the starting microstructure will effect τ, because S_v is definitely governed by the starting microstructural morphology. Maybe this is the reason why α_b+γ and α_a+γ have different kinetic behaviours during reaustenitisation.

In the case of specific amount of reaustenitisation for the same starting microstructure, the equation V.12 can be simplified as the following relation:

$$\tau \propto \frac{1}{\alpha_1^2} \qquad (V.13)$$

5.2.2 Determination of Parabolic Thickening Rate Constant

α_1 value can be deduced by applying Fick's law of diffusion and the principle of conservation of mass. Figure V.5 shows the carbon concentration profiles in α and γ before reaustenitisation and during reaustenitisation. In Figure V.5a, the carbon concentration of γ is the same C_1 before reaustenitisation. In Figure V.5b, the carbon concentration of γ at γ/α interface during reaustenitisation is $C^{\gamma\alpha}$, and the carbon concentration of γ far away from the interface remains C_1. It is assumed that the carbon concentration of α remains the same, $C^{\alpha\gamma}$, before and during reaustenitisation. Co-ordinate Z is defined normal to γ/α interface.

During reaustenitisation the flux of carbon toward γ/α interface, at the position of interface can be expressed as:

$$J = -D_{11}\{C^{\gamma\alpha}\}\frac{\partial C}{\partial Z} \qquad (V.14)$$

The diffusion coefficient of carbon in austenite, D_{11}, is known to be strongly concentration dependent [168]. The weighted average diffusivity, $\bar{D}_{11}$, can adequately represent the effective diffusivity of carbon [169], and is given by:

$$\bar{D}_{11} = \int_{C_1}^{C^{\alpha\gamma}} D_{11}\, dC/(C^{\alpha\gamma} - C_1) \qquad (V.15)$$

The rate at which carbon concentration of γ is diluted can be written as:

$$R = \upsilon (C_1 - C^{\alpha\gamma}) \tag{V.16}$$

where υ is the velocity of interface.

Because the position of interface along co-ordinate z can be described as:

$$Z = \alpha_1 t^{1/2}$$

$$\text{therefore} \quad \upsilon = \frac{dZ}{dt} = \frac{1}{2}\alpha_1 t^{-1/2} \tag{V.17}$$

Combining equation V.16 and 17, the rate at which carbon concentration of γ is diluted can be expressed as:

$$R = (C_1 - C^{\alpha\gamma})(\alpha_1 t^{-1/2})/2 \tag{V.18}$$

Conservation of mass at the interface requires that (i.e., combining equations V.14 and 18):

$$(C_1 - C^{\alpha\gamma})(\alpha_1 t^{-1/2})/2 = -\bar{D}_{11}\{C^{\gamma\alpha}\}(\partial C/\partial Z)_{z=Z} \tag{V.19}$$

where z is the co-ordinate normal to the interface plane and Z is the position of the interface along co-ordinate z. Equation V.19 simply states that the amount of carbon partitioned from the γ, per unit time equals the carbon flux away from the γ/α interface. From Fick's laws, the differential equation for the matrix is given by:

$$\partial C/\partial t = \partial(\bar{D}_{11}\{C\}(\partial C/\partial Z))/\partial Z \tag{V.20}$$

subject to the boundary condition $C = C^{\gamma\alpha}$ at $z = Z\{t\}$, and $C = C_1$ at $t = 0$, and equation V.19.

The equation has been solved [25] to give an implicit relation for α_1 as a solution of the form:

$$f_1 = H_1\{\bar{D}_{11}\} = \frac{C_1 - C^{\gamma\alpha}}{C_1 - C^{\alpha\gamma}} \tag{V.21}$$

where

$$H_1\{\bar{D}_{11}\} = (0.25\pi/\bar{D}_{11})^{0.5}\ \alpha_1[\mathrm{erfc}\{0.5\alpha_1/(\bar{D}_{11})^{0.5}\}]\exp\{\alpha_1^2/(4\bar{D}_{11})\} \qquad (V.22)$$

Finally the α_1 can be calculated from equation V.21 and 22.

5.2.3 The Relation between the Parabolic Rate Constant and TTT Curves

The parabolic thickening rate constant (α_1) at different reaustenitisation temperatures has been calculated using the computer program and the data given in Table V.3. An attempt was then made to find the relation between the time taken (τ) for the detectable amount (or some specific amount) of reaustenitisation from starting microstructures bainite plus austenite ($\alpha_b+\gamma$) and acicular ferrite plus austenite ($\alpha_a+\gamma$). Figure V.6 and 7 show τ is experimentally found to be proportional to $1/\alpha_1^2$. In Figure V.6 for detectable amount of transformation, the correlation coefficients for the linear relation between τ and $1/\alpha_1^2$ were found to be 0.99 and 0.97, in the case of starting microstructure $\alpha_a+\gamma$ and $\alpha_b+\gamma$ respectively. In the case of volume fraction of γ increasing by 0.05, Figure V.7 presents correlation coefficients for above linear relation to be 0.91 and 0.96 for starting microstructure $\alpha_a+\gamma$ and $\alpha_b+\gamma$, respectively. In Figure V.2 and 3, it is shown that at the same reaustenitisation temperature, the time taken (τ) for detectable amount (or 0.05) transformation is longer with the starting microstructure $\alpha_a+\gamma$ than with the starting microstructure $\alpha_b+\gamma$. For these two different starting microstructures, the mean number of intercepts $(1/\bar{L})$of γ/α boundary per unit length of test line in each case has been measured on transmission electron micrographs (using 50 test lines at random on 5 electron micrographs magnified by 10000X for the two different starting microstructures, respectively). The results are $(1/\bar{L})$= 0.78 ± 0.15 μm^{-1} for $\alpha_a+\gamma$, and $(1/\bar{L})$= 1.07 ± 0.12μm^{-1} for $\alpha_b+\gamma$. Therefore the surface area can be determined as well; S_v = 1.56±0.30μm^{-1} for $\alpha_a+\gamma$ and S_v = 2.14±0.24μm^{-1} for $\alpha_b+\gamma$.

For a specific amount of reaustenitisation, the equation V.12 can be expressed as:

$$\tau \propto 1/(S_v\alpha_1)^2 \qquad (V.23)$$

It is clear that the amount of γ/α grain boundary area per unit volume is an important factor. That is the reason why the value of τ is larger in the case of $\alpha_a+\gamma$. The transformation kinetics of reaustenitisation from $\alpha_a+\gamma$, or $\alpha_b+\gamma$ can then be understood.

5.3 Continuous Heating Transformation

High speed dilatometry was used to study the continuous heating transformation of unhomogenised and homogenised weld metals. The as-deposited weld metals used were

WB, WC1 and WC2, and the corresponding homogenised weld metals were designated as HWB, HWC1 and HWC2. The dilatometer specimens were heated from room temperature to 950°C at different heating rates of 0.06 - 56 °C/s. Figures V.8,9 and 10 show the relative length change and temperature profiles, monitored by the chart recorder on the dilatometer during continuous heating. From the profiles, the transformation start temperature has been obtained, and the curves for transformation start temperature versus heating rate are plotted in Figure V.11 and 12.

For all homogenised and unhomogenised weld metals, there was no decomposition during heating even at a very slow heating rate, 0.06 °C/s, as shown in Figure V.8,9 and 10. From the experimental continuous heating transformation curves in Figure V.11, it is evident that homogenised weld metals transform at higher temperature than unhomogenised weld metals in all cases. This is to be expected due to the segregation in unhomogenised weld metals. Alloying elements are not uniformly distributed in as-deposited weld metals, and solute-rich areas will transform to austenite earlier than regions containing average levels of alloying elements. However, at the same heating rate the difference of transformation start temperature between homogenised weld metals and unhomogenised weld metals is only about 10°C. This is presumably because the degree of segregation is not so large. It has been shown [70] that in carbon containing 0.68 wt% steel weld deposit, columnar austenite grain consists of a bundle of fine regular hexagonal cell all having approximately the same crystallographic orientation in space. For the weld metals studied in this investigation, the segregation cell structure within the columnar austenite grain has not been found as yet. This is probably because the segregation is not heavy, therefore this kind of cell structure is difficult to reveal.

In Figure V.12, the continuous heating transformation behaviours among the homogenised weld metals HWB, HWC1 and HWC2, and among the unhomogenised weld metals WB, WC1 and WC2 can be compared. In Figure V.12(a), it has been shown that continuous transformation curves of HWC1 and HWC2 are nearly at the same position, but that of HWB is about 15°C below. similar results were presented for unhomogenised weld metals WC1, WC2 and WB (Figure V.12(b). The M_s temperatures for homogenised weld metals studied have been calculated as shown in Figure II.1(a), and are 400, 425 and 427°C for HWB, HWC1 and HWC2, respectively. The M_s temperature of HWB is significantly lower than that of the other two weld metals. The carbon concentration of residual austenite can be calculated from the T_0' curve at M_s temperature, although at ambient temperature some austenite will transform to martensite. The carbon content of retained austenite will effect the reaustenitisation process, and this is the reason why the transformation start temperature for HWB (or WB) is lower.

5.4 Conclusions

A theory of kinetic isothermal reaustenitisation for starting microstructures $\alpha_a+\gamma$ and $\alpha_b+\gamma$ has been proposed, and it has very good agreement with experimental data. This theory indicates that for a specific amount of reaustenitisation, the transformation time is governed by not only parabolic rate constant (α_1) but also the surface area of γ/α boundary per unit volume. In the same volume fraction of α_a and α_b for starting microstructures of $\alpha_a+\gamma$ and $\alpha_b+\gamma$, the reaustenitisation rate at specific temperature for $\alpha_b+\gamma$ is faster than for $\alpha_a+\gamma$, simply because the surface area of γ/α boundary per unit volume for $\alpha_b+\gamma$ is larger. Using this theory the Time-Temperature-Transformation curve of isothermal reaustenitisation can be predicted.

The continuous heating transformation for homogenised and unhomogenised weld metals has been studied using dilatometry at a wide range of heating rates. It is found that at the same heating rate the difference of transformation start temperature between homogenised and unhomogenised weld metals studied is not so significant, and it is assumed that the degree of segregation in weld metals studied is not very large. In this study the carbon concentration of austenite has also strong influence on the reaustenitisation although the starting microstructure may consist of more than three phases - acicular ferrite (bainite), martensite and austenite etc.

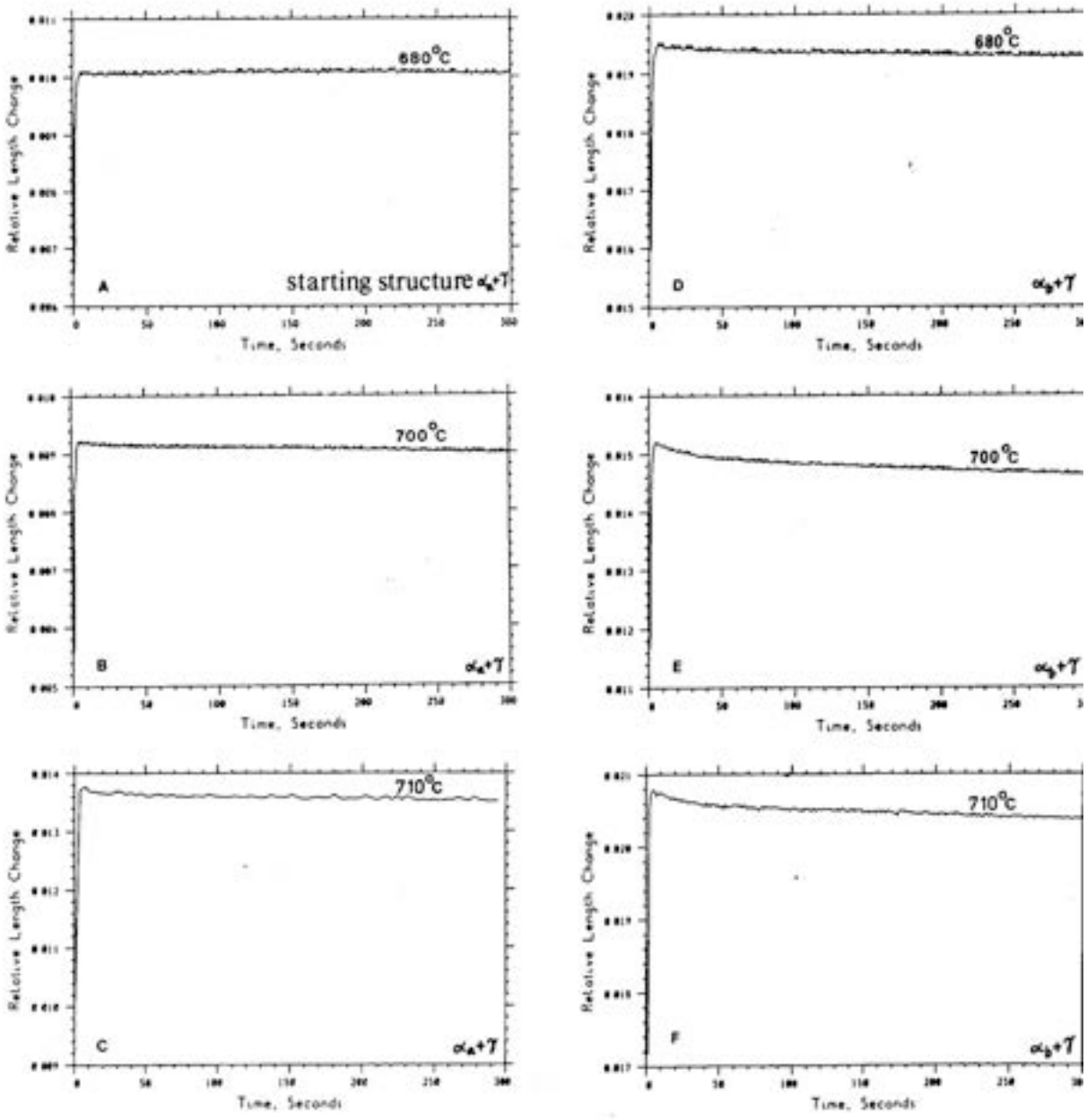

Figure V.1 - Showing the dilatometry of isothermal reaustenitisation at the initial stage of 300 seconds. (A),(B) and (C) for starting microstructure of $\alpha_a+\gamma$; (D), (E), and (F) for starting microstructure of $\alpha_b+\gamma$.

Table V.1 - The Time Taken for the Detectable Reaustenitisation in the Case of Starting Microstructure $\alpha_a+\gamma$ and $\alpha_b\gamma$.

Temperature (°C)	$\alpha_a+\gamma$ Time (Seconds)	$\alpha_b+\gamma$ Time (Seconds)
680	250	30
690	90	15
700	30	6
710	10	4
720	5	3

Table V.2 - The Time Taken for Increasing the Volume Fraction of γ by 0.05 in the Case of Starting Microstructures $\alpha_a+\gamma$ and $\alpha_b+\gamma$.

Temperature (°C)	$\alpha_a+\gamma$ Time (Seconds)	$\alpha_b+\gamma$ Time (Seconds)
680	548	300
690	370	150
700	192	110
710	114	70
720	43	26

Table V.3 - The Parabolic Constant (α_1) at Different Reaustenitisation Temperature.

Temperature (°C)	α_1(cm/s$^{0.5}$)	$1/\alpha_1^2$ (s/cm^2)
680	0.9968×10^{-5}	0.1006×10^{11}
690	0.2017×10^{-4}	0.2459×10^{10}
700	0.3350×10^{-4}	0.8911×10^{9}
710	0.5679×10^{-4}	0.3101×10^{9}
720	0.8300×10^{-4}	0.1452×10^{9}

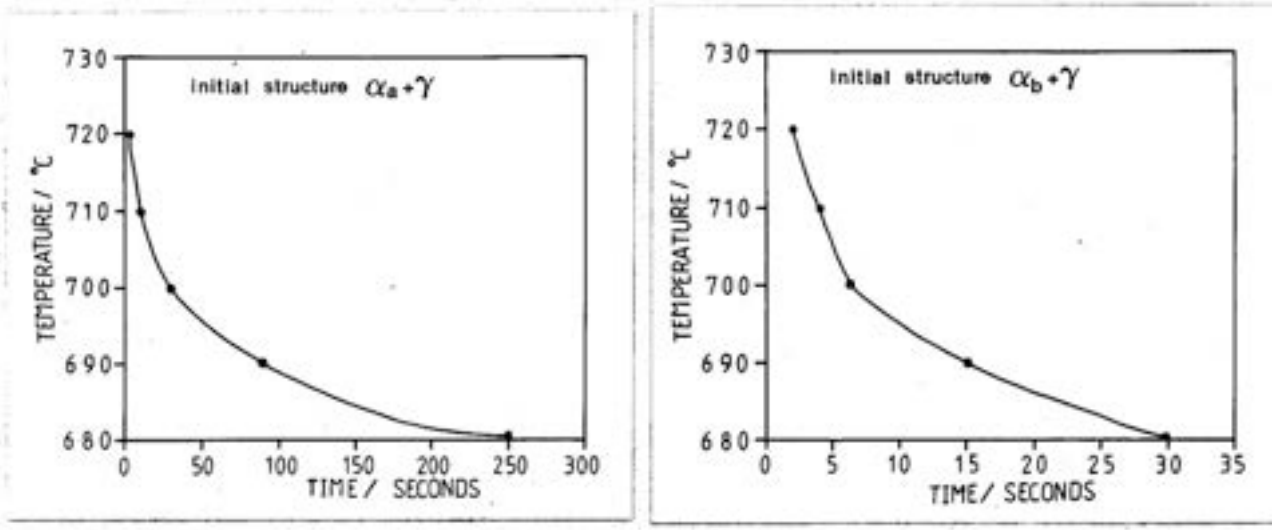

Figure V.2 - TTT curves of reaustenitisation of minimum detectable austenite growth. (a) starting microstructure $\alpha_a+\gamma$. (b) starting microstructure $\alpha_b+\gamma$.

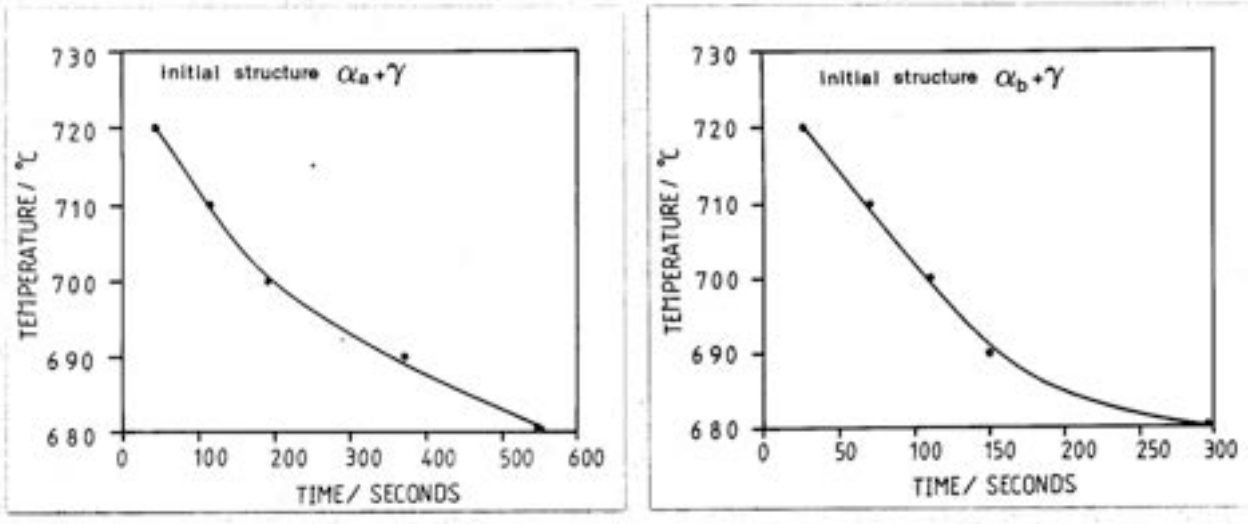

Figure V.3 - TTT curves of reaustenitisation for increasing austenite volume fraction by 0.05. (a) starting microstructure $\alpha_a+\gamma$. (b) starting microstructure $\alpha_b+\gamma$.

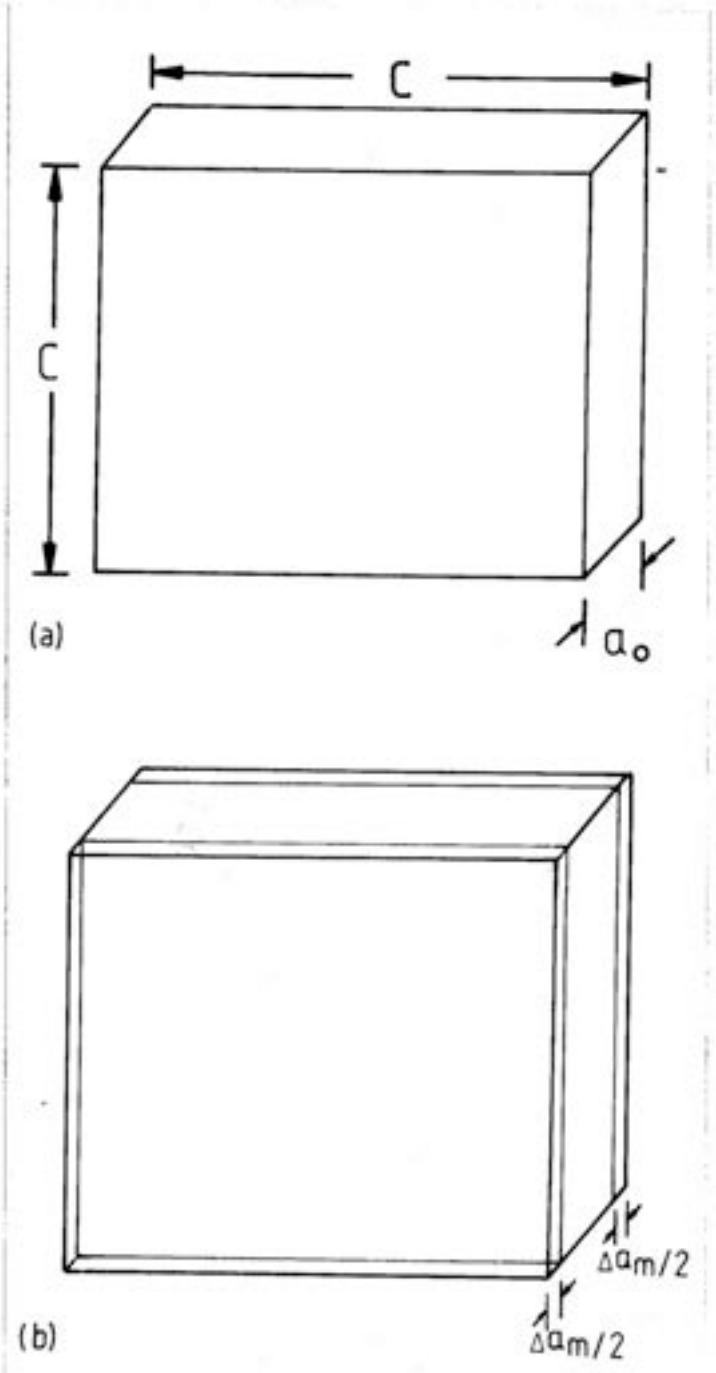

Figure V.4 - Schematic diagrams showing (a) the original layer of austenite before reaustenitisation and (b) the thickening layer of austenite during reaustenitisation.

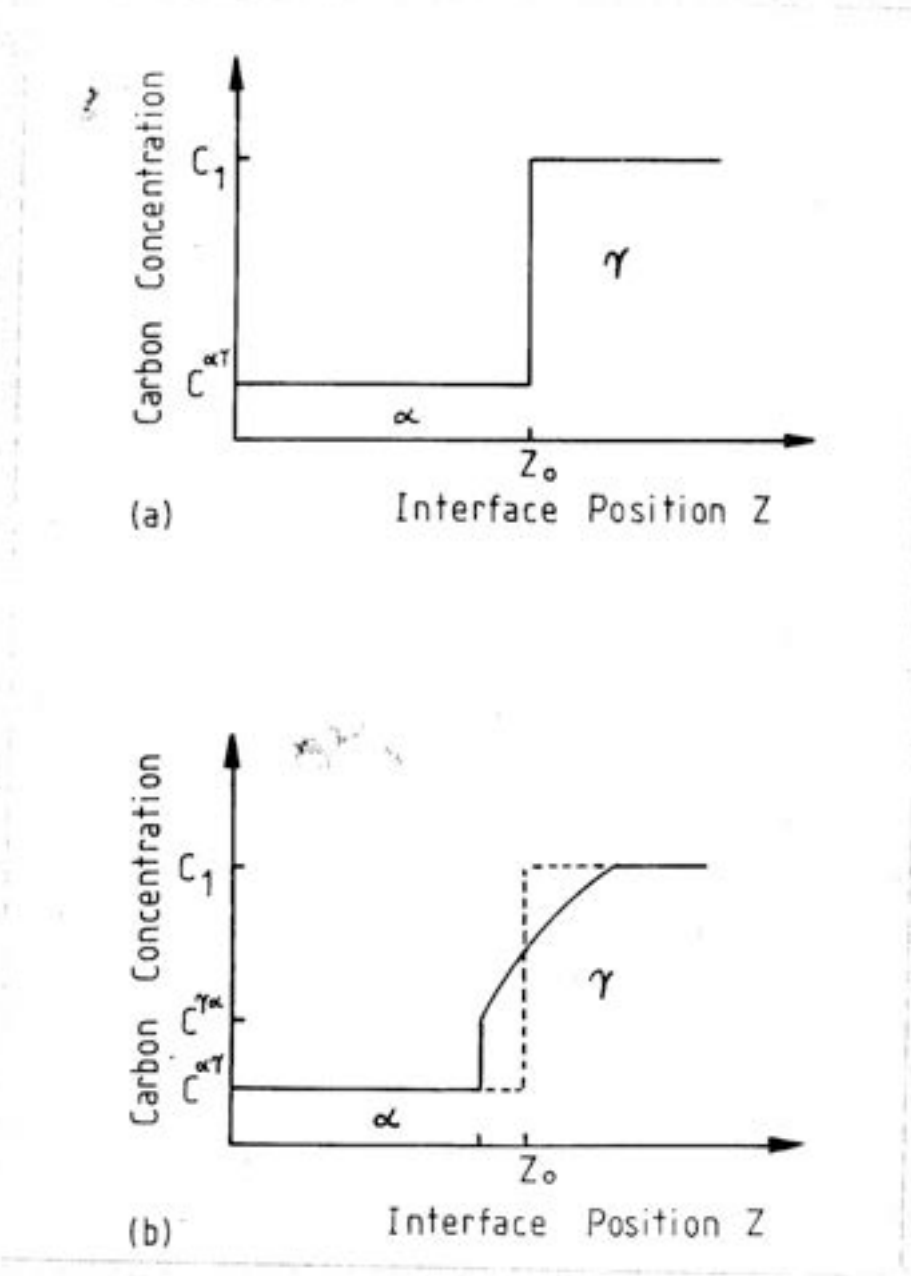

Figure V.5 - Showing the carbon concentration profile (a) before reaustenitisation and (b) during reaustenitisation. The interface position (Z) is defined normal to the γ/α interface. C_1 is carbon concentration in γ, $C^{\gamma\alpha}$ is carbon concentration in γ at γ/α interface during reaustenitisation, and $C^{\alpha\gamma}$ is carbon concentration in α at α/γ interface during reaustenitisation.

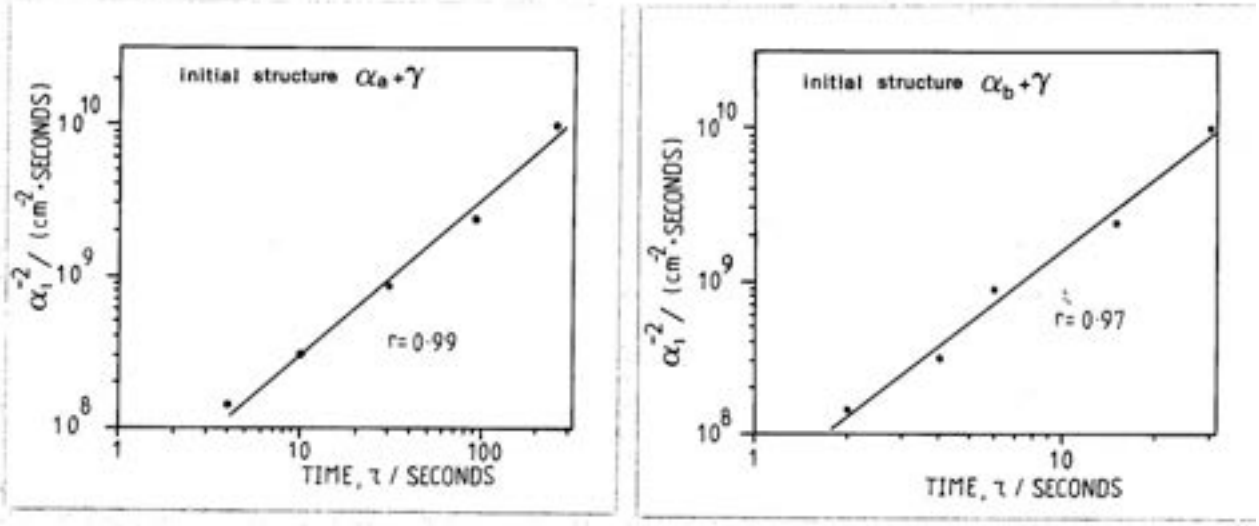

Figure V.6 - Showing that the time taken for detectable amount of transformation (τ) is proportional to $1/\alpha_1^2$. (a) In the case of initial structure $\alpha_a+\gamma$, the correlation coefficient for the above linear relation was found to be 0.99; and (b) in the case of initial structure $\alpha_b+\gamma$, the correlation coefficient to be 0.97.

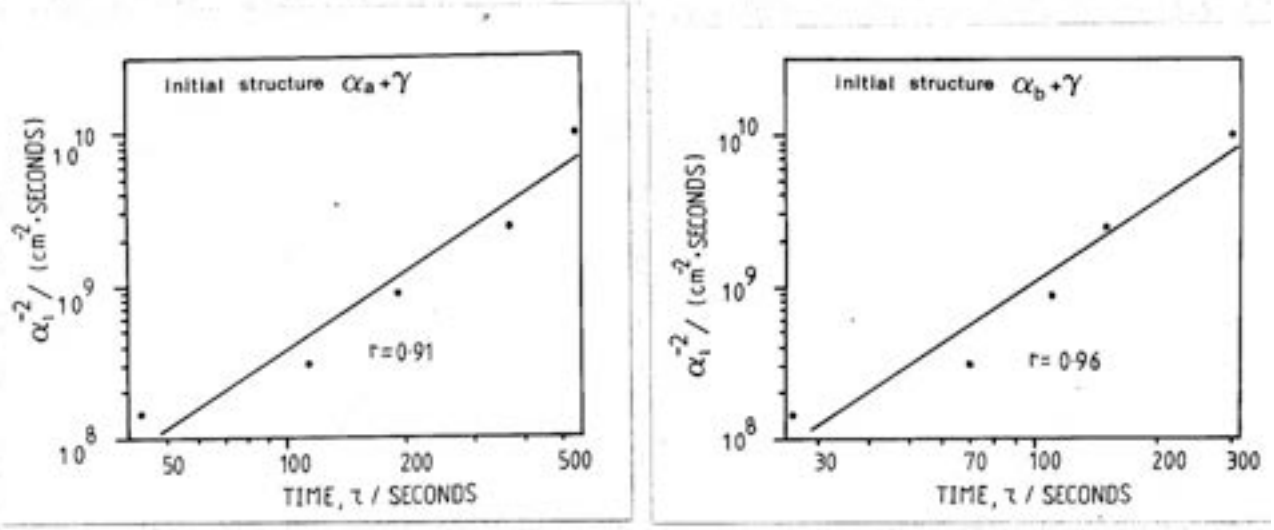

Figure V.7 - Showing that the time taken for increasing volume fraction of γ by 0.05, τ, is proportional to $1/\alpha_1^2$. (a) In the case starting microstructure $\alpha_a+\gamma$, the correlation coefficient for the above linear relation was found to be 0.91; and (b) in the case of starting microstructure $\alpha_b+\gamma$, the correlation coefficient to be 0.96.

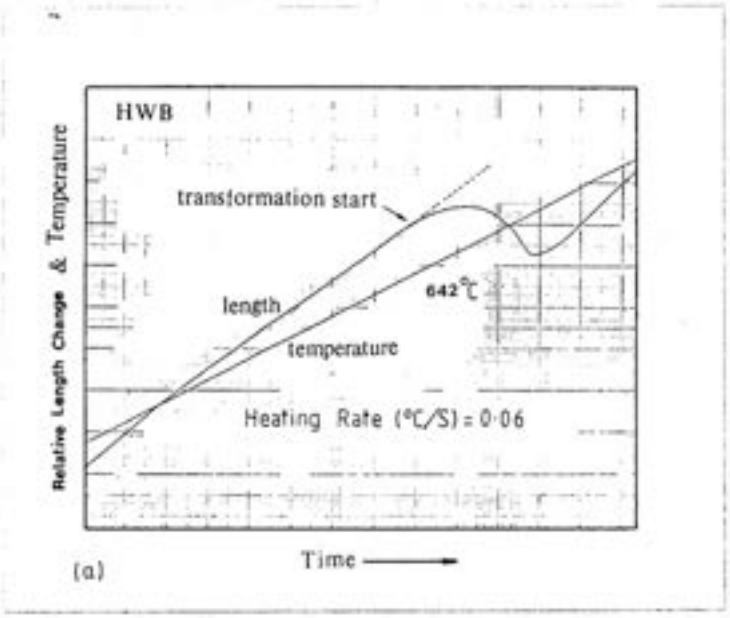

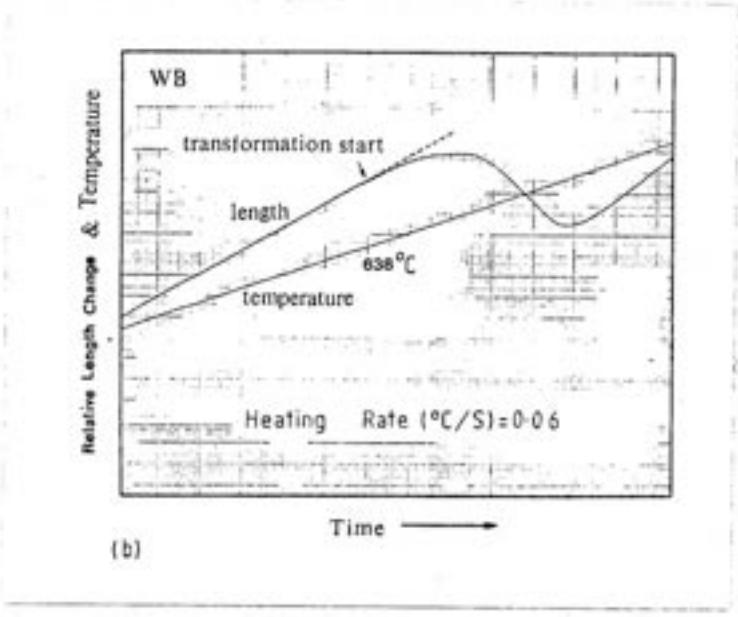

Figure V.8 - Showing the relative length change and temperature profiles on dilatometry during continuous heating for weld metals HWB and WB, monitored by the chart recorder.

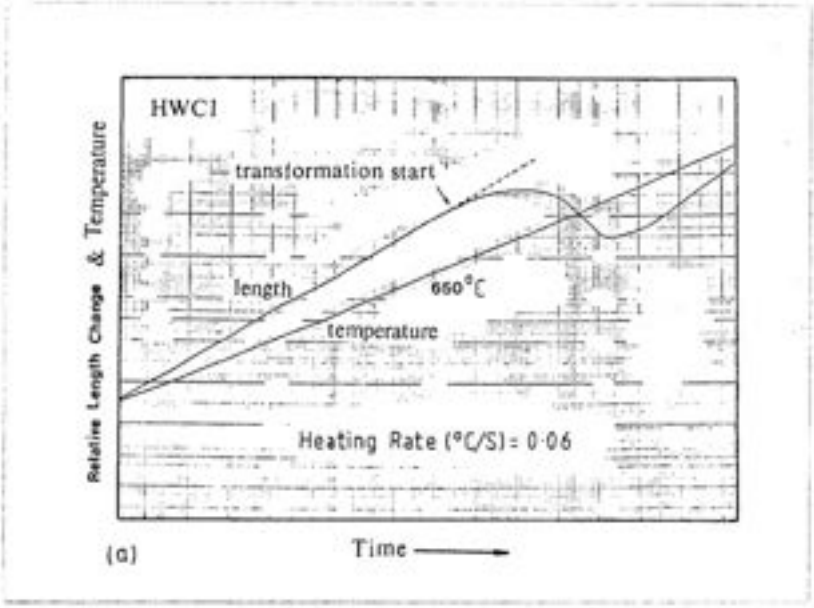

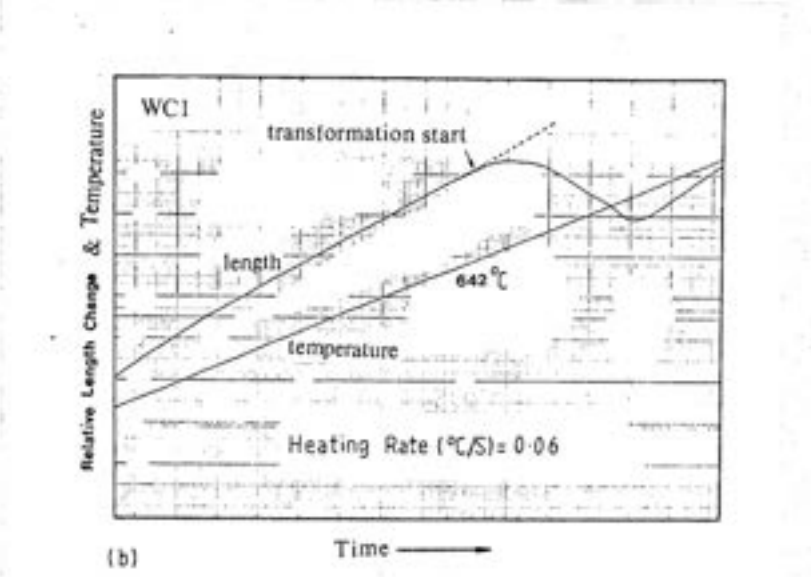

Figure V.9 - Showing the relative length change and temperature profiles on dilatometry during continuous heating for weld metals HWC1 and WC1, monitored by the chart recorder.

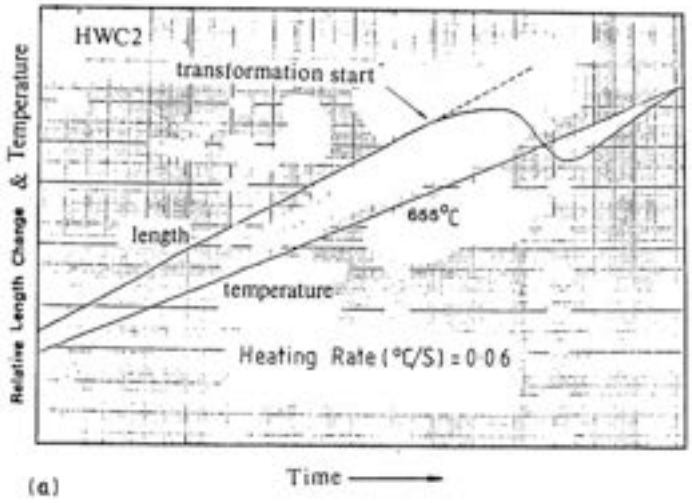

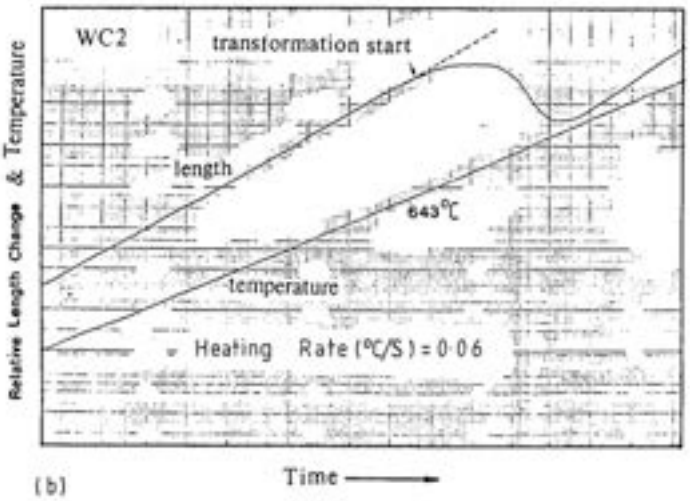

Figure V.10 - Showing the relative length change and temperature profile on dilatometry during continuous heating for the weld metals HWC2 and WC2, monitored by the chart recorder.

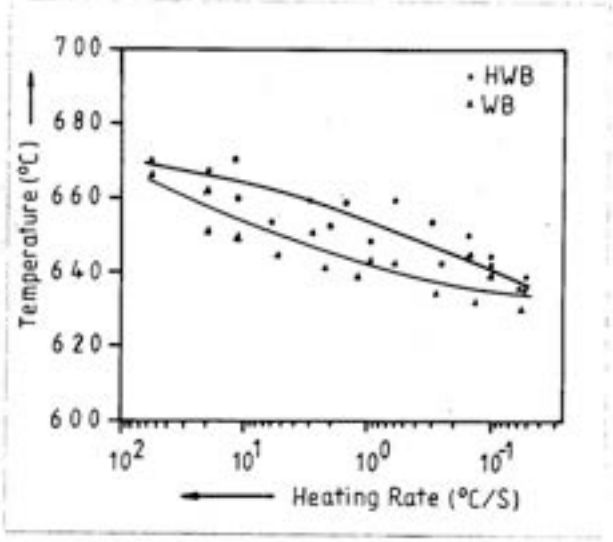

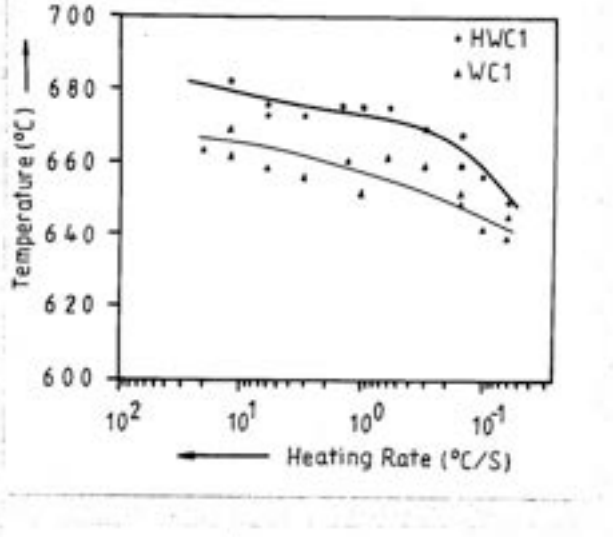

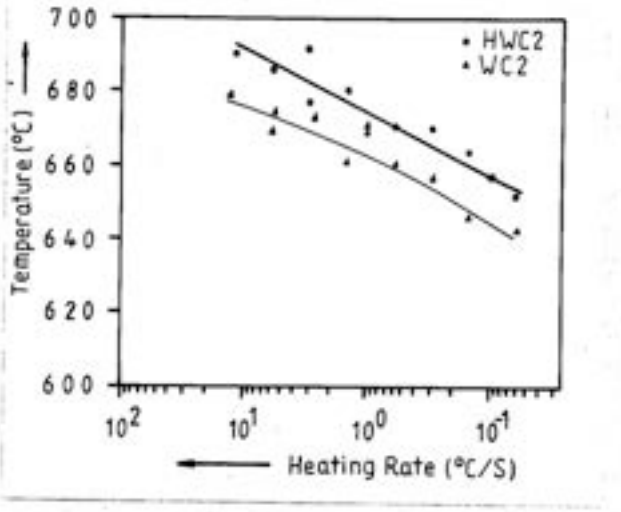

Figure V.11(a)(b)(c) - Showing continuous heating transformation curves (transformation start temperature versus heating rate) for HWB, WB, HWC1, WC1, HWC2 and WC2.

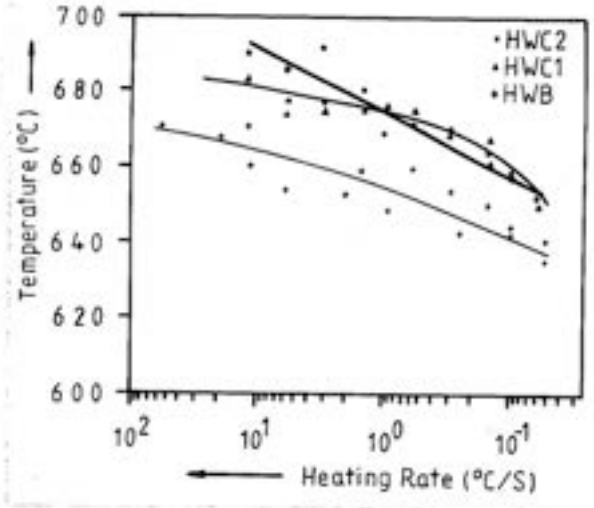

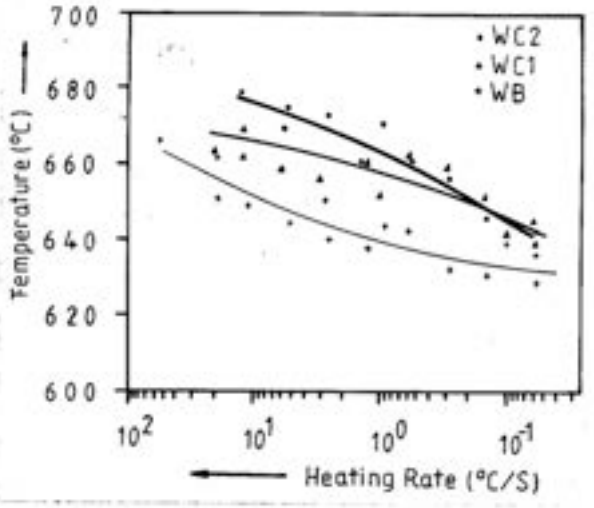

Figure V.12 - Showing continuous heating transformation curves (transformation start temperature versus heating rate) for (a) homogenised weld metals HWB, HWC1 and HWC2, (b) as-deposited weld metals WB, WC1 and WC2.

Chapter Six

The Orientation Relation between Adjacent Acicular Ferrite Plates and the Measurement of the Dislocation Density for Acicular Ferrite

6.1 Introduction

Acicular ferrite is the most desirable phase in steel weld deposits since its present correlates directly with improved toughness [53-55]. Its transformation mechanism has been known to be displacive where the parent lattice changes into that of the product by some kind of deformation of the former. In these circumstances, the two lattices must always be intimately related [25]. It has been demonstrated [65] that acicular ferrite has a rational (KS/NW type) orientation relation with the austenite. As to the orientation relationship between the adjacent variants of acicular ferrite, some authors [56-58] have proposed a "high-angle" interface between the acicular ferrite plates. Ito et al. [57] stated that the angle was 26° in their research. However, any misorientation between grains should include both an axis and an angle of rotation about that axis to form a complete description [59]. Some authors [56,58] have also suggested that individual acicular ferrite plates contain a relatively high dislocation density, but there are no quantitative data on this. In this Chapter the orientation relation between adjacent variants of acicular ferrite and the dislocation density of acicular ferrite are investigated using transmission electron microscopy. The material studied in this investigation is as-deposited weld metal WD2, and its preparation has been described in Chapter Two. The chemical composition of the weld metal is shown in Table II.1.

6.2 Orientation Relationships between Grains of Identical Structure

The relationship between two cubic crystals X and Y which are of identical structure but which are misorientated with respect to each other can be described in terms of a rotation matrix (Y J X) representing the rigid body rotation which can be imagined to generate crystal Y from crystal X. From the definition of a coordinate transformation matrix [59], each column of (Y J X) gives the components of a basis vector of X in the basis Y. Any rotation of this type, which leaves the common origin of the two crystals fixed, can also be described in terms of a rotation of 180° or less about an axis passing through that origin. If an axis of rotation is represented as a unit vector (or in general, a vector of fixed magnitude), then only three independent quantities are needed to define a misorientation between grains: two components of the axis of rotation, and a right handed angle of rotation. It follows that a rotation matrix must also have only three independent terms. In fact the component of the rotation matrix can be written in term of the vector $\underline{u} = [u_1\ u_2\ u_3]$ which lies along the axis of rotation (such that $u_1u_1 + u_2u_2 + u_3u_3 = 1$),

and in terms of the right-handed angle of rotation θ as follows [59]:

$$(Y\ J\ X) = \begin{pmatrix} u_1u_1(1-m)+m & u_1u_2(1-m)+u_3n & u_1u_3(1-m)-u_2n \\ u_1u_2(1-m)-u_3n & u_2u_2(1-m)+m & u_2u_3(1-m)+u_1n \\ u_1u_3(1-m)+u_2n & u_2u_3(1-m)-u_1n & u_3u_3(1-m)+m \end{pmatrix} \quad \text{(VI.1)}$$

where $m = \cos\theta$ and $n = \sin\theta$

The right-handed angle of rotation can be obtained from the fact that

$$J_{11} + J_{22} + J_{33} = 1 + 2\cos\theta \quad \text{(VI.2)}$$

and the components of the vector $\underline{u}$ along the axis of rotation are given by

$$\begin{aligned} u_1 &= (J_{23} - J_{32}) / (2\sin\theta) \\ u_2 &= (J_{31} - J_{13}) / (2\sin\theta) \\ u_3 &= (J_{12} - J_{21}) / (2\sin\theta) \end{aligned} \quad \text{(VI.3)}$$

It is noted that

$$(Y\ J\ X) = \begin{pmatrix} J_{11} & J_{12} & J_{13} \\ J_{21} & J_{22} & J_{23} \\ J_{31} & J_{32} & J_{33} \end{pmatrix} \quad \text{(VI.4)}$$

There are 24 matrices (as shown in Table VI.1) which represent symmetry rotations in cubic systems, therefore, a cubic bicrystal can be represented in 24 equivalent ways, with 24 axis-angle pairs. Any rotation matrix like (Y J X) when multiplied by rotation matrices representing symmetry operations will lead to the 24 axis-angle pair representations.

6.3 Orientation Relationships between Adjacent Crystallographic Variants of Acicular Ferrite

In addition to intragranular nucleation on inclusions, acicular ferrite also nucleates sympathetically at austenite/acicular ferrite interfaces (Figures II.7c and d), giving rise to an interlocking formation of lenticular plates. Therefore the adjacent variants in intimate contact can arise either from hard impingement between unrelated variants or from sympathetic nucleation. In this section, an attempt is made to find possible orientation relationships between adjacent variants of acicular ferrite. The material used is a high-hardenability weld deposit WD2 as mentioned in Chapter Two. The transmission electron microscopy specimens were prepared from the top layer of as-deposited weld metal.

The results of seventeen experiments are listed in Table VI.2. Eleven examples are illustrated as follows. Figure VI.1 shows the electron micrographs and the corresponding diffraction patterns from a pair of acicular ferrite (α_a) plates A and B. The selected area diffraction patterns (Figures VI.1b,c and d) clearly display that grain A and B have the same zone axis <001>, and a right-handed rotation* of 15° about <001> zone axis would lead to the same orientation between the lattices of grains A and B. This orientation can also be represented by a rotation of 180° about <0.1305 0.9914 0.0000>. Figure VI.2 shows that the acicular ferrite grains B and C also have the same zone axis <001>, and a rotation of 16° about <001> can make the same orientation relation between the lattices of grains B and C. The axis/angle pair relating the grains B and C can also be represented by <0.1392 0.9903 0.0000>/180°. Figure VI.3 shows that the acicular ferrite grains C and D have the same zone axis <001> as well, and a rotation of 13° about <001> will result in the same orientation relation between the lattices of grains C and D. The axis/angle pair relating the grains C and D can also be represented by <0.1132 0.9936 0.0000>/180°. The above results imply that adjacent variants have nearly the same orientation in space, since there is a rotation of ~180° about <001>. This is very significant because even though the variants have nearly the same orientation in space, they have different habit planes (see C-D pair in Figure VI.3). Figure VI.4 shows the electron micrograph and the corresponding diffraction patterns from a pair of acicular ferrite plates E and F. The interface boundary between grains E and F is clearly displayed in Figure VI.4a. The axis/angle pair relating the grains E and F can be demonstrated to be <0.8842 0.2579 0.3894>/174°. Figure VI.5 presents that the acicular ferrite grains G and H have the same zone axis <001> that grains A, B, C and D (Figures VI.1,2 and 3) do, and a rotation of 15° about <001> zone axis would lead to the same orientation between the lattices G and H.

Figure VI.6 shows six acicular ferrite plates designed I, J, K, L, M and N, which are in intimate contact. Figure VI.7 displays the corresponding diffraction patterns from the pair of acicular ferrite plates I and J. It is found that the grains I and J have the same zone axis $<1\bar{1}\bar{1}>$, and a rotation of ~ 0 or 180° will make the same orientation relation between the lattices of grains I and J. These data are ambiguous when the rotation angle about <111> is, within experimental error, ~ 0 or 180°. Because the rotation angle could be 180°, making a twin with this zone axis, it cannot distinguish a twin from two grains which are in identical orientation. Figure VI.8 show that the corresponding diffraction patterns for the pair of acicular ferrite plates I and L have the same zone axis $<1\bar{1}\bar{1}>$ as well, and a rotation of 11° about this axis will result in the same orientation. The

* The right-handed sense of rotation about an axis is used in description of axis-angle pairs. Note also that although specific indices are usually quoted for the axes of rotation, the initial choice of basis vectors is of course arbitrary. Therefore the form <001> instead of the form [00$\bar{1}$] is used.

equivalent axis/angle pair for grains I and L can be represented by <0.7430 0.0783 0.6647>/180°. Figure VI.9 shows that the corresponding diffraction patterns for the pair of acicular ferrite plates J and K have the same zone axis $<1\bar{1}\bar{1}>$, and the axis/angle pair $<1\bar{1}\bar{1}>/11°$ is the same as that for grains I and L (Figure VI.8). Figure VI.10 shows the corresponding diffraction patterns for the pair of acicular ferrite plates K and L also have the same zone axis $<1\bar{1}\bar{1}>$, and a rotation of ≈ 0 or 180° will make the same orientation for these two grains. As mentioned in Figure VI.7 for the same case, the two grains may be twin-related or in identical orientation. However, the exact orientation relationship cannot be determined without further work. The corresponding diffraction patterns for the pair of acicular ferrite plates L and M are shown in Figure VI.11. These two grains have also the same zone axis $<1\bar{1}\bar{1}>$, and the axis/angle pair can be described by $<1\bar{1}\bar{1}>/8°$ or <0.7339 0.0570 0.6769>/180°. Figure VI.12 shows the similar results for the pair of acicular ferrite grains L and M. The axis/angle pair for adjacent grains L and M can be represented by $<1\bar{1}\bar{1}>/6°$ or <0.7291 0.0463 0.6828>/180°. From the results shown in Figures VI.6,8,9,11 and 12, the adjacent acicular ferrite pairs I-L, J-K, L-M and L-N seem to be in closer identical orientation, because there is a rotation of ≈180° about <110>. It should be noted again that although the adjacent variants have nearly the same orientation, they have different habit planes.

All the results except the pairs I-J and L-K are listed in Table VI.2, where axis-angle pairs relating adjacent variants of acicular ferrite are presented with the greatest angle of rotation, out of the 24 possibilities for each pair of acicular ferrite plates. Judging from the data, it appears that the adjacent variants have nearly the same orientation in space, since there is a rotation of ≈180° about <001>, or ≈180° about <110>. This is very significant because even though the variants have nearly the same orientation in space, they have different habit planes (for example, C-D, I-L, J-K, L-M and L-N in Figures VI.3 and 6). This is strong evidence for sympathetic nucleation - if the habit planes were not different then the shape change of adjacent variants would be identical and the strain energy would be large and the plates would be parallel. The classical bainitic transformation involves a sympathetic nucleation to form as sheaves, which contain very closer identical orientation related sub-unit ferrite platelets. The fact that the habit plates of adjacent variants of acicular ferrite in approximately the same orientation are not parallel means that the formation of a plate triggers the formation of another whose orientation is nearly the same, but habit plane (and therefore displacement vector) is different, probably in a way which does not oppose the shape change of the original plate. This is like the autocatalytic nucleation found in the classical bursts of martensitic transformation.

6.4 Measurement of the Dislocation Density of Acicular Ferrite

The dislocation structure observed in transmission electron microscopy thin foils can be considered to be equivalent to those existing in bulk material if precautions are taken during the preparation of foils. A minor amount of dislocations may be introduced by mechanical deformation during thinning. It is unlikely that the conventional electrolytic polishing introduces any dislocation into a foil but the subsequent handling of the specimen frequently leads to accidental deformation. The dislocations introduced in this way tend to be long and nearly straight [170] since they lie parallel to the foil surface. This damage is easily recognised with experience and can be avoided in ordinary polycrystalline specimens. Other factors such as surface image forces may make the dislocation leave the foil, but the use of oxidising polishing solutions usually leaves a thin oxide film of the surface of the foil and prevents any such losses. Obviously, the best test for any dislocation distribution which is suspect is the reproducibility from one specimen to another or from one area of a foil to another.

The specimens studied in this investigation were taken from the top layer (fusion zone) of weld metal WD2. The same preparation of thin foils has been described as in Chapter Two. The microscopy was conducted on a Philips EM400T transmission electron microscope operated at 120kV. The dislocation density of acicular ferrite was determined from ten micrographs at the magnifications of 60,000 ~ 100,000X. These magnifications were chosen because they were high enough to resolve individual dislocations and the dislocation density in a micrograph could still be representative of the average dislocation density. Typical micrographs used for determining the dislocation density are shown in Figure VI.13. Ham [171] and Hirsch et al. [170a] showed that provided the dislocations are randomly oriented, their density measured in units of m/m^3 is given by $\rho = 2NM/Lt$, where N is the number of intersections that a random straight test line laid on a transmission electron micrograph makes with the dislocations, L is the total length of the test line, t is the thickness of foil and M is the magnification of the micrograph. In order to minimise any dislocation orientation effects, the method to count the intersections with a series of circles instead of using random straight lines has been used [172,173]. In the present work two concentric circles 4.40 and 6.28cm in circumference were used. The dislocation density of acicular ferrite in different areas of a foil or in different foils has been calculated.

To determine the dislocation density ρ from the relation $\rho = 2NM/Lt$ the foil thickness (t) has to be determined. The foil thickness was calculated by counting extinction contours [170b]: provided the diffraction conditions are such that one reflection is operating (two-beam case) the foil thickness is given by $t = \eta_g \zeta_g$, where η_g is the

number of extinction fringes of acicular ferrite grain for diffraction vector $\vec{g}$ and ζ_g is the extinction distance for the corresponding $\vec{g}$ and electron energy. The thickness is given by $t = \eta_g \zeta_g$ only when the foil is tilted so that the grain examined is at the exact Bragg condition [170b,174] in which the spacing between fringes is a maximum. The main operating reflection was determined by selected area diffraction. If as a result of selected area diffraction it was seen that there was more than one operating reflection, the foil was tilted to the two-beam case. The values of extinction distances (ζ_g) for 120 kV electron energy are given in Table VI.3, which are obtained [170c] from those for 100 kV electron energy by multiplying by a factor $\upsilon 120/\upsilon 100$, where $\upsilon 120$ and $\upsilon 100$ are the velocity of electron at 120 and 100 kV, respectively. A series of micrographs have been taken in bright field with a single strong reflection $\vec{g}$ = 100, 200 or 112. In this study the diffraction conditions of two-beam render some dislocations invisible, however, the percentage of invisible dislocation can easily be calculated if the assumptions are as follows:

(i) All dislocations have Burgers vectors of the type $\vec{b}$ = a/2 <111>, where a is the lattice parameter of acicular ferrite, i.e., all the dislocations are undissociated.

(ii) The dislocations were randomly distributed both in space and among the four possible variants of the Burgers vectors.

(iii) All dislocations satisfying the invisibility criterion ($\vec{g} \cdot \vec{b}$ = o) are completely out of contrast.*

The value of $\vec{g} \cdot \vec{b}$ for the first three reflections and the a/2<111> Burgers vectors in BCC metals are listed in Table VI.5. The proportion of the a/2<111> Burgers vectors invisible in BCC metals under different two-beam diffraction conditions are summarised in Table VI.4.

Electron micrograph Figure VI.13 shows the bright field image of acicular ferrite under the two-beam condition $\vec{g}$ = <1$\bar{2}$1>. It clearly displays 5 extinction fringes on the grain boundary, therefore the thickness of this grain is 2690Å. The average foil thickness for the measurements is of the order of 2455±440Å. After the dislocation density had been measured directly from the electron micrograph, the corrected dislocation density was calculated by adding the part invisible under corresponding two-beam diffraction condition to the measured dislocation density. A complete list of experimental data in this

* In fact, the invisibility criterion $\vec{g} \cdot \vec{b}$ = o can only be applied for screw dislocation. For edge dislocation both $\vec{g} \cdot \vec{b}_e$ and $\vec{g} \cdot \vec{b}_e \wedge \vec{u}$ (where $\vec{b}_e$ and $\vec{u}$ are Burgers vector of edge dislocation and a unit vector along the edge dislocation line, respectively) must all be zero for complete invisibility, which is a very restricted criterion compared with the $\vec{g} \cdot \vec{b}$ = o criterion. However, in practice only faint residual contrast generally occurs for edge dislocation when $\vec{g} \cdot \vec{b}$ = o (i.e., $\vec{g} \cdot \vec{b}_e$ = o), but $\vec{g} \cdot \vec{b}_e \wedge \vec{u} \neq$ o and this has been interpreted as indicating dislocation invisibility [175].

work is presented in Table VI.6. The average corrected dislocation density of acicular ferrite is of the order of (3.90±1.97) x $10^{14}m^{-2}$.

6.5 Summary and Conclusions

The orientation relationship between adjacent acicular ferrite plates has been been studied. It has found that many adjacent variants of acicular ferrite have a very close identical orientation even though they have different habit planes. This is strong evidence for sympathetic nucleation - if the habit planes were not different then the shape change of adjacent variants would be identical and the plates would be parallel, as the case of classical bainite. The fact that the habit planes of variants in nearly the same orientation are not parallel implies that the formation of a plate triggers the formation of another whose orientation is nearly the same, but habit plane (and therefore displacement vector) is different, probably in a way which does not oppose the shape change of the original plate.

The dislocation density of acicular ferrite has also been measured using two-beam technique, and is of the order of $10^{14}m^{-2}$. The high dislocation density is consistent with the high temperature displacive transformation mechanism in which there is some plastic accommodation of the shape change due to transformation.

Table VI.1 - 24 matrices representing all the symmetry rotations in cube systems.

$$\begin{pmatrix}1&0&0\\0&1&0\\0&0&1\end{pmatrix}, \quad \begin{pmatrix}\bar{1}&0&0\\0&1&0\\0&0&1\end{pmatrix}, \quad \begin{pmatrix}1&0&0\\0&\bar{1}&0\\0&0&1\end{pmatrix}, \quad \begin{pmatrix}1&0&0\\0&1&0\\0&0&\bar{1}\end{pmatrix},$$

$$\begin{pmatrix}1&0&0\\0&0&1\\0&1&0\end{pmatrix}, \quad \begin{pmatrix}\bar{1}&0&0\\0&0&1\\0&1&0\end{pmatrix}, \quad \begin{pmatrix}1&0&0\\0&0&1\\0&\bar{1}&0\end{pmatrix}, \quad \begin{pmatrix}1&0&0\\0&0&\bar{1}\\0&1&0\end{pmatrix},$$

$$\begin{pmatrix}0&1&0\\1&0&0\\0&0&1\end{pmatrix}, \quad \begin{pmatrix}0&1&0\\\bar{1}&0&0\\0&0&1\end{pmatrix}, \quad \begin{pmatrix}0&\bar{1}&0\\1&0&0\\0&0&1\end{pmatrix}, \quad \begin{pmatrix}0&1&0\\1&0&0\\0&0&\bar{1}\end{pmatrix},$$

$$\begin{pmatrix}0&0&1\\1&0&0\\0&1&0\end{pmatrix}, \quad \begin{pmatrix}0&0&1\\\bar{1}&0&0\\0&1&0\end{pmatrix}, \quad \begin{pmatrix}0&0&1\\1&0&0\\0&\bar{1}&0\end{pmatrix}, \quad \begin{pmatrix}0&0&\bar{1}\\1&0&0\\0&1&0\end{pmatrix},$$

$$\begin{pmatrix}0&1&0\\0&0&1\\1&0&0\end{pmatrix}, \quad \begin{pmatrix}0&1&0\\0&0&1\\\bar{1}&0&0\end{pmatrix}, \quad \begin{pmatrix}0&\bar{1}&0\\0&0&1\\1&0&0\end{pmatrix}, \quad \begin{pmatrix}0&1&0\\0&0&\bar{1}\\1&0&0\end{pmatrix},$$

$$\begin{pmatrix}0&0&1\\0&1&0\\1&0&0\end{pmatrix}, \quad \begin{pmatrix}0&0&1\\0&1&0\\\bar{1}&0&0\end{pmatrix}, \quad \begin{pmatrix}0&0&1\\0&\bar{1}&0\\1&0&0\end{pmatrix}, \quad \begin{pmatrix}0&0&\bar{1}\\0&1&0\\1&0&0\end{pmatrix}.$$

Table VI.2 - Experimentally determined axis-angle pairs relating adjacent variants of acicular ferrite.

Adjacent Acicular Ferrite Plates	Varient Set*	Axis-Angle Pair	
A-B	1-18	<0.1305 0.9914 0.0000>	180°
B-C	1-18	<0.1392 0.9903 0.0000>	180°
C-D	1-18	<0.1132 0.9936 0.0000>	180°
E-F	1-17	<0.8845 0.2579 0.3894>	174°
G-H	1-18	<0.1305 0.9914 0.0000>	180°
I-J	Description is given in Section 6.2.2		
I-L	1-14	<0.7430 0.0783 0.6647>	180°
J-K	1-14	<0.7430 0.0783 0.6647>	180°
K-L	Description is given in Section 6.2.2		
L-M	1-14	<0.7339 0.0570 0.6769>	180°
L-N	1-14	<0.7291 0.0463 0.6828>	180°
–	1-2	<0.6388 0.6169 0.4596>	179°
–	1-23	<0.2077 0.6092 0.7853>	175°
–	1-10	<0.3676 0.5926 0.7167>	173°
–	1-4	<0.7661 0.6346 0.1016>	175°
–	1-16	<0.4808 0.7974 0.3646>	179°
–	1-21	<0.4828 0.1684 0.8594>	175°

*One of the 24 equivalent axis-angle pairs, with the greatest angle of rotation is chosen for each pair of adjacent acicular ferrite plates in order to interpret easily.

Table VI.3 - Extinction distance ζ_g (Å) in ferrite for 100 and 120 kV electron energy, respectively.

Reflection $\vec{g}$	Extinction distance ζ_g (Å)	
	100 kV	120 kV
110	270	289
200	395	423
211	503	538
220	606	648
310	712	762

Table VI.4 - Proportion of Burgers vectors a/2 <111> invisible in BBC lattice under different two-beam diffraction conditions.

Diffraction conditions	Proportion of invisible Burgers vectors
Two-beam	
$\vec{g}$ = <110>	0.5
$\vec{g}$ = <200>	0
$\vec{g}$ = <211>	0.25

Table VI.5 - The volume of $\vec{g}\vec{b}$ for the first three reflections and the a/2 <111> Burgers vectors in BCC lattice.

Reflection	Possible Burgers vector (times a/2) 1/2[111]	1/2[$\bar{1}$11]	1/2[1$\bar{1}$1]	1/2[11$\bar{1}$]
110	1	0	0	1
101	1	0	1	0
011	1	1	0	0
$\bar{1}$10	0	1	$\bar{1}$	0
$\bar{1}$01	0	1	0	$\bar{1}$
0$\bar{1}$1	0	0	1	$\bar{1}$
200	1	$\bar{1}$	1	1
020	1	1	$\bar{1}$	1
002	1	1	1	$\bar{1}$
$\bar{2}$00	$\bar{1}$	1	$\bar{1}$	$\bar{1}$
0$\bar{2}$0	$\bar{1}$	$\bar{1}$	1	$\bar{1}$
00$\bar{2}$	$\bar{1}$	$\bar{1}$	$\bar{1}$	1
112	2	1	1	0
121	2	1	0	1
211	2	0	1	1
$\bar{1}$12	1	2	0	$\bar{1}$
$\bar{1}$21	1	2	$\bar{1}$	0
$\bar{2}$11	0	2	$\bar{1}$	$\bar{1}$
1$\bar{2}$2	1	0	2	$\bar{1}$
12$\bar{1}$	0	$\bar{1}$	2	$\bar{1}$
2$\bar{1}$1	1	$\bar{1}$	2	0
11$\bar{2}$	0	$\bar{1}$	$\bar{1}$	2
12$\bar{1}$	1	0	$\bar{1}$	2
21$\bar{1}$	1	$\bar{1}$	0	2

Table VI.6 - Experimental data for dislocation density calculation

Two-beam condition $\vec{g}$	No. of extinction fringes η_g	Thickness of thin foil t (Å)	measured dislocation density (m^{-2})	corrected dislocation density (m^{-2})
<112>	5	2690	1.87×10^{14}	2.49×10^{14}
<110>	5	1445	4.90×10^{14}	8.90×10^{14}
<112>	5	2690	2.05×10^{14}	2.73×10^{14}
<200>	6	2538	2.47×10^{14}	2.47×10^{14}
<112>	5	2690	2.60×10^{14}	3.46×10^{14}
<112>	5	2690	2.53×10^{14}	3.37×10^{14}
<110>	6	1734	3.16×10^{14}	6.32×10^{14}
<112>	5	2690	2.18×10^{14}	2.91×10^{14}
<112>	5	2690	2.29×10^{14}	3.05×10^{14}
<112>	5	2690	2.46×10^{14}	3.28×10^{14}

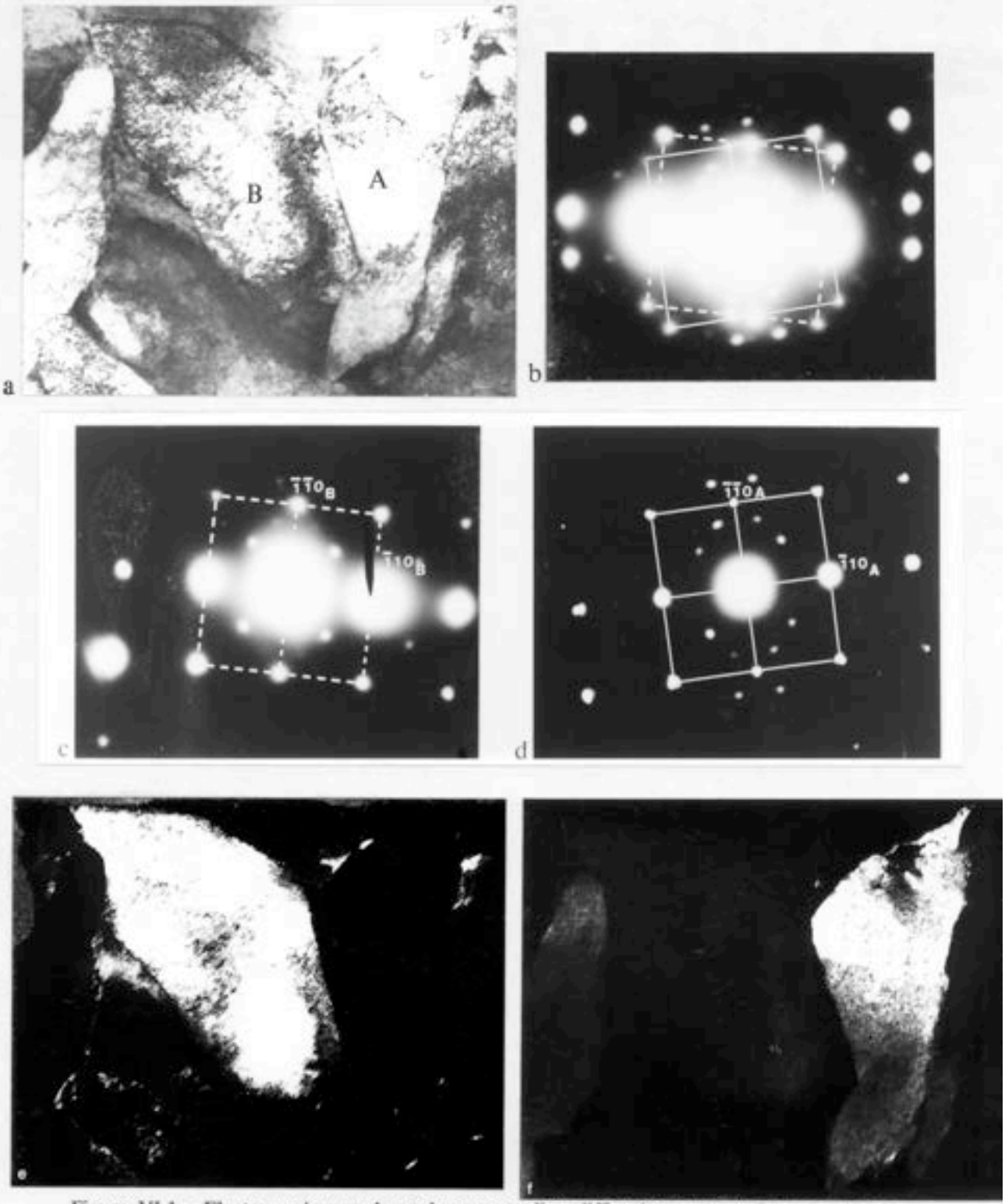

Figure VI.1 - Electron micrographs and corresponding diffraction patterns from a pair of α_a plates A and B. (a) Bright field image. (b) Selected area diffraction pattern (SADP) from interface of grains A and B. (c) SADP from grain B. (d) SADP from grain A. (e) Dark field image of grain B using $(110)_B$ reflection. (f) Dark field image of grain A using $(110)_A$ reflection. The central bright spots are Fe_2O_3 surface oxide reflections.

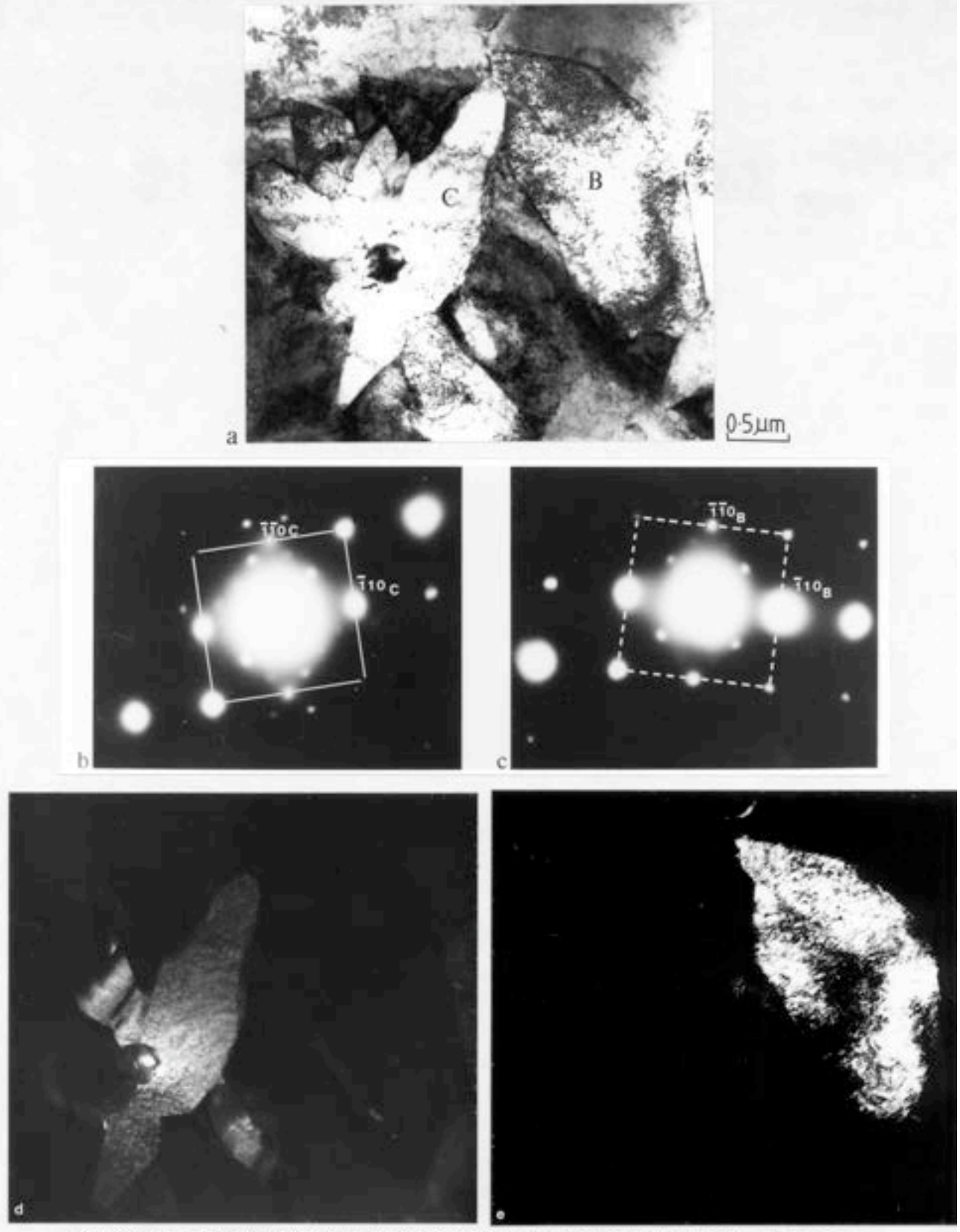

Figure VI.2 - Electron micrographs and corresponding diffraction patterns from a pair of α_a plates B and C. (a) Bright field image. (b) SADP from grain C. (c) SADP from grain B. (d) Dark field image of grain C using $(\bar{2}00)_C$ reflection. (e) Dark field image of grain B using $(110)_B$ reflection. The central bright spots are Fe_2O_3 surface oxide reflections.

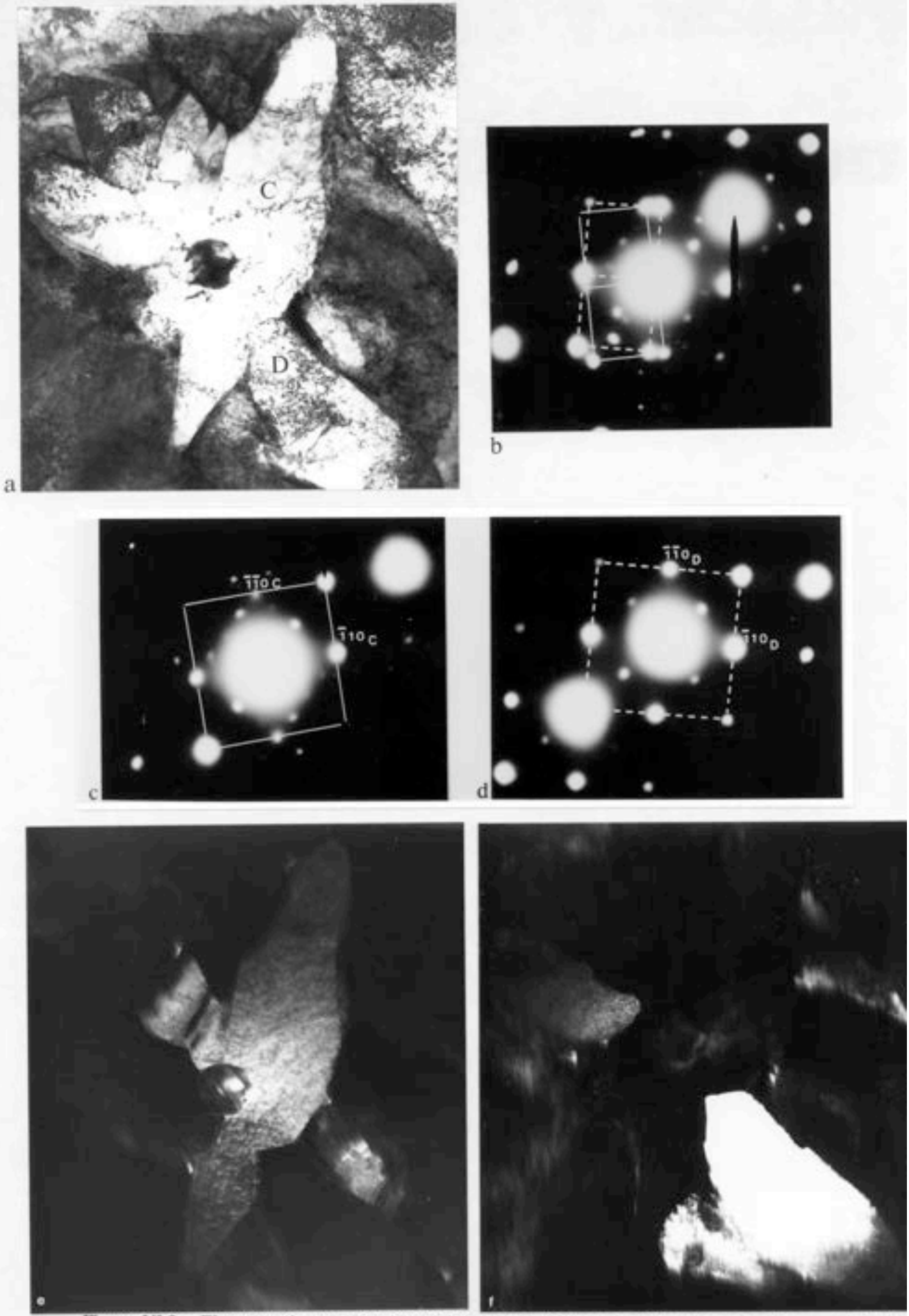

Figure VI.3 - Electron micrographs corresponding diffraction patterns from a pair of α_a plates C and D. (a) Bright field image. (b) SADP from interface of grains C and D. (c) SADP from grain C. (d) SADP from grain D. (e) Dark field image of grain C using $(\bar{2}00)_C$ reflection. (f) Dark field image of grain D using $(200)_D$ reflection. The central bright spots are Fe_2O_3 surface oxide reflections.

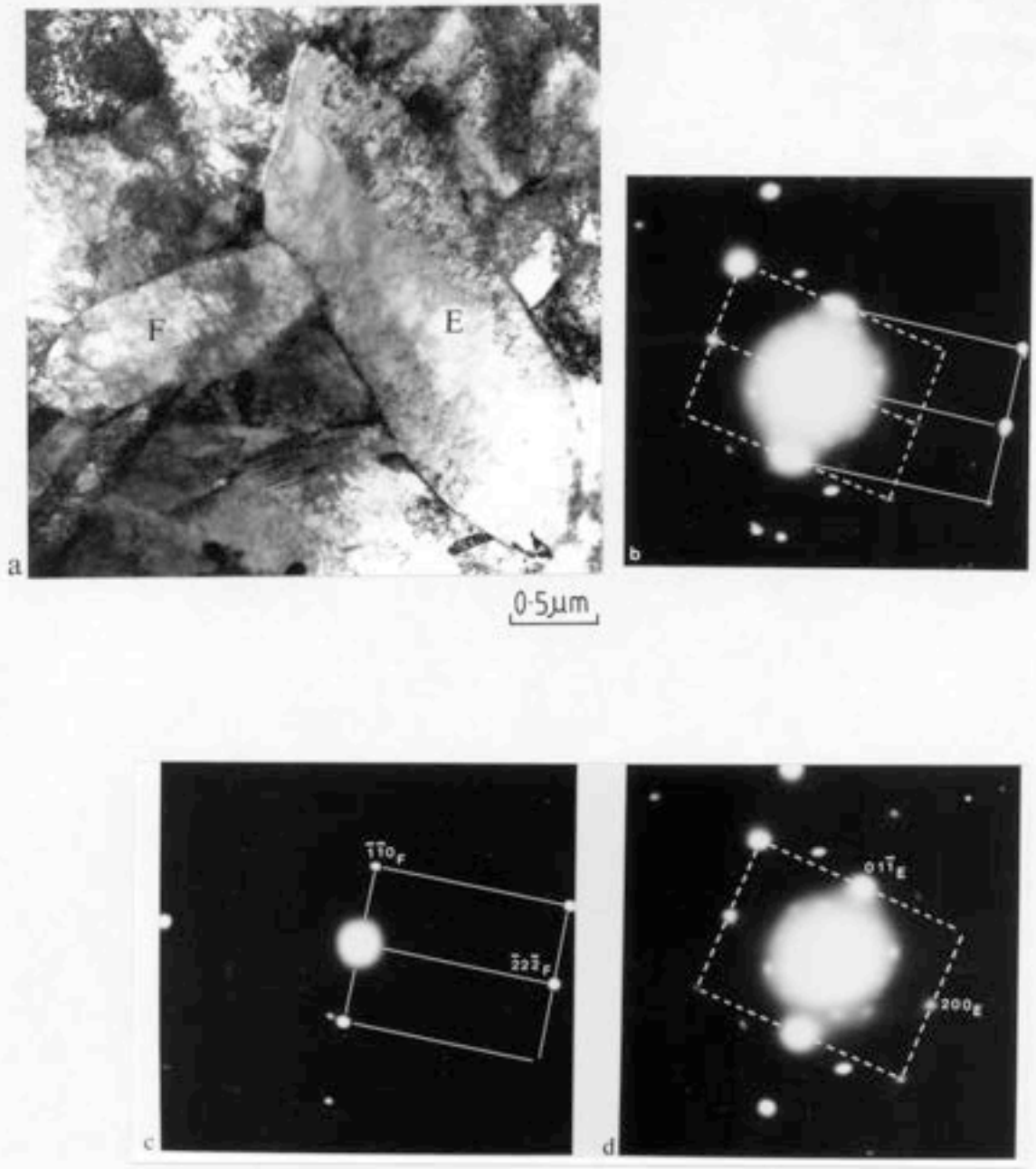

Figure VI.4 - Electron micrograph and corresponding diffraction patterns from a pair of α_a plates E and F. (a) Bright field image. (b) SADP interface of grains E and F. (c) SADP from grain F. (d) SADP from grain E. The central spots are Fe_2O_3 surface oxide reflections.

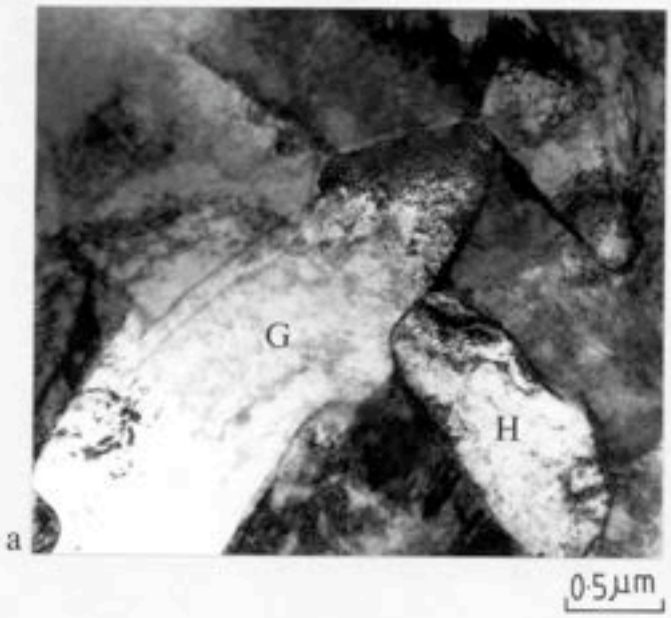

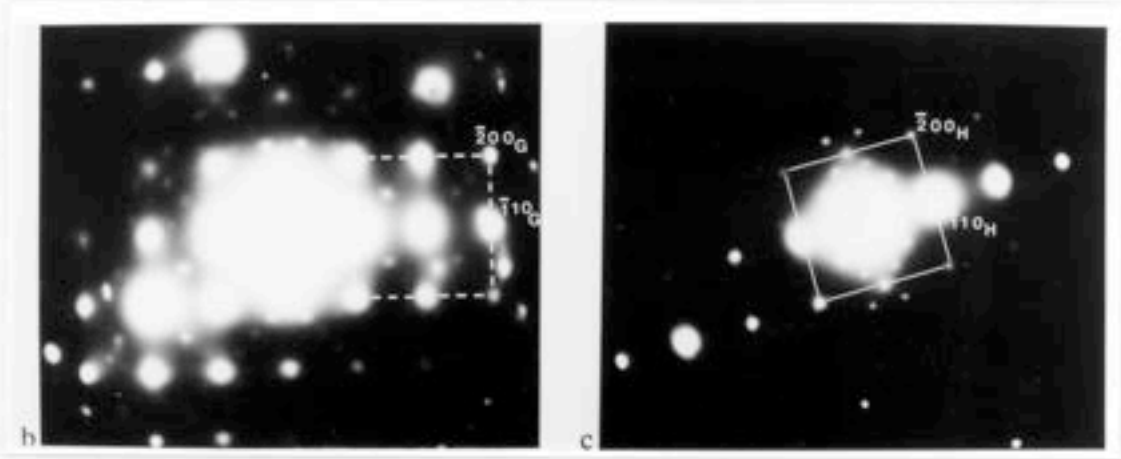

Figure VI.5 - Electron micrograph and corresponding diffraction patterns from a pair of α_a plates G and H. (a) Bright field image. (b) SADP from grain G. (c) SADP from grain H. The central bright spots are Fe_2O_3 surface oxide reflections.

Figure VI.6 - Electron micrograph shows six acicular ferrite plates designated I,J,K,L,M and N, which are in intimate contact.

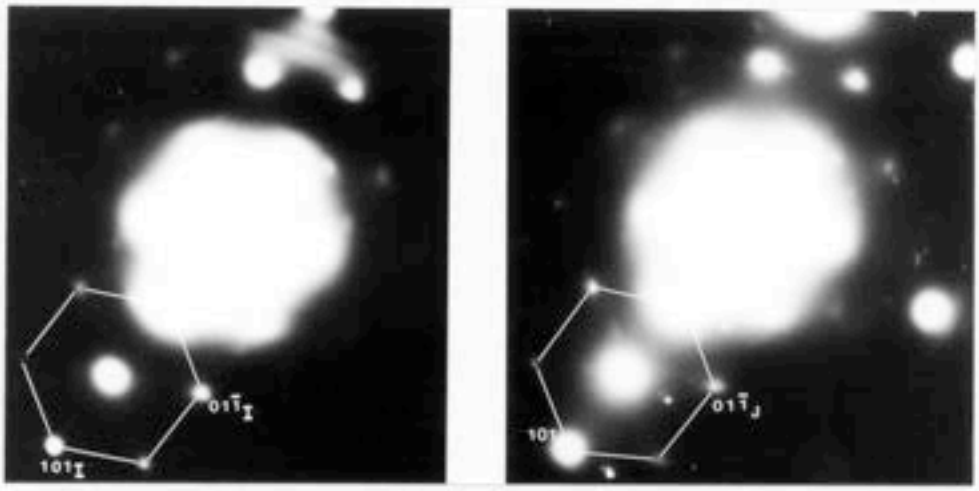

Figure VI.7 - Showing the corresponding selected area diffraction patterns (SADP) from the pair of acicular plates I and J, respectively. Details of orientation relationship are discussed in text.

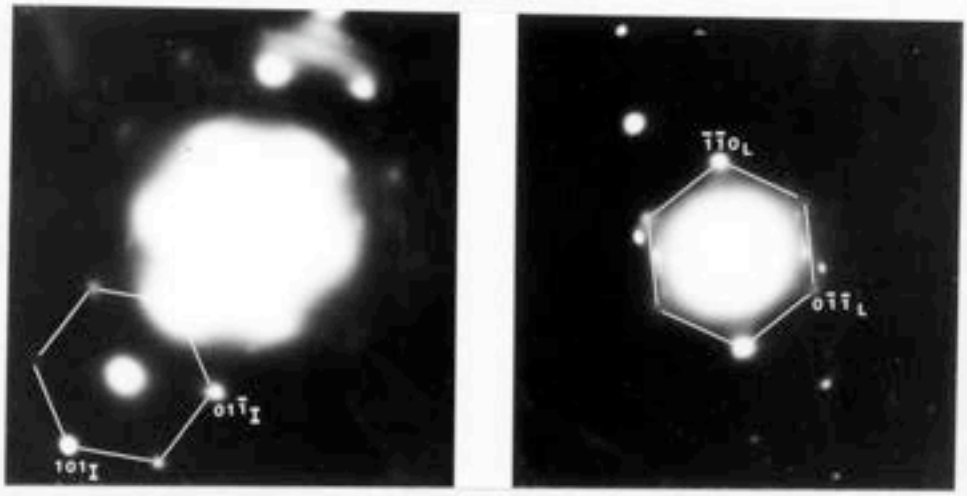

Figure VI.8 - Showing the corresponding SADP from the pair of acicular ferrite plates I and L, respectively. The axis/angle pair can be represented by <111>/11°.

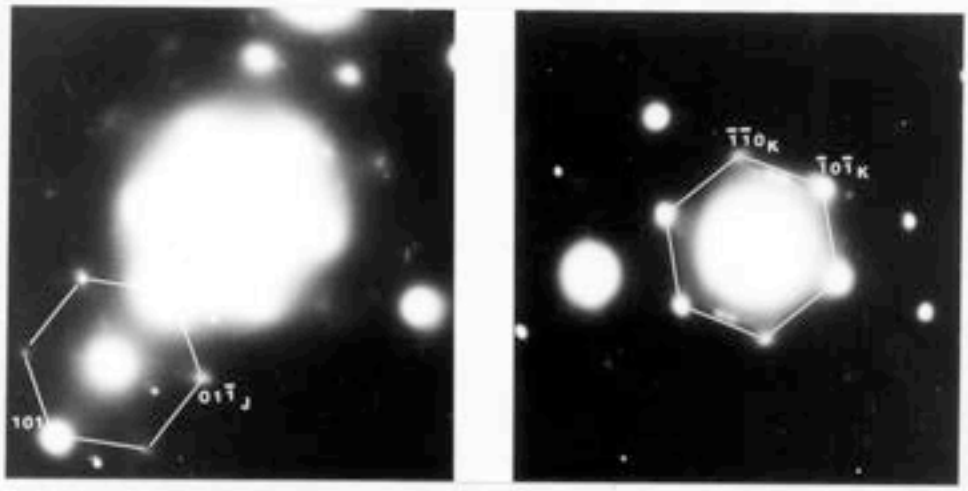

Figure VI.9 - Showing the corresponding SADP from the pair of acicular ferrite plates J and K, respectively. The axis/angle pair can be represented by <111>/11°.

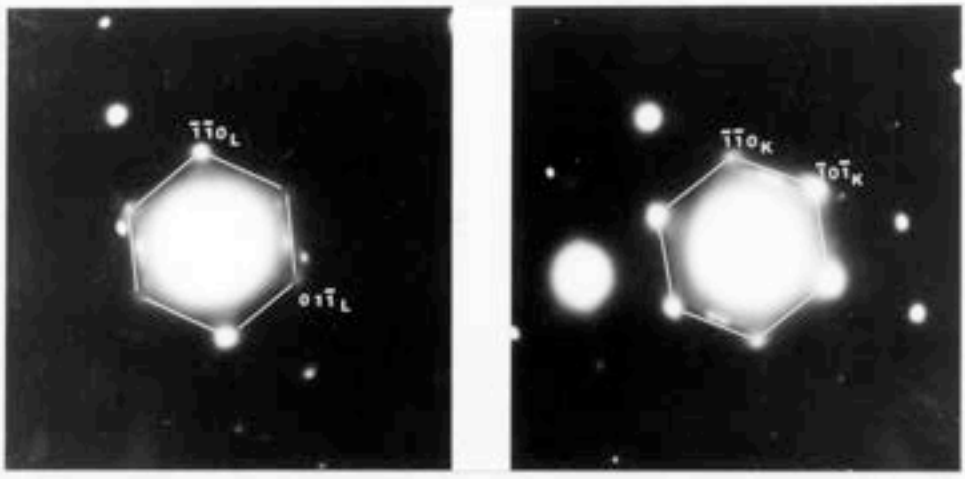

Figure VI.10 - Showing the corresponding SADP from the pair of acicular ferrite plates L and K, respectively. Details of orientation relationship are discussed in text.

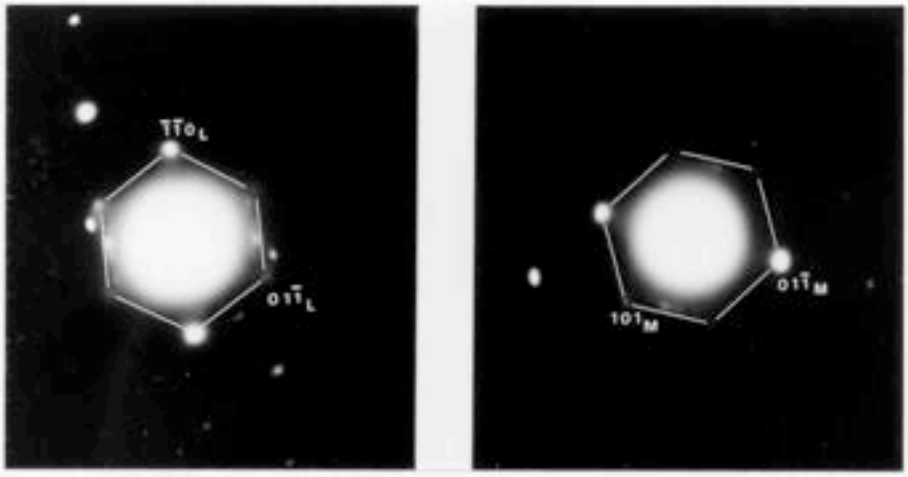

Figure VI.11 : Showing the corresponding SADP from the pair of acicular ferrite plates L and M, respectively. The axis/angle pair can be represented by <111>/8°.

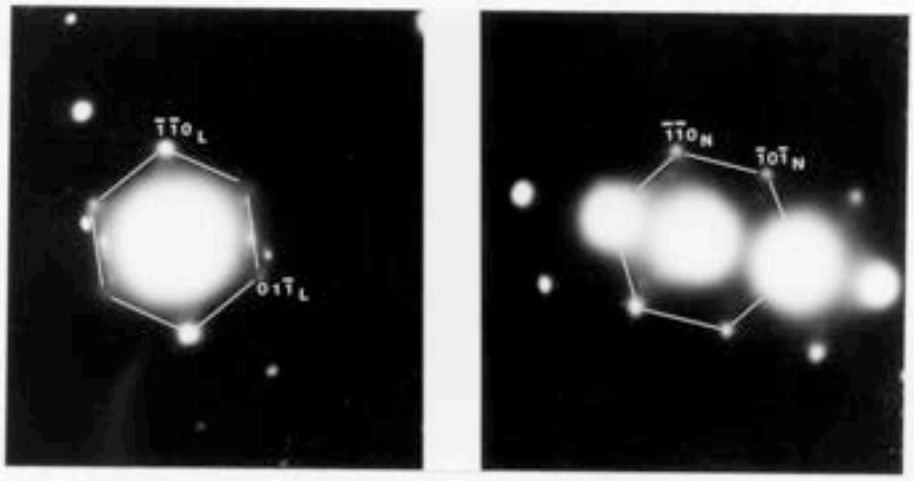

Figure VI.12 - Showing the corresponding SADP from the pair of acicular ferrite plates L and N, respectively. The axis/angle pair can be represented by <111>6°.

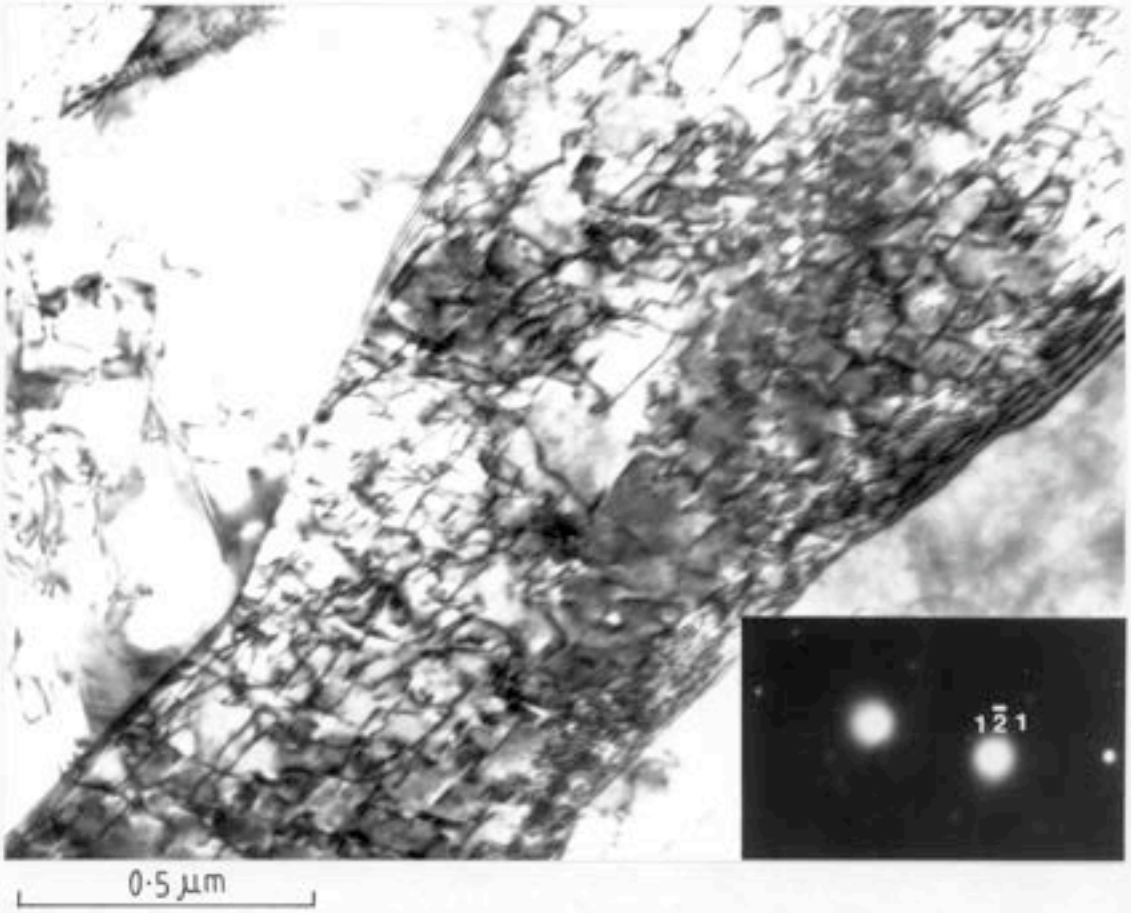

Figure VI.13 - Electron micrograph shows the bright field image of acicular ferrite under two-beam condition $\vec{g}$ = <121>.

Chapter Seven

Reaustenitisation in Bainitic Steels

7.1 Introduction

Work on reaustenitisation in high-strength steel weld deposits has been reported in Chapter 4 and 5. In this chapter, reaustenitisation in bainitic steels is investigated further. Bainitic ferrite possesses high strength and high toughness properties especially in some silicon containing alloy steels [176,177]. The microstructures have been exploited to improve mechanical properties compared with those of conventional tempered martensite based microstructures, In order to develop these bainitic steels in the construction of submarines, off-shore plateforms and many other applications, their weldability is crucial.

The specific aim of the present work is to elucidate the effect of the carbon content of residual austenite on reaustenitisation in bainitic steels which contain high concentrations of silicon. The high silicon concentration allows transformation to first bainitic ferrite and residual austenite (i.e., no carbides). If this microstructure is, without cooling from the isothermal transformation temperature, rapidly reheaded then the reaustenitisation process requires no nucleation of austenite, permitting a controlled study of the growth of austenite. On the other hand, the mixture of bainite and austenite can be tempered to decompose the austenite into ferrite plus carbide; reaustenitisation of the resultant microstructure ferrite plus carbide would then require the nucleation of austenite, permitting a study of nucleation effects. Both isothermal and continuous heating experiments have been carried out.

7.2 Experimental Procedure

The experimental details are essentially the same as in Section 4.2 and 5.3, and are not restated here. The steels used were prepared from high purity base materials as 20 kg vacuum induction melts and were hot worked to 8mm diameter rod. The ingots were sealed in quartz capsules (under a partial pressure of argon) and homogenised for three days at 1250°C, before hot reduction to 3.2mm diameter rods. The chemical composition of the alloy studied is Fe-0.43C-3.00Mn-2.02Si, wt.%.

7.3 Results and Discussion

7.3.1 The Nature of Bainite (α_b)

Figure VII.1a shows the isothermal transformation curves of bainite for the alloy austenitised at 950°C for 10 minutes followed by isothermal transformation at 350, 380

and 410°C, respectively. The maximum extent of transformation to upper bainite increases as the transformation temperature decreases. In steels where the bainite transformation can develop without interference from other reactions, this is known to exhibit an "incomplete reaction phenomenon" [25,89,100]; in this, the transformation stops prematurely, well before the carbon concentration of the residual austenite (X_γ) reaches its equilibrium or paraequilibrium concentration. The transformation stops when X_γ reaches approximately a concentration (X_{T_0}) given by T_0 curve on the phase diagram. The T_0 curve on a plot of temperature versus carbon concentration represents the locus of all points where ferrite and austenite of the same composition have equal free energy. To take account of invariant-plane strain shape change accompanying the formation of bainite, a T_0' curve is defined in which the free energy of ferrite is increased by 400 J/mol [100]. In the present work, it is found that for the alloy studies the bainite transformation terminates when the X_γ reaches T_0 curve (Figure VII.1b). This can be expected due to plastic relaxation and interactions between sheaves of bainite [180].

It was noted that the alloy required about 30 minutes to achieve maximum transformation at 350°C. An upper bainite microstructure (Figure VII.2) was obtained following isothermal transformation at 350°C for 120 minutes. The microstructure was a mixture of 55% bainitic ferrite and 45% residual austenite (some of the residual austenite transformed to martensite during cooling), as determined by the techniques discussed in Section 3.2. Austenite was found to occur in two forms: blocky and film morphologies (Figure VII.2). The former originates from the geometrical partitioning of the prior austenite grain by sheaves of bainite whereas the latter is confined between bainitic ferrite subunits (Figure VII.3). Although there are two kind morphologies of austenite, the carbon content of all forms of austenite may be expected to be the same.

7.3.2 Reaustenitisation by Continuous Heating

If after isothermal transformation to bainite at 350°C for only 10 minutes, the specimen is continuously heated, the residual austenite is found to decompose during heating, before the onset of reaustenitisation. This was found to be particularly the case with low heating rates as shown in Figure VII.4. Figures VII.4a and b present the relative length change versus temperature curves for continuous heating at heating rates of 0.06 and 0.15°C/s, respectively, after isothermal transformation at 350°C for 10 minutes. A pearlite-like microstructure formed (Figure VII.5a) from the large regions of blocky residual austenite when the temperature reached about 600°C at a heating rate of 0.06°C/s. This was expected because the starting microstructure contained a high volume fraction of relatively low carbon untransformed austenite, since the specimen had only been transformed to a low volume fraction of bainitic ferrite. It was also found that the film

austenite had decomposed into bands of discretely nucleated carbides in the same condition (Figure VII.5b).

Figures VII.6a and b present the continuous heating curves for samples transformed isothermally to bainite at 350°C for 120 minutes, followed immediately by continuous heating at 0.06 and 0.15°C/s, respectively. The results also demonstrate that the relative length change versus temperature curves deviate from linearity during heating before the process of reaustenitisation begins in both the experiments. The deviations indicate decomposition of austenite during heating. Figures VII.7, 8 and 9 show the electron micrographs corresponding to Figure VII.6a (heating rate = 0.06°C/s) from specimens which were quenched after temperature reaching 600, 700 and 730°C, respectively. Such slow heating also leads to the diffusional decomposition of high carbon residual austenite into tiny particles of carbides (Figure VII.7) located between bainitic ferrite plates. Micrograph (Figure VII.8) shows that the carbide particle coalesce along the bainitic ferrite boundaries when a temperature as high as 700°C is reached. The austenite forms from the larger elongated carbide particles (Figure VII.9) as the temperature rises beyond 720°C.

In order to elucidate the effect of carbon content of residual austenite on reaustenitisation, specimens austenitised at 950°C for 10 minutes were isothermally transformed to bainite for 120 minutes (i.e., longer than needed to complete the bainitic reaction). Figure VII.10 shows the reaustenitisation start temperature versus heating rate for four different starting microstructures, which are three bainite microstructures and one tempered bainite microstructure (Figure VII.11). It is clear that the carbon content of residual austenite influences the reaustenitisation behaviour. Because of the negative slope of T_0 curve, for the higher bainitic transformation temperature the lower carbon content of residual austenite is obtained. It was expected that the bainite formed at higher temperature should be reaustenitised at a higher temperature (Figure VII.12), as predicted by the theoretical analysis mentioned in Section 4.3. As the heating rate is lower than 0.6°C/s, these three bainite structures have nearly the same reaustenitisation temperature (Figure VII.10), simply because the residual austenite first decomposes to ferrite plus carbide during heating before the onset of reaustenitisation. Figure VII.11 shows carbide particles in tempered bainite; the elongated carbide particles were formed from carbon-enriched residual austenite, and the tiny carbide particles precipitated in supersaturated bainitic ferrite plates. When the tempered bainite is heated at a fast heating rate, the reaustenitisation start temperature is higher than that of bainite structure. This is probably because the effect of austenite nucleation retards the rate of reaustenitisation.

7.3.3 Isothermal Reaustenitisation

Specimens austenitised at 950°C for 10 minutes were isothermally transformed to bainite at temperature 350°C for 2 hours and then, without cooling below 350°C, rapidly up-quenched to a higher temperature for isothermal reaustenitisation. Some of the dilatometric curves are shown in Figure VII.13. Some length changes were detected dilatometrically even at relatively low isothermal transformation temperature, but for the temperature less than 720°C, electron microscopies (Figures VII.14a and b) showed that the length changes were due to the diffusional decomposition of austenite into ferrite plus carbide, rather than due to reaustenitisation. When the isothermal transformation was at 720°C, the thickness of austenite layer increased slightly and no carbide particles could be found (Figure VII.14c). Therefore, the lowest isothermal reaustenitisation temperature is found to be 720°C. This is consistent with the theoretical analysis as shown by point a in Figure VII.12. Electron micrographs of Figures VII.14d, e and f show the austenite growth at 750, 780 and 800°C, respectively for 2 hours. The result of isothermal reaustenitisation at 820°C for 2 hours is shown in Figures VII.14g and h. It demonstrates that full reaustenitisation can not be complete in such condition. Even after isothermal reaustenitisation at 835°C for 6.5 hours, a little ferrite could still be found (Figure VII.14i). However, if the specimen was isothermally reaustenitised at 780°C for 1 week, after isothermally transformed to bainite at 350°C for 2 hours, the alloy became fully austenitic (Figure VII.15). The results are consistent with the fact that the last stages of reaustenitisation, which involve the long-range diffusion of substitutional elements, are tortuously slow, but a fully austenitic sample can be obtained at 780°C, consistent with theory (point b, Figure VII.12).

Microanalytical measurements have been carried out using energy dispersive X-ray analysis on a Philips EM400T transmission electron microscope. The technique has been mentioned in Chapter Two, and will not be restated here. The microanalytical data (Figure VII.16 and Table VII.1) cover a range of isothermal reaustenitisation temperatures. The results show that for 2 hours of transformation time, the degree of partitioning of alloying elements (as indicated by the deviation of the partition coefficient ki from unity, where ki = Xi^{γ}/Xi^{α}) decreases with increasing reaustenitisation temperature. At 835°C for 2 hours, the partition coefficient for Mn is close to unity, but that for Si still significantly deviates from unity. The results are generally consistent with the hypothesis that less partitioning can be tolerated during transformation at higher driving forces (higher temperature in the present context).

7.3.4 Coalescence of Carbides

In Section 7.3.2, it was demonstrated that when a slow heating rate was used for the reaustenitisation of a mixture of bainitic ferrite plus residual austenite, the residual austenite decomposed into bands of discretely nucleated carbides (Figure VII.7), and then the carbide particles coalesced into an elongated morphology (Figures VII.8 and 9) along the original bainitic ferrite boundary before the onset of austenitisation. At higher heating rates, coalescence was not observed, the size of the carbide particles being small, and their shape being equiaxed. Due to the surface energy contribution to the bulk free energy necessary for the formation of stable austenite nuclei, the tiny carbide particles seem to be not easily transformed to austenite.

In order to study the coalescence of carbides to form elongated particles, further experiments have been done. Figure VII.17 shows the tempered bainite microstructure which was formed by isothermal transformation at 350°C for 2 hours and subsequently tempered at 600°C for 42.7 hours. Although the majority of carbide particles have coalesced into elongated forms, some small equiaxed particles remain. Figure VII.18 shows that after tempering the bainite at 680°C for 14 days, the carbide particles become plump (about 0.2μm thick and 0.5μm long) and are located at the grain boundaries of extensively recovered ferrite. However, after tempering the bainite at 600°C for 30 minutes and then annealing at 715°C for 25 minutes, the carbide particles combine and become extremely long (Figure VII.19-23) as was observed for the reaustenitisation experiments carried out at slow heating rates. These long particles have been proved to be cementite. They grow in a specific direction, and are parallel each other. The morphology is similar to that of pearlite, except that pearlite possesses three dimensionally continuous lamellar layers of cementite. Further work is needed to analyse the detailed orientation relationship between the long particles of cementite and the matrix ferrite, and in order to understand the growth mechanism.

7.4 Summary and Conclusions

The process of reaustenitisation from bainite in a silicon steel has been investigated, and the results are found to be consistent with the theory developed earlier. Reaustenitisation only begins when the carbon concentration of the residual austenite exceeds its equilibrium carbon concentration. The experimental results can also be explained by the theoretical model presented in Section 4.3. Due to the high level of alloying additions, the complete transformation to austenite at the Ac_3 temperature of the alloy takes an extremely long time. Microanalytical data show that the partition coefficient decreases as the driving force for transformation increases. The decomposition of residual

austenite during slow heating has also been studied. At slow heating rates, the residual austenite decompose into bands of discretely nucleated carbides, then the carbide particles coalesce along original bainitic ferrite boundaries, and finally transformed to austenite as the temperature rises.

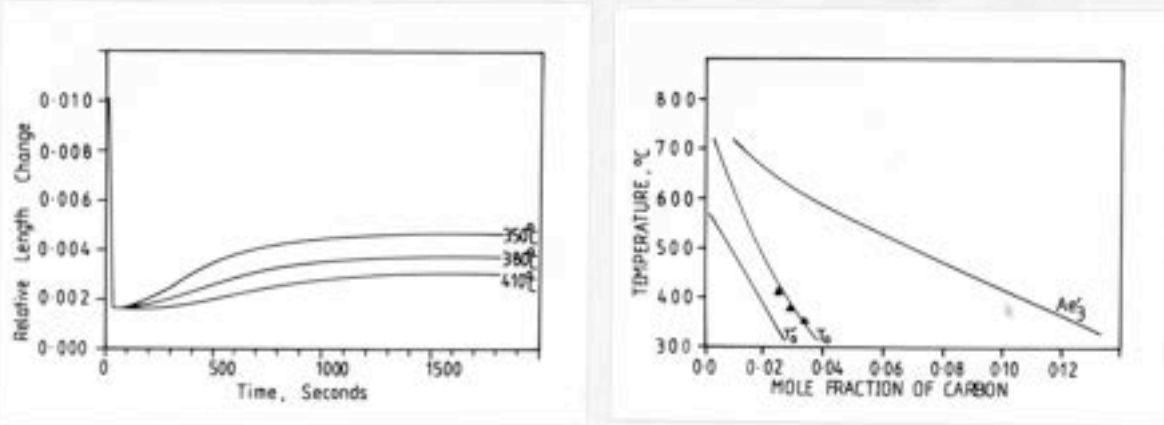

Figures VII.1 - (a) Dilatometric curves showing isothermal transformation to bainite after austenitisation at 950°C for 10 minutes. (b) Calculated phase diagram for Fe-0.43C-3.00Mn-2.02Si, and experimental data indicating that the transformation to bainite stops when X_γ reaches the T_o curve.

Figure VII.2 - Optical micrograph showing the upper bainitic ferrite and residual austenite (blocky and film morphologies) following isothermal transformation at 350°C for 120 minutes.

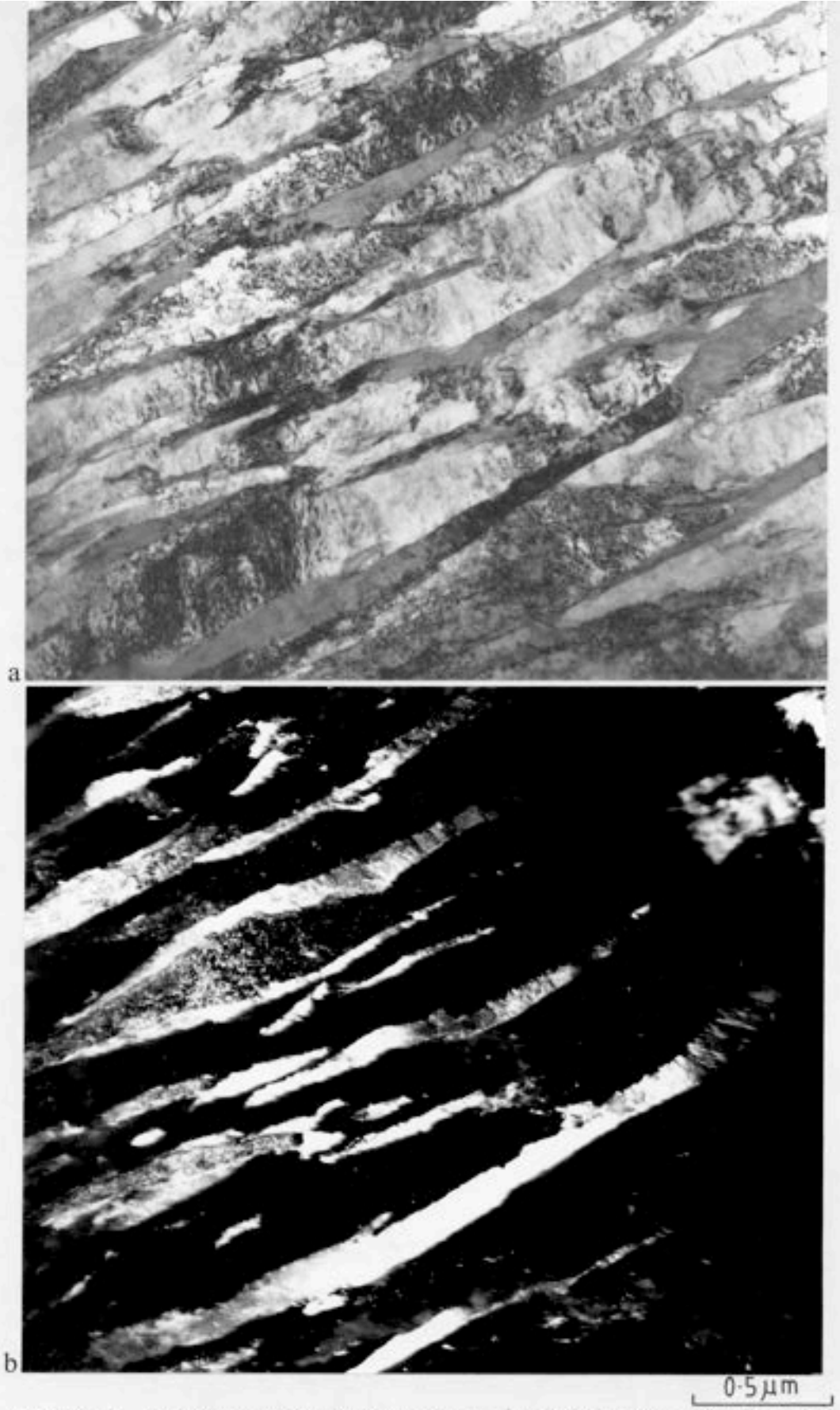

Figure VII.3 - Typical upper bainite microstructure of Fe-0.43C-3.00Mn-2.02Si alloy. (a) Bright field image of an isothermally transformed (at 350°C for 120 mins) specimen. (b) Corresponding retained austenite dark field image.

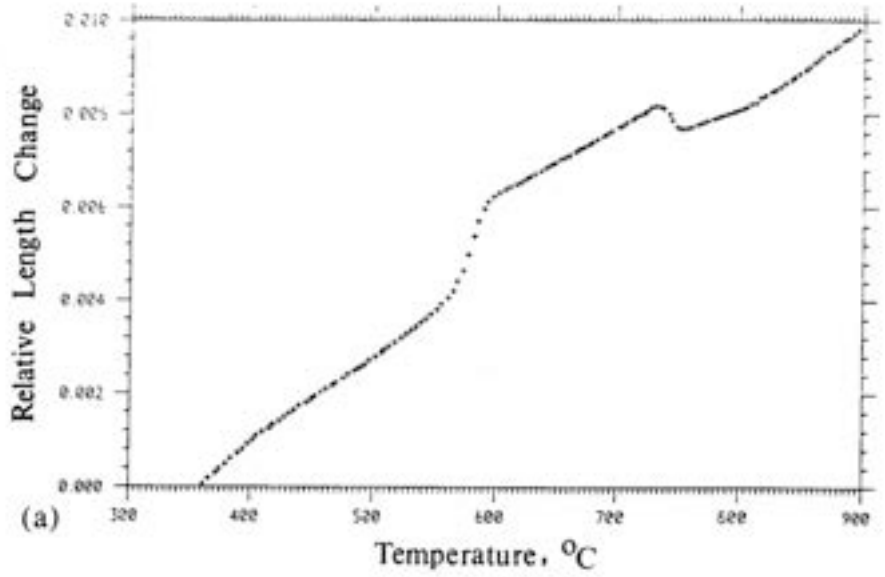

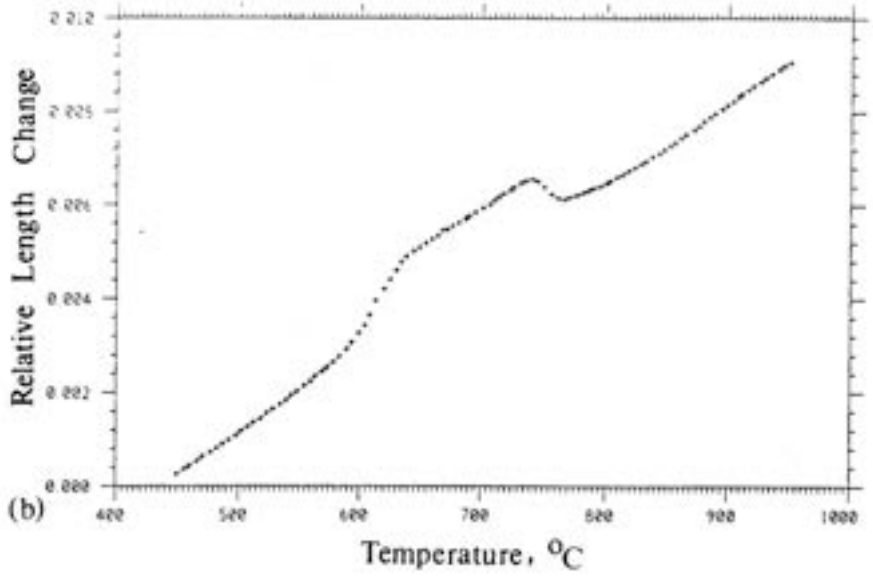

Figure VII.4(a) and (b) - Showing the relative length change versus temperature curves at heating rates, 0.06 and 0.15°C/s respectively, after isothermal transformation at 350°C for 10 minutes.

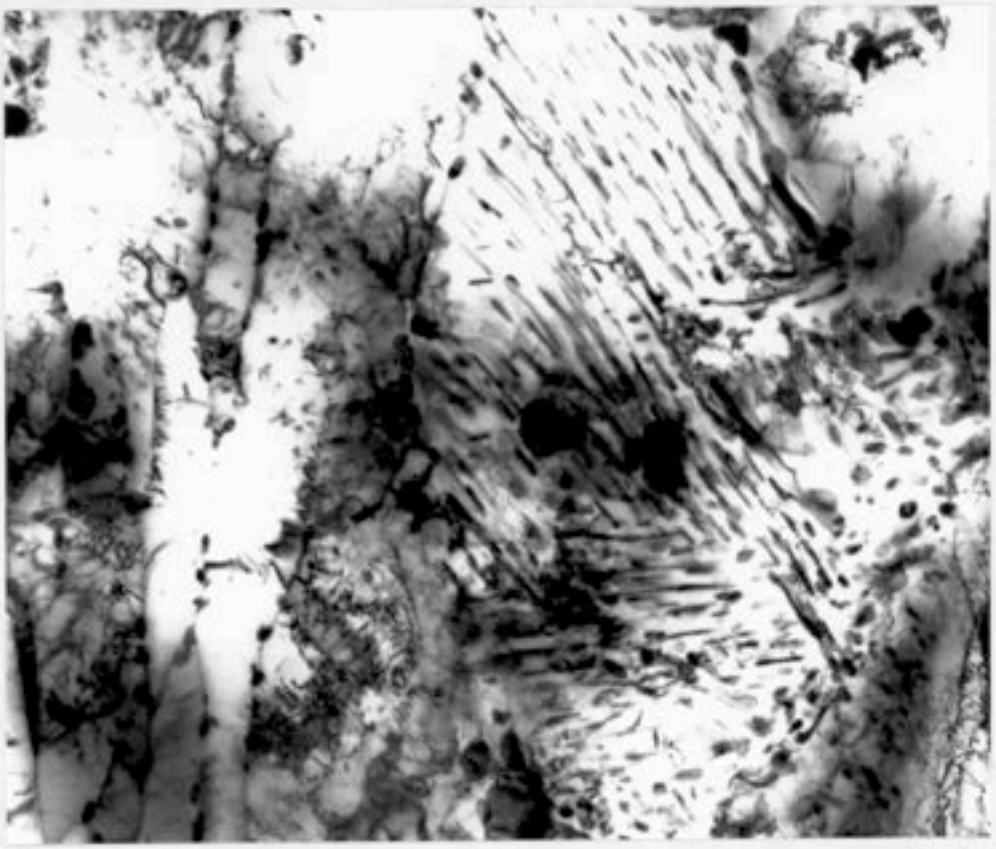

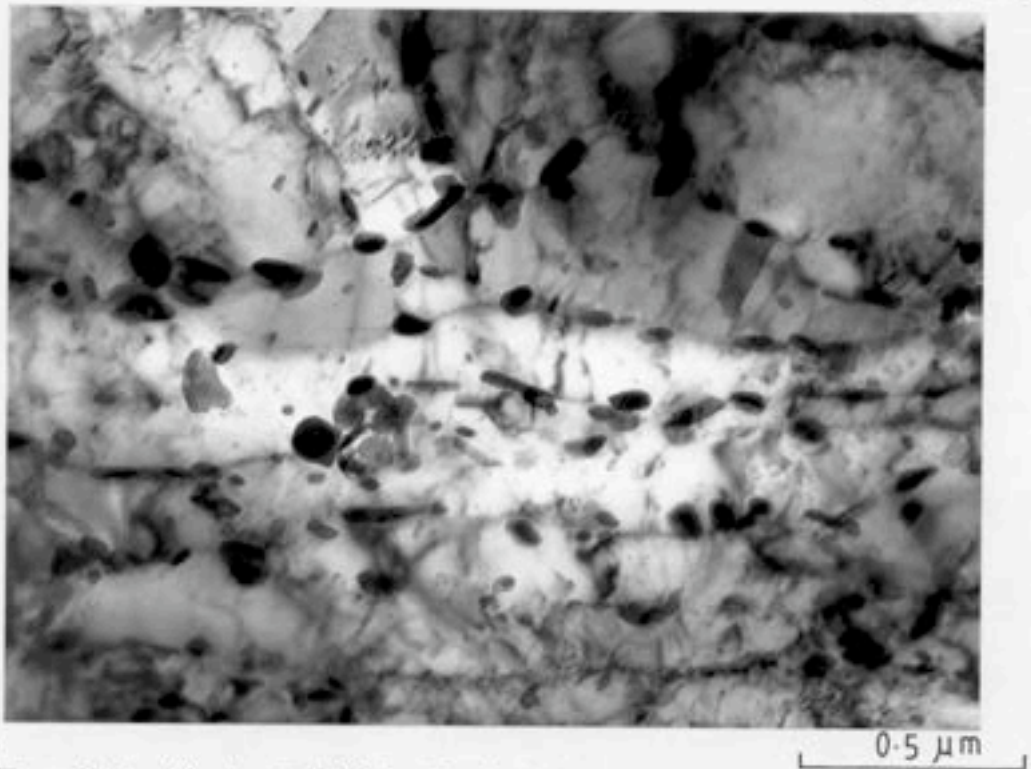

Figure VII.5 - 10 mins @ 950°C → 10 mins @ 350°C → continuous heating until 600°C (heating rate = 0.06°C/s) → quenched by helium gas. (a) Electron micrograph showing a pearlite-like microstructure. (b) Electron micrograph showing the discretely nucleated carbides.

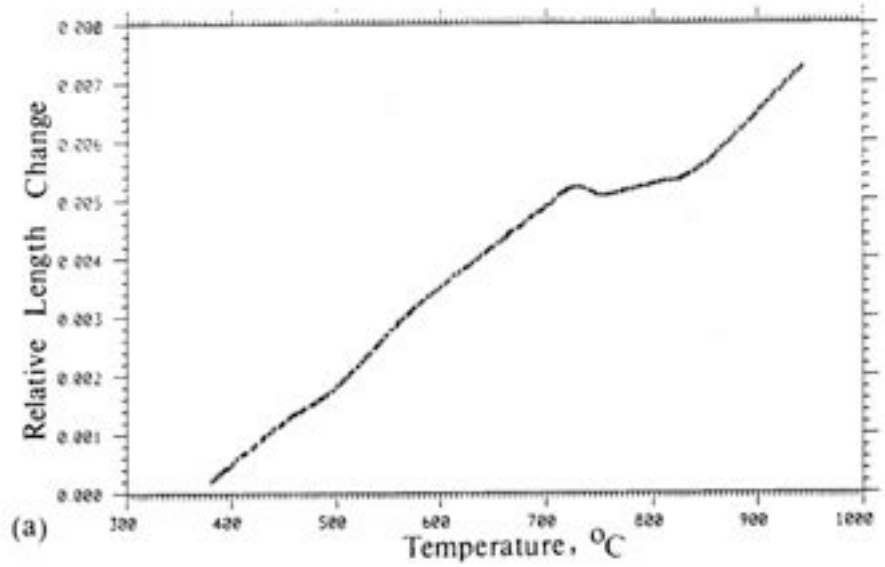

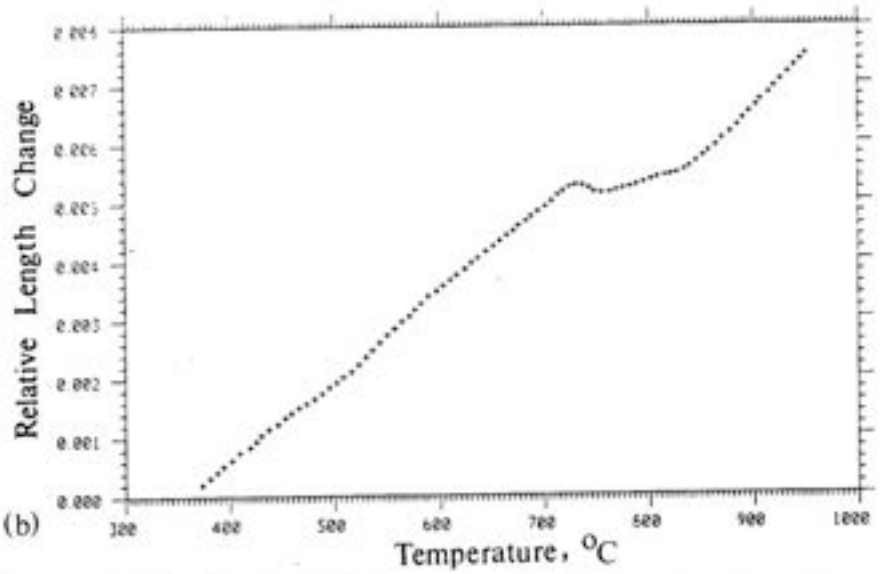

Figure VII.6(a) and (b) - Showing the relative length change versus temperature curves at heating rates 0.06 and 0.15°C/s respectively, after isothermal transformation at 350°C for 120 minutes.

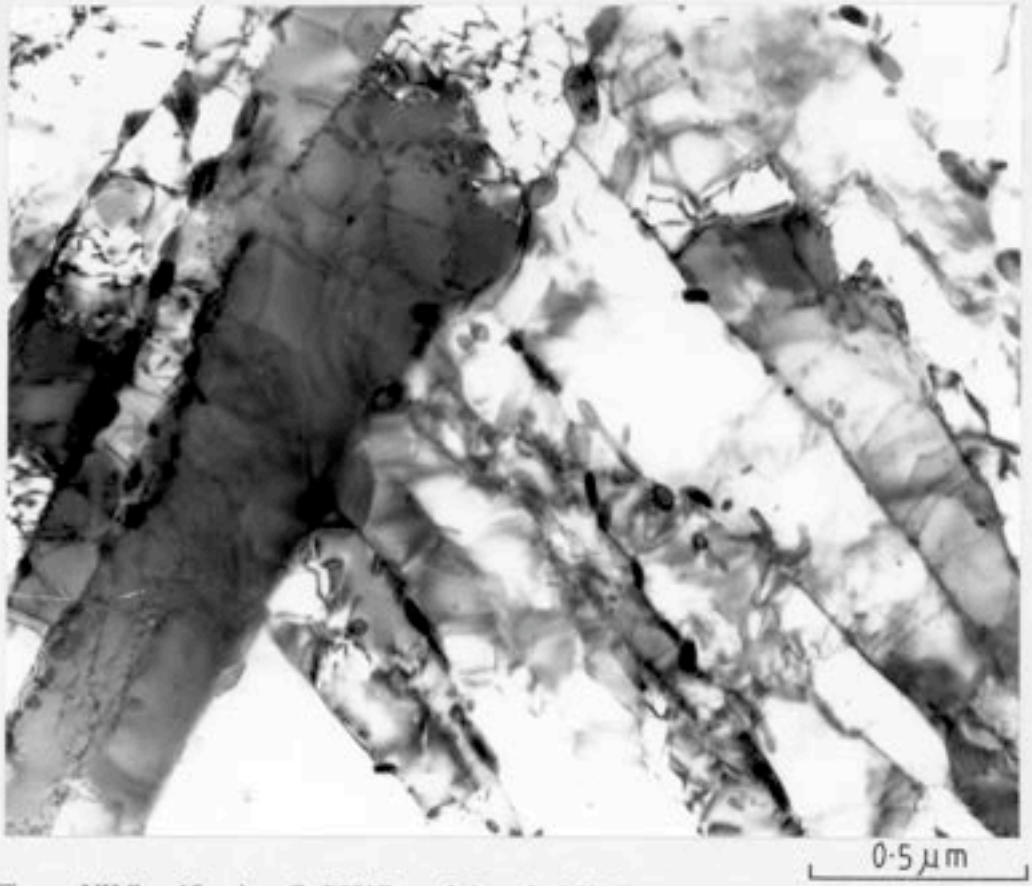

Figure VII.7 - 10 mins @ 950°C → 2 hrs @ 350°C → continuous heating until 600°C (heating rate = 0.06°C/s) → quenched by helium gas.

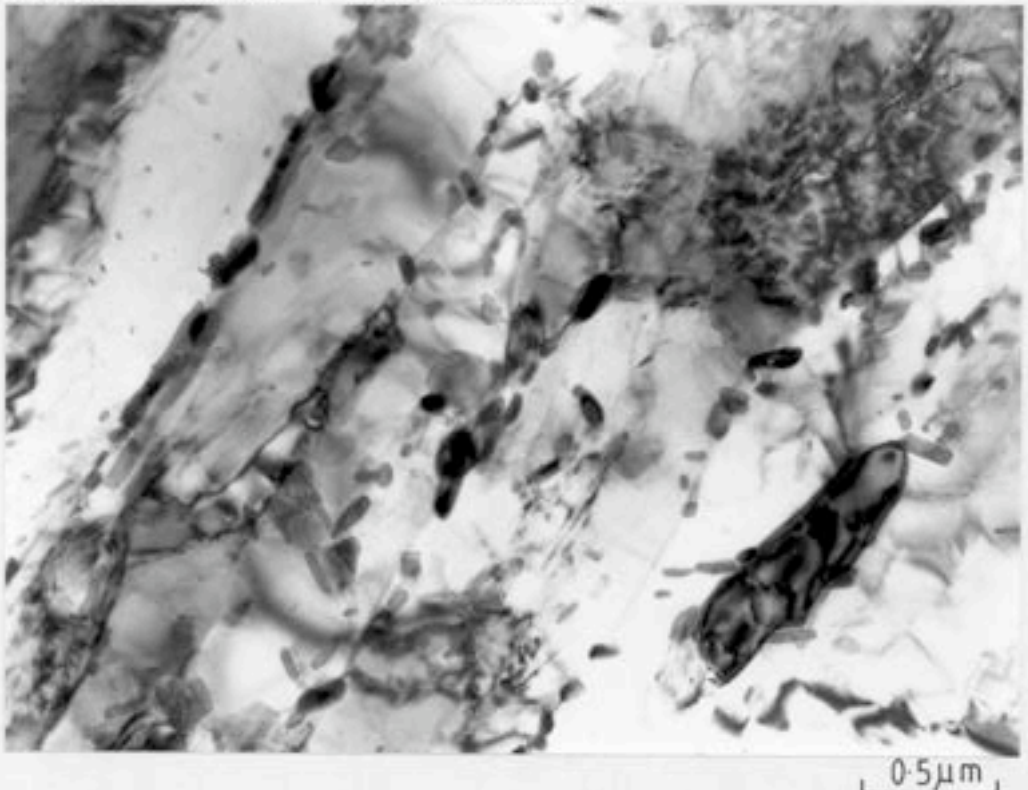

Figure VII.8 - 10 mins @ 950°C → 2 hrs @ 350°C → continuous heating until 700°C (heating rate = 0.06°C/s) → quenched by helium gas.

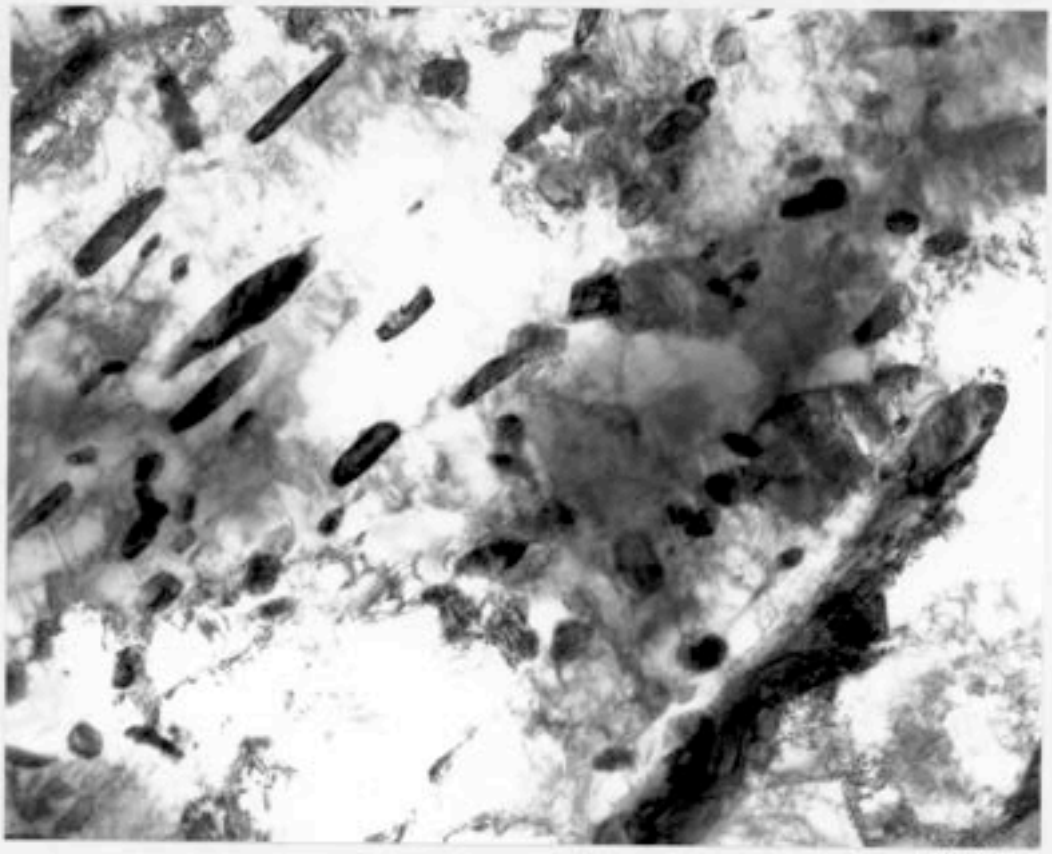

Figure VII.9 - 10 mins @ 950°C → 2 hrs @ 350°C → continuous heating until 730°C (heating rate = 0.06°C/s) → quenched by helium gas.

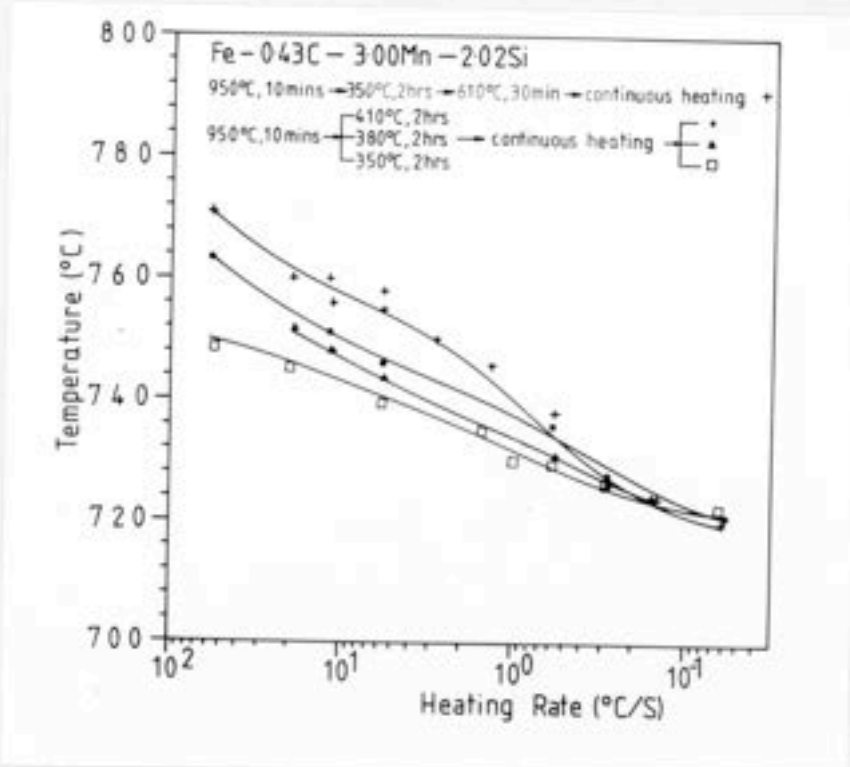

Figure VII.10 - Showing reaustenitisation start temperature versus heating rate for four different starting microstructures.

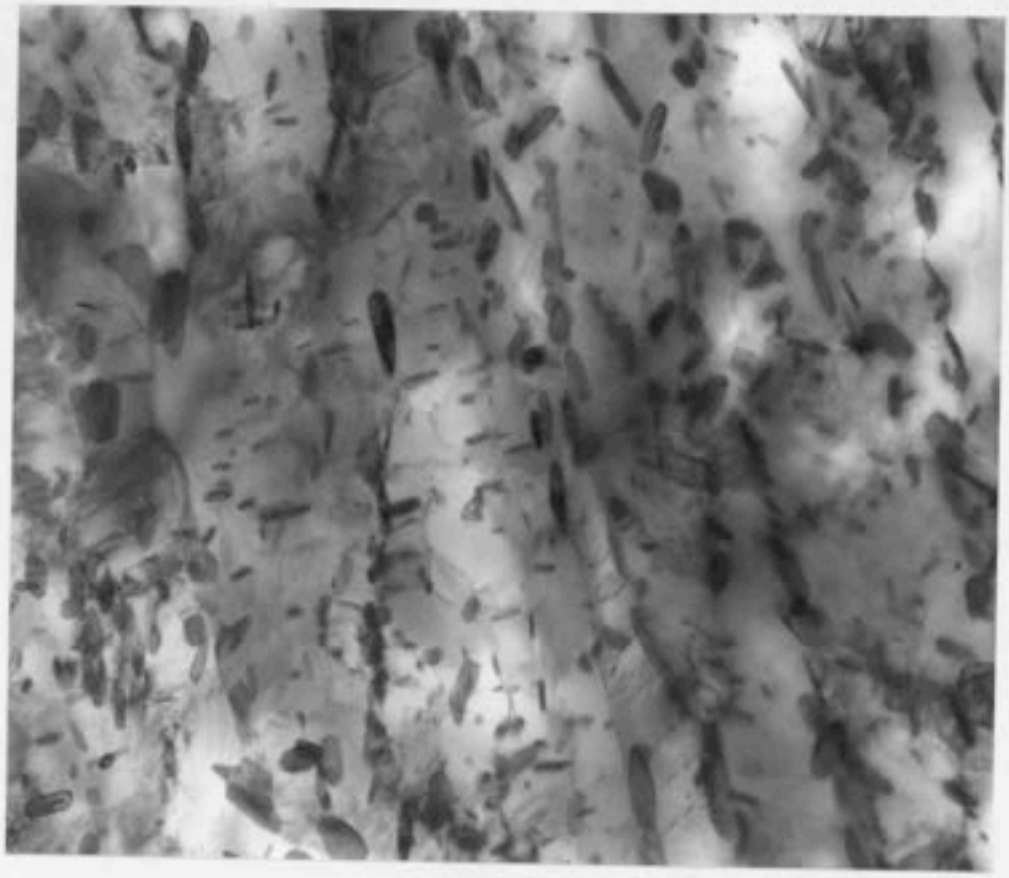

Figure VII.11 - Microstructure of tempered bainite formed by isothermal transformation at 350°C for 2 hrs, and subsequently tempered at 610°C for 30 minutes.

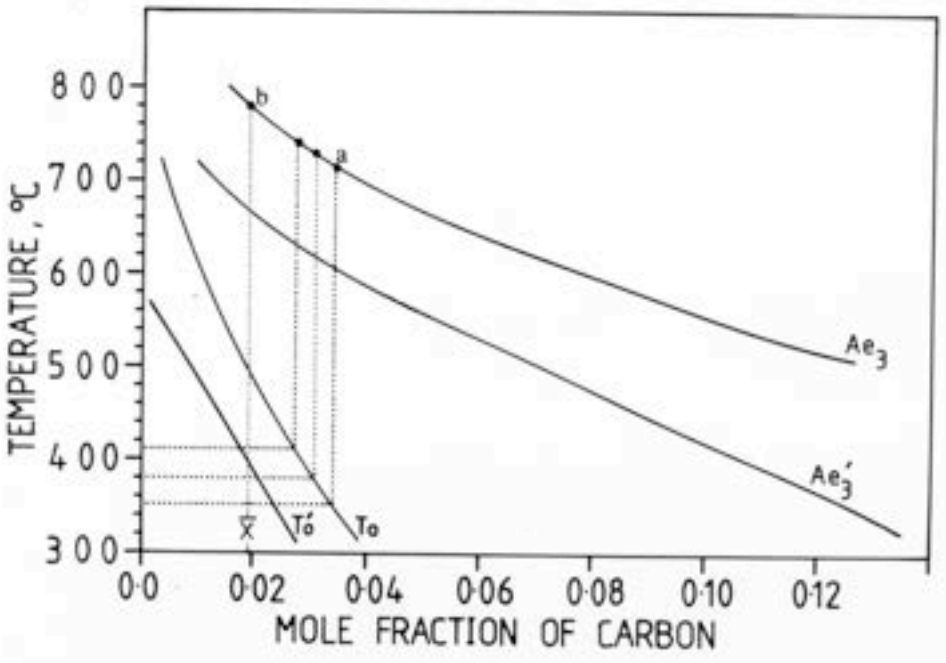

Figure VII.12 - Phase diagram showing the Ae_3, Ae'_3, T_o and T'_o for Fe-0.43C-3.00Mn-2.02Si, wt.% alloy. The Ae'_3, T_o and T'_o curves are calculated as in Ref. 89,100, and the Ae_3 curve is calculated as in Ref. 181. ($\bar{x}$ is the average carbon content of the alloy).

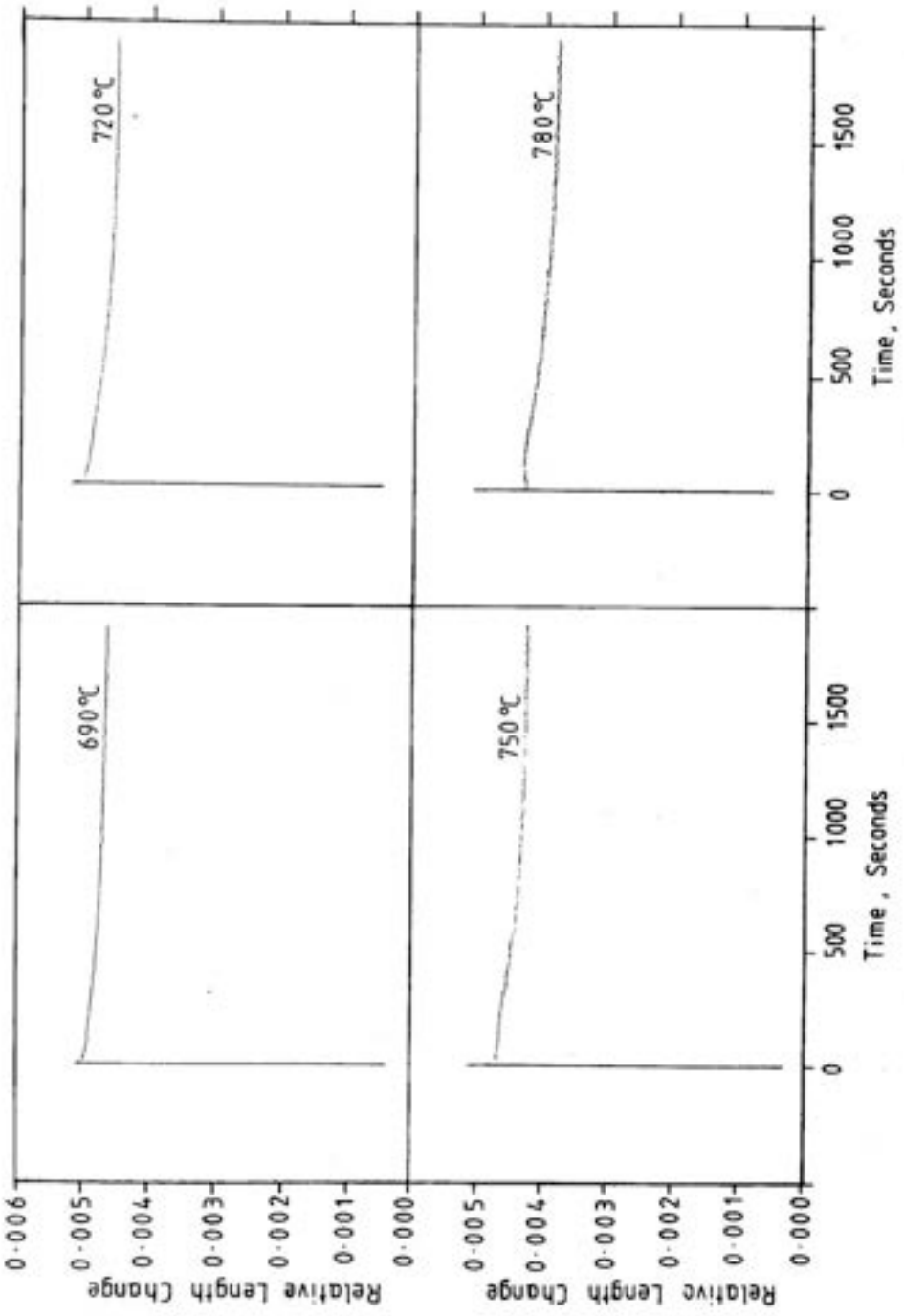

Figure VII.13 - Dilatometric curves showing isothermal reaustenitisation.

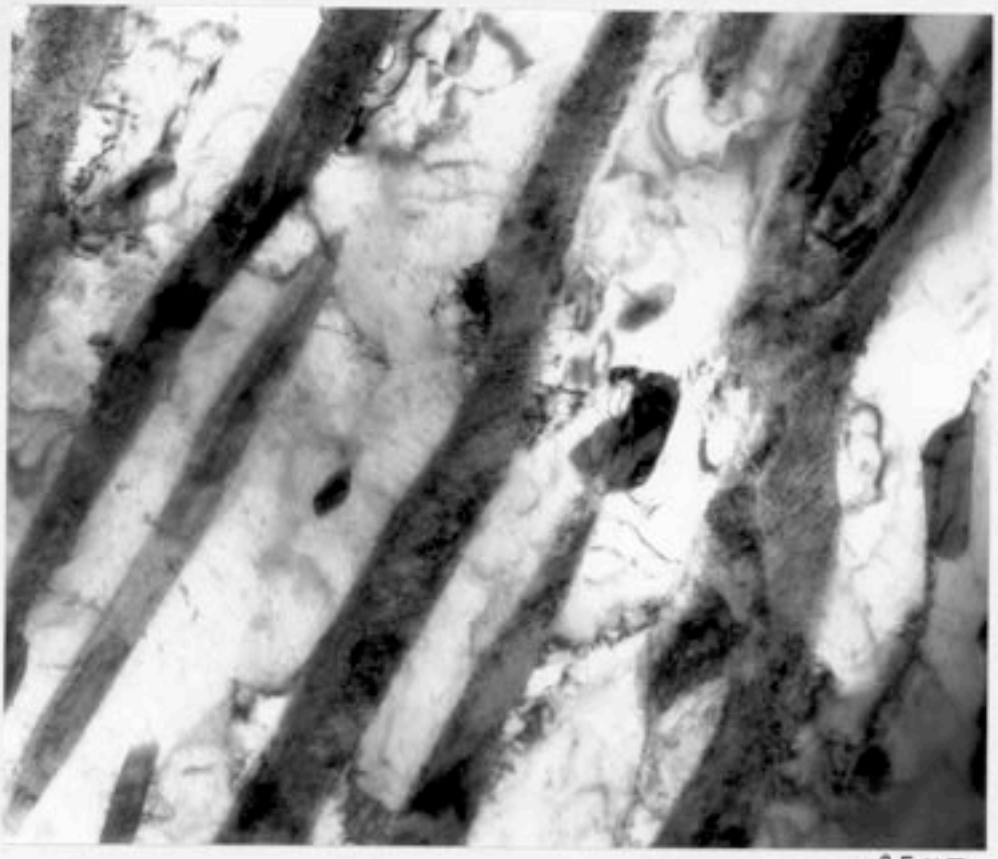

Figure VII.14a - Electron micrograph showing decomposition of austenite into carbide. (10 mins @ 950°C → 2 hrs @ 350°C → 2 hrs @ 690°C → quenched by helium gas).

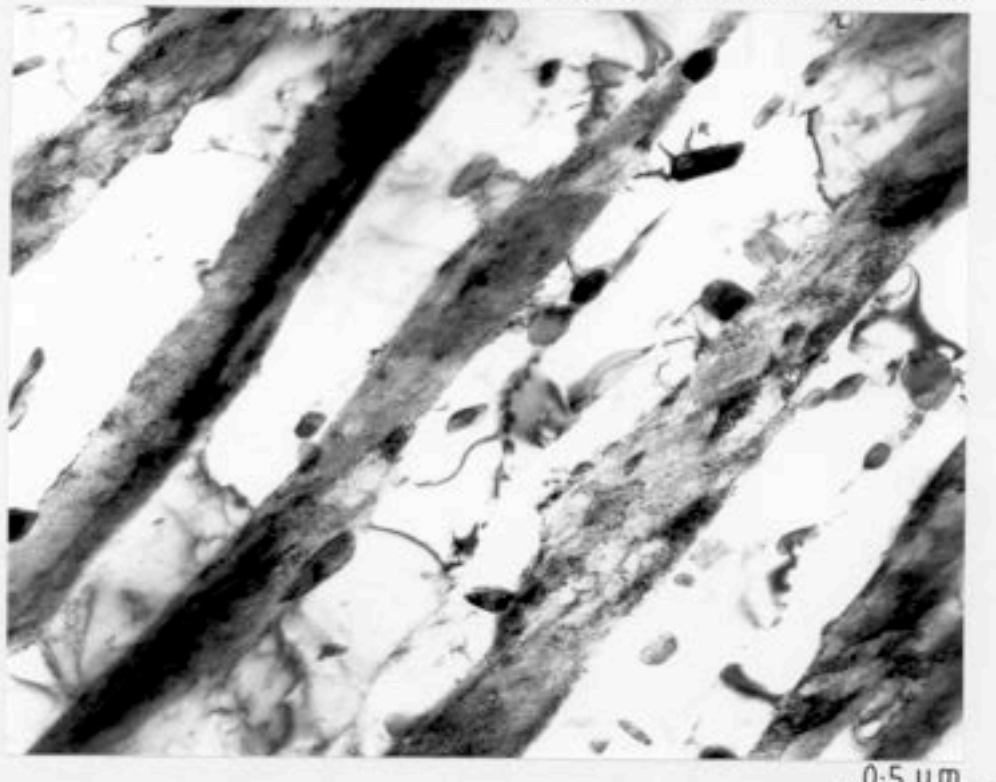

Figure VII.14b - Electron micrograph showing decomposition of austenite into carbide. (10 mins @ 950°C → 2 hrs @ 350°C → 2 hrs @ 710°C → quenched by helium gas).

Figure VII.14c - 10 mins @ 950°C → 2 hrs @ 350°C → 2 hrs @ 720°C → quenched by helium gas.

Figure VII.14d - 10 mins @ 950°C → 2 hrs @ 350°C → 2 hrs @ 750°C → quenched by helium gas.

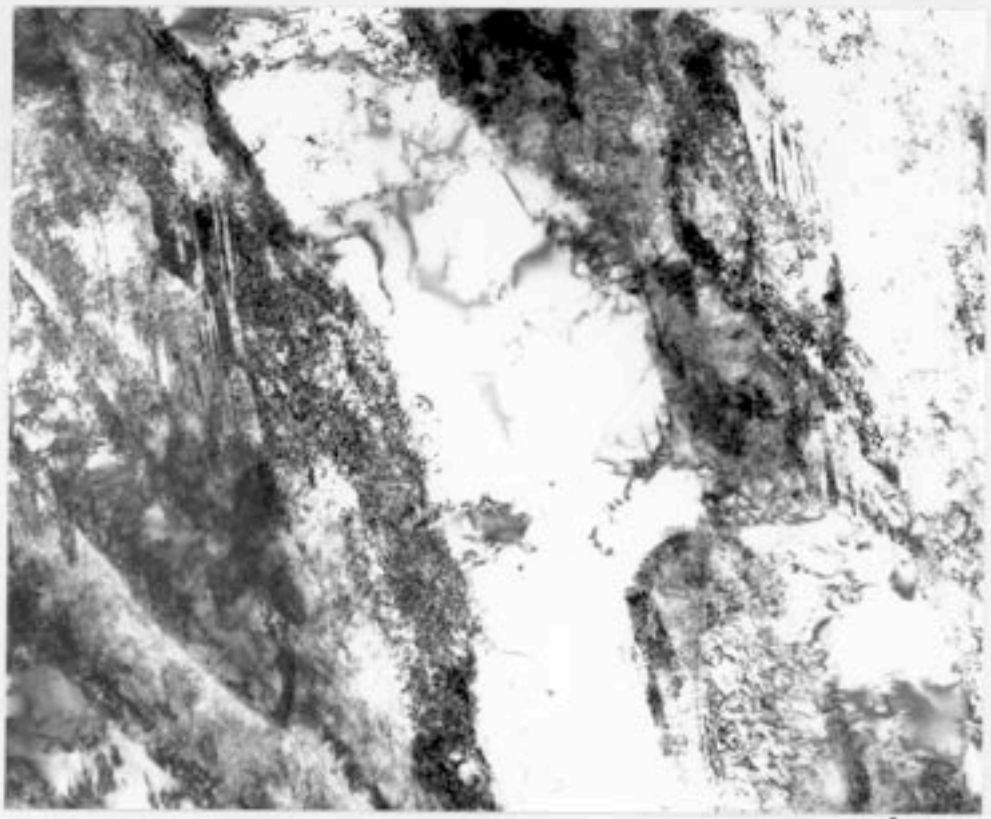

Figure VII.14e - 10 mins @ 950°C → 2 hrs @ 350°C → 2 hrs @ 780°C → quenched by helium gas.

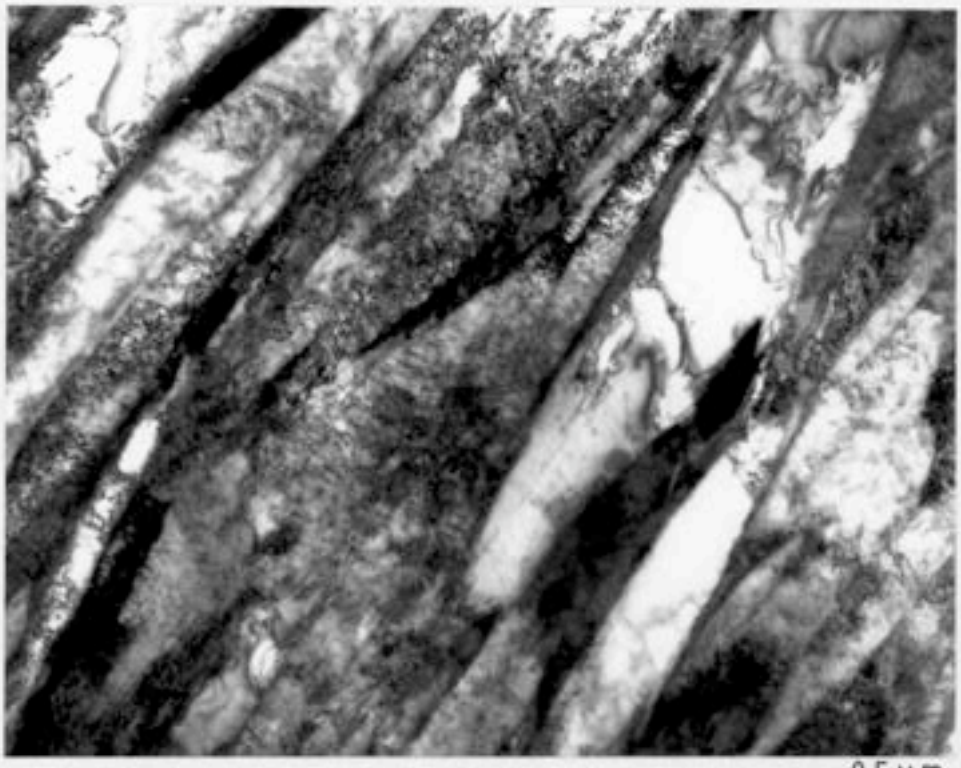

Figure VII.14f - 10 mins @ 950°C → 2 hrs @ 350°C → 2 hrs @ 800°c → quenched by helium gas.

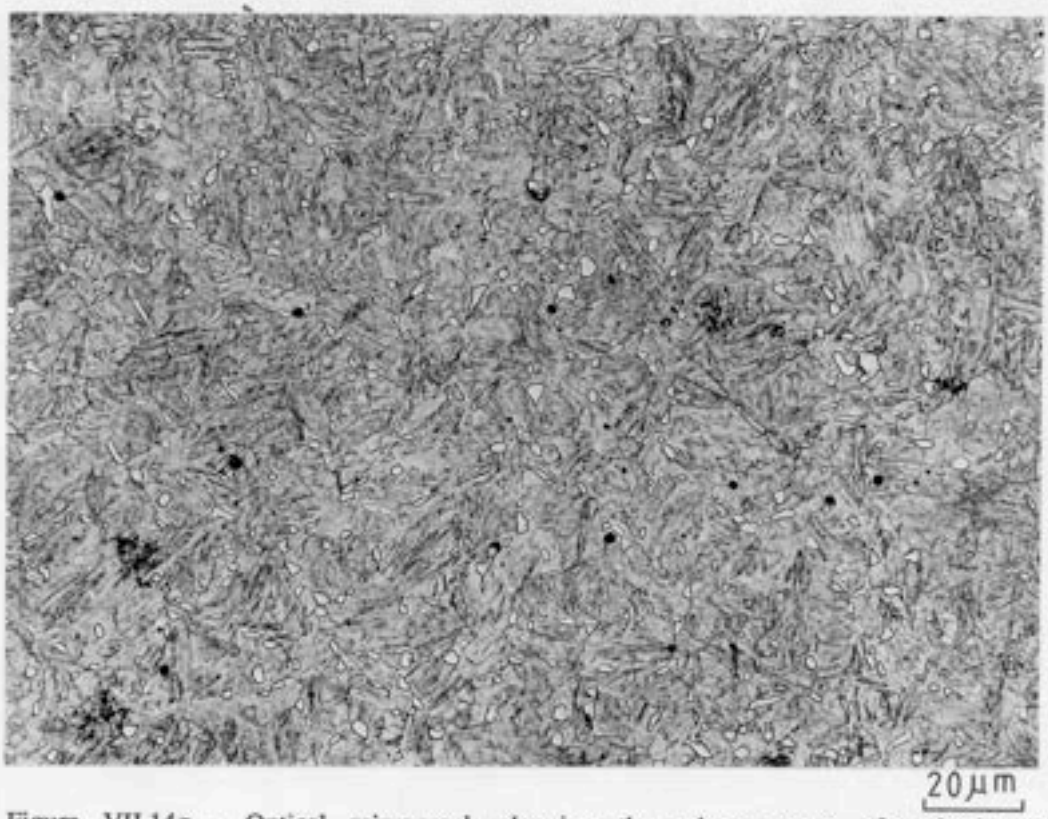

Figure VII.14g - Optical micrograph showing the microstructure after isothermal reaustenitisation at 820°C for 2 hrs. (10 mins @ 950°C → 2 hrs @ 350°C → 2 hrs @ 820°C → quenched by helium gas).

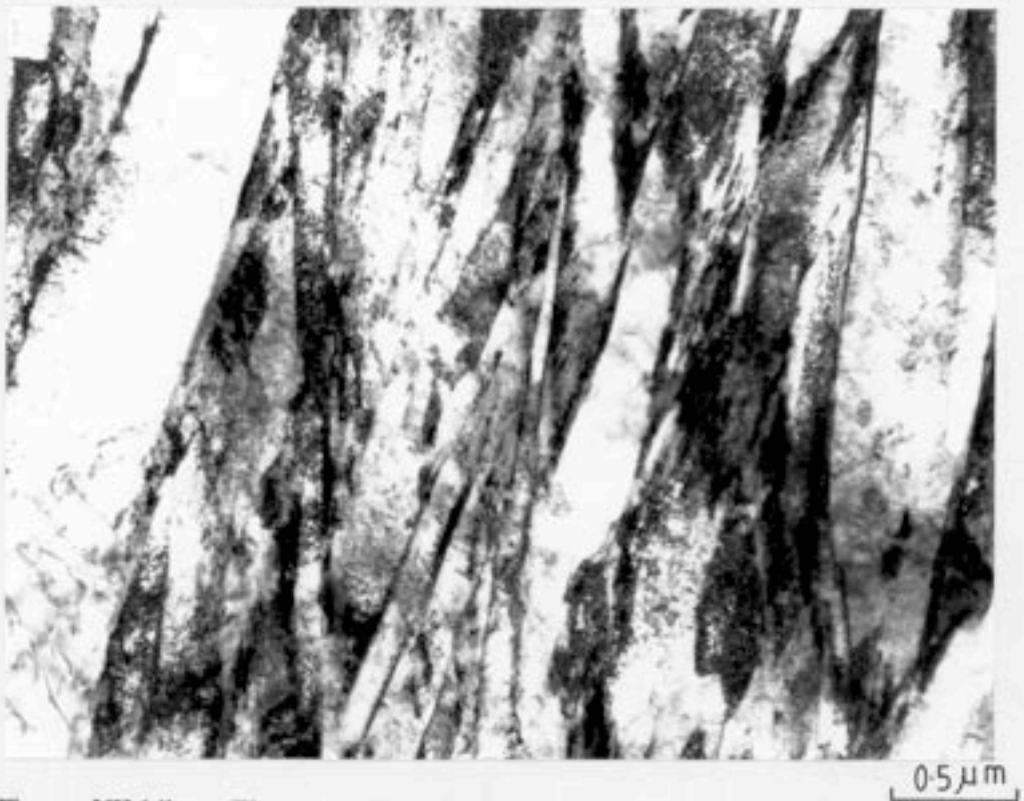

Figure VII.14h - Electron micrograph showing the microstructure after isothermal reaustenitisation at 820°C for 2 hrs. (10 mins @ 950°C → 2 hrs @ 350°C → 2 hrs @ 820°C → quenched by helium gas).

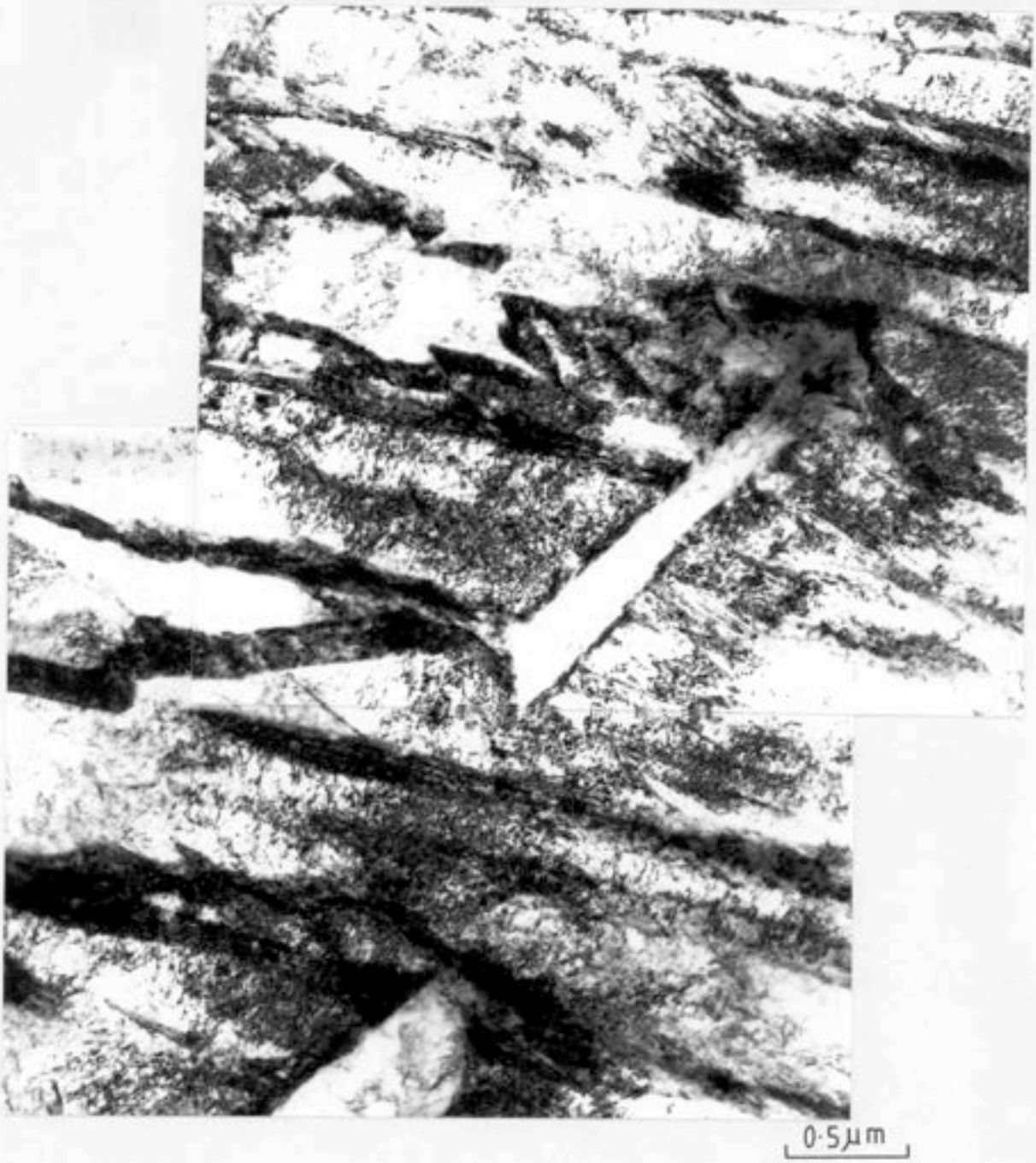

Figure VII.14i - Electron micrograph showing the microstructure after isothermal reaustenitisation at 835°C for 6.5 hrs. (10 mins @ 950°C → 2 hrs @ 350°C → 6.5 hrs @ 835°C → quenched by helium gas). A little amount of ferrite can still be found.

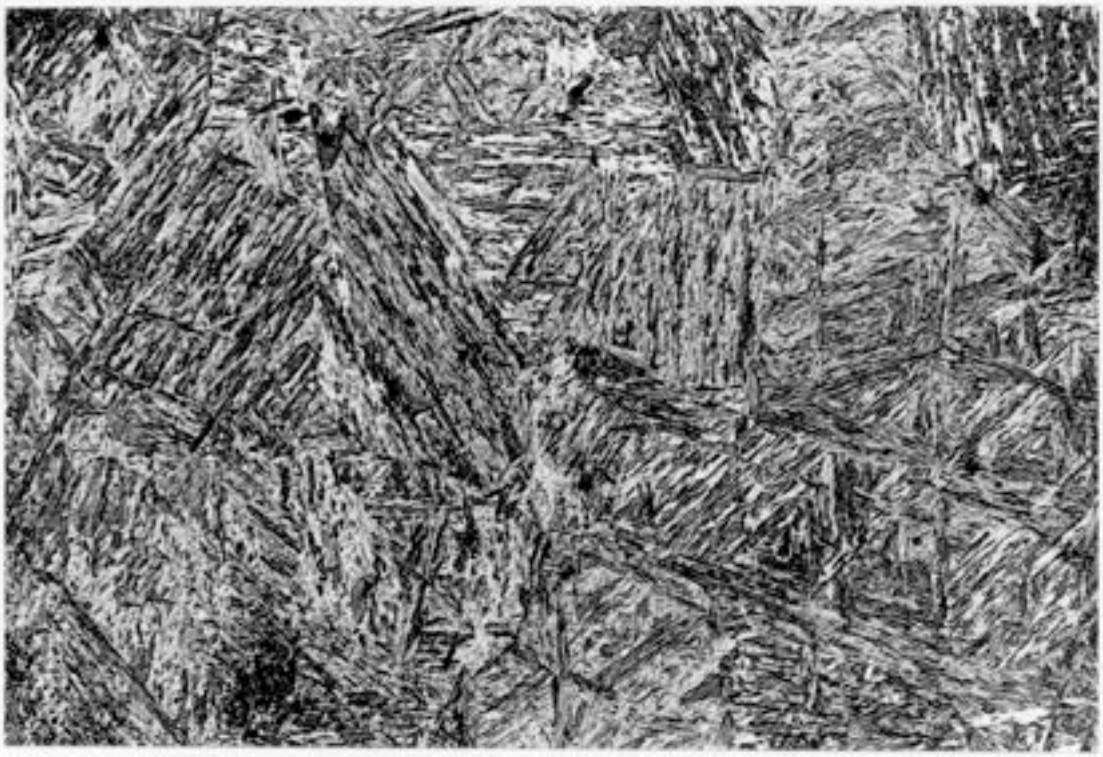

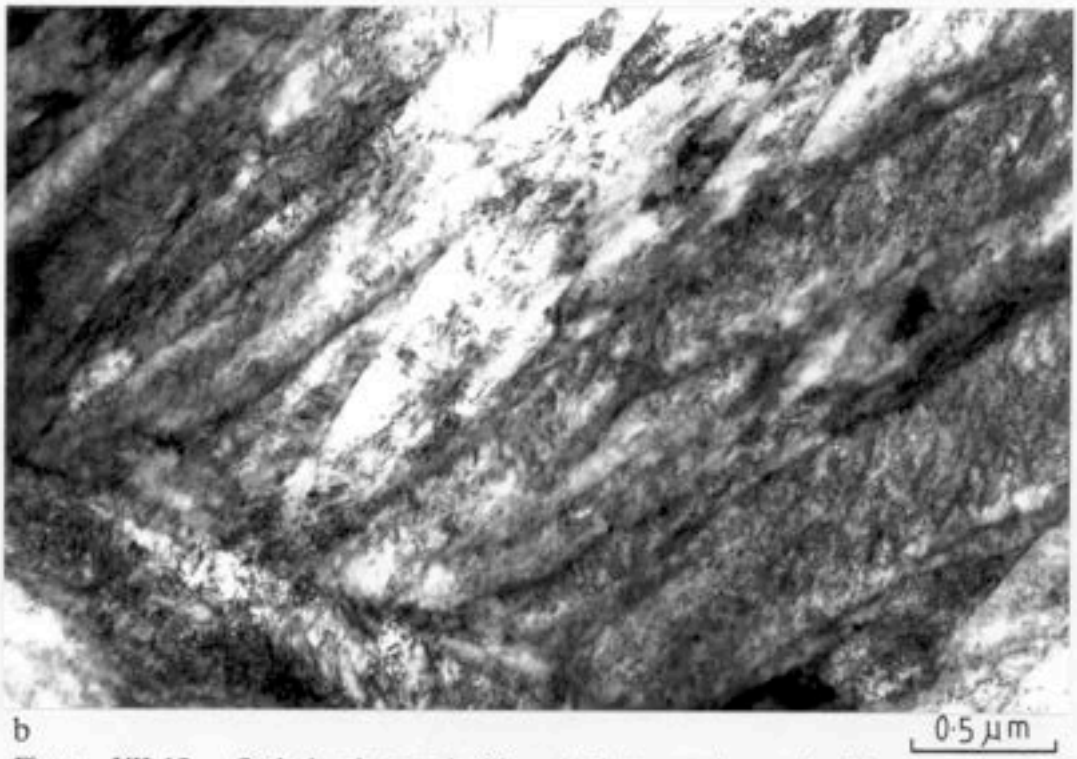

Figure VII.15 - Optical micrograph (a) and electron micrograph (b) show the full martensite structure. (10 mins @ 950°C → 2 hrs @ 350°C → 168 hrs @ 780°C → water quench).

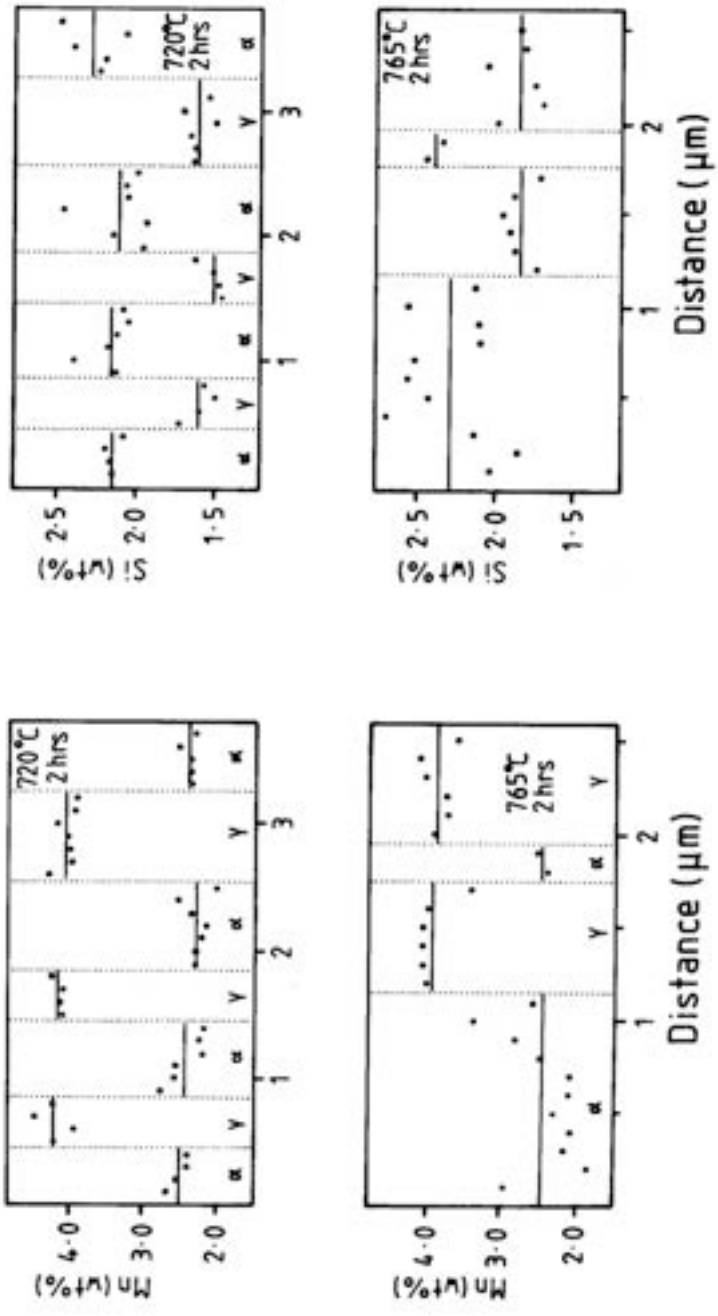

Figure VII.16(a) - Microanalytical data obtained using energy dispersive X-ray analysis on a Philips EM400T for specimens reaustenitised.

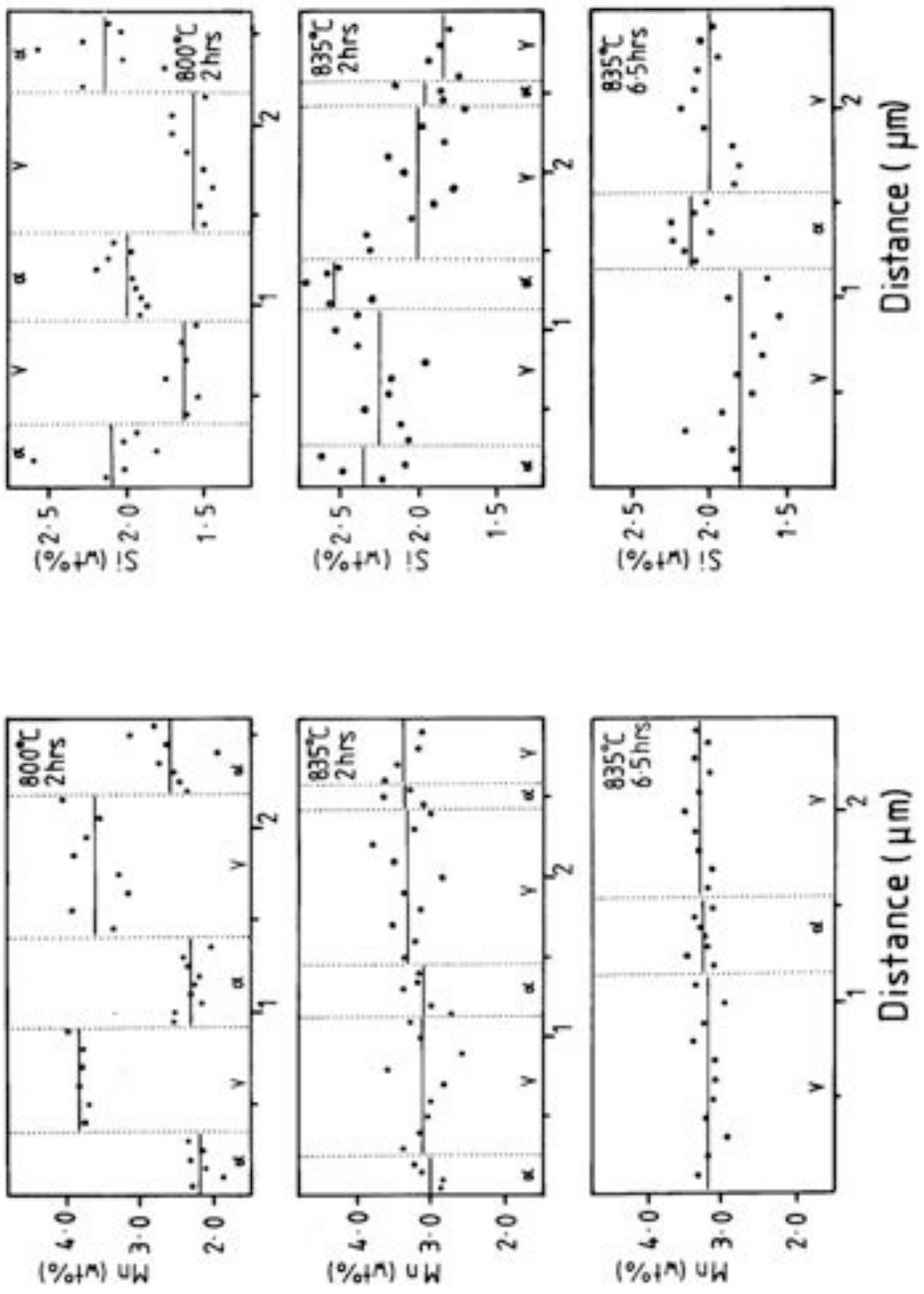

Figure VII.16(b) - Microanalytical data obtained using energy dispersive X-ray analysis on a Philips EM400T for specimens reaustenitised.

Table VII.1 - Microanalytical data (wt.%, error = ± 0.20) for the γ and α during reaustenitisation from starting microstructure $\alpha_b + \gamma$.

Temp.(°C)	Time(hr)	MN γ	Mn α	Si γ	Si α
720	2	4.11	2.37	1.58	2.15
765	2	3.91	2.42	1.85	2.31
800	2	3.70	2.37	1.58	2.04
835	2	3.21	3.18	2.09	2.25
835	6.5	3.22	3.20	1.86	2.08

Figure VII.17 - 10 mins @ 950°C → 2 hrs @ 350°C → 42.7 hrs @ 600°C.

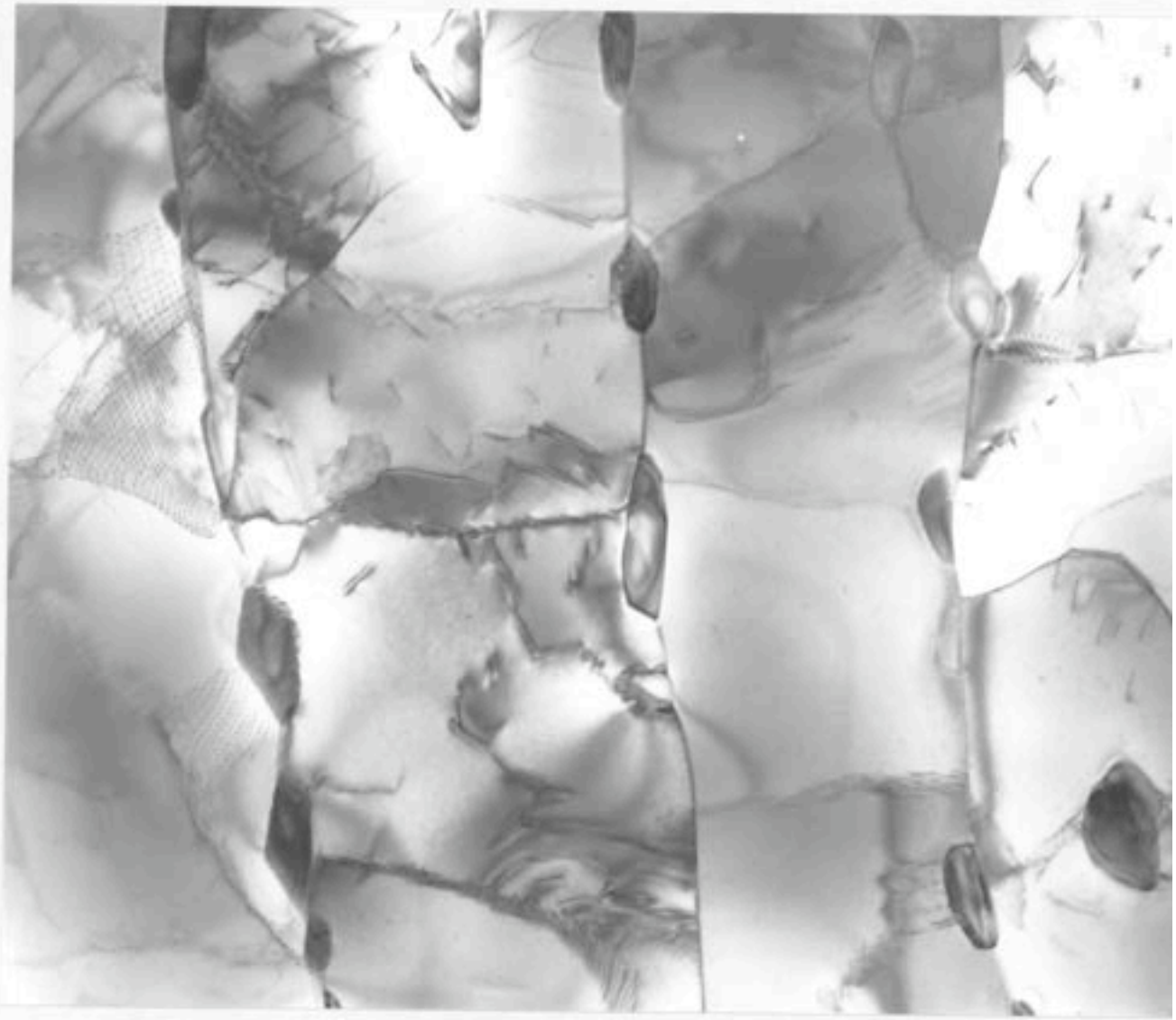

Figure VII.18 - Electron micrograph showing that the cementite particles are located at the gain boundaries of extensively recovered ferrite. Mesh-like subgrain boundaries are displayed in the left side of the micrograph. (10 mins @ 950°C → 2 hrs @ 350°C → 14 days @ 680°C).

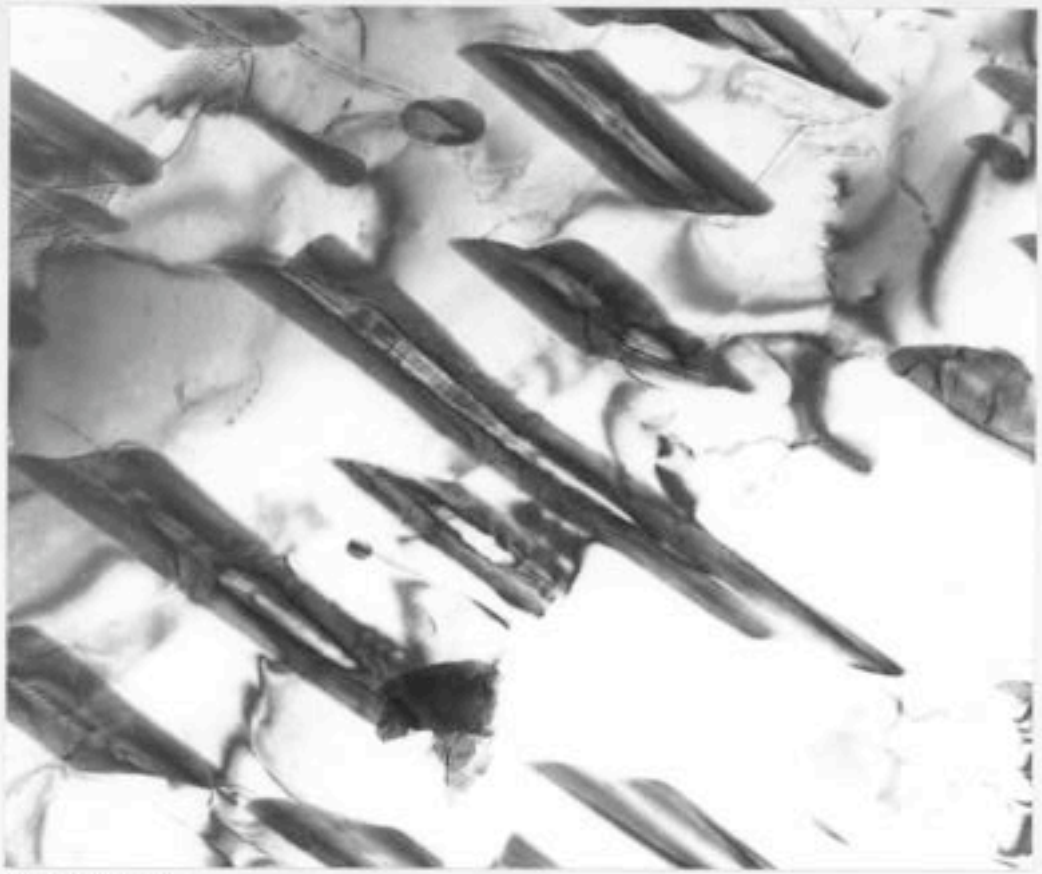

Figure VII.19a

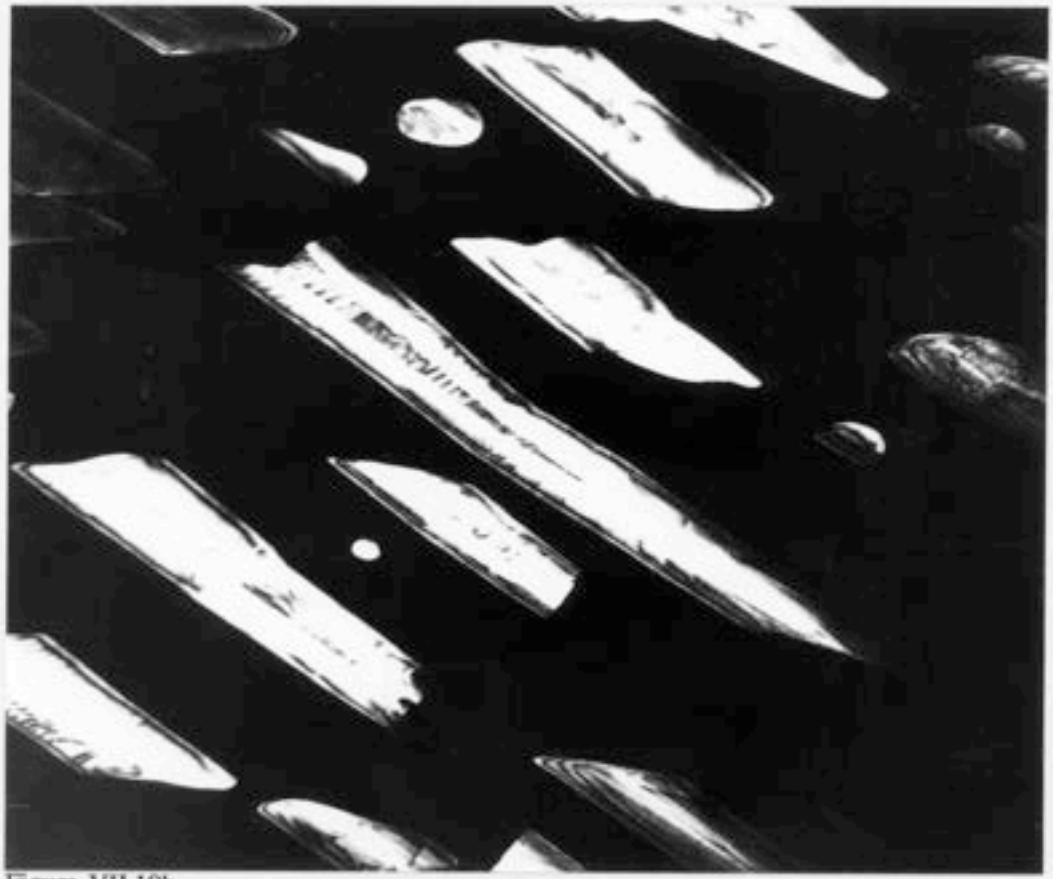

Figure VII.19b

0·5 µm

c

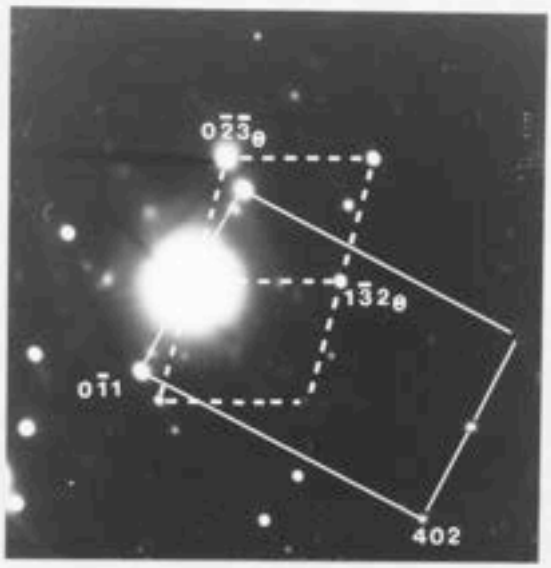

d

Figure VII.19:
10 mins @ 950°C → 2 hrs @ 350°C → 30 mins @ 600°C → 25 mins @ 715°C.
(a) Bright field image.
(b) Cementite dark field image using $(0\bar{2}\bar{3})_\theta$ reflection.
(c) Corresponding diffraction pattern.
(d) Interpretation of (c).

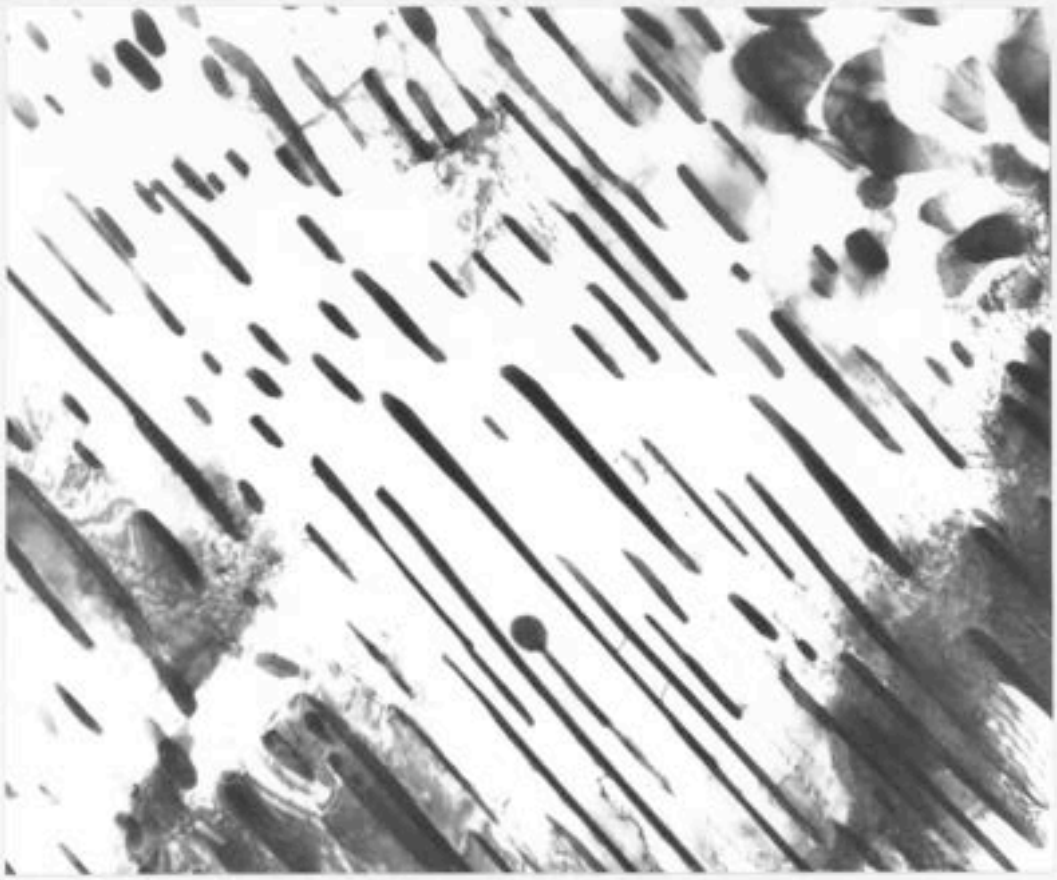

a

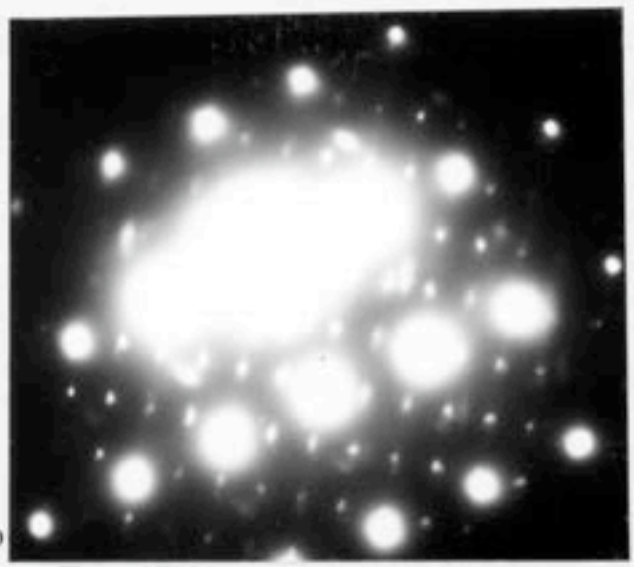

b

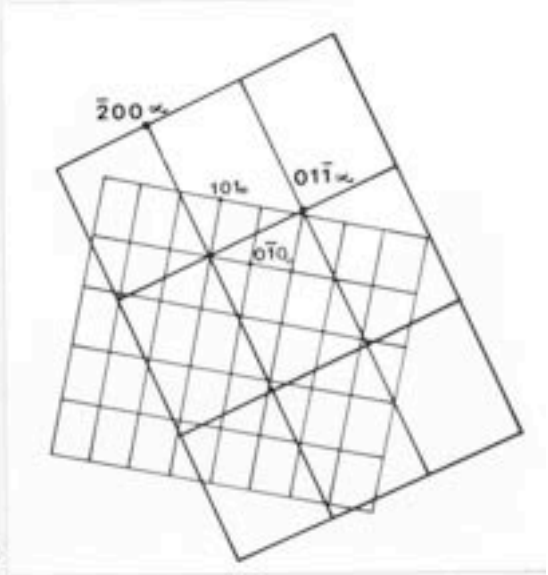

c

Figure VII.20:
10 mins @ 950°C → 2 hrs @ 350°C → 30 mins @ 600°C → 25 mins @ 715°.
(a) Bright field image.
(b) Corresponding diffraction pattern.
(c) Interpretation of (b).

Figure VII.21a

Figure VII.21b

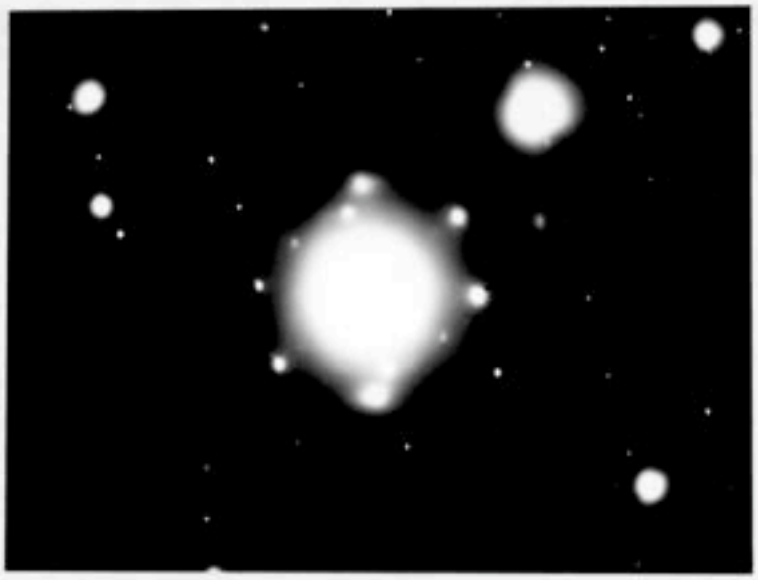

Figure VII.21c

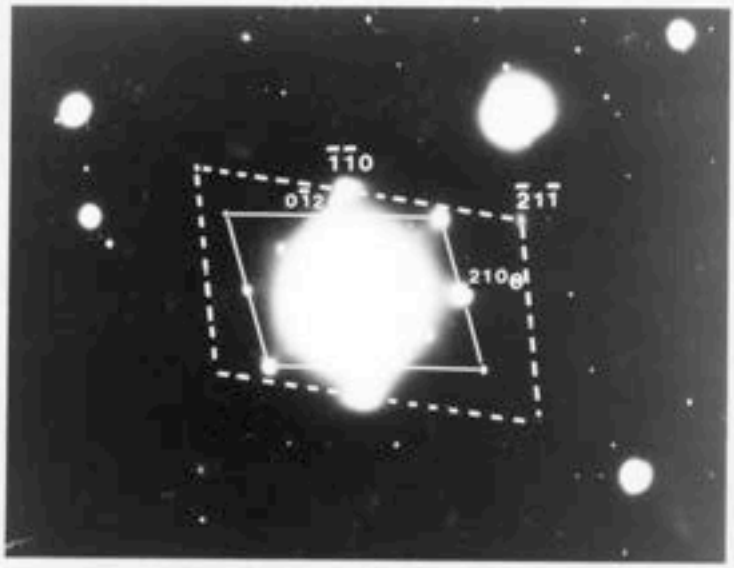

Figure VII.21d

Figure VII.21:
10 mins @ 950°C → 2 hrs @ 350°C → 30 mins @ 600°C → 25 mins @ 715°C.
(a) Bright field image.
(b) Cementite dark field image using $(210)_\theta$ reflection.
(c) Corresponding diffraction pattern.
(d) Interpretation of (c).

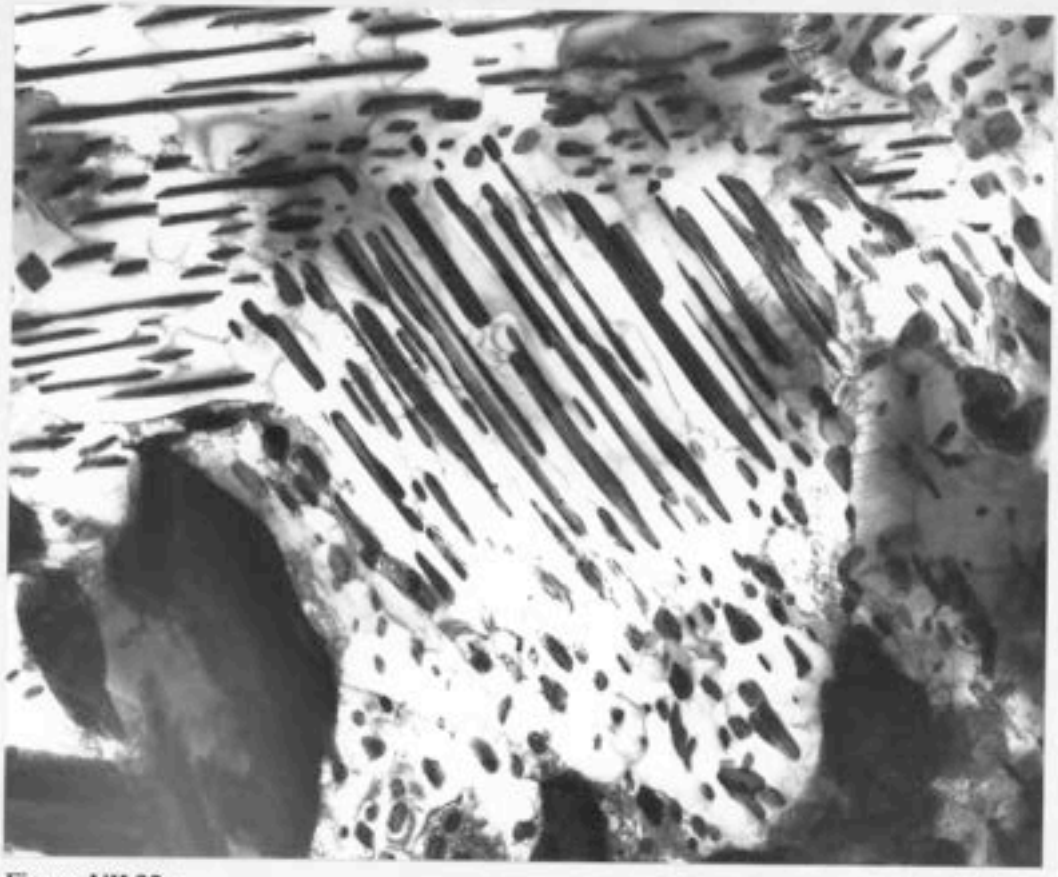

Figure VII.22a

Figure VII.22b

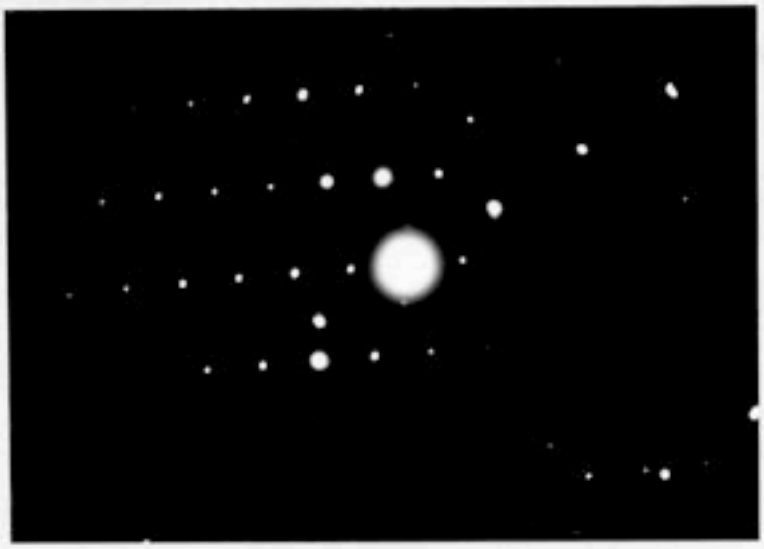

Figure VII.22c

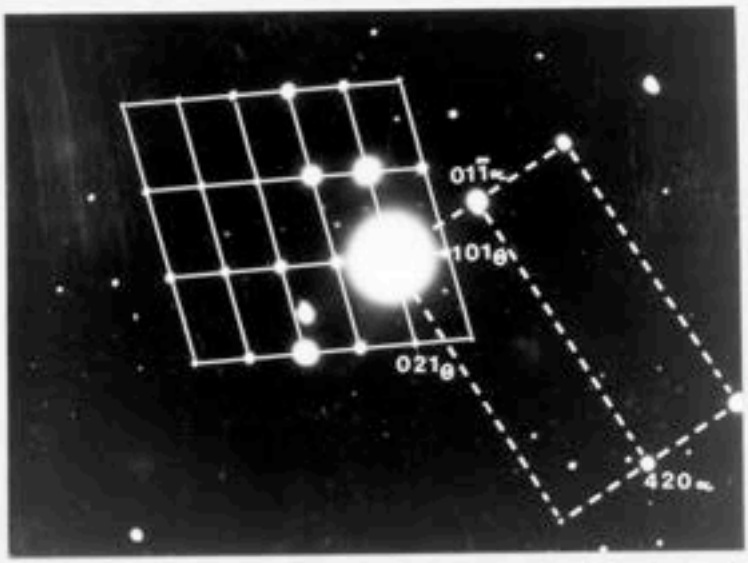

Figure VII.22d

Figure VI.22
10 mins @ 950°C → 2 hrs @ 350°C → 30 mins@ 600°C → 25 mins @ 715°C.
(a) Bright field image.
(b) Cementite dark field images using $(0\bar{2}\bar{1})_\theta$ reflection.
(c) Corresponding diffraction pattern.
(d) Interpretation of (c).

Figure VII.23a

Figure VII.23b

1·0 µm

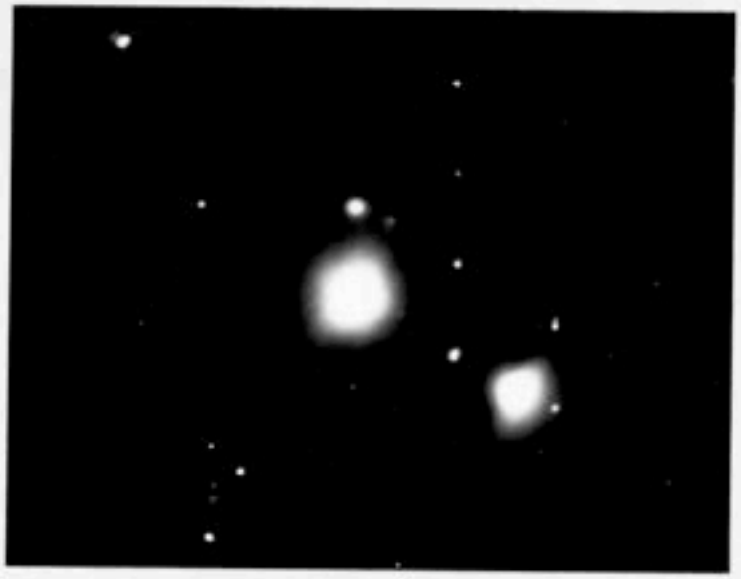

Figure VII.23c

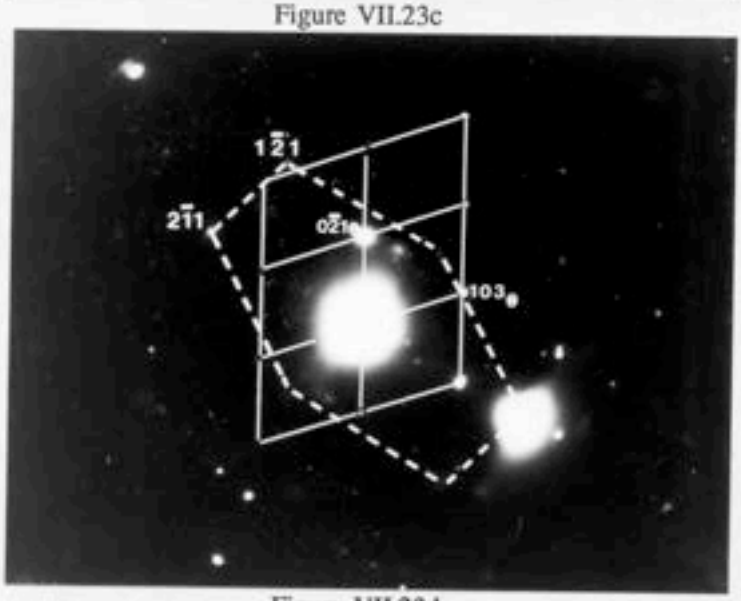

Figure VII.23d

Figure VII.23
10 mins @ 950°C → 2 hrs @ 350°C → 30 mins @ 600°C 25 mins @ 715°C.
(a) Bright field image.
(b) Cementite dark field image using $(0\bar{2}1)_\theta$ reflection.
(c) Corresponding diffraction pattern.
(d) Interpretation of (c).

Chapter Eight

The Microstructure of Heat Affected Zone

8.1 Introduction

During welding, microstructural changes occur within the heat affected zone (HAZ) of the base plate surrounding the molten weld-bead. Grain growth and the formation of martensite in this region are serious problems as far as mechanical properties are concerned. The larger austenite grain size displaces the C.C.T. curve to longer reaction times producing more Widmanstätten ferrite, or increasing the possibility of martensitic or bainitic transformation products on cooling. Although some work has been done [141-146] on the study of microstructure in HAZ, a model for directly predicting the microstructure has not yet been developed. At this stage, it is important to rationalise quantitatively the kinetics of austenite transformation, which depend on its grain size and chemical composition.

In this work, a low alloy steel has been investigated, and its composition is Fe-0.17C-0.33Si-1.42Mn (wt%). The microstructure of its heat affected zone has been examined and the kinetics of austenite transformation for different grain sizes also studied experimentally.

8.2 The Microstructure of the Heat Affected Zone in a Low Alloy Steel

The microstructure of the heat affected zone studied was taken from the parent plate of a high-strength weld. The plate thickness was 20mm and the arc energy was about ≈ 2 kJ/mm. The details of the welding technique used have been mentioned in Section 2.1, and are not restarted here. Figure VIII.1 shows the macrograph of the heat affected zone adjacent to the capping layer of the multirun weld (see the low magnification macrograph, Figure II.4). The austenite grain size near the fusion boundary is very large, of the order of 200μm. The corresponding detailed microstructures in different regions of Figure VIII.1 are shown in Figure VIII.2a-j. (For example, Figure VIII.2a corresponds to the region marked a and Figure VIII.2b corresponds to the region marked b in Figure VIII.1, etc.) It is apparent that in the coarse austenite grain zone, the Widmanstätten ferrite grows mainly from the allotriomorphic ferrite-austenite boundaries in the form of secondary Widmanstätten ferrite plates. The microstructure in this zone also contains large amounts of martensite, with some allotriomorphic ferrite and Widmanstätten ferrite, making the zone brittle, and susceptible to cold cracking and reheat cracking. As the austenite grain size decreases (Figure VIII.2c), the amount of allotriomorphic ferrite increases significantly simply because of the large interfacial area of austenite grain boundaries

available for allotriomorphic ferrite nucleation and growth. Figure VIII.2c illustrates the transition from the coarse austenite grain zone to a more refined structure. The micrograph also shows that when the austenite grain size is smaller than a critical value (≈20μm), the Widmanstätten ferrite and martensite do not form, the transformation products being just allotriomorphic ferrite and fine pearlite (the presence of fine pearlite has been established by transmission electron microscopy as shown in Figure VIII.3). The typical microstructure of the fine grained region is presented in Figure VIII.2d, consisting of allotriomorphic ferrite and fine pearlite. Figure VIII.2e clearly shows the transition from the austenite grain refined region to a partially transformed region; the peak temperature of this transition boundary is Ar_3. Some of the untransformed original pearlite in this region has been spheroidised, as illustrated in Figure VIII.2f. Figure VIII.2g displays the transition boundary (peak temperature Ar_1) from the partially transformed zone to the tempered zone. The pearlitic colonies in this tempered zone (Figure VIII.2h) are spheroidised to a lesser extent than in the partially transformed zone consistent with the lower temperature experienced. The detailed microstructure of the pearlite colonies in the tempered zone has been examined by transmission electron microscopy (Figure VIII.4). The electron micrograph shows that the lamellar cementite has been partially spheroidised. The transition boundary from the tempered zone to unaffected zone is of coarse rather diffuse and is shown in Figure VIII.2i. The cementite layers of course pearlite (Figure VIII.2j) can clearly be seen in the unaffected base material which contains about 0.75 volume fraction of ferrite and 0.25 volume fraction of pearlite.

The austenite grain size in the heat affected zone has been measured using a linear intercept method. Because austenite grains adjacent the fusion boundary are very large, only fifteen of them could be taken into account. The plot of austenite grain size versus distance from the fusion boundary is presented in Figure VIII.5. Hardness measurements were made on the polished and etched specimens, using a Vicker's micro-hardness machine. A load of 0.5 kg was used, and the indentation was large enough to cover the specific representative microstructure in the different sub-zone of the HAZ. The hardness profile in the HAZ adjacent to the capping layer of the multirun weld is shown in Figure VIII.6. It is clear that the hardness increases with austenite grain size and reaches a maximum value near the fusion boundary. The hardness of the partially transformed zone and the tempered zone are slightly higher than that of the unaffected base plate.

8.3 The Influence of Austenite Grain Size on the Kinetics of Transformation

In order to predict the microstructure of the heat affected zone, a knowledge of transformation kinetics is vital. The work presented here is limited initially to a

characterisation of the influence of austenite grain size on the kinetics of the allotriomorphic ferrite transformation. A theory for allotriomorphic ferrite formation proposed by Bhadeshia et al. [39] will first be reviewed in Section 8.3.1. Isothermal dilotometric experiments have also been carried out and the results will be presented in Section 8.3.2.

8.3.1 Theory for Allotriomorphic Ferrite Formation

Recently, Bhadeshia et al. [39] have presented a new model for the development of microstructure in welds, in which the allotriomorphic ferrite grains prior to site-saturation are modelled as discs (parallel to the austenite grain boundary planes of half-thickness q, radius ηq). The aspect ratio η of the allotriomorphs is considered constant because in reality, the lengthening and thickening processes are coupled. Soft impingement between allotriomorphs growing from opposite grain boundaries should not occur at the usual cooling rates encountered in welding, and this analysis takes account of hard impingement. It has been demonstrated [39] that this disc model is a better approximation than the layer model (see Figure I.4). The detailed theory for the disc model is discussed briefly as follows.

The analysis uses the concept of extended area or volume [178]. Consider a plane surface of total area O parallel to a particular boundary. The extended area O_α^e is defined as the sum of the areas of intersection of the discs with this plane. It ensues that the change dO_α^e in O_α^e due to disc nucleated between t=τ and t=τ+dτ is:

$$dO_\alpha^e = \pi O_b I_B [(\eta\alpha_1)^2(t-\tau)]d\tau \qquad \text{for } \alpha_1(t-\tau)^{0.5} > y \qquad \text{(VIII.1)}$$

$$\text{and } dO_\alpha^e = 0 \qquad \text{for } \alpha_1(t-\tau)^{0.5} < y$$

where O_α^e = extended area due to α allotriomorph,
O_b = area of a particular grain boundary,
I_B = grain boundary nucleation rate per unit area,
η = ratio of length to thickness of allotriomorph,
α_1 = one-dimensional parabolic thickening rate constant,
τ = incubation time for the nucleation of one particle,
and y = the distance between the boundary and an arbitary plane parallel to the boundary.

It should be noted that only particles nucleated for $\tau > (y/\alpha_1)^2$ can contribute to the extended area intersected by the plane at y, the whole extended area is given by:

$$O_\alpha^e = \int_0^{t-(y/\alpha_1)^2} (\eta\alpha_1)^2 \pi O_b I_B (t - \tau) d\tau$$

$$= 0.5\pi O_b I_B (\eta\alpha_1)^2 t^2 [1 - \theta^4] \qquad \text{(VIII.2)}$$

where $\theta = y/\alpha_1 t^{0.5}$

The relationship between extended area O_α^e and and actual area O_α is given by [178]

$$O_\alpha^e / O = -\ln\{1 - [O_\alpha / O]\}$$

Therefore $O_\alpha = O_b(1 - \exp\{-O_\alpha^e/O_b\})$ (VIII.3)

Assuming that there is no interference with allotriomophs from other boundaries, the total volume V_b of material originating from this grain boundary is given by integrating for all y between negative and positive infinity; in terms of θ, the integral amounts to:

$$V_b = \int_0^1 2(\alpha_1 t^{0.5}) O_b (1 - \exp\{-O_\alpha^e/O_b\}) d\theta$$

$$= \int_0^1 2O_b(\alpha_1 t^{0.5})(1 - \exp\{-0.5\pi I_B (\eta\alpha_1)^2 t^2 [1-\theta^4]\}) d\theta$$

$$= 2O_b(\alpha_1 t^{0.5}) f\{\theta, \eta\alpha_1, I_B, t\} \qquad \text{(VIII.4)}$$

where $f\{\theta,\eta\alpha_1,I_B,t\} = \int_0^1 (1 - \exp\{-0.5\pi I_B (\eta\alpha_1)^2 t^2 [1-\theta^4]\}) d\theta$

If the total grain boundary area is $O_B = \Sigma O_B$, then by substituting O_B for O_b in equation VIII.4 the total extended volume V_α^e of material emanating from all boundaries is found; this is an extended volume because allowance was not made for impingement of discs originating from different boundaries. Therefore,

$$V_\alpha^e = 2O_B(\alpha_1 t^{0.5}) f\{\theta, \eta\alpha_1, I_B, t\}$$

and if V is the total volume, and S_v the austenite grain surface area per unit volume, then:

$$V_\alpha^e / V = 2S_v(\alpha_1 t^{0.5}) f\{\theta,\eta\alpha_1,I_B,t\}$$

It can be converted into the actual volume, V_α, using the equation:

$$V_\alpha / (V\phi) = 1 - \exp\{-V_\alpha^e / (V\phi)\}$$

$$\text{where } \phi = (x^{\gamma\alpha} - \bar{x})/(x^{\gamma\alpha} - x^{\alpha\gamma})$$

Finally, it follows that:

$$-\ln\{1 - \zeta\} = (2S_v/\phi)(\alpha_1 t^{0.5}) f\{\theta, \eta\alpha_1, I_B, t\} \qquad \text{(VIII.5)}$$

where ζ the volume of α divided by its equilibrium volume, i.e.,

$$\zeta = V_\alpha / (V\phi) .$$

As I_B increases or time increases, the value of the integral f tends to unity due to site saturation. In this condition, equation VIII.5 simplifies to one dimensional thickening:

$$-\ln\{1-\zeta\} = (2S_v / \phi)(\alpha_1 t^{0.5}) \qquad \text{(VIII.6)}$$

The relationship between $\bar{L}$ the mean linear intercept for austenite grains and S_v the austenite grain surface area per unit volume, can be written as:

$$S_v = 2 / \bar{L} .$$

It is clear that equation VIII.5 already provides an interpretation of austenite grain size effect on the kinetics of allotriomorphic ferrite transformation. However, theory is still needed for the prediction of ferrite nucleation rates.

8.3.2 Dilatometry

This work studied here is initially limited to isothermal dilatometry, and the austenite grain size effect on the kinetics of allotriomorphic ferrite transformation has been investigated. The experimental technique is essentially the same as in Section 3.2. The experiments were carried out on the homogenised base materials austenitised at four different temperature 870, 950, 1100 and 1200°C, respectively, for 10 minutes, and then isothermally transformed in a temperature range (680–760°C) for only allotriomorphic ferrite reaction. The austenite grain sizes have been measured using linear intercept method on the optical specimens, and are 16±3, 25±5, 46±8, 159±22μm, respectively, for the specimens austenitised at 870, 950, 1100 and 1200°C for 10 minutes. The isothermal

dilatometric curves for allotriomorphic ferrite formation are shown in Figure VIII.7(a)~(e).

Figure VIII.7(a) shows isothermal transformation of allotriomorphic ferrite at 760°C for the four different starting austenite grain sizes. The amount of the transformation is very small even for a very long time in any one of the four cases, and this implies that 760°C is very close to the Ae_3 temperature. It also clearly demonstrates that the time taken for the initiation of allotriomorphic ferrite transformation becomes significantly longer as the austenite grain size increases. Figure VIII.7(b)~(e) present the same tendency in grain size effect; i.e., when austenite grain size is small, the transformation rate of allotriomorphic ferrite will be large. For the same grain size of austenite, the transformation rate increases as the isothermal transformation temperature decreases from 760°C to 680°C. Figure VIII.7(e) shows that at isothermal temperature 680°C the incubation time of allotriomorphic ferrite transformation is too small to detect for the austenite grain sizes 16 and 25μm (austenitised at 870°C and 950°C, respectively, for 10 minutes). This indicates that the nose of diffusional C curve is in the vicinity of 680°C. All the dilatometric data consistently show that as the austenite grain size decreases, the amount of allotriomorphic ferrite transformation increases at the same isothermal temperature for the same period of time. This indicates that the grain boundary area is a important factor in the kinetics of transformation of allotriomorphic ferrite.

The microstructure of dilatometer specimens has also been studied (Figure VIII.8). The optical micrograph (Figure VIII.8a) shows a few allotriomorphs forming after austenitisation of base metal at 1200°C for 10 minutes followed by isothermal transformation at 760°C for 2 hours prior to quenching to ambient temperature (the helium gas quenching rate in dilatometer ≈60°C/s). Because of kinetic restrictions (large austenite grain size), the residual austenite has mainly transformed to martensite, some bainite and a small amount of Widmanstätten ferrite. On the other hand, Figure VIII.8b shows the microstructure for the dilatometric specimen austenitised at 870°C for 10 minutes followed by isothermal transformation at the same 760°C for 2 hours before quenching to room temperature. It is clear that a large amount of allotriomorphic ferrite forms during cooling in this case. (Dilatometric curves in Figure VIII.7a shows little transformation at 760°C for 2 hours). The optical micrographs (Figures VIII.8c and d) show the microstructure for the specimens austenitised at 1200°C and 1100°C, respectively, for 10 minutes followed by isothermal transformation at 720°C for 2 hours before quenching to room temperature. The results show that the austenite grain boundaries rapidly become decorated with a layer of polycrystalline allotriomorphic ferrite, and besides the allotriomorphic ferrite the microstructure consists chiefly of martensite, with some bainite and Widmanstätten ferrite. Comparing the microstructure shown in Figure VIII.8c and that in Figure VIII.8d, it is found that the latter (small

austenite grain size) contains a higher volume fraction of Widmanstätten ferrite. It should be noted that as the isothermal transformation temperature is reduced (for example at 700 and 680°C), the carbon composition of residual austenite will increase due to the partitioning of carbon between α and γ, and the transformation during cooling will be influenced. Figures VIII.8e and f present the corresponding microstructure for the specimens austenitised at 1200°C and 1100°C, respectively, for 10 minutes followed by isothermal transformation at 700°C for 2 hours before quenching to room temperature. Figures VIII.8g and h show the corresponding microstructure for the specimens austenitised at 1200°C and at 1100°C, respectively, for 10 minutes followed by isothermal transformation at 680°C for 2 hours before quenching to ambient temperature. It is clear that when the carbon content of the residual austenite is large, the formation of Widmanstätten ferrite during quenching is suppressed.

8.3.3 Further Study

It is necessary to convert the dilatometric data (Figure VIII.7) from "the relative length change versus time" to "the volume fraction of allotriomorphic ferrite formed versus time", for the purpose of investigating quantitatively kinetics of allotriomorphic ferrite transformation. The calculation is the same as given by equation III.1, and the linear expansion coefficients and lattice parameters of ferrite and austenite are required. It will be interesting to compare experimental data with the model discussed in Section 8.3.1.

Equation VIII.6 can be written as:

$$V_\alpha/V = \phi\,[1-\exp\{-(2S_V/\phi)(\alpha_1 t^{0.5})\}] \qquad \text{(VIII.7)}$$

Therefore, after determining S_v and α_1 value, the theoretical data can be calculated. This forms a basis for future work.

8.4 Summary

The microstructure of the heat affected zone adjacent to the capping layer of a multirun weld has been studied. It has been found that as austenite grain decreases, the rate of allotriomorphic ferrite formation increases significantly. This is simply because of the large interfacial area of austenite grain boundaries available for allotriomorphic ferrite nucleation and growth. A theory which provides an interpretation of austenite grain size effect on the kinetics of allotriomorphic ferrite transformation has been reviewed. The isothermal dilatometric experiments have also been carried out, and the kinetic data has been obtained. It needs more work to elucidate the kinetic theory.

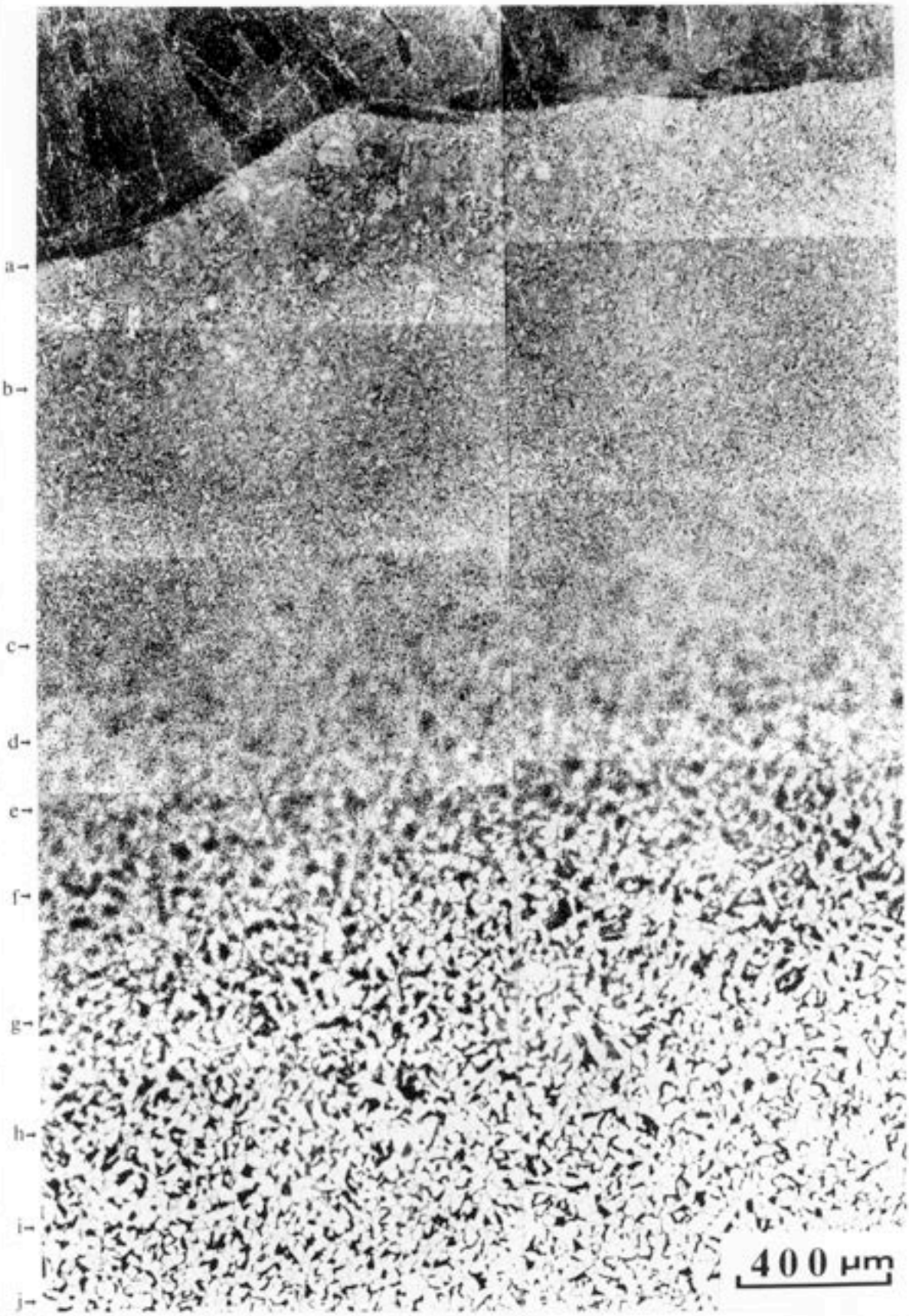

Figure VIII.1 - Showing the macrograph of heat affected zone adjacent to the capping layer of the multirun weld.

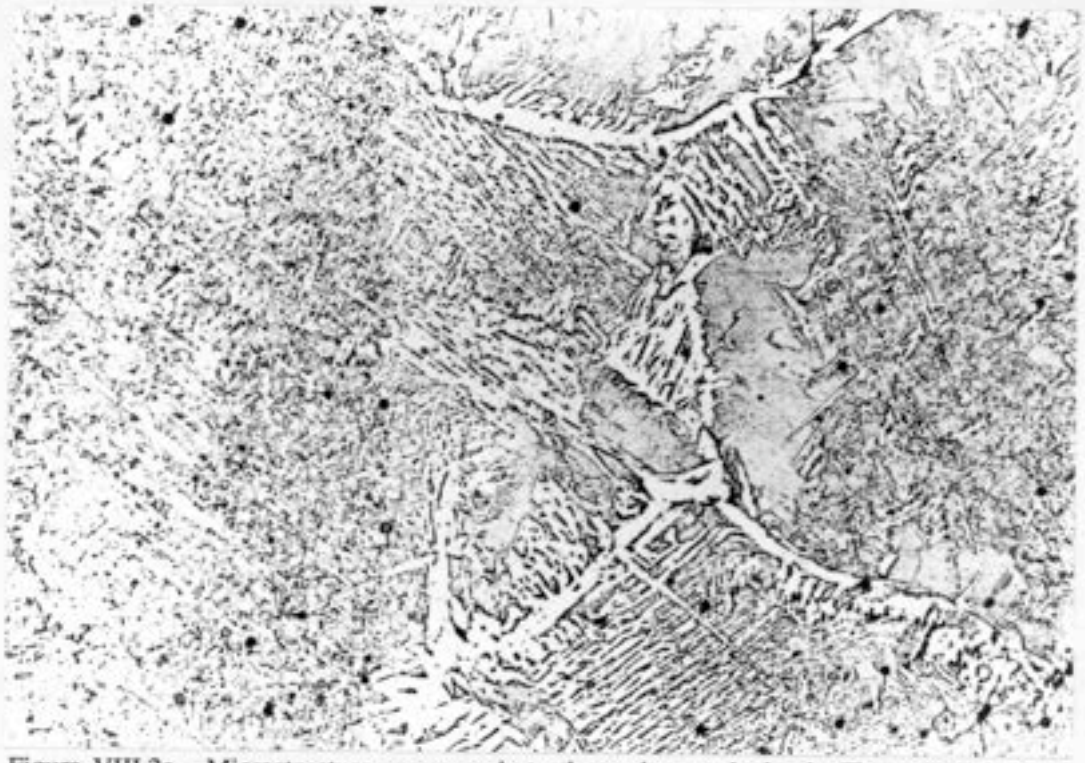

Figure VIII.2a - Microstructure corresponds to the region marked a in Figure VIII.1. The micrograph shows the microstructure adjacent to the fusion boundary. The microstructure of HAZ in this region contains some allotriomorphic ferrite and Widmanstätten ferrite and large amount of martensite (grey areas). 20μm

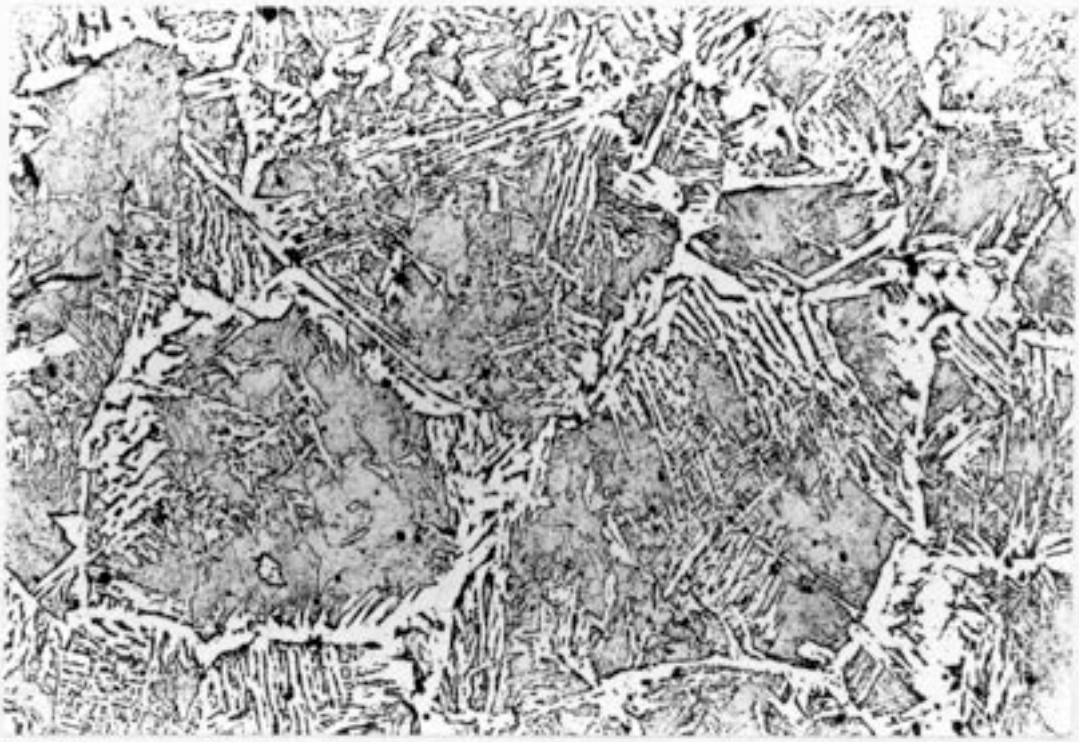

Figure VIII.2b - Microstructure corresponds to the region marked b in Figure VIII.1.

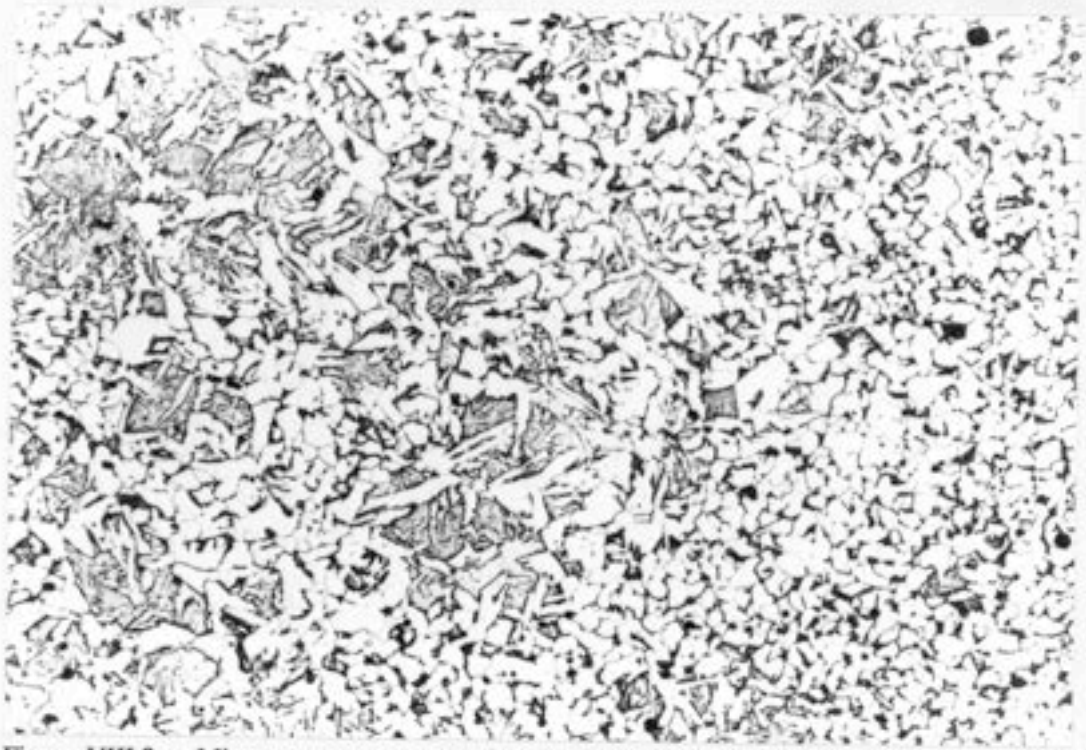

Figure VIII.2c - Microstructure corresponds to the region marked c in Figure VIII.1. 20μm

Figure VIII.2d - Microstructure corresponds to the region marked d in Figure VIII.1. 20μm

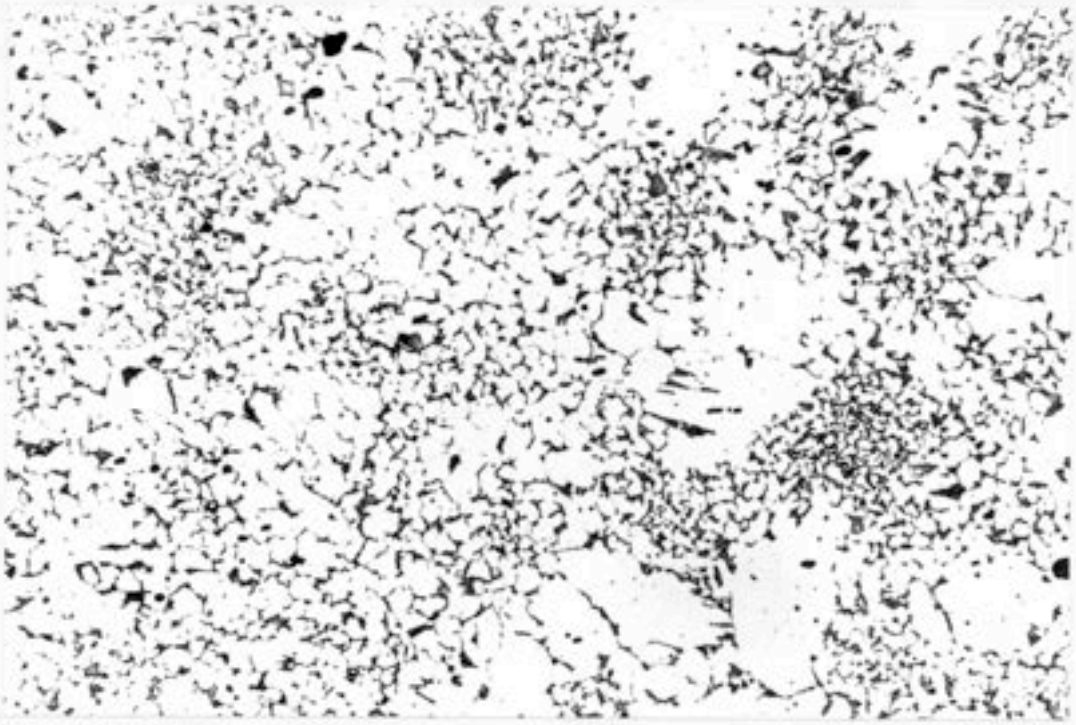

Figure VIII.2e - Microstructure corresponds to the region marked e in Figure VIII.1. 20μm

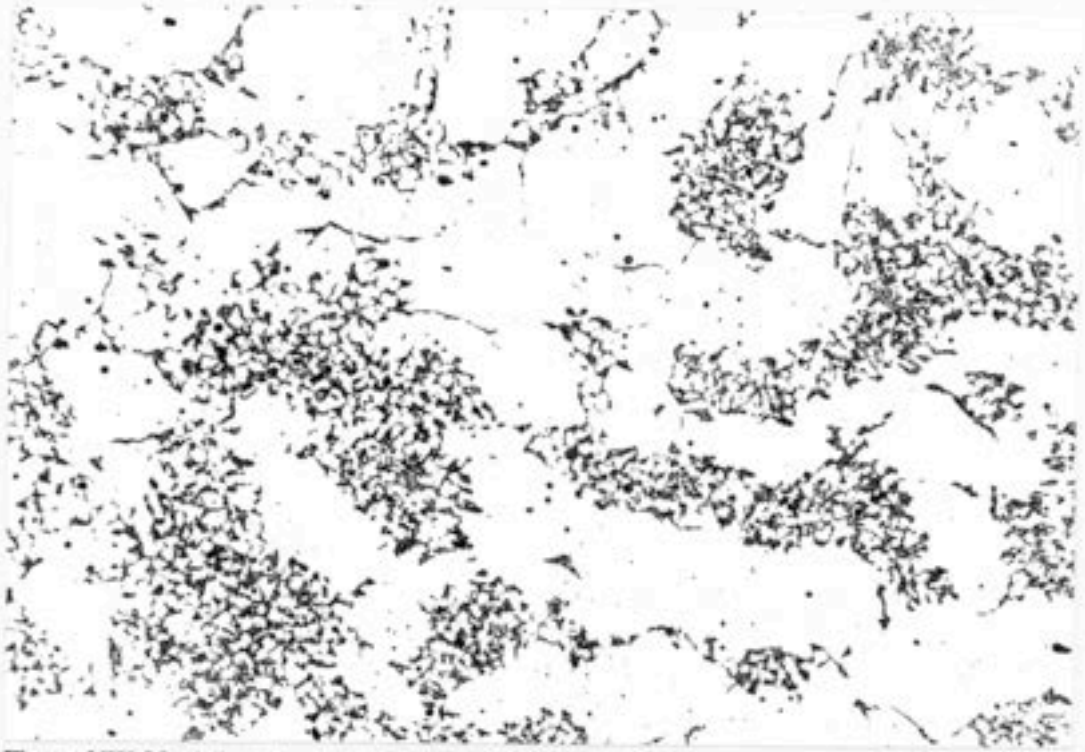

Figure VIII.2f - Microstructure corresponds to the region marked f in Figure VIII.1. 20μm

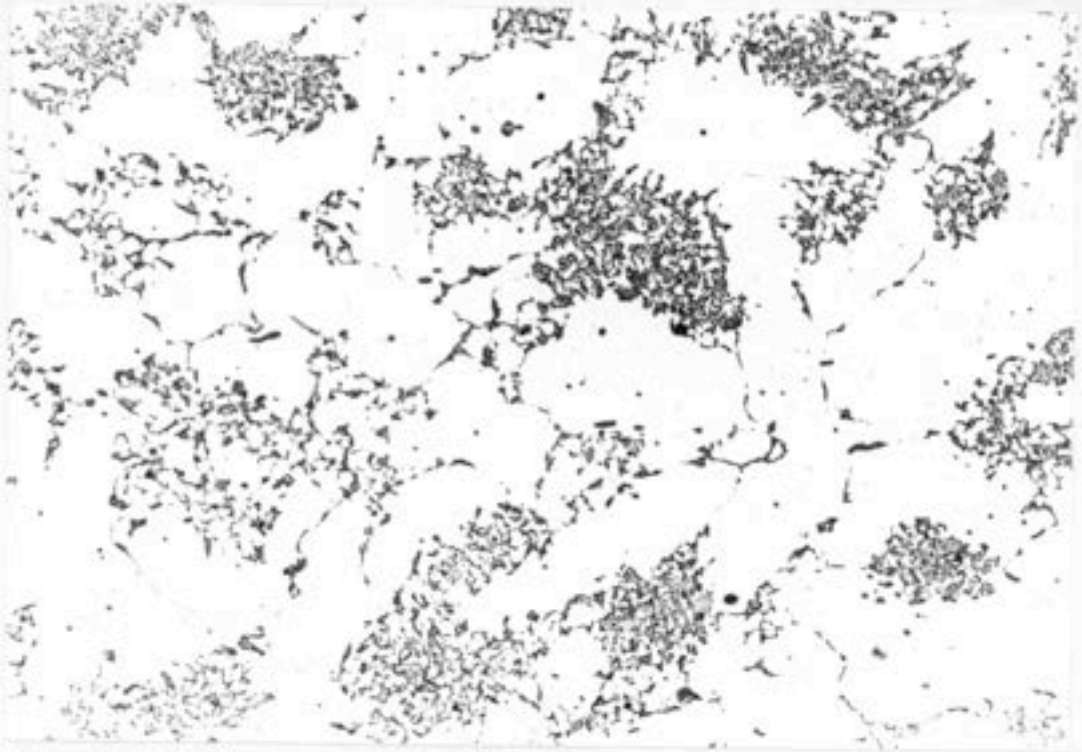

Figure VIII.2g - Microstructure corresponds to the region marked g in Figure VIII.1. 20 µm

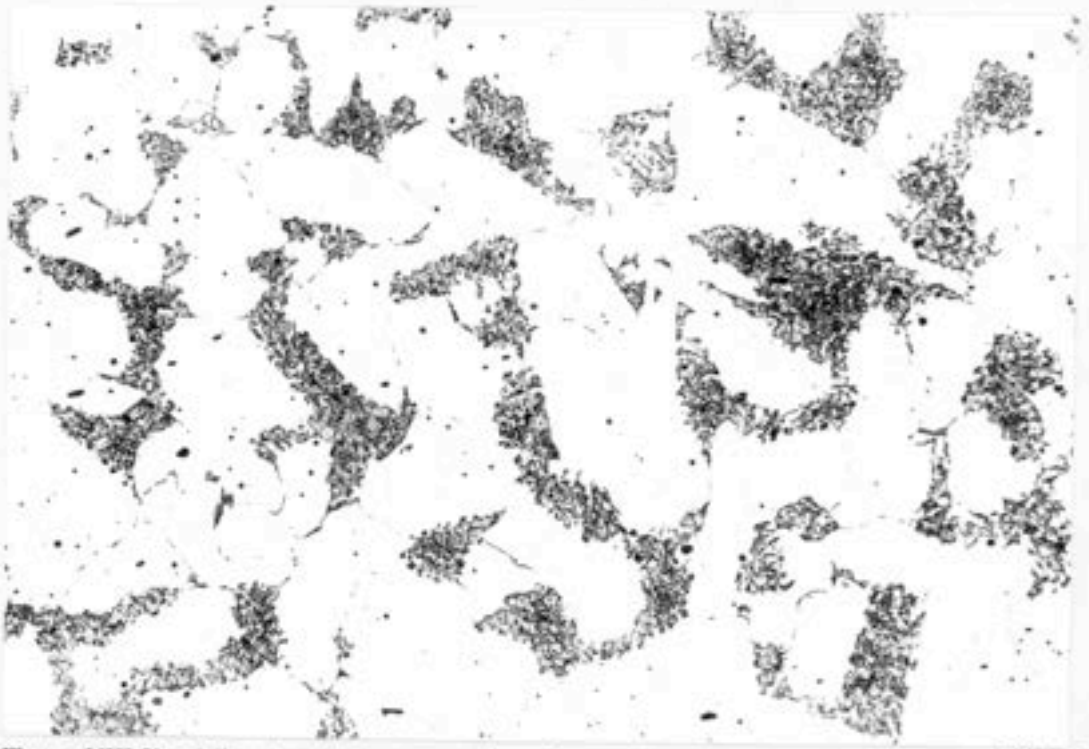

Figure VIII.2h - Microstructure corresponds to the region marked h in Figure VIII.1. 20 µm

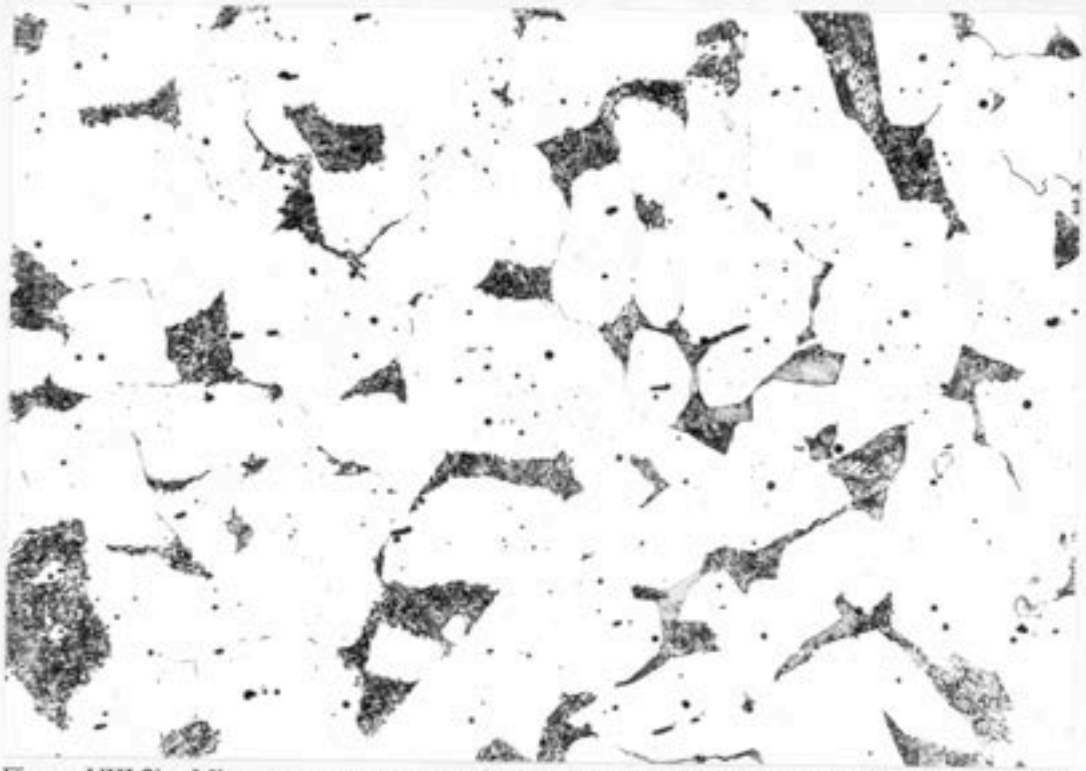

Figure VIII.2i - Microstructure corresponds to the region marked i in Figure VIII.1. 20 µm

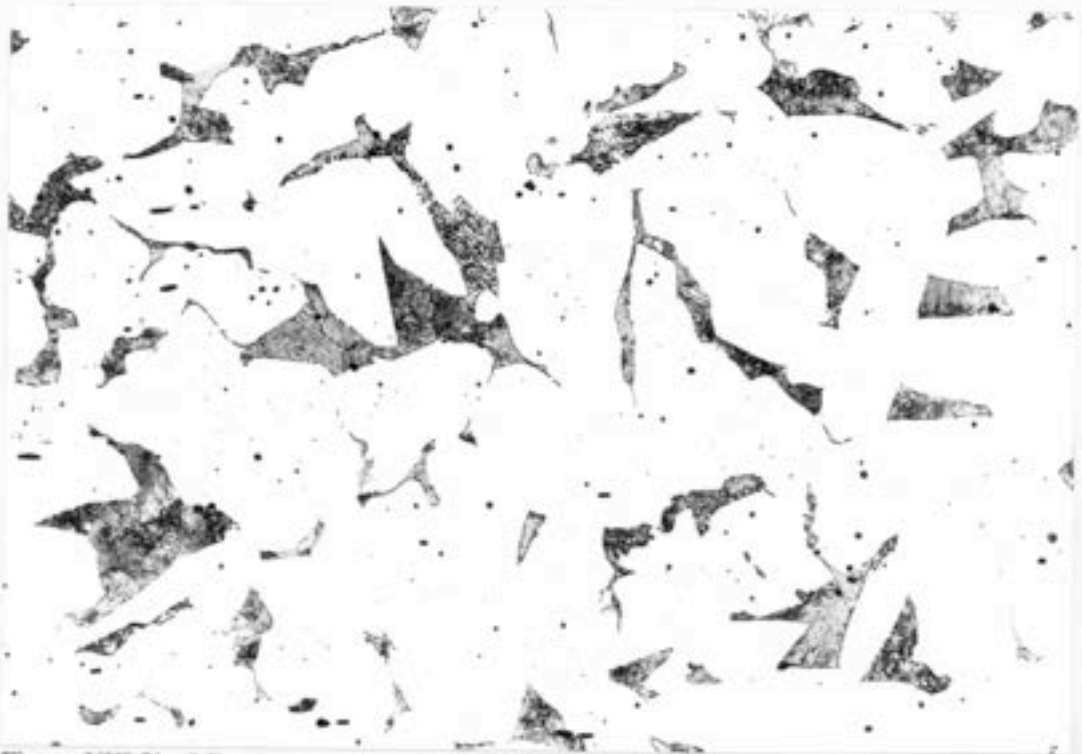

Figure VIII.2j - Microstructure corresponds to the region marked j in Figure VIII.1. 20 µm

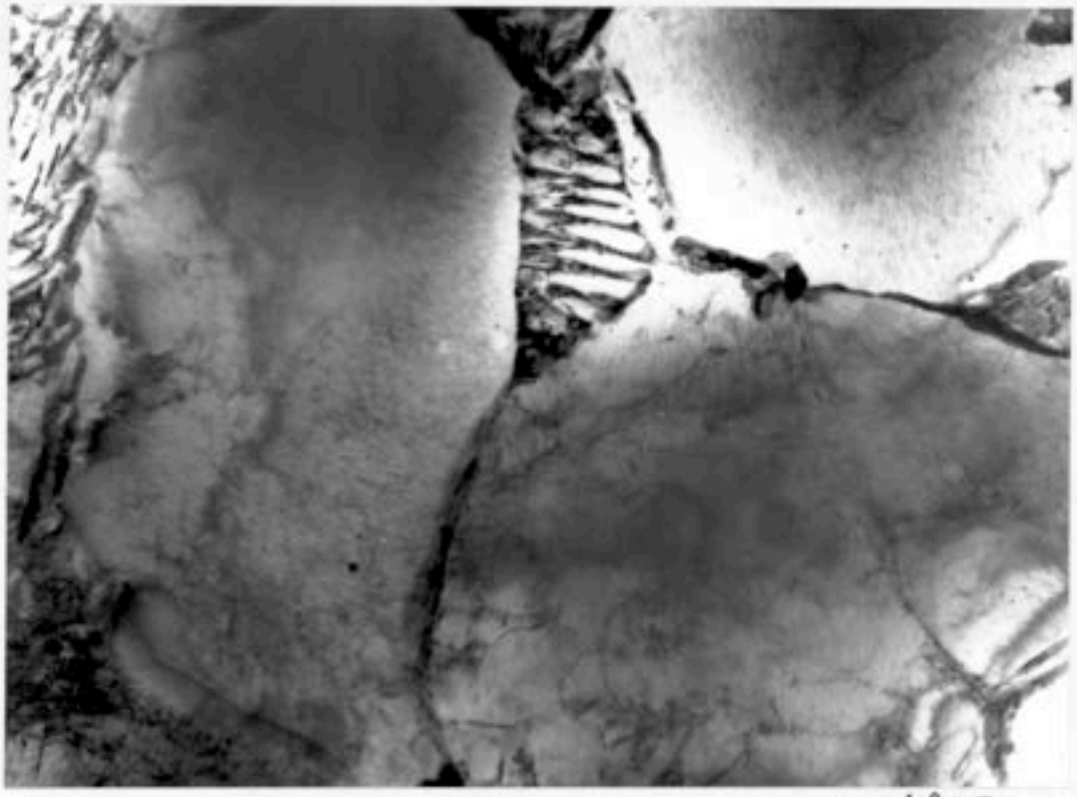

Figure VIII.3 - Electron micrograph shows fine pearlite in the austenite grain refined zone.

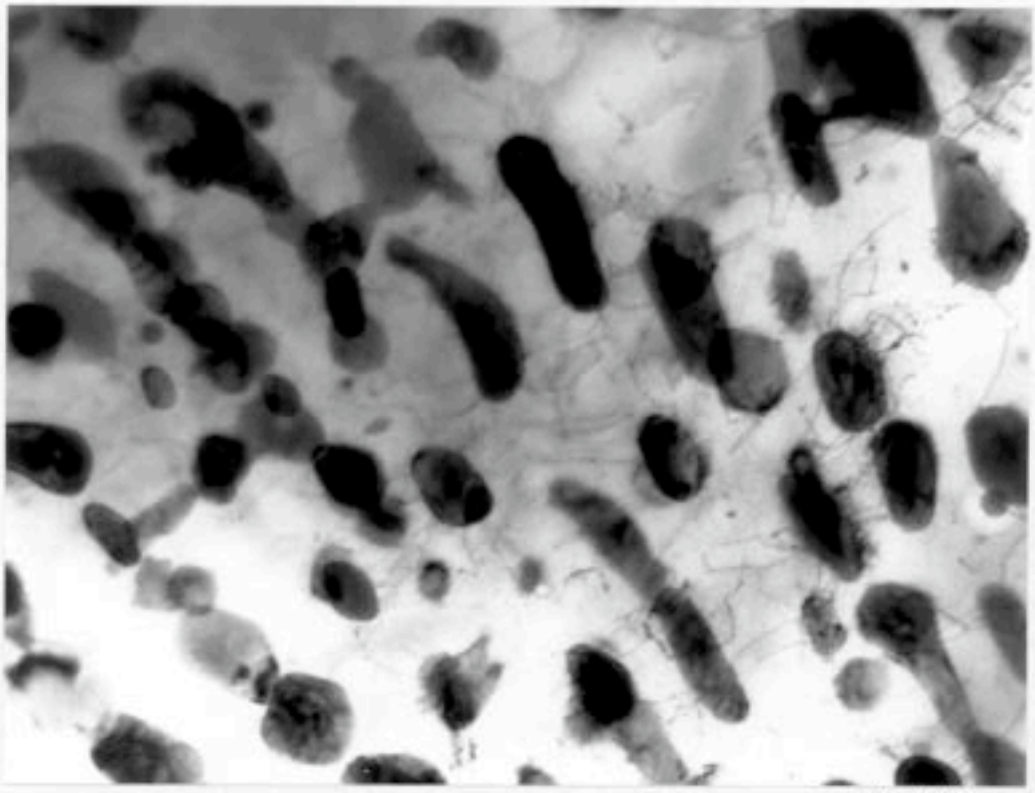

Figure VIII.4 - Electron micrograph shows that the lamellar cementite has been partially spheroidised.

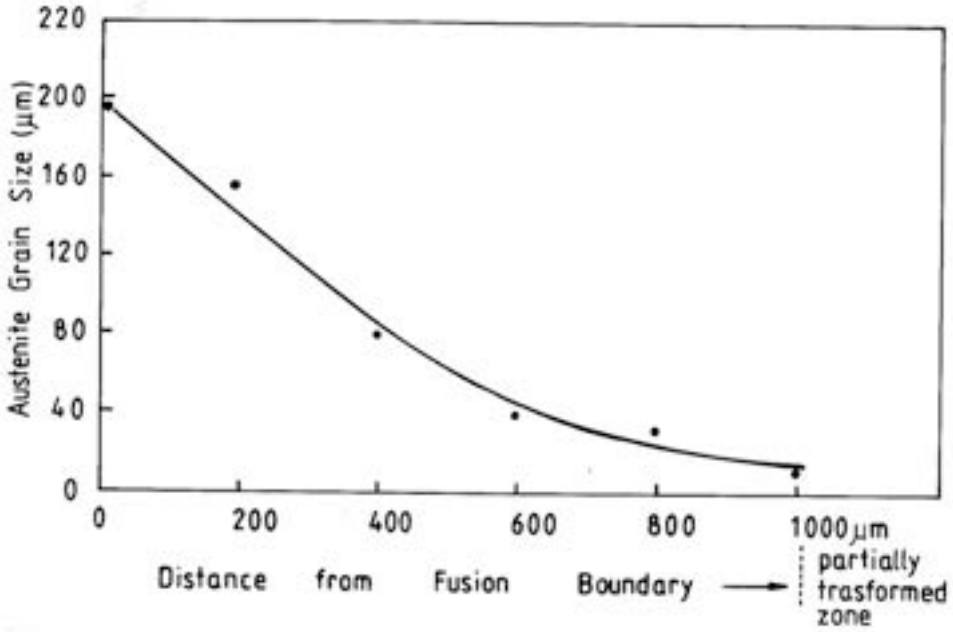

Figure VIII.5 - Showing the austenite grain size versus the distance from the fusion boundary.

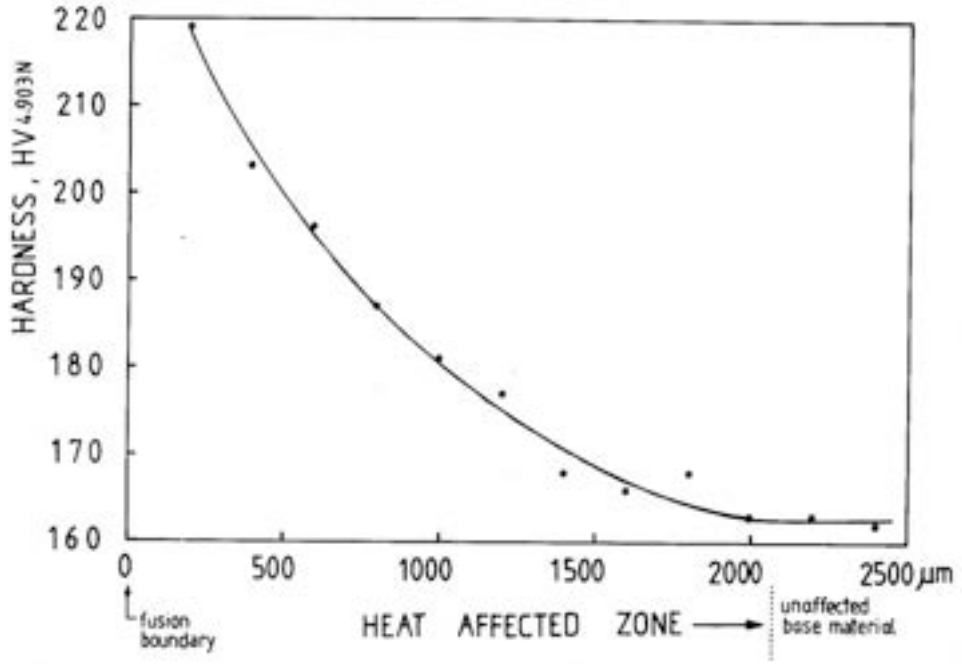

Figure VIII.6 - Showing the hardness profile in heat affected zone.

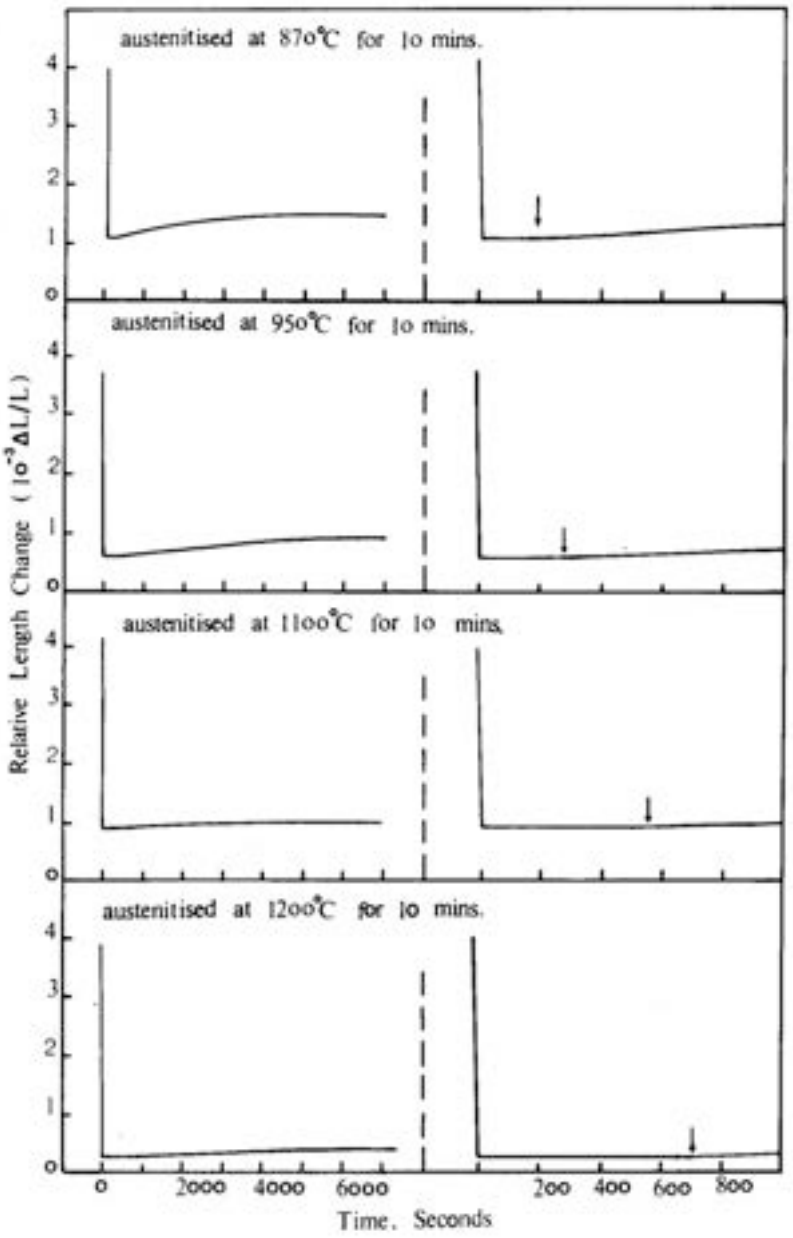

Figure VIII.7(a) - Dilatometric curves show isothermal transformation at 760°C. The left part of the figure presents for the long isothermal transformation time; the right part, for the short isothermal transformation time.

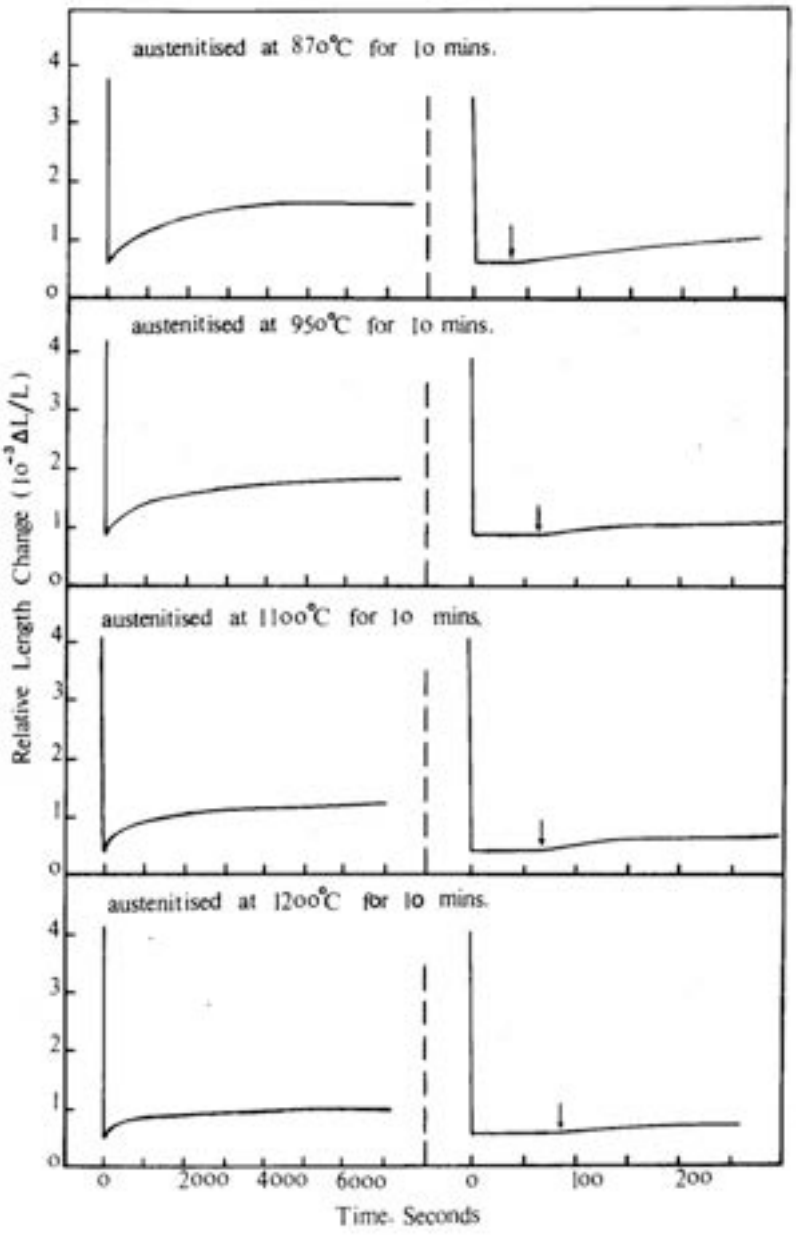

Figure VIII.7(b) - Dilatometric curves show isothermal transformation at 740°C.

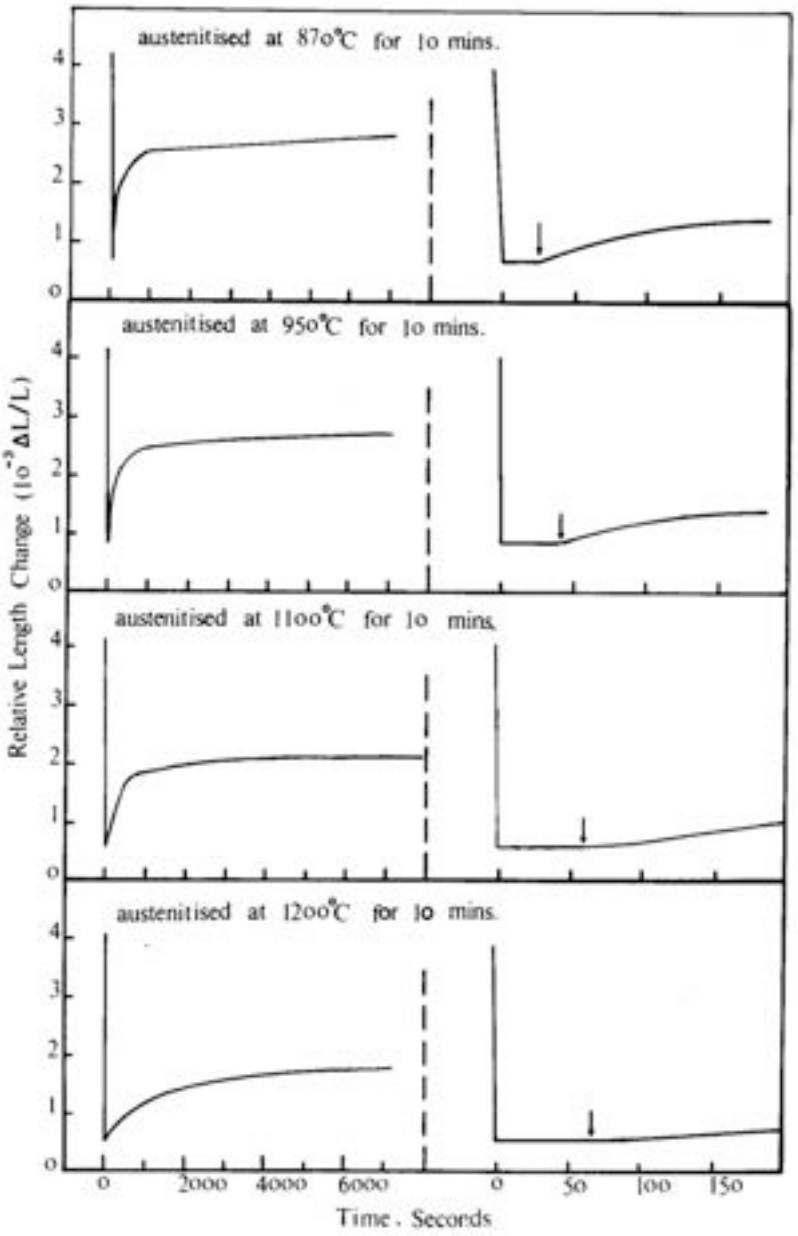

Figure VIII.7(c) - Dilatometric curves show isothermal transformation at 720°C.

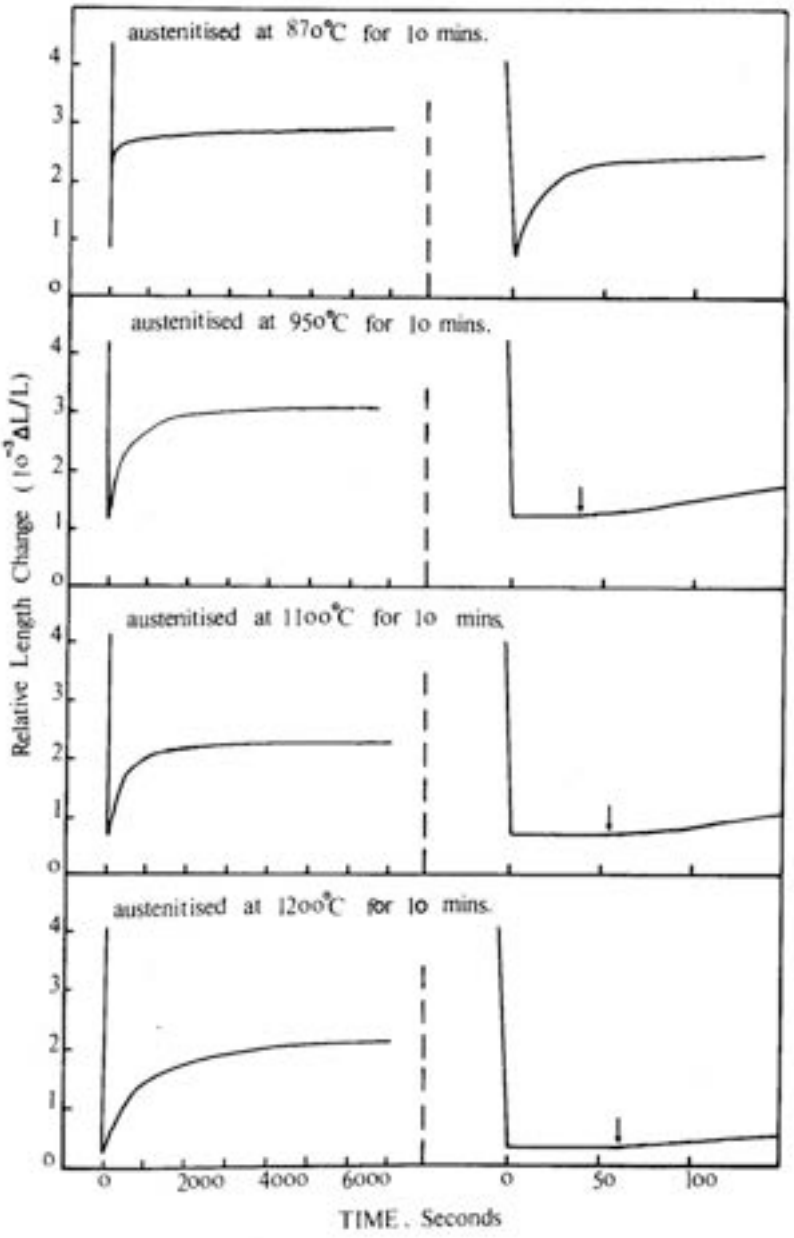

Figure VIII.7(d) - Dilatometric curves shows isothermal transformation at 700°C.

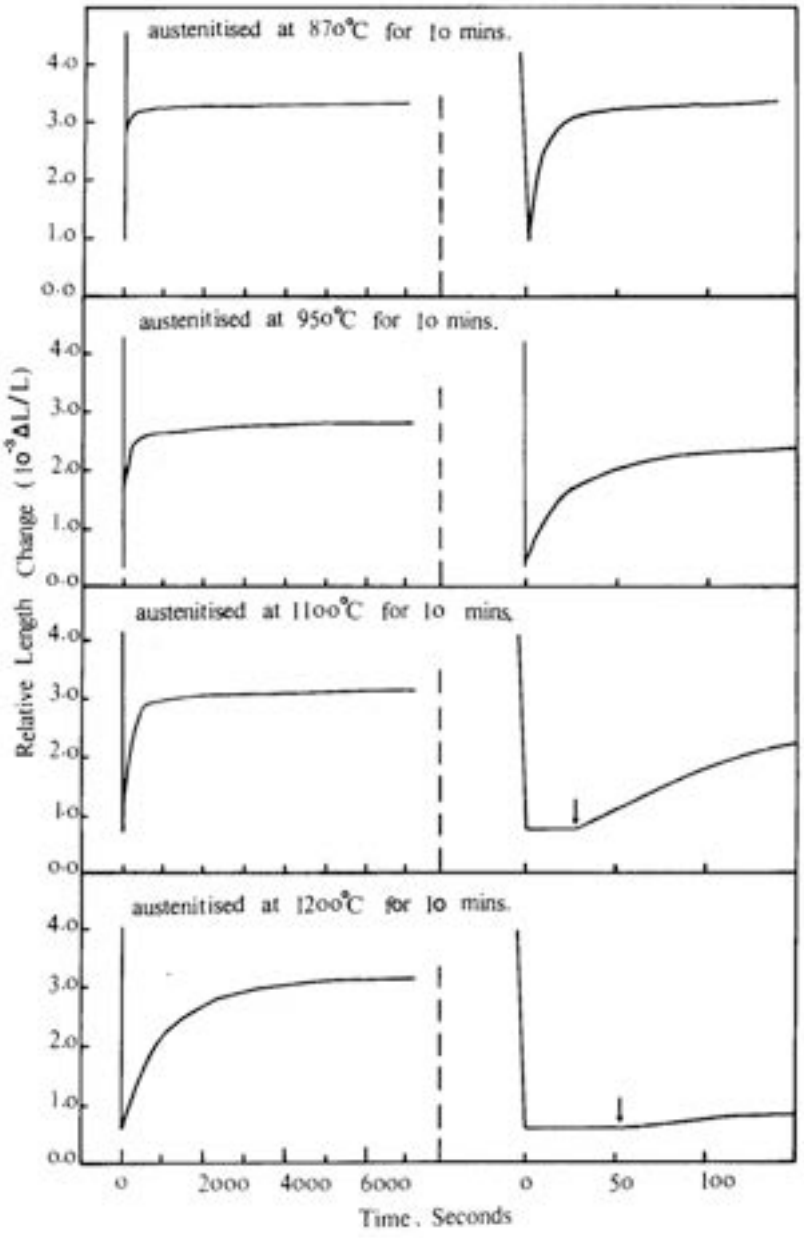

Figure VIII.7(e) - Dilatometric curves shows isothermal transformation at 680°.

Figure VIII.8(a) - 10 mins @ 1200°C → 2 hrs @ 760°C → quenched by helium gas. 100 µm

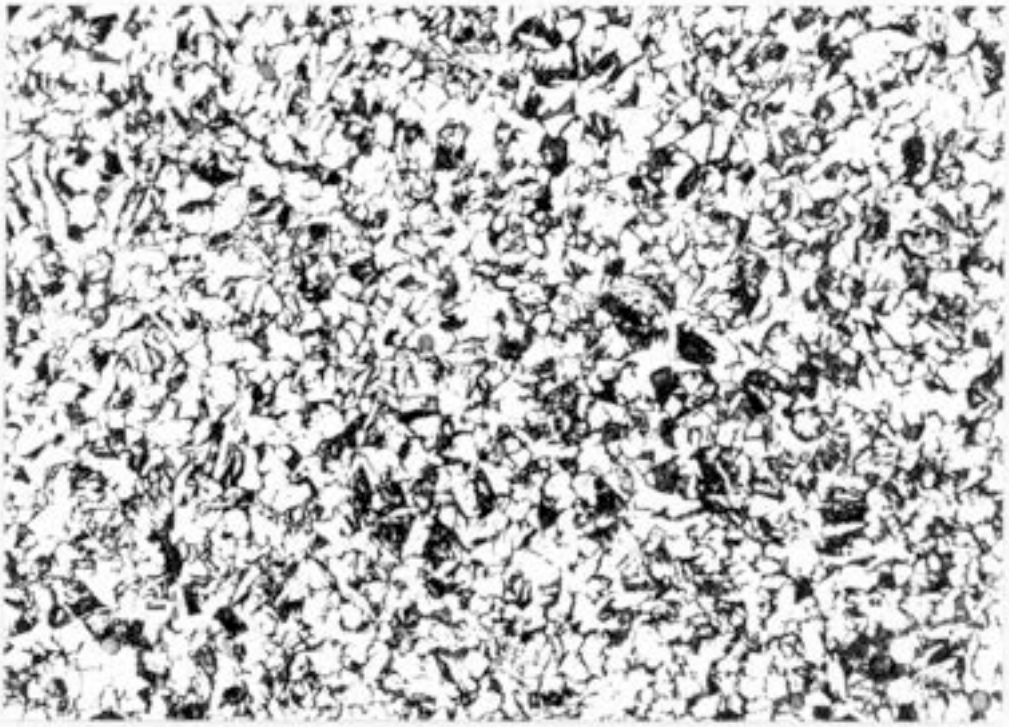

Figure VIII.8(b) - 10 mins @ 870°C → 2 hrs @ 760°C → quenched by helium gas. 20 µm

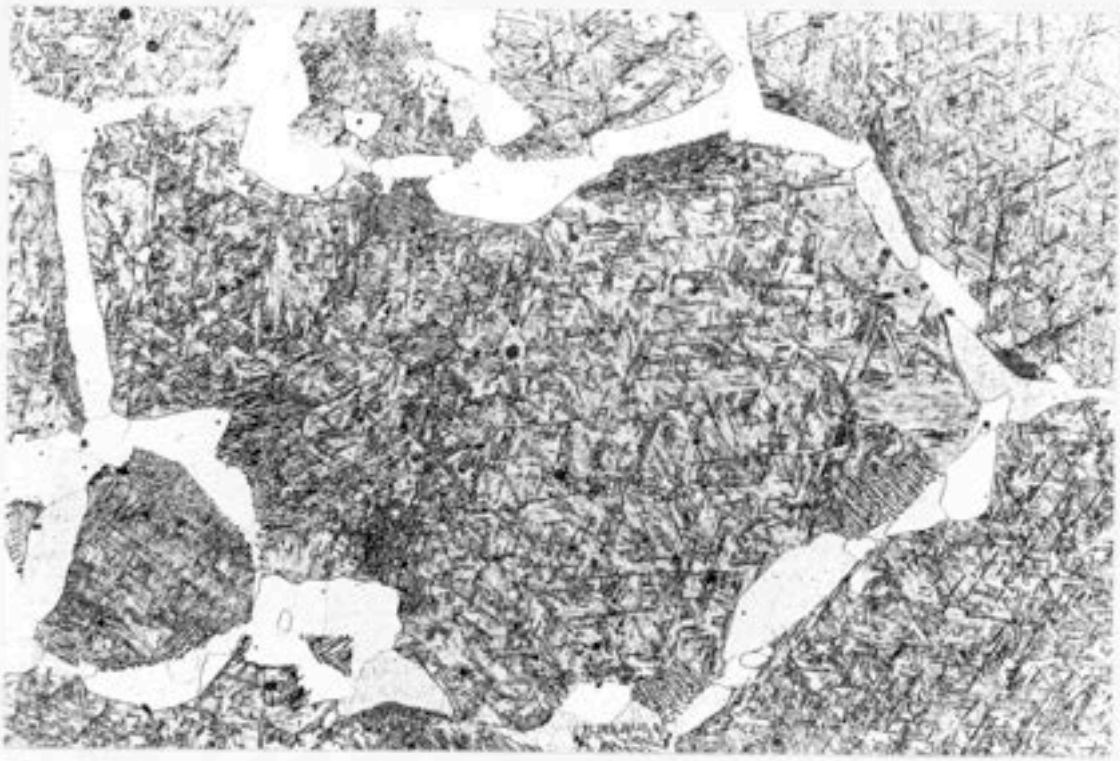

Figure VIII.8(c) - 10 mins @ 1200°C → 2 hrs @ 720°C → quenched by helium gas. 50μm

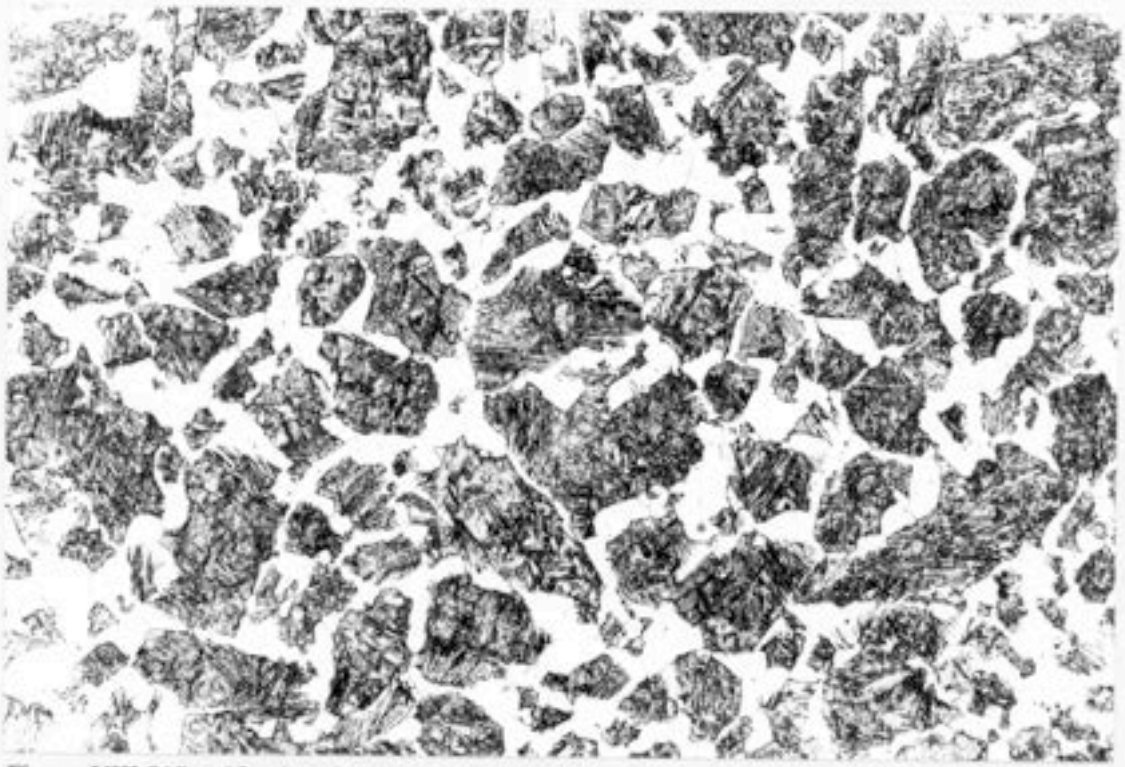

Figure VIII.8(d) - 10 mins @ 1100°C → 2 hrs @ 720°C → quenched by helium gas. 50μm

Figure VIII.8(e) - 10 mins @ 1200°C → 2 hrs @ 700°C → quenched by helium gas. 50μm

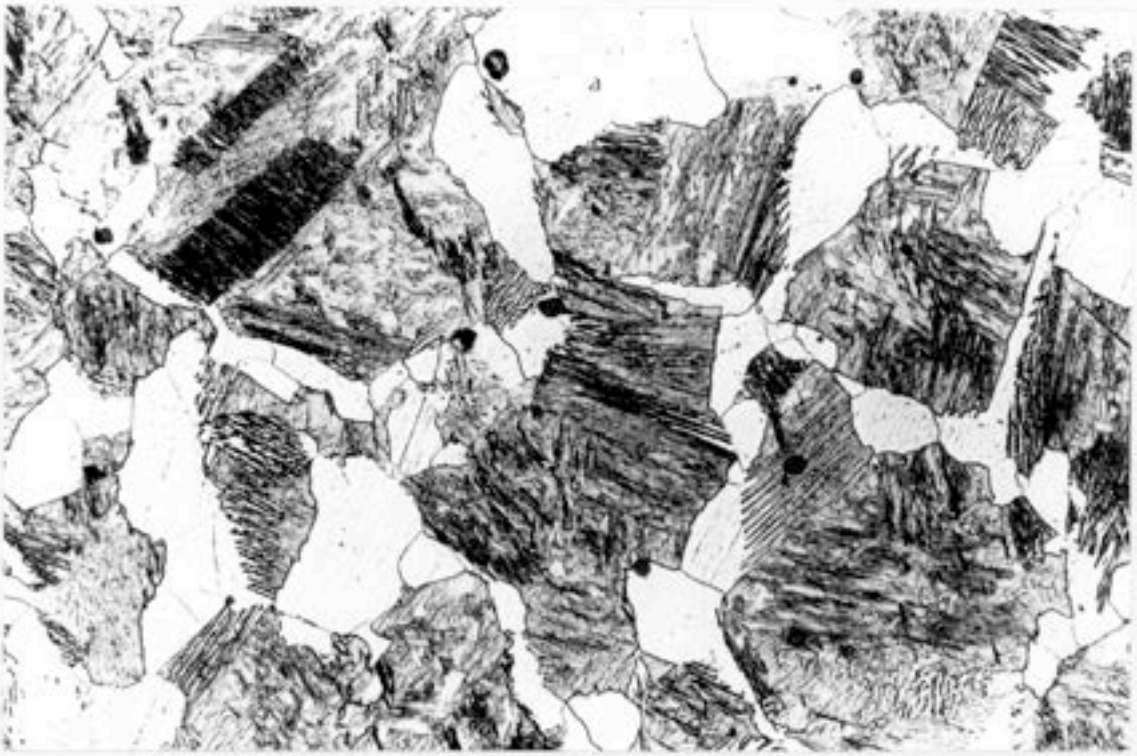

Figure VIII.8(f)-10 mins @ 1100°C → 2 hrs @ 700°C → quenched by helium gas. 20μm

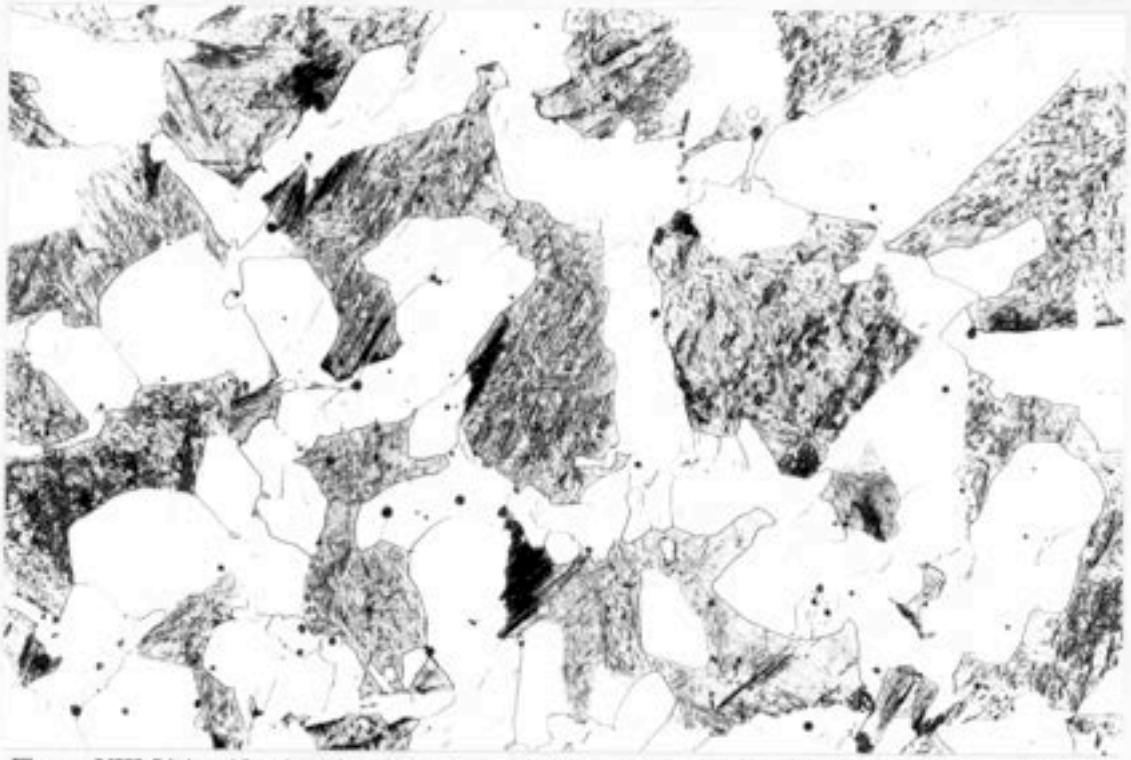

Figure VIII.8(g) - 10 mins @ 1200°C → 2 hrs @ 680°C → quenched by helium gas. 50μm

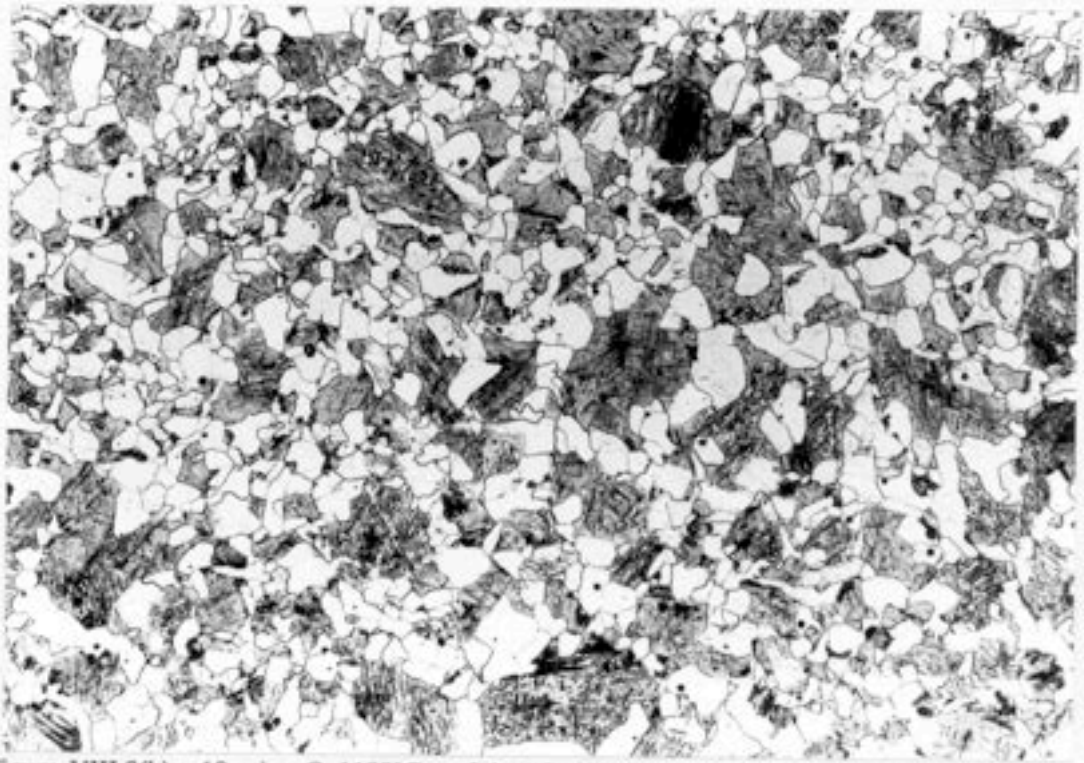

Figure VIII.8(h) - 10 mins @ 1100°C → 2 hrs @ 680°C → quenched helium gas. 50μm

Chapter Nine

Further Research

The present work has gone some way towards an understanding of the mechanism of acicular ferrite formation. This is of importance in placing the reaction in the context of other reactions that arise in steels, in computing the effects of alloying elements and thermomechanical treatments on the design of steel microstructures and ultimately in the improvement of weld quality. However, much further work needs to be carried out to ensure that the thermodynamic description can be extended to permit detailed calculations of the nucleation and growth kinetics of acicular ferrite. Measurements of the nucleation and growth kinetics seem vital. The mechanism by which acicular ferrite improves mechanical properties is not established although very qualitative relationships can be found in the literature. In particular, the micromechanisms of fracture resistance of acicular ferrite should be most interesting to investigate.

The model developed for reaustenitisation already permits a calculation of the TTT curves for the growth of austenite from a specified starting microstructure. However, this is only the tip of the iceberg and to adapt the work to industrially relevant situations it is necessary to address complications such as the nucleation rate of austenite, and reaustenitisation from a variety of possibly mixed microstructures.

APPENDIX 1

```
C ***********************************************************************
C PROGRAM FOR THE CALCULATION OF LENGTH CHANGE
C ACCOMANYING REAUSTENTISATION FROM A MIXTURE OF
C AUSTENITE AND BAINITIC FERRITE
C ***********************************************************************

      IMPLICIT REAL*8(A-H,K-Z)

      DOUBLE PRECISION A(8),WT0(8),WF(8),WAE3(8),W4(8)
C AG=AUSTENITE LATTICE PARAMETER AS A FUNCTION OF COMP, TEMP
C AF=FERRITE LATTICE PARAMETER AS A FUNCTION OF COMP, TEMP
C  AGF AND AFF ARE CORRESPONDING FUNCTIONS TO GIVE THESE
PARAMETERS
C XBAR=AVERAGE ALLOY CARBON, MOLE FRACTION
C XAE3=CARBON, MOL FRAC CORRESPONDING TO AE3 CURVE
C XF=CARBON CONTENT OF ALPHA
C XT0= CARBON, MOL FRAC, CORRESPONDING TO T0 CURVE
C T=TEMPERATURE, CENTIGRADE
C EG,EF EXPANSIVITIES OF GAMMA AND FERRITE
C    TBAIN,TAUST=CENTIGRADE,  ISOTHERMAL  TRANSF  TEMPS  FOR
BAINITE,AUSTENITISATION
C COMPOSITIONS READ IN WT.PCT.
C VB=VOLUME FRACTION OF BAINITE AT TBAIN
C  V1=VOLUME  OF  GAMMA+ALPHA  MIX,BEFORE  TRANSFORMATION,  AT
TAUST
C  V2=VOLUME  OF  GAMMA+ALPHA  MIX,AFTER  TRANSFORMATION,  AT
TAUST
C  DELTAL=RELATIVE  LENGTH  CHANGE,AFTER  TRANSFORMATION,  AT
TAUST
C DEL5V=RELATIVE LENGTH CHANGE DUE TO INCREASING THE VOLUME
FRACTION
C OF AUSTENITE BY 0.05, DURING TRANSFORMATION, AT TAUST
C ***********************************************************************

      READ(5,*)C,SI,MN,NI,MO,CR,V,EG,EF,TBAIN

      CALL ATOM(A,C,SI,MN,NI,MO,CR,V)

      WRITE(6,1)C,SI,MN,NI,MO,CR,V,A(1),A(2),A(3),A(4),A(5),A(6),

     &A(7),EG,EF,TBAIN

      XBAR=A(1)/100.0

      XF=0.0D+00

      XT0=XT0F(TBAIN)

      VB=(XT0-XBAR)/(XT0-XF)

      WRITE(6,2)VB,XT0,XF,XBAR
C VOLUME OF MIXTURE (V1) OF VB BAINITE AND (1-VB)GAMMA, AT TAUST

      WRITE(6,3)
```

```
      DO 5 I=600,850,5
      TAUST=I*1.0D+00
      CALL WEIGHT(WT0,XT0,C,SI,MN,NI,MO,CR,V)
      CALL WEIGHT(WF,XF,C,SI,MN,NI,MO,CR,V)
      CALL AFF(AF,EF,WF(1),SI,MN,NI,MO,CR,V,TAUST)
      CALL AGF(AG,EG,WT0(1),SI,MN,NI,MO,CR,V,TAUST)
      V1=VB*2.0D+00*AF**3 + (1.0D+00-VB)*AG**3
      XAE3=XAE3F(TAUST)
      IF(XAE3 .GT. XT0) GOTO 5
      IF(XAE3 .LT. XBAR) GOTO 6
      VF=(XAE3-XBAR)/(XAE3-XF)
      GOTO 7
6     VF=0.0D+00
      XAE3=XBAR
7     CALL WEIGHT(WAE3,XAE3,C,SI,MN,NI,MO,CR,V)
      CALL WEIGHT(WF,XF,C,SI,MN,NI,MO,CR,V)
      CALL AFF(AF,EF,WF(1),SI,MN,NI,MO,CR,V,TAUST)
      CALL AGF(AG,EG,WAE3(1),SI,MN,NI,MO,CR,V,TAUST)
      V2=VF*2.0D+00*AF**3 + (1.0D+00-VF)*AG**3
      DELTAL=(V2-V1)/(3.0D+00*V1)
      DEL5V=(0.05*AG**3-0.05*2*AF**3)/(3.0D+00*V1)
      WRITE(6,4)DELTAL,TAUST,VF,DEL5V
5     CONTINUE
1     FORMAT(' C SI MN NI MO CR V'/
     &7F8.4, ' WT.PCT'/7F8.4,' ATOMIC PCT'/
     &' EXPANSION COEFFICIENT OF AUSTENITE=',D10.4,
     &' EXPANSION COEFFICIENT OF FERRITE=',D10.4/
     &' TRANSFORMED TO BAINITE AT DEGREES CENTIGRADE=',F8.2)
2     FORMAT(' VOLUME FRACTION OF BAINITIC FERRITE=',F8.3,
     &' MOL. FRAC. XT0=',F8.4/' MOL. FRAC. XF=',D10.4,
     &' AVERAGE ALLOY MOL. FRAC. XBAR=',F8.3)
3     FORMAT(' DELTAL TAUST VF DEL5V ')
4     FORMAT(D14.4,F8.0,F8.3,D14.4)
```

```
      STOP

      END
C ***********************************************************************

      DOUBLE PRECISION FUNCTION XT0F(T)
C T01=INTERCEPT ON TEMP AXIS OF ST. LINE REPRESENTING T0 CURVE
C SLOPE=RECIPROCAL MAGNITUDE OF SLOPE OF T0 LINE

      XT0F=0.14885-6.4052D-04*T+1.2219D-06*T**2-9.2707D-10*T**3

      RETURN

      END
C ***********************************************************************

      DOUBLE PRECISION FUNCTION XAE3F(T)
C T01=INTERCEPT ON TEMP AXIS OF ST. LINE REPRESENTING AE3 CURVE
C SLOPE=RECIPROCAL MAGNITUDE OF SLOPE OF AE3 LINE

      XAE3F=0.34227-3.5370D-04*T-6.7065D-07*T**2+7.2111D-10*T**3

      RETURN

      END
C ***********************************************************************

      SUBROUTINE AGF(AG,EG,C,SI,MN,NI,MO,CR,V,T)

      IMPLICIT REAL*8(A-H,K-Z)
C     CONCENTRATIONS IN WT. PCT., PARAMETER IN ANGSTOMS,
EG=EXPANSIVITY
C TEMPERATURE IN CENTIGRADE

      AG=0.00095*MN-0.0002*NI+0.0006*CR+0.0031*MO+0.0018*V

      &+0.033*C+3.578

      AG=AG*(1.0D+00 + EG*(T-25))

      RETURN

      END
C ***********************************************************************

      SUBROUTINE AFF(AF,EF,C,SI,MN,NI,MO,CR,V,T)

      IMPLICIT REAL*8(A-H,K-Z)
C     CONCENTRATIONS IN WT. PCT., PARAMETER IN ANGSTOMS,
EF=EXPANSIVITY
C TEMPERATURE IN CENTIGRADE
C SPEICH, P.111: CARBON, MO, V, NOT ACCOUNTED FOR

      DOUBLE PRECISION A(8)

      CALL ATOM(A,C,SI,MN,NI,CR,MO,V)
```

```
      AF=2.866-0.0003*A(2)+0.0005*A(6)+0.0006*A(3)+0.0007*A(4)
      AF=AF*(1.0D+00 + EF*(T-25))
      RETURN
      END
C*****************************************************************************
      SUBROUTINE ATOM(A,C,SI,MN,NI,CR,MO,V)
C SUBROUTINE FOR CONVERTING WT.% TO ATOMIC %
      DOUBLE PRECISION A(8),C,SI,MN,NI,CR,MO,V,B
      A(1)=C/12.0115
      A(2)=SI/28.09
      A(3)=MN/54.94
      A(4)=NI/58.71
      A(5)=MO/95.94
      A(6)=CR/52.0
      A(7)=V/50.94
      A(8)=(100.0-C-SI-MN-NI-MO-CR-V)/55.84
      B=A(1)+A(2)+A(3)+A(4)+A(5)+A(6)+A(7)+A(8)
      DO 1 I=1,8
      A(I)=A(I)*100.0/B
1 CONTINUE
      RETURN
      END
C*****************************************************************************
      SUBROUTINE WEIGHT(A,XMOL,C,SI,MN,NI,MO,CR,V)
C SUBROUTINE FOR CONVERTING MOL.FRACTION OF CARBON TO WT.%
CARBON
C C READ IN AS MOL.FRAC, AND AS AVERAGE ALLOY WT.%, REST AS
AVERAGE ALLOY WT.%
      DOUBLE PRECISION A(8),B(8),C,SI,MN,NI,CR,MO,V,B1
      B(2)=SI/28.09
      B(3)=MN/54.94
      B(4)=NI/58.71
      B(5)=MO/95.94
```

```
      B(6)=CR/52.0

      B(7)=V/50.94

      B(8)=(100.0-C-SI-MN-NI-MO-CR-V)/55.84

      B(1)=XMOL*(B(2)+B(3)+B(4)+B(5)+B(6)+B(7)+B(8))/(1.0D+00-XMOL)

      B1=B(1)+B(2)+B(3)+B(4)+B(5)+B(6)+B(7)+B(8)

      DO 2 I=1,8

      B(I)=B(I)*100.0D+00/B1
    2 CONTINUE

      A(1)=B(1)*12.0115

      A(2)=B(2)*28.09

      A(3)=B(3)*54.94

      A(4)=B(4)*58.71

      A(5)=B(5)*95.94

      A(6)=B(6)*52.0

      A(7)=B(7)*50.94

      A(8)=B(8)*55.84

      B1=A(1)+A(2)+A(3)+A(4)+A(5)+A(6)+A(7)+A(8)

      DO 1 I=1,8

      A(I)=A(I)*100.0/B1
    1 CONTINUE

      RETURN

      END
```

APPENDIX 2

```
C ***************************************************************
C PROGRAM FOR ANALYSIS OF DATA FROM BBC/DILATOMETER
C ***************************************************************
C Remember that the first line contains length in mm

   DIMENSION XX(6000), COEFF(6000), TIME(6000), X(6000), Y(6000)

   READ(5,*)ALEN

   AMAG=4.9162

   J1=40

   N1=0

   NMAX = 6000
C ALEN=original length of specimen at ambient
C J1=number of data over which expansivity is averaged
C AMAG= magnification, with dilatometer set at 10000
C COEFF contain expansion coefficients at temperatures XX
C YY contains length change per unit length at temps X, centigrage

   N = 0

   10 N = N + 1
C X IS TEMPERATURE AND Y IS LENGTH. A IS TIME/100, SES

   READ (5, *, END=20) X(N)

   X(N)=10.01836*X(N)+0.0187719

   B=X(N)

   IF(B .LT. 0.643) GOTO 300

   IF(B .LT. 1.78)GOTO 301

   IF(B .LT. 4.221)GOTO 302

   IF(B .LT. 7.656)GOTO 303

   IF(B .LT. 10.74)GOTO 304

   IF(B .LT. 12.06)GOTO 306
300 B=0.3677+176.4*B-33.57*B*B

   GOTO 305
301 B=10.26+146.0*B-9.573*B*B

   GOTO 305
302 B=32.33+121.2*B-2.485*B*B

   GOTO 305
303 B=44.79+114.7*B-1.591*B*B
```

```
      GOTO 305
304 B=68.41+108.0*B-1.117*B*B

      GOTO 305
306 B=205+83.33*B+8.385E-05*B*B
305 X(N)=B

      READ (5, *, END=20) Y(N)

      Y(N)=Y(N)/(ALEN*AMAG)

      READ (5, *, END=20) TIME(N)

      TIME(N)=TIME(N)/100.0

      IF (N .EQ. NMAX) GOTO 30

      GOTO 10

      20 N = N - 1
C GRST2S(ASPECT) - initialise package and specify the aspect ratio
30 DO 310 I1=1,2000

      IF(I1*J1 .GT. N) GOTO 312

      B1=0.0

      B2=0.0

      B3=0.0

      B4=0.0

      DO 311 J=1,J1

      N1=N1+1

      B1=B1+Y(N1)*X(N1)

      B2=B2+X(N1)

      B3=B3+Y(N1)

      B4=B4+X(N1)*X(N1)
311 CONTINUE

      COEFF(I1)=(J1*B1-B2*B3)/(J1*B4-B2*B2)

      XX(I1)=B2/J1
310 CONTINUE
312 I1=I1-1

      CALL GRST3S(1.0,150.0)

      CALL GRLM2S(0.3,0.9,0.1,0.6)

      CALL GRTY5S(-1,1)
```

```
      CALL GRFT3S(2.5,1.0,0,190,0.0,20)
C GRGR6S(X,Y,N) - draw linear graph of N (X,Y) values
      CALL GRGR6S (X, Y, N)
      CALL GRAN6S('A',0,'Centigrade',10,'Relative Length Change',22)
      CALL GRMS3S(1.0)
      CALL GRLM2S(0.3,0.9,0.1,0.6)
      CALL GRTY5S(-1,1)
      CALL GRFT3S(2.5,1.0,0,190,0.0,20)
      CALL GRGR6S(XX,COEFF,11)
      CALL GRAN6S('A',0,'Centigrade',10,'Exp. Coeff.',11)
      CALL GRMS3S(1.0)
      CALL GRLM2S(0.3,0.9,0.1,0.6)
      CALL GRTY5S(-1,1)
      CALL GRFT3S(2.5,1.0,0,190,0.0,20)
      CALL GRGR6S(TIME,Y,N)
      CALL GRAN6S('A',0,'Time, Seconds',13,'Relative Length Change',22)
      CALL GRMS3S(1.0)
      CALL GRLM2S(0.3,0.9,0.1,0.6)
      CALL GRTY5S(-1,1)
      CALL GRFT3S(2.5,1.0,0,190,0.0,20)
      CALL GRGR6S(TIME,X,N)
      CALL GRAN6S('A',0,'Time, Seconds',13,'Centigrade',10)
C GRST9S - close package
      CALL GRST9S
      STOP
      END
```

APPENDIX 3

```
C ***********************************************************************
C  PROGRAM TO CALCULATE THE MAGNIFICATION FACTOR FOR DILATOMETER
C ***********************************************************************
C Platinum specimen calibration
C ANOT is the Pt length, ALPHA +BETA*T=expansivity of Pt
C T is temperature in centigrade, initial data from BBC/dilatometer

   DIMENSION YY(1200), X(1200), Y(1200)

   REAL ALPHA, BETA, ANOT, T0, A1, A2

   INTEGER N

   A3=0.0

   NMAX = 1200

   ALPHA=8.8631E-06

   BETA=0.0026E-06

   ANOT=15.24

   T0=26.21

   N = 0

   10 N = N + 1
C X IS TEMPERATURE AND Y IS AAAGTH. A IS TIME/100, SES

   READ (5, *, END=20) X(N)

   X(N)=10.01836*X(N)+0.0187719

   B=X(N)

   IF(B .LT. 0.643) GOTO 300

   IF(B .LT. 1,78)GOTO 301

   IF(B .LT. 4.221)GOTO 302

   IF(B .LT. 7.656)GOTO 303

   IF(B .LT. 10.74)GOTO 304
300 B=0.3677+176.4*B-33.57*B*B

   GOTO 305
301 B=10.26+146.0*B-9.573*B*B

   GOTO 305
302 B=32.33+121.2*B-2.485*B*B

   GOTO 305
303 B=44.79+114.7*B-1.591*B*B
```

```
      GOTO 305
304 B=68.41+108.0*B-1.117*B*B
305 X(N)=B

      READ (5, *, END=20) Y(N)

      IF (N .EQ. 1) GOTO 306

      A1=AAA(X(1),ALPHA,BETA,ANOT)

      A2=AAA(X(N),ALPHA,BETA,ANOT)

      YY(N)=(Y(N)-Y(1))/(A2-A1)

      GOTO 307
306 YY(N)=5.0
307 WRITE(6,311)YY(N),X(N)
311 FORMAT(F8.4,F8.2)

      READ (5, *, END=20)A

      IF (N .EQ. NMAX) GOTO 30

      GOTO 10

      20 N = N - 1
C GRST2S(ASPECT) - initialise package and specify the aspect ratio
30 DO 312 I=1,N

      A3=A3+YY(I)
312 CONTINUE

      A3=A3/N

      WRITE(6,313)A3
313 FORMAT(' AVERAGE MAGNIFICATION=', F12.6)

      CALL GRST3S(1.0,300.0)

      CALL GRLM2S(0.1,0.9,0.1,0.6)

      CALL GRTY5S(-1,1)

      CALL GRFT3S(2.5,1.0,0,190,0.0,50)
C GRGR6S(X,Y,N) - draw linear graph of N (X,Y) values

      CALL GRGR6S (X, YY, N)
C GRST9S - close package

      CALL GRST9S

      STOP

      END

      FUNCTION AAA(T,A,B,ANOT)
```

```
TT=26.21
AAA=A*T + B*T*T/2 + A*A*T*T/2 - A*A*TT*T + A*B*T**3/2
&-A*B*T*T*TT + A*B*TT*TT*T/2 + B*B*T**4/8 -
&B*B*T**3*TT/3 + B*B*T*T*TT*TT/4
AAA=ANOT*AAA
RETURN
END
```

References

1. H.K.D.H. Bhadeshia., L.- E. Svensson and B.Gretoft, Acta Metall. 33 (1985) 1271.

2. H.K.D.H. Bhadeshia., L. -E. Svensson and B. Gretoft. J. Mater. Sci. 21 (1986) 3947.

3. G. J. Davies and J.G. Garland, Int. Metall. Rev. 20 (1975) 83.

4. W.F. Savage., C.D. Lundin and A.H. Aaronson, Weld J. 44, (1965) 175.

5. W.F. Savage and A.H. Aaronson, Weld J. 45 (1966) 85.

6. B. Chalmers, "Principles of Solidification" (John Wiley & Sons, New York, (1964) p. 151.

7. M.C. Flemings, "Solidification Processing" (McGraw-Hill, New York, 1974) p. 58.

8. F.A. Calvo., K.P. Bently and R.G. Baker, "Studies of Welding Metallurgy of Steel" (BWRA, Abington, Cambridge, 1963) p. 71.

9. M. Dadian, "Advances in Welding Science and Technology" ed. S.A. David, (Metal Park, OH: American Society of Metals, 1987) p. 187.

10. D.J. Widgery and G.G. Saunders, Weld. Inst. Res. Bull, 16 (1975) 277.

11. T. Edvardson., H. Fredricksson and I. Svensson, Met. Sci. 10 (1976) 298.

12. H. Fredriksson and J. Stejerndahl, ibid. 16 (1982) 575.

13. H. Fredriksson, Acta Universitats Ouluensis, Series C, 26-4, Proceedings of the 3rd Scandinasm Symposium on Materials Science, 1983 (Oulu University Press, Finland, 1983) p. 1.

14. H.K.D.H. Bhadeshia, "Structural Steels for the 1980's", Graduate Lecture (1985), University of Cambridge.

15. D.P. Woodruff, 'The Solid-Liquid Interface' (Cambridge University Press, Cambridge, 1973) p. 84.

16. P.L. Harrison and R.A. Farrar, J. Mater. Sci., 16 (1981) 2218.

17. M. Ferrante and R.A. Farrar, ibid., 17 (1982) 3293.

18. R.C. Cochrane and P.R. Kirkwood, in "Trends in Steels and Consumables for Welding", Proceedings of the Welding Institute Conference, London (1978) p. 103.

19. G.S. Barrite., R.A. Ricks and P.R. Howell, in "Quantitative Microanalysis with High Spatial Resolution", (Metal Society, London, 1981) p. 112.

20. D.J. Widgery, Welding Institution Research Members Seminar on Toughness of Weld Metals, Newcastle-upon-Tyne (1977).

21. C.A. Dubé., H.I. Aaronsson and R.F. Mehl, Rev. Met. 55 (1958) 201.

22. E. Levine and D.C. Hill, Metall. Trans. 8A (1977) 1453.

23. C.L. Chol and D.C. Hill, Weld. J. Res. Supp. 57-8 (1978) 23.

24. R.C. Cochrane, "Weld Metal Microstructures", Int. Inst. Welding Doc. IX-1248-82 (1982).

25. H.K.D.H. Bhadeshia, Progress in Materials Science, 29 (1985) 321.

26. C.S. Smith, Trans. A.S.M. 45 (1953) 533.

27. R.W.K. Honeycombe, in "Perspectives in Metallurgical Development" (The Metals Society, London, 1984) p. 163.

28. M. Hillert, in "The Decomposition of Austenite by Diffusional Process" (Interscience, New York, 1962) p. 197.

29. C. Atkinson., H.B. Aaron., K.R. Kinsman, and H.I. Aarsonsson, Met. Trans. 4 (1973) 783.

30. J.R. Bradley., J.M. Rigbee, and H.I. Aaronsson, Met. Trans. 8A (1977) 323.

31. H.K.D.H. Bhadeshia., L.-E. Svensson and B. Gretoft, J. Mater. Sci. Letters 4 (1985) 305.

32. M. Hillert, Jern. Ann. 136 (1952) 25.

33. J.W. Christian, in "Theory of Transformations in Metal and Alloys", Part I, 2nd ed. (Pergamon, Oxford, 1975) p. 482.

34. D.E. Coats, Metall. Trans. 4 (1973) 2313.

35. J.S. Kirkaldy, Adv. Mater. Res. 4 (1970) 55.

36. H.I. Aaronson., H. Domian, TMS-AIME 236 (1966) 781.

37. J.B. Gilmour., G.R. Purdy and J.S. Kirkaldy, Met. Trans. 3 (1972) 1455.

38. H.K.D.H. Bhadeskia, L.-E. Svensson and B. Gretoft: Proc. of Int. Conf. on "Welding and Performance of Pipe Welds", London, Pub. Welding Institute, Abington, Cambridge, Nov. 1986, p. P17-1.

39. H.K.D.H. Bhadeshia, L.-E. Svensson and B. Gretoft, Symposium "Welding Metallurgy of Structural Steels" (at the AIME Annual Meeting, Denver, Colorado, 1987), in press.

40 J.H. Devletion and W.E. Wood, Metals Handbook, Ninth Edition, Volume 6, American Society for Metals, (1983) p. 21.

41. Y. Ito., M. Nakanishi and Y. Komizo, Metal Construction, September, 1982, p. 472.

42. J.H. Tweed and J.F. Knott, Metal Science, 17 (1983) 45.

43. E. Levine and D.C. Hill, Met. Const. 9 (1977) 346.

44. El Levine and D.C. Hill, Met. Trans. 8A (1977) 1453.

45. D.J. Abson and R.E. Dolby, Int. Inst. Welding, Doc. IXJ-29-80 (1980).

46. M.N. Watson., P.L. Harrison and R.A. Farr, Welding and Metal Fabrication, March 1981, p. 101.

47. H.K.D.H. Bhadeshia, Acta Metall. 29 (1981) 1117.

48. J.D. Watson and P.G. McDougall, Acta Metall. 21 (1973) 961.

49. M.N. Watson., P.L. Harrison and R.A. Farrar, Welding and Metal Fabrication, March 1981, p. 101.

50. Y. Kikuta, "Classification of Microstructures in Low Carbon-Low Alloy Steel Weld Metal and Terminology", Committee of Welding of Japan Welding Society, Report No. IX-1-281-83 (1983), p. 14.

51. J.W. Christian, "Decomposition of Austenite by Diffusional Processes", eds. V.F. Zackay and H.I. Aaronson, Interscience, New York, (1962), p. 371.

52. P.L. Harrison., M.N. Watson and R.A. Farrar, Welding and Metal Fabrication, April 1981, p. 161.

53. J. Garland and P. R. Kirkwood: Met. Constr. May 1975, p. 275.

54. R.E. Dolby, "Factor Controlling Weld Toughness - the Present Position, Part II - Weld Metals" Welding Institute Research Report No. 14/1976/M (Welding Institute, Abingdon, Cambridge, 1976).

55. L.G. Taylor, and R.A. Farrar, Welding and Metal Fabrication, 43 (1975) 305.

56. Y. Kikuta, "Classification of Microstructures in Low C-Low Alloy Steel Weld Metal and Terminology", Committee of Welding Metallurgy of Japan Welding Society, Report No. IX-1281-83 (1983), p. 15.

57. Y. Ito., M. Nakanishi and Y. Komizo, "Effect of Oxygen on Transformation of Low Carbon Weld Metal', IIW Doc. IX-1194-81 (1981).

58. P.L. Harrison., M.N. Watson and R.A. Farrar, Welding and Metal Fabrication, April, 1981, p. 161.

59. H.K.D.H. Bhadeshia, in "Worked Examples in the GEOMETRY OF CRYSTALS" (The Institute of Metals, London, 1987) p. 76.

60. R.E. Dolby, Metal Technology, 10 (1983) 349.

61. D.J. Abson, "The role of inclusions in controlling weld metals microstructure in c-Mn steel" Report No. 69/1978/M, 1978, Cambridge, The Welding Institute.

62. R.A. Ricks., P.R. Howell and G.S. Barrite, J. Mater. Sci. 17 (1982) 732.

63. H.I. Aaronson, and C. Wells, J. Metals. October 1956, p. 1216.

64. J.R. Yang and H.K.D.H. Bhadeshia, "Advances in Welding Science and Technology", ed. S.A. David (Metal Park, OH: American Society for Metals, 1987) p. 187.

65. M. Stangwood and H.K.D.H. Bhadeshia, ibid., p. 209.

66. R.A. Ricks., G.S. Barritte and P.R. Howell, "Solid → Solid Phase Transformations", ed. H.I. Aaronson et al. (The Metallurgical Society of AIME, 1981) p. 463.

67. A.C. Steel, Weld. Res. Intl., 2 (1972) 37.

68. S.S. Tuliani., T. Boniszewsi and N.F. Eaton, Welding and Metal Fabrication, 40 (1972) 247.

69. J.H. Tweed and J.F. Knott, Metal Sci., 17 (1983) 45.

70. A.A.B. Sugden and H.K.D.H. Bhadeshia, Metall. Trans. A, 1987, in press.

71. Y. Ito., M. Nakanishi and Y. Komizo, Metal Construction, September 1982, p. 472.

72. R.C. Cochrane and P.R. Kirkwood, in "Trends in Steels and Consumables for Welding", Proc. Conf., Welding Inst., London (1978).

73. J.G. Garland and P.R. Kirkwood, Metal Construction, 7 (1975) 275.

74. D.J. Abson and R.E. Dolby, The Welding Institute Research Bulletin, April 1980, p. 100.

75. J.G. Garland and P.R. Kirkwood, Metal Construction, 7 (1975) 320.

76. G.J. Davies and J.G. Garland, International Metallurgical Reviews, 20 (1975) 83.

77. L.-E. Svensson., B. Gretoft and H.K.D.H. Bhadeshia, Scand. J. Metallurgy 15 (1986) 97.

78. B. Gretoft., H.K.D.H. Bhadeshia and L.-E. Svensson, Acta Stereologica (1986) p. 365.

79. H.K.D.H. Bhadeshia., L.-E. Svensson and B. Gretoft, in "Advance in Welding Science and Technology", ed. S.A. David, (Metal Park, OH: American Society for Metals, 1987) p. 225.

80. M. Hillert, Met. Trans. 6A (1975) 5.

81. J.S. Kirkaldy, Con. J. Phys. 36 (1958) 907.

82. G.R. Purdy., D.H. Weichert and J.S. Kirkaldy, TMS-AIME 230 (1964) 1025.

83. M. Hillert, 'The Mechanism of Phase Transformation in Crystalline Solids", (Institute of Metals, London), Monograph No. 13 (1969) 231.

84. D.G. Miller, Chem. Rev. 60 (1960) 15.

85. L.S. Darken and R.W. Gurry, "Physical Chemistry of Metals", (McGraw Hill, New York, 1953) p. 146.

86. A. Hultgren: Jernkont. Ann. 135 (1951) 403.

87. J.W. Christian and D.V. Edmonds, "Phase Transformation in Ferrous Alloys", ed. A.R. Marder and J.I. Goldstein, (The Metallurgical Society of AIME, 1983), p. 293.

88. J.W. Christian, "The Theory of Transformations in Metals and Alloys", (Pergamon Press, Oxford, 1965) p. 824.

89. H.K.D.H. Bhadeshia and D.V. Edmonds, Acta Metall. 28 (1980) 1265.

90. H.K.D.H. Bhadeshia and D.V. Edmonds, Meta. Trans. 10A (1979) 895.

91. Y. Ohmori, Trans. Iron Steel Inst. Japan, 11 (1971) 95.

92. S. Hoekstra, Acta Metall. 28 (1980) 507.

93. B.P.J. Sandvik, Meta. Trans. 13A (1982) 777.

94. W. Pitsch, Acta Metall. 10 (1962) 897.

95. H.K.D.H. Bhadeshia, Acta Metall. 28 (1980) 1103.

96. G.R. Srinivasan and C.M. Wayman, Acta Metall. 16 (1968) 609.

97. Y.A. Bagaryatskii, Dokl. Akad. Nauk SSSR 73 (1950) 1161.

98. G. Kurdjumov and G. Sachs, Z. Physik. 64 (1930) 325.

99. Z. Nishiyama, Sci. Rep. Tohoku Univ. 23 (1934) 638.

100. H.K.D.H. Bhadeshia, Acta Metall. 29 (1981) 1117.

101. H.K.D.H. Bhadeshia and A.R. Waugh, Acta. Metall. 30 (1982) 775.

102. K.R. Kinsman and H.I. Aaronson, in "Transformation and Hardenabilty in Steel", (Climax Molybdenum Company, Ann Arbor, MI, 1967) p. 39.

103. H.K.D.H. Bhadeshia, in "Phase Transformations in Ferrous Alloys", ed. A.R. Marder and J.I. Goldstein (The Matallurgical Society of AIME, 1983) p. 293.

104. C Zener, Trans. AIME, 167 (1946) 50.

105. H.K.D.H. Bhadeshia, in "Solid → Solid Phase Transformations," ed. H.I. Aaronson et al. (The Metallurgical Society of AIME, 1981) p. 1041.

106. W. Steven and A.G. Haynes, JISI 183 (1956) 349.

107. M. Hillert, Metall. Trans. 6A (1975) 5.

108. V. Raghavan and M. Cohen, Metall. Trans. 2 (1971) 2409.

109. H.K.D.H. Bhadeshia, Metal . Sci., April 1981, p. 175.

110. K. Easterling, in "Introduction to Physical Metallurgy of Welding", (Butterworths, London, 1983) p. 152.

111. G.R. Speich., V.A. Demarest and R.L. Miller, Met. Trans. 12A (1981) 1419.

112. C.I. Garcia and A.J. Deardo, Met. Trans. 12A (1981) 521.

113. M.M. Souza., J.R.C. Guimaraes and K.K. Chawla, Met. Trans. 13A (1982) 575.

114. G.R. Speich., R.L. Miller, in "Solid → Solid Phase Transformations", ed. H.I. Aaronson et al. (The Metallurgical Society of AIME, 1981) p. 843.

115. C.I. Garcia and A.J. Deardo, ibid., p. 855.

116. S.W. Thompson., G.S. Fan and P.R. Howell, in "Phase Transformations in Ferrous alloys", ed. A.R. Marder et al. (The Metallurgical Society of AIME, 1984) p. 43.

117. X.L. Cal., A.J. Garratt-Reed and W.S. Owen, Met. Trans. 16A (1985) 543.

118. D.Z. Yang., E.L. Brown., D.K. Matlock and G. Krauss, Met. Trans. 16A (1985) 1523.

119. E. Navara., B. Bengtsson and K.E. Easterling, Mater. Sci. and Tech. 2 (1986) 1196.

120. M. Hillert and G.R. Purdy, Acta Metall. 26 (1978) 333.

121. R.W. Balluffi and J.W. Cohn, Acta Metall. 29 (1981) 493.

122. C. Li and M. Hillert, Acta Metall. 29 (1981) 1949.

123. N. Nemoto, Met. Trans. 8A (1977) 431.

124. G.A. Roberts and R.F. Mehl, Transaction ASM, 31 (1943) 613.

125. G.R. Speich and A. Szirmae, TMS-AIME, 245 (1969) 1063.

126. A. Roosz., Z. Gacsi and E.G. Fuchs, Acta Metall. 31 (1983) 509.

127. R.R. Judd and H.W. Paxton, TMS-AIME, 242 (1968) 206.

128. M. Hillert., K. Nilsson and L.E. Torndahl, JISI, 209 (1971) 49.

129. G.R. Speich and H. Warlimont, JISI 206 (1968) 385.

130. W.L. Haworth and J. Gordon Parr, Trans. ASM 58 (1965) 476.

131. G. Thomas and J.Y. Koo, "Structure and Properties of Dual-Phase Steels", ed. R.A. Kot and J.W. Morris, (The Metallurgical Society of AIME, Warrendale, 1979) p. 183.

132. J.Y. Koo and G. Thomas, Met. Trans. 8A (1977) 525.

133. M.R. Plichta and H.I. Aaronson, Met. Trans. 5 (1974) 2611.

134. S. Matsuda and Y. Okamura, Trans. ISIJ, 14 (1974) 445.

135. S. Watanabe and T. Kunitake, ibid., 16 (1976) 29.

136. S. Matsuda, in "Proceedings of First JIM International Symposium on the New Aspects of Martensitic Transformation", (The Japan Institute of Metals, Kobe, 1976) p. 363.

137. S. Watanabe., Y. Ohmori and T. Kunitake, ibid., p. 369.

138. J.W. Christian, "The Theory of Transformation in Metals and Alloys", 2nd. ed. Part I (Pergamon, Oxford, 1981) p. 418.

139. A.E. Nehrenberg, Trans. AIME 188 (1950) 162.

140 K.J. Ivine and F.B. Pickering, JISI 201 (1963) 944.

141. M.F. Ashby and K.E. Easterling, Acta Metall. 30 (1982) 1969.

142. M.F. Ashby and K.E. Easterling, Acta Metall. 32 (1984) 1935.

143. J.C. Ion., K.E. Easterling and M.F. Ashby, Acta Metall. 32 (1984) 1949.

144. E. Räsänen and J. Tenkula, Scand. J. Metallurgy 1 (1972) 75.

145. P.J. Alberry and W.K.C. Jones, Metal Technology 9 (1982) 419.

146. P.J. Alberry and W.K.C. Jones, Metal Technology 4 (1977) 360.

147. K.E. Easterling, "Introduction to the Physical Metallurgy of Welding", (Butterworths, London, 1983) p. 184.

148. D. Rosenthal, Trans. Am. Soc. Metals 68 (1946) 849.

149. K. Easterling, "Introduction to the Physical Metallurgy of Welding", (Butterworths, London, 1983) p. 114.

150. H.S. Ferguson and D.L. Hollinger, "Advances in Welding Science and Technology", ed. S.A. David, (Metal Park. OH: American Society for Metals, 1987) p. 279.

151. G.A. Roberts and R.F. Mehl, TMS-AIME 154 (318) 1943.

152. K.E. Easterling, "Advances in Welding Science and Technology", ed. S.A. David, (Metal Park, OH: American Society for Metals, 1987) p. 177.

153. J.W. Cohn, Acta Metall. 10 (1962) 789.

154. H. Hu and B.B. Rath, Metall. Trans. 1 (1970) 3181.

155. P.J. Alberry., B. Chew and W.K.C. Jones, Metals Tech. 4 (1977) 317.

156. H.K.D.H. Bhadeshia, Metal Science 16 (1982) 159.

157. C. Zener, Trans. AIME, 167 (1946) 50.

158. K.C. Russell, Acta Metall. 17 (1969) 1123.

159. BISRA, 'Atlas of isothermal transformation diagram of B.S. En steels'. Special report no. 56, 2ed. (1956), London, The Iron and Steel Institute.

160. K. Easterling, 'Introduction to the Physical Metallurgy of Welding', (Butterworths, London, 1983) p. 93.

161. D.J. Abson and R.J. Pargeter, International Metals Review 31 (1986) 141.

162. E. Räsänen and J. Tenkula, Scandinavian Journal of Metals, 1 (1972) 75.

163. H.K.D.H. Bhadeshia, Mater. Sci. and Tech. 1 (1985) 497.

164. H.K.D.H. Bhadeshia, Journal de Physique, Collogue C4, No. 12, Vol 43, 1982, P.C4-443.

165. D.J. Dyson and B. Holmes, JISI 277 (1970) 469.

166. B.D. Cullity, 'Elements of X-ray Diffraction', Addison-Wesley, Reading, N.Y., (1956) p. 330.

167. W.C. Leslie, 'The Physical Metallurgy of Steels', international student edition, NcGraw-Hill, Inc., (1982) p. 111.

168. R.P. Smith, Acta Metall. 1 (1953) 578.

169. R. Trivedi and G.M. Pound, J. Appl. Phys. 38 (1967) 3569.

170. P. Hirsch, A Howie, R.B. Nicholson, D.W. Pashley and M.J. Whelan, "Electron Microscopy of Thin Crystals", Robert E. Krieger, N.Y. (1977); (a) p. 422; (b) p. 416, (c) p. 510.

171. R.K. Ham, Phil. Mag. 6 (1961) 1183.

172. J.W. Steeds, Institute of Physics Conference on Eletron Microscopy (1963), Cambridge.

173. M.R. Staker and D.L. Holt, Acta Metall. 20 (1972) 569.

174. L.E. Murr, "Electron Optical Applications in Materials Science", McGraw-Hill (1970) p. 320.

175. J.W. Edington, "Practical Electron Microscopy in Material Science", MacMillan, London, (1975) p. 119.

176. H.K.D.H. Bhadeshia and D.V. Edmonds, Metal Science 17 (1983) 411.

177. H.K.D.H. Bhadeshia and D.V. Edmonds, Metal Science 17 (1983) 420.

178. J.W. Christian, "Theory of Transformations in Metals and Alloys", Part 1, 2nd., Pergamon Press, Oxford (1975), p. 17.

179. A.A.B. Sugden and H.K.D.H. Bhadeshia, Unpublished research based on the method of J.S. Kirkaldy, B.A. Thomas and E. Bagains, "Hardenability Concept with Applications to Steel", Ed. D.V. Doane and J.S. Kirkaldy, Pub. ASM, Warrendale, U.S.A. 1977, p. 82.

180. H.K.D.H. Bhadeshia and A.R. Waugh, Acta Metall. 30 (1982) 775.

181. Unpublished work.